THE UNIVERSITY OF CHICAGO

INFRARED CARRIER DYNAMICS IN MERCURY CHALCOGENIDE QUANTUM DOTS: FROM FUNDAMENTAL SPECTROSCOPY TO NEXT-GENERATION OPTOELECTRONICS

A DISSERTATION SUBMITTED TO
THE FACULTY OF THE DIVISION OF THE PHYSICAL SCIENCES
IN CANDIDACY FOR THE DEGREE OF
DOCTOR OF PHILOSOPHY

DEPARTMENT OF CHEMISTRY

BY
CHRISTOPHER MELNYCHUK

CHICAGO, ILLINOIS
DECEMBER 2022

To my family.

"Understand the physics, write down the correct equations, then let Nature do the calculations!"

-Peter Debye, as told by Richard Bersohn

TABLE OF CONTENTS

LIST OF FIGURES

LIST OF TABLES

ACKNOWLEDGMENTS

I first wish to express my gratitude to my advisor, Prof. Philippe Guyot-Sionnest. His group was nowhere to be found in my application materials for the University of Chicago, and I only added him to my meeting list in a moment of serendipity upon finding that I had an (optional) unfilled slot. I am so glad that I did. His sharp intuition, intellectual integrity, and total command of the "basics" set the high standards which I hope to maintain in my professional life, and I have tried to absorb as much as possible his keen sense for when rigor is needed and when "good enough" is sufficient. Above all, I will miss his generosity, language quirks, and palpable verve for science. It has been a great pleasure to work alongside somebody who so clearly loves what he does.

I am also grateful to the other members of my thesis committee, Profs. Norbert Scherer, Dmitri Talapin and Gregory Engel, for their many insightful questions and comments during and after my defense. All three of them brought rather different and valuable perspectives to my work, and it was an honor to have captured their attention and interest.

Two outstanding professors at the University of Rochester deserve special mention. The first is my undergraduate research advisor, Prof. Lewis Rothberg. He welcomed me into his lab, handing me keys and complete freedom to explore, fail and learn as much as I could. His close, personal mentorship played an enormous role in my decision to pursue a PhD, and I will always admire his philosophical approach to science and life. The second is Prof. James Farrar, who through his quantum mechanics course opened my eyes to the wonders of physical chemistry. Those lectures remain my personal benchmark for engagement and clarity. Prof. Farrar was also an invaluable source of counsel as I explored the possibility of graduate school.

My graduate work would not have been possible without the shared facilities available in the James Franck Institute and MRSEC. I am particularly grateful to Luigi Mazzenga, who taught me everything I know about machining; without his guidance, my fabrications of innumerable sample cells, mounts and gizmos would surely have been a much slower and sloppier undertaking.

Past and present members of the PGS group have enriched my time in graduate school as

sources of camaraderie and insightful discussions, and Ananth Kamath and Matthew Ackerman deserve particular mention for their friendship within and beyond the lab. Ananth has been a wonderful conversation partner and desk neighbor, and I always appreciated his willingness to selflessly contribute time and mathematical cleverness to a problem I was struggling with. Matt was Ananth's desk predecessor, and he and I were often the last ones working in the lab during the early years. More often than not, a quick question or chat between measurements evolved into a wide-ranging discussion stretching long into the night, and I will miss his rare breed of curiosity.

I have been fortunate to develop many colleagues and friends during my time in Chicago. Working with Lauren McNamara on infrared molecular photophysics during the past few months has been an unexpected treat, and I have enjoyed watching our relationship evolve from that of a host and a prospective student to a fruitful scientific collaboration. Teaching the Modern Materials and Technology colloquium at Lindblom Math and Science Academy has also been immensely gratifying, thanks in no small part to the support from Chicago Public Schools and many individuals at the University. I am particularly indebted to Ed Hershey, Wennie Wang, James Callahan, Bipul Pandey and Jeff Gustafson for their roles in making the course a reality for four consecutive years, and to Caitlin Bellora and Spencer Guo for assisting at a time when help was hard to come by.

Jonathan Fetherolf, Malte Lange, Ayush Gupta, Laura Tociu and Harry Ryu were the source of many fond memories at the Pub and in the Kent basement offices during the early years. Lukas Whaley-Mayda has been a consistent source of thoughtful insights on nonlinear spectroscopy, craft beer and classical music. It has also been incredible fun to have Lawson Lloyd, Greta Koerner, Maggie Kelty and Tim Grabnic as "roommates" and friends. Together we cover a lot of ground in personalities, tastes and viewpoints, and one would be hard-pressed to construct another group that can so naturally flow between the serious and ridiculous during an evening of drinks and conversation.

Perhaps the most unexpected and pleasurable surprise in Chicago has been my companionship

with Hannah Yi. She gave me cause to seek a more balanced blend of personal priorities, and our time together has been a source of incredible joy.

I finally wish to thank my mother, father, sister and grandparents for their love, support and guidance throughout my entire life. I owe so much of who I am to you.

ABSTRACT

The mercury chalcogenide quantum dots are an emerging class of infrared nanomaterial being developed as next-generation infrared photodetectors and light sources. Although considerable progress has been made on the development of near- and mid-infrared detectors and light sources based on these systems, the basic material photophysics remains relatively unexplored. In this thesis, I describe time-resolved spectroscopy investigations of HgTe and HgSe quantum dots in the near- and mid-infrared. Transient absorption measurements on HgTe show that biexciton Auger recombination is much slower than in bulk materials of similar gaps, and comparable to that in quantum dots with gaps an order of magnitude larger. This suggests that the Auger mechanism is modified in quantum dots compared to bulk semiconductors, and possibly scattering-assisted. Using a simple detailed-balance model of thermal carrier generation and recombination in an HgTe quantum dot solid, I then show how the slow Auger recombination leads to thermodynamic detector performance limits which exceed those of commercial devices by an order of magnitude. In HgSe, transient photoluminescence upconversion measurements show near-total Auger suppression in mid-infrared *n*-type particles and typical quantum dot Auger behavior in near-infrared intrinsic particles. Auger suppression is a fundamental benefit for mid-infrared photodetection and lasing, and this phenomenon is ascribed to the different densities of states in the two situations. In the single-exciton regime, spectrally-resolved photoluminescence dynamics reveal conduction fine structure and direct phonon-mediated intersublevel relaxation at early times. The mid-infrared nonradiative relaxation at longer times is investigated through quantum yield and lifetime measurements on *n*-type HgSe and HgSe/CdS core/shell structures. Modeling indicates that near-field energy transfer to infrared-absorbing species remains the dominant nonradiative pathway out to the regime of several nanoseconds, and the ~2% quantum yields measured in thick-shell *n*-type HgSe/CdS are the largest reported to date in mid-infrared colloidal nanomaterials. This thesis highlights several unique aspects of carrier dynamics in small-gap quantum dots, and it fundamentally justifies continued work on devices made from these materials.

CHAPTER 1

INTRODUCTION

1.1 Background and Motivation

Quantum dots are a class of semiconductor nanomaterial in which all dimensions exist at the length scale of roughly ten nanomaters (ten billionths of a meter) or less. In this special regime where quantum confinement effects become particularly pronounced, quantum dots exhibit electrical and optical properties which are seldom observed in nature [1, 2, 3, 4, 5]. This can have significant consequences for the operating characteristics of optoelectronic devices which are made from these materials. Quantum dots are prepared by simple solution chemistries to form ink-like colloidal suspensions, enabling simple fabrication of conventional devices and the creation of new devices which are difficult or impossible to realize with traditional "hard" materials [6]. The colloidal nature also facilitates direct tuning of electrical and optical properties through chemistry [2]. This unique set of characteristics opens up the potential for quantum dots to bring about impactful advances to a variety of emerging and everyday technologies.

The infrared, depicted in Figure 1.1, holds particular promise for technological disruption from quantum dots because incumbent technologies remain especially expensive despite decades of research [7]. Infrared technology is economically dominated by bulk semiconductor photon detectors based on single crystals of InGaAs, InSb, InAsSb, and HgCdTe [7, 8, 9]. Growth of these crystals is difficult and time-intensive, and detectors are created by interfacing the crystals to silicon readout electronics using the delicate process of "flip bonding." Infrared detectors also operate best when cooled, and the overall situation creates bulky, costly devices. The gold standard beyond 3 μm is the HgCdTe photovoltaic. This mature technology offers fast, sensitive detection at the fundamental limits imposed by the HgCdTe band structure [10, 11]. The most developed SWIR material is InGaAs, operating out to 2.6 μm. InGaAs detectors do not reach fundamental material limits, however, and their performance drops substantially beyond 1.7 μm due to imperfect lattice

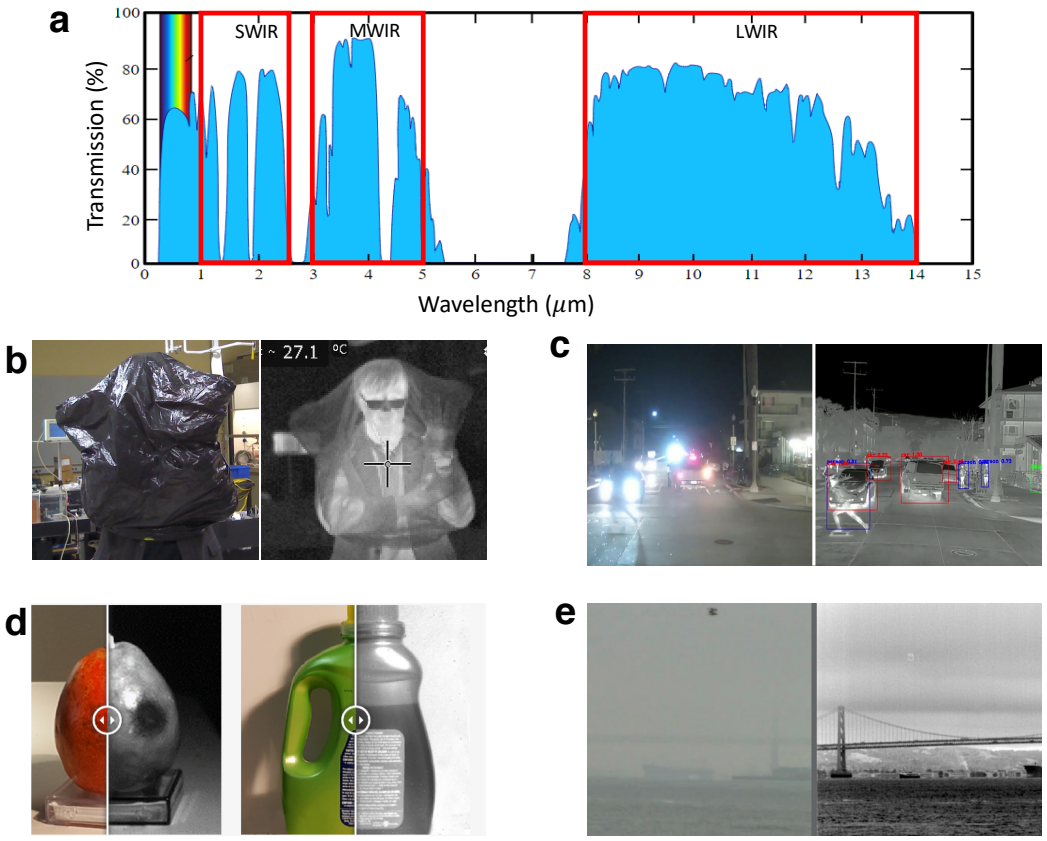

Figure 1.1: Summary of the infrared spectrum and practical applications. (a) Transmission spectrum of Earth's atmosphere with the short-wave infrared (SWIR), mid-wave or mid-infrared (MWIR), and long-wave infrared (LWIR) bands denoted; (b) visible (left) and LWIR (right) image of the author's advisor inside a trash bag; (c) visible (left) and MWIR (right) images of a busy traffic intersection at night; (d) visible and SWIR images of bruised fruit and a detergent bottle; (e) visible (left) and SWIR (right) images of the Golden Gate Bridge in fog. Images courtesy of Teledyne Judson (c) and SWIR Vision Systems (d, e).

matching with InP substrates. Infrared light sources face many of the same challenges as infrared detectors. They are dominated by quantum well lasers, LEDs and thermal blackbody emitters offering even more severe performance-cost tradeoffs than infrared detectors [12, 13, 14, 15]. Beyond the traditional focus on military and astronomy applications, there is increasing interest in commercial infrared applications such as automated product sorting and evaluation, safe and autonomous driving technologies, and medical diagnostics [7, 16, 17, 18, 19]. Excessive costs have inhibited this widespread adoption, motivating the development of new and inexpensive infrared

materials.

Mercury chalcogenide quantum dots have received growing attention over the past decade for their potential as next-generation infrared detectors [20, 21, 22, 23, 24] and light sources [25, 26], and the performances of SWIR and MWIR HgTe photovoltaic detectors are approaching those of commercial devices [27, 28]. Quantum confinement allows complete spectral tunability, and the solution-processable nature leads to simplified device fabrication. Solution-processing has also been exploited to demonstrate fundamentally new device designs and functionalities [28, 29, 30, 31, 32]. This offers the enticing possibility of superior device performances at greatly reduced costs.

Although there has been considerable applied work on mercury chalcogenide devices, there have been relatively few fundamental investigations of the material photophysical properties. Yet, these are the very characteristics which set the upper limits on achievable device performances [33, 34]. The ultimate competitive viability of infrared detectors and light sources made from these materials can therefore be addressed via basic spectroscopic investigations.

In tandem, mercury chalcogenide quantum dots present a unique platform for the more general study of electronic structure and carrier dynamics in confined semiconductors. The small infrared energy gaps enable facile doping and steady-state study of features traditionally associated with excited states, and they minimize spectroscopic artifacts associated with high-energy charges. General perceptions of quantum dot behavior have been overwhelmingly shaped by the study of large-gap quantum dots such as CdSe and PbS, and the degree to which "prototypical" quantum dot behaviors generalize at lower energies is not known. From a different perspective, the infrared presents the special situation of electronic transitions which lie in the same energy range as molecular vibrations. This enables the direct study photophysical mechanisms which are harder to access in conventional systems.

This thesis describes some of the first time-resolved spectroscopic studies of single and multi-carrier lifetimes in HgTe and HgSe quantum dots, and discusses their implications for fundamental

device performance limits. The following sections introduce quantum dots and the mercury chalcogenides, followed by an overview of infrared nonradiative processes. We then connect nonradiative processes to the operating limitations of quantum dot devices, and the chapter concludes with an outline of the subsequent chapters.

1.2 An Introduction to Mercury Chalcogenide Quantum Dots

Quantum dots occur when electrons, holes, or electron-hole pairs are confined in all three dimensions to length scales on the order of their natural quantum-mechanical size. In this regime the charges display well-defined orbital angular momenta and their energy spectra become discrete, hence the common description of quantum dots as "artificial atoms." Quantum dots are most commonly realized as small semiconductor crystals with surface ligands that impart colloidal stability and passivate undercoordinated surface atoms. These structures are usually made through controlled nucleation and growth in a supersaturated solution of chemical precursors [2]. Known as colloidal or nanocrystal quantum dots, they constitute the sole focus of this thesis. Quantum dots may also be realized as small regions of narrow-gap semiconductor epitaxially embedded in or grown upon semiconductor with a wider gap. These are known as epitaxial or surface-grown quantum dots. A simple description of quantum dot physics is given in the following paragraphs, followed by an overview of the mercury chalcogenides. A more detailed treatment of quantum dots with additional general references may be found in Appendix A.

A good intuition for the physics of quantum dots comes from the introductory quantum mechanics problem of a particle in a box. When a particle of mass m is confined to an infinitely-deep potential energy well (a "box") of length L, the particle cannot possess any kinetic energy value, as it can when unconfined. The energy instead takes on discrete values $E_n = n^2\pi^2\hbar^2/8mL^2$ where $\hbar$ is the reduced Planck constant and n is any positive integer. The lowest possible kinetic energy is therefore nonzero, and the particle is always in motion. The inverse dependence of E_n on L exemplifies the so-called confinement effect *i.e.* an increasing kinetic energy with decreasing length

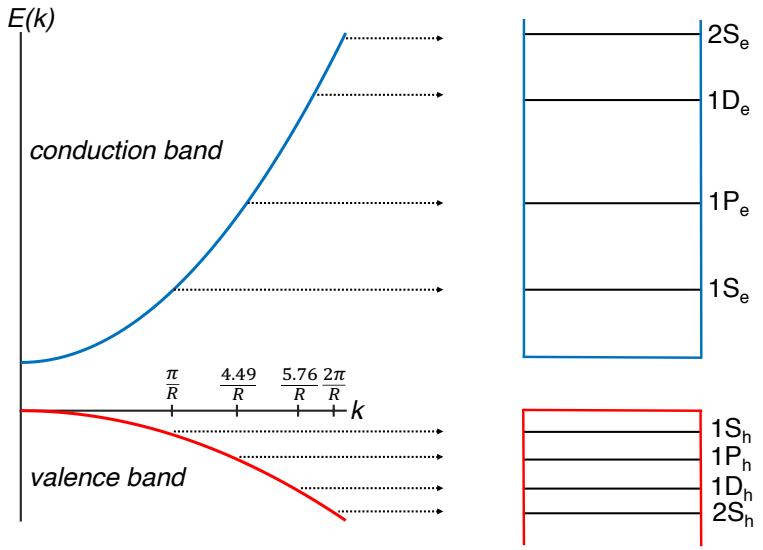

Figure 1.2: Illustration of the generic relationship between bulk semiconductor bands and quantum dot single-particle energy levels for parabolic bulk dispersion. The quantum dot states are labeled as nL where n is the principal quantum number and L gives the orbital angular momentum following the atomic naming convention. e and h subscripts denote electron and hole levels.

scale. This feature is characteristic of all quantum systems as a manifestation of the Heisenberg relation $\Delta p \Delta q \geq \hbar/2$ relating the momentum standard deviation Δp to the position standard deviation Δq. Indeed, taking $\Delta q = L$ with a kinetic energy $(\Delta p)^2/2m$, by simple substitution we obtain an energy uncertainty $\hbar^2/8mL^2$ displaying all the general features outlined above.

The defining property of a bulk semiconductor is the presence of an energy gap between a continuum of filled states, called the valence band, and a continuum of empty states, called the conduction band. In the parabolic band approximation, single-particle energies take the form $E = \hbar^2 k^2/2m^*$ where m^* is the effective mass and k is the wavevector [35]. Parabolic conduction and valence bands are shown on the left side of Figure 1.2. For a particle in a three-dimensional spherical "box," k takes on discrete values which depend on the sphere radius R and the first few values are shown on the k axis. The resulting energy levels are shown on the right.

Promotion of an electron from the valence to the conduction band, for example by photon absorption, creates a positively-charged hole in the valence band. The electron-hole pair is the fundamental excitation in semiconductors and is called an exciton when in a bound state. Al-

though excitons in bulk semiconductors only persist when the electron-hole Coulomb attraction exceeds the thermal energy, the physical boundaries of the nanocrystal force the charges into spatial proximity, and quantum dot excitons can always exist in the absence of trapping. The Coulomb interaction is usually weak compared to the confinement energy so quantum dot excitons can often be approximated as quasi-independent electrons and holes. A significant exception occurs when quantitative knowledge of the valence states is required, for example in highly accurate calculations of interband relaxation rates and excitonic level structure. Valence states are usually very closely spaced, either due to large effective masses or multivalley band character, and this promotes complex level splitting and mixing.

The mercury chalcogenides are II-VI semiconductors of zincblende crystal structure [36, 37, 38]. HgTe is the most widely studied mercury chalcogenide due to its relation to HgCdTe for infrared detection applications, and the entire family of compounds has received attention as topological insulators [39]. Bulk HgTe is a semimetal with an inverted band structure, meaning the conduction band is *p*-like and the highest valence band is *s*-like [36, 38, 40]. Due to the lack of a bulk gap, the quantum dot gap is tunable throughout the entire infrared, from the SWIR to the THz regime [41, 42, 43, 44, 45]. The band structure of HgTe is shown in Figure 1.3a and the electronic structure of HgSe is rather similar. Bulk HgS displays a positive gap of about 0.5 eV (4000 cm^{-1}) and normal band structure [36, 40].

In the form of quantum dots, all three mercury chalcogenides display well-defined excitonic structure in absorption [41, 42, 43, 5, 48]. These features are most visible in HgTe due to the larger particle sizes typically studied, and the smaller relative effect of a typical diameter polydispersity of $\sim$ 10%. The interband $1S_h - 1S_e$ transition redshifts upon cooling in HgTe and HgSe due to conduction band flattening, and the stronger effect at larger particle sizes has been attributed to electron-phonon effects in HgTe [49].

The absolute positions of mercury chalcogenide conduction bands are low relative to the typical environmental Fermi level, as shown in Figure 1.3e. This leads to natural *n*-doping in the

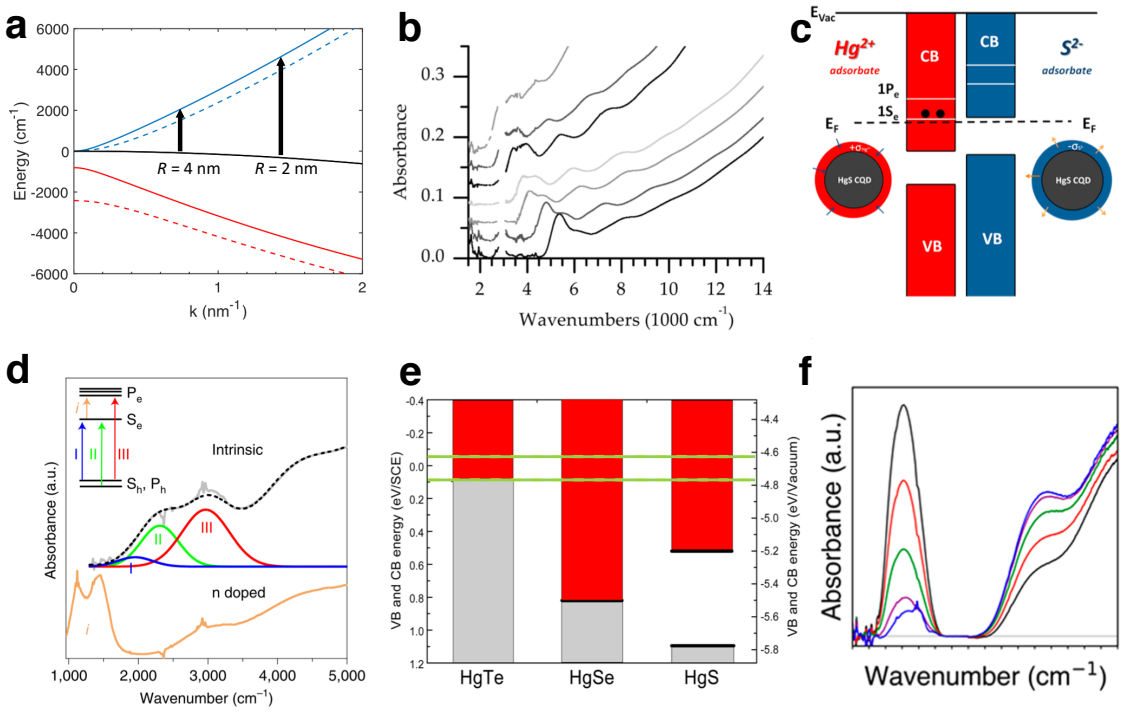

Figure 1.3: Representative data on mercury chalcogenide quantum dots. (a) Band structure of HgTe at 300 k (solid lines) and 80 K (dashed lines) with $1S_h - 1S_e$ absorption labeled at the indicated particle sizes; (b) Optical absorption spectra of intrinsic HgTe quantum dots; (c) Illustration of the electrostatic doping model; (d) Optical absorption spectra of intrinsic and *n*-type HgTe quantum dots with assigned transitions inset; (e) Absolute band positions of bulk HgTe, HgSe and HgS relative to a calomel electrode potential (left) and vacuum (right) with the ambient Fermi level range shown by green bars; (f) Modulation of the intraband and interband absorption in HgSe as a function of surface Cd^{2+} coverage. Figures are adapted and reproduced with permission from [46] (b), [47] (c), [5] (d), [40] (e), [48] (f).

bulk materials, and HgSe, HgS and large HgTe quantum dots. It also enables doping modification through surface chemistry [47, 40, 43]. The surface doping effect in mercury chalcogenide quantum dots is usually viewed through an electrostatic picture wherein surface adsorbates shift the quantum dot state energies relative to a fixed Fermi level [40, 47, 50, 51]. Positive surface adsorbates lower the internal potential to promote *n*-doping, while negative adsorbates produce the opposite effect, as shown in Figure 1.3c. The optical consequences of this effect are illustrated in Figure 1.3f for Cd-treated HgSe, showing bleaching of the interband absorption and growth of the intraband absorption upon increasing Cd^{2+} surface coverage. The absolute band positions are

such that HgTe is rather ambipolar, while HgSe and HgS are most stable when intrinsic or n-type. Very strong n-doping has been observed in HgS quantum dots, leading to metal-like behavior and surface plasmon resonances [52]. Although these electrostatic effects apply to any quantum dot system, they have less direct relevance on the optics at wider gaps due to the small electrostatic potentials which are easily achievable [50]. Systematic n-doping allows the direct study of the conduction states which would otherwise be accessible only through excited state spectroscopy. The $1S_e - 1P_e$ intraband absorption in HgTe has received the most attention, and it displays a rich fine structure derived from spin-orbit coupling and particle shape effects on $1P_e$ [42, 53, 54]. HgSe also shows evidence of conduction fine structure, as discussed in Chapter 3.

1.3 Concepts and Theories in Infrared Quantum Dot Photophysics

Photophysics describes the manner in which excitations dissipate energy. This dissipation can occur by radiation production (luminescence), excitation of the electronic or vibrational environment, and the initialization of chemical reactions. In most device applications one wishes to maximize the luminescence efficiency, while environmental excitation is the dominant nonradiative pathway which must be suppressed. Quantum dots provide an especially rich landscape for photophysical investigations due to their unique place in the zone between molecules and bulk materials, and they display behaviors which are characteristic of both regimes. Furthermore, infrared quantum dots can display phenomena not ordinarily seen at higher energies because electronic and vibrational energies are comparable. Infrared photophysics in quantum dots was traditionally studied in the context of excited-state $1P_e - 1S_e$ relaxation in neutral systems [55, 56, 57, 58, 59, 60]. In the mercury chalcogenide quantum dots, however, infrared photophysics is relevant even for the lowest excited state, either the $1S_h - 1S_e$ interband exciton in intrinsic systems or the $1S_e - 1P_e$ intraband exciton in n-type systems, and it directly affects the gross features of device operation. In this section we provide an introduction to the general photophysical phenomenology of quantum dots, with an emphasis on mechanisms which are modified or especially prominent in the infrared.

1.3.1 Radiative and nonradiative recombination

Central concepts in photophysics are the distinctions between radiative and nonradiative recombination or relaxation, and the competition between them. This competition is typically quantified by the radiative quantum yield ϕ which gives the probability that an excited electron emits a photon in terms of the radiative rate γ_r and the rates γ_{nr} of various nonradiative processes:

$$\phi = \frac{\gamma_r}{\gamma_r + \gamma_{nr1} + \gamma_{nr2} + ...} \tag{1.1}$$

In many different optoelectronic applications, the fundamental performance limits are related to the value of ϕ, and it is desirable to maximize this quantity.

Radiative recombination in quantum dots can be described as the spontaneous dipole emission from a two-level electron. The rate γ_r of this process in cgs units is

$$\gamma_r = \frac{2\omega^2 e^2 f}{mc^3} F^2 \sqrt{\epsilon_2} \tag{1.2}$$

where ω is the light angular frequency, c is the vacuum speed of light, e is the electron charge, m is the free electron mass, f is the oscillator strength, ϵ_2 is the optical dielectric constant of the environment, and $F = 3\epsilon_2/(\epsilon_1 + 2\epsilon_2)$ is a local field screening factor with ϵ_1 denoting the optical dielectric constant of the nanoparticle.

The oscillator strength describes the strength of an optical transition between states $|i\rangle$ and $|j\rangle$ relative to that of a classical electron oscillator at the same frequency as $f_{ij} = \gamma_{r_{ij}}/3\gamma_{r,cl}$ where $\gamma_{r,cl}$ is the classical rate [61, 62, 63]. It obeys a sum rule such that the lowest allowed transition carries the most oscillator strength, and it is calculable from wavefunctions as described in Appendix A. Quantum dot wavefunctions are products of Bloch and envelope functions, and f is dominated by one or the other depending on the optical transition. For interband transitions such as $1S_e - 1S_h$, it depends solely on the Bloch functions because the transition moment between envelope functions of the same angular momentum is zero. For intraband transitions such as $1P_e - 1S_e$, it is dominated

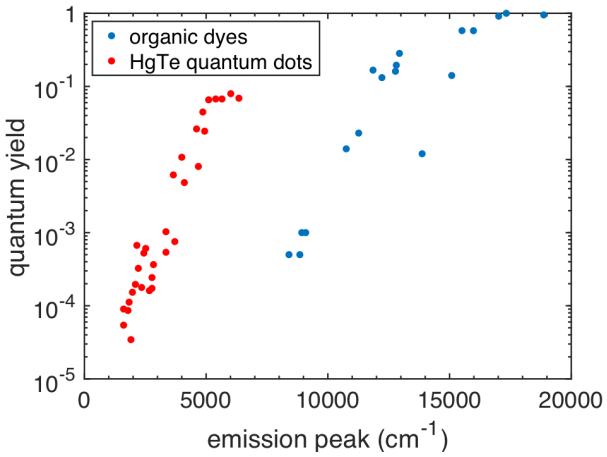

Figure 1.4: Compiled quantum yield data for HgTe quantum dots and organic dyes as a function of the emission peak energy.

by the envelope functions with a smaller Bloch function contribution associated with the latter's k-dependence. Oscillator strengths in near- and mid-infrared mercury chalcogenide quantum dots cover the approximate range 2 - 10, increasing with increasing particle size and decreasing gap energy.

Vacuum radiative lifetimes $1/\gamma_r$ for $f = 1$ increase from 4 ns at 500 nm wavelength (20000 cm^{-1}) and to 400 ns at 5 μm wavelength (2000 cm^{-1}), and the screening situation $\epsilon_1 > \epsilon_2$ further decreases the radiative efficiency in nanoparticle colloidal solutions. This illustrates one difficulty for achieving large quantum yields at low energies in quantum dots – values of γ_{nr} which are negligible in the visible can become very consequential in the infrared.

As shown in Figure 1.4, a strong decrease of the quantum yield at low energies is a generic feature of both organic dyes and HgTe quantum dots [46]. The nonradiative mechanism underlying this behavior is a central question in quantum dot infrared carrier dynamics, and various proposals for its origin include near-field energy transfer, semiclassical and coherent couplings to phonons, and highly nonadiabatic dynamics associated with surface anharmonicities. These mechanisms are discussed below.

1.3.2 Near-field energy transfer

When an excitation is spatially-close to a resonant ground-state absorber, the absorber can act as a source of nonradiative relaxation through the mechanism of near-field energy transfer. In the original formulation, known as Förster Resonance Energy Transfer (FRET), one considers a donor-acceptor dipole pair separated by some distance R and the rate dU/dt at which the donor electromagnetic energy is dissipated by the acceptor. This leads to a nonradiative rate $(dU/dt)/\hbar\omega$ that scales as $1/R^6$ and an absolute magnitude that depends on the acceptor absorption strength and donor radiative rate. Physically, the $1/R^6$ scaling arises from the square of the dipole electric field (itself falling off as $1/R^3$) via the field energy or squared dipole matrix element.

For quantum dots with energy gaps in the infrared, the most relevant situation is slightly different because the environment is often filled with infrared-absorbing material. This comes from the molecular vibrations of organic ligands used to passivate the nanoparticle surface, and possibly from solvents or solid matrices. To calculate the analogue of FRET for absorbing ligands on a nanoparticle surface, one can model the system as a dipole surrounded by a uniform spherical shell of thickness ΔR at a radial distance R. Classically, the dipole electric field drives charges in the shell which are described by a damped equation of motion, and the nonradiative rate is obtained from the energy loss as in standard FRET. In the approximation that the ligand shell is treated as a uniform medium with dissipation characterized by an imaginary dielectric constant ϵ'', the nonradiative rate is

$$\gamma_{nr} = \frac{3\epsilon'' c^3 \gamma_r}{4\omega^3 n} \int_R^{R+\Delta R} \frac{dr}{r^4} \approx \frac{3\epsilon'' c^3 \gamma_r}{4\omega^3 n} \times \frac{\Delta R}{R^4} \tag{1.3}$$

where $n = \sqrt{\epsilon_2}$ is the environmental refractive index and the second step utilizes the approximation $\Delta R \ll R$. The $1/R^4$-dependence here arises from the product of a $1/R^6$ dipole factor and an R^2 spherical surface area. This mechanism was first presented in [58] and a full classical derivation may be found in the supporting information of [64]. An essentially identical expres-

sion was later derived quantum-mechanically [65]. Energy transfer to ligands has been proposed by several groups dominate nonradiative relaxation in a variety of infrared nanocrystal systems [46, 64, 66, 67]. One may also consider the similar situation of a nanocrystal in an absorbing matrix. This can be approximated by integrating the above equation across the entire near-field region $\sim \lambda/n$, giving

$$\gamma_{nr} = \frac{3\epsilon'' c^3 \gamma_r}{4\omega^3 n} \int_R^{\lambda/n} \frac{dr}{r^4} \approx \frac{\epsilon'' c^3 \gamma_r}{4\omega^3 n} \times \frac{1}{R^3} \tag{1.4}$$

where λ is the vacuum wavelength and the second step takes $\lambda/n \gg R$.

There are a few important features to note about the near-field mechanism. First, because the rate is linear in γ_r, quantum yields which are limited by these processes will be independent of the radiative rate. This is a generic feature of nonradiative processes involving near-field dipole coupling and it precludes the use of cavities or other methods that increase ϕ via γ_r. Second, because the coupling occurs through the field, the temperature-dependence of the nonradiative rate will be limited to the variations of ϵ'' and γ_r. Finally, the polynomial dependence on R indicates that larger particles with the same optical properties should exhibit slower nonradiative relaxation. Examples include growing thick type-I shells or comparing intraband and interband lifetimes at the same energy.

Figure 1.5 shows calculations of the quantum yields and nonradiative lifetimes produced by these mechanisms using parameters representative of a mid-infrared HgTe quantum dot film. Typical experimental quantum yields are around 10^{-3} in the mid-infrared, as shown in Figure 1.4, and this does not require very large infrared absorption. As qualitative references in terms of the absorption coefficient $\alpha = 2\pi\epsilon''/n\lambda$, 1 mm of material with $\alpha = 1$ cm^{-1} absorbs just 10% of the optical power, and an absorption coefficient of 0.1 cm^{-1} is that of standard float glass for 600 nm visible orange light. This illustrates the need for a very infrared-transparent nanoparticle environment. Essentially all existing quantum dot synthetic protocols and post-synthetic processing schemes were optimized on visible-gap systems where residual infrared absorption is irrelevant, and this presents a unique challenge in infrared quantum dot chemistry.

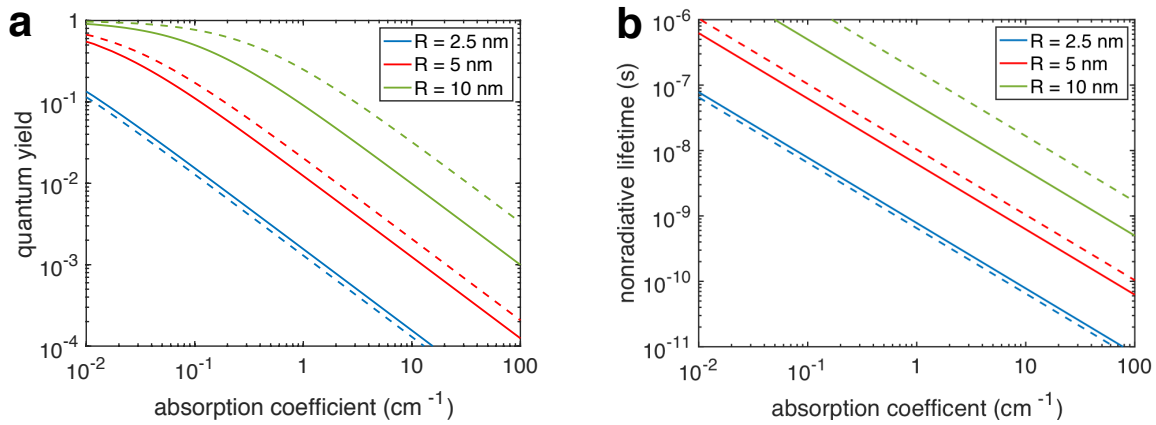

Figure 1.5: Calculated quantum yields (a) and nonradiative lifetimes (b) for energy transfer to the surroundings (solid lines) and 1 nm thick ligand shell (dashed lines) as a function of the absorption coefficient $\alpha = 2\pi\epsilon''/n\lambda$ using $1/\lambda = 2000$ cm^{-1} and $1/\gamma_r = 500$ ns.

Although the near-field mechanism is straightforward, generic, and successfully utilized in Chapter 3, it presents some practical issues when highly accurate predictions are desired for infrared quantum dots. In the early works on excited state intraband relaxation in CdSe quantum dots, it was straightforward to accurately obtain ϵ'' from the nanocrystal absorption spectrum because those systems displayed no ground state electronic infrared absorption [58, 59]. The choice of ΔR, however, involved accurately mapping a surface ligand coverage onto an effective continuous dielectric medium. The true ligand coverage is not easily determined and instead usually derived from a close-packing assumption. For infrared quantum dots, the uncertainty in ΔR remains while the absorption spectrum is completely dominated by the electronic contribution. This forces one to obtain ϵ'' by less precise methods, such as extrapolating from the neat ligand absorption, and this neglects all microscopic details of the real nanoparticle surface.

1.3.3 Quantum coupling to vibrations

Another generic class of nonradiative processes involves quantum mechanical coupling between vibrations and the excitation. Importantly, and in contrast to energy transfer and trapping mechanisms, quantum vibrational mechanisms are intrinsic to the system, and may not be modifiable

depending on the details. Although these mechanisms are generally considered to be mature topics in the photophysics of molecules and semiconductor impurities [68, 69], they have received very little attention in nanocrystal quantum dots. An understanding of their operation in quantum dots will be crucial in quantifying the fundamental upper limits to nonradiative lifetimes and quantum yields.

Quantum vibrational mechanisms can be grouped into three general classes. In the first, initially proposed in the context of small-gap epitaxial quantum dots, the excitation undergoes Rabi-like oscillations with the ground state that are phenomenologically damped by a semiclassical phonon bath [70]. This process does not obey energy conservation but it is numerically reasonable when $E_0 \lesssim 2\hbar\omega_v$ [71] in the notation of Figure 1.6. In the second process, one considers the rate at which an electron thermalized within the excited electronic potential relaxes through weak nonadiabatic coupling to a degenerate vibronic level of the ground electronic potential. This mechanism is quantum-mechanically correct, but the associated calculations are difficult and necessitate various approximations. In the molecular context, development of this model was motivated by the exponential decrease of organic molecular photoluminescence quantum yields with decreasing HOMO-LUMO gap, known as the "energy gap law" [72, 73, 74, 75, 76]. This behavior is illustrated in Figure 1.4. This model's parallel development in solid state physics was motivated by a desire to improve upon the semiclassical Landau-Zener picture for thermal excitation and relaxation of semiconductor impurities [68, 77, 78, 79, 80]. In the third mechanism, known as anharmonic polaronic decay, the excited state is described in a polaron formalism. The polaron decays according to the finite lifetime of the phonon component which arises from anharmonicity. It was developed to improve upon the semiclassical Rabi-type model for epitaxial dots with very small gaps and has been used to successfully model electronic relaxation in those systems [71, 81, 82].

In the most common version of the weak nonadiabatic coupling mechanism, nonradiative relaxation is initiated by the dependence of the excited electronic wavefunction on Q for specific

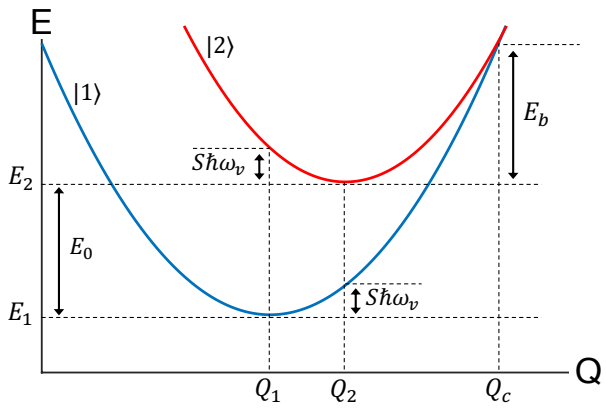

Figure 1.6: Harmonic configuration coordinate diagram for adiabatic electronic states $|1\rangle$ and $|2\rangle$. E is the energy, Q is the nuclear configuration coordinate, ω_v is the angular vibrational frequency, S is the Huang-Rhys factor, $E_b = (E_0 - S\hbar\omega_v)^2/4S\hbar\omega_v$ is the classical energy barrier, and $Q_c = E_0/\sqrt{2S}\hbar\omega_v + \sqrt{S/2} + Q_1$. The reorganization energy is $S\hbar\omega_v$ and $2S\hbar\omega_v$ is the photoluminescence Stokes shift.

vibrational modes, known as the promoting modes [73]. These are traditionally assigned to skeletal modes in organic molecules, and to longitudinal phonons in solids. Accepting modes then act as a sink for the electronic energy, and their ability to do so depends on their Franck-Condon factors. The Franck-Condon factors decrease exponentially with increasing vibrational quantum number in the limit of large quantum numbers [68, 78]. Since the required quanta of accepting vibration increases as $E_0/\hbar\omega$, this produces gap law behavior [68, 75, 76]. The accepting modes in molecules are usually assumed to be to the highest-frequency vibrations, typically the C-H stretches, because this minimizes the number of vibrational quanta; established [83] and recent [84] experimental works, however, indicate that the situation may be more complex. Accepting and promoting modes are usually taken to be the same longitudinal phonon in semiconductors [68, 78, 79, 80]. Closed-form rate expressions in weak coupling require harmonic potentials and $E_0/S\hbar\omega_v \gg 1$, and the resulting approximate rates exhibit monotonic dependencies on E_0. Numerical evaluations of these theories display resonance effects associated with stricter energy conservation that are absent in closed-form expressions [85, 86, 87, 88]. In all formulations, whether for molecules or solids, symmetry considerations and selection rules are assumed to be satisfied.

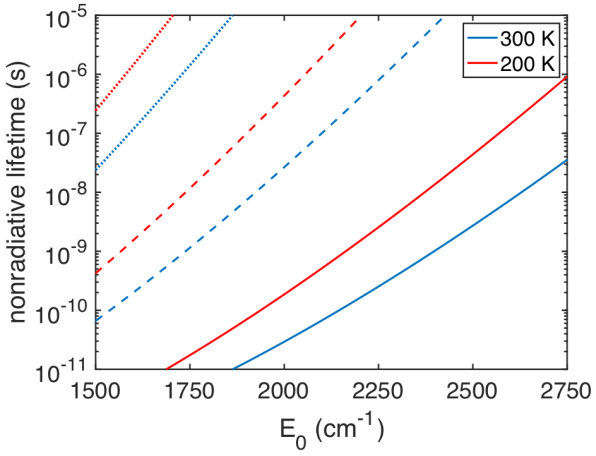

Figure 1.7: Calculated nonradiative lifetimes as a function of the electronic gap E_0 and parameterized to temperature and Huang-Rhys parameter. These smooth curves are obtained by replacing $p!$ with $\Gamma(p+1)$. Calculations used $\omega_v/2\pi c = 140$ cm^{-1}, the LO phonon frequency in HgTe, and Huang-Rhys parameters of 2 (solid lines), 1 (dashed lines) and 0.5 (dotted lines).

As an illustrative example of this mechanism, one may consider the semiconductor impurity model in the limit $E_0 \gg S\hbar\omega_v$. The nonradiative rate is [68, 79, 80]

$$\gamma_{nr} = \gamma_0 (n+1)^p \exp(-2nS) \tag{1.5}$$

where $n = 1/(\exp(\beta\hbar\omega_v) + 1)$ is the Bose-Einstein factor with $\beta = 1/k_B T$, $p = E_0/\hbar\omega_v$ is the nominal number of involved vibrational quanta, and S is the Huang-Rhys parameter. The prefactor is

$$\gamma_0 \approx 0.18 \times 2\pi\omega_v \frac{S^p p(p-1)\exp(-S)}{p!} \times \frac{V_2}{V_1} \tag{1.6}$$

where V_2 and V_1 are the volumes of the two electronic states. In the limit that $\hbar\omega_v \gg k_B T$, this rate exhibits the same dependence on material parameters as the Englman-Jortner formula for molecules [75]. An approximation for quantum dots could be $V_2/V_1 = 1$, and the corresponding nonradiative lifetimes are plotted in Figure 1.7. The strong energy-dependence is associated with the Franck-Condon factors, the lifetimes vary strongly over 100 K, and they are very sensitive to S. These are generic features of nonadiabatic gap-law models involving low-frequency vibrations.

In the polaron model, the excited state is calculated as an eigenstate of the harmonic polaron Hamiltonian and anharmonic perturbations initiate the nonradiative decay [71, 89]. This can be loosely viewed as a variation upon the weak-coupling nonadibatic model in the sense that the former considers a perturbative electron-vibrational coupling and assumes a rapid vibrational relaxation, while the polaron model employs a vibronic (polaronic) eigenstate and perturbatively calculates the vibrational relaxation. The phonon component of the polaron decays into various isoenergetic combinations of acoustic and optical phonons under strict energy and momentum conservation, leading to a nonmonotonic dependence of the overall rate on energy. Absolute rates are governed by the anharmonicity strength and the amount of phonon character in the polaron. Although this model has not been extended to the regime where the polaron energy exceeds more than a few multiples of the optical phonon energy, the average behavior still follows an approximate gap law trend [89].

There has been very little work addressing any of these mechanisms' relevance to mid-infrared quantum dot nonradiative relaxation, and the few attempts to address quantum dot multiphonon relaxation have relied on simulations which are difficult generalize. One study applied the Rabi-like model to intraband relaxation in atomistically-defined CdSe nanocrystals and predicted that $\sim$ 1 ns is the upper limit to the nonradiative lifetimes around 2000 cm^{-1} [90]. Although this would be very significant if correct, it is not clear that the underlying model is valid at these energies. Another atomistic simulation on small CdSe suggested that lifetimes around 200 ps and nonadiabatic couplings around 10 cm^{-1} are characteristic of intraband relaxation at 3200 cm^{-1} [91], also putting into question the fundamental attainability of large infrared quantum yields.

Both of the results above are somewhat inconsistent with expectations formed on the basis of closed-form expressions, but those predictions are complicated by several factors. In the molecular picture, the rate is quadratic in the nonadiabatic coupling and exponential in the mean vibrational frequency, total reorganization energy, and the fraction of the reorganization energy due to accepting modes [75, 76, 85]. These parameters are difficult to obtain without accurate simulations or

sophisticated spectroscopy. Furthermore, different analytical methods applied to the same gross process can produce different absolute rates [86, 87, 88]. The situation improves somewhat in a semiconductor view, but as shown above, these established theories predict lifetimes which are at odds with simulations when conventional parameters ($\sim$ 100 cm^{-1} phonon, $S \lesssim 0.5$) are used. Although molecular dynamics simulations [92, 93] and scattering experiments [94] on lead and cadmium chalcogenides have challenged the conventional picture by revealing the presence of additional broadband vibrations associated with the nanocrystal surface, these vibrations have been associated with small reorganization energies in CdSe [93]. Recent Raman experiments have also suggested that quantum dot excitations may quantum-mechanically couple to high frequency surface ligand vibrations in certain cases [95, 96].

The overall picture of vibrational coupling and relaxation in quantum dots remains unclear even in the model lead and cadmium systems, and there are no data so far on mercury chalcogenides. Experiments can constrain the various models and validate or challenge simulations. If ligand vibrations are involved, the rate should exhibit minimal temperature-dependence due to the higher vibrational frequencies but decrease exponentially with a type-I shell thickness due to tunneling wavefunction overlap. If bulk phonons are active, the rate will be unaffected by type-I shells but show a strong temperature-dependence. If broadband surface vibrations are involved, the rates would be temperature-dependent only if their frequencies are low, and they should decrease even with a thin type-I shell provided that growth is epitaxial. Although prior work on HgTe and HgSe indicated weak effects of temperature and thin type-I shells on the steady-state photoluminescence, suggesting that none of the aforementioned cases apply [46, 97], lifetimes were not measured and the shell qualities were not ideal. Chapter 3 examines the effects of thick, conformal shells on *n*-type HgSe photoluminescence using time-resolved and steady-state measurements, and proposes that quantum vibrational coupling remains of limited relevance even at lifetimes up to several nanoseconds.

1.3.4 Defects and trapping

Defects in crystals are any instance of broken lattice translational symmetry. This can arise through stacking faults or dislocations across crystal planes, and nonbonded orbitals on undercoordinated atoms. Defect states are characterized by their local nature and typically extend over just a few lattice sites. When the defect energy lies within the gap, delocalized carriers can localize at the defect to become "trapped." The rapid nonradiative recombination that typically ensues occurs by quantum coupling to vibrations in the strong coupling regime because S increases with charge density. The nonradiative rate takes the form

$$\gamma_{nr} = \gamma_0 \exp\left(\frac{-E_b}{k_B T}\right) \tag{1.7}$$

where E_b is the classical energy barrier and γ_0 depends on the temperature regime [68, 98].

Defects in quantum dots are typically ascribed to surface atoms with orbitals that are insufficiently passivated by ligands [99, 100]. Modifying the surface chemistry, for example by using improved ligands or by growing an epitaxial type-I shell [101, 100], usually strongly reduces the trapping rate to manifest in the lifetime and quantum yield. Another characteristic feature of trapping is the strong temperature-dependence associated with the energy barrier for relaxation, and temperature-dependent lifetime and quantum yield measurements can provide compelling evidence for or against the relevance of this process. Trapping is by far the dominant nonradiative mechanism in visible and near-infrared quantum dots. All else being equal, trapping effects may be less pronounced at smaller energy gaps due to the lower probability that a defect state has an energy within the gap.

1.3.5 Auger recombination

The nonradiative processes discussed so far involve excitons or single carriers. In bulk semiconductors and quantum dots, however, the system can sustain multiple excitations. The dynamics

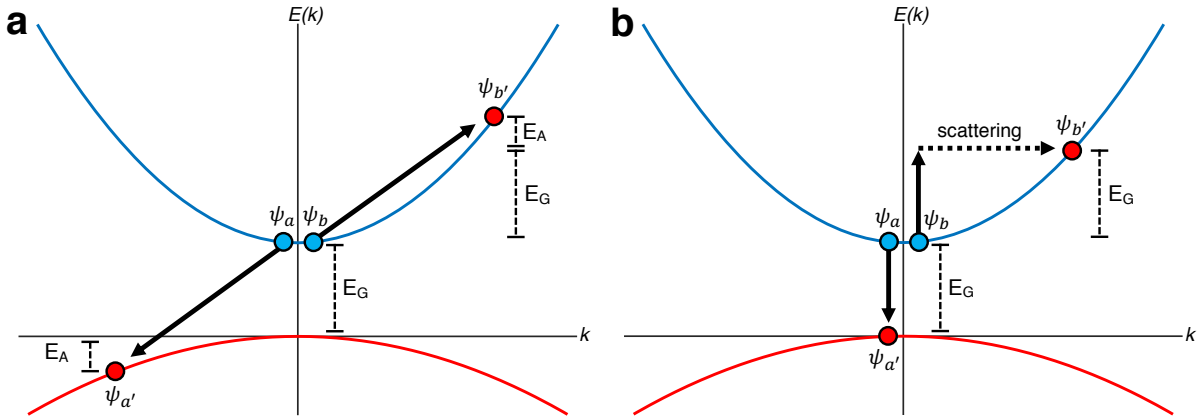

Figure 1.8: Illustrations of electron-electron Auger recombination in semiconductors. (a) "Pure band" Auger recombination; (b) Scattering-assisted Auger recombination. Blue circles are electrons, red circles are holes, E_A is the activation energy associated with simultaneous momentum and energy conservation, E_G is the gap energy, and the ψ denote the wavefunctions for the initial and final states of electrons a and b.

associated with these multicarrier states are primarily governed by nonradiative Auger processes. These are a class of two-carrier scattering phenomena that involve simultaneous excitation of one carrier and relaxation of the other. There are several distinct multicarrier processes and here we focus on Auger ionization and recombination because they dominate multicarrier nonradiative relaxation. These processes involve an interaction between like carriers, with ionization resulting in excitation to a free-particle state and recombination resulting in excitation to a bound state. Both processes manifest as a hastening of the average nonradiative rate with increasing carrier density and are illustrated in Figure 1.8 for the electron-electron interaction. Auger processes have received widespread attention in bulk semiconductors since the late 1950s [4, 102], and they are especially well-studied in small-gap semiconductors because Auger is the main limitation to detector performance in the MWIR and LWIR [10, 103]. Auger recombination in quantum dots were first observed in the late 1980s [104, 105] and has been extensively studied over the past two decades as an essential aspect of quantum dot photophysics [4]. Here we provide an overview of the mechanisms and conceptual issues in quantum dot Auger recombination, and many further details can be found in [4] and the references therein.

Auger recombination in bulk semiconductors is kinetically understood as a three-body process involving two carriers of like sign and one of the opposite sign, and it is often characterized by an Auger coefficient C_A defined by $dn/dt = -C_A n^3$ and $\gamma_A = C_A n^2$, where n is the carrier density and γ_A is the instantaneous rate (reciprocal lifetime). Its fundamental rate is calculated at the unit cell level from the Coulomb interaction through first-order perturbation theory with the initial state being a double excitation near the gap energy, and the final state being a single excitation at at twice the energy. Crystal momentum and energy must be simultaneously conserved in any process involving bands, and this is not possible with both carriers at band extrema unless one band is flat. Auger recombination involving bands therefore exhibits an activation energy associated with the probability that a suitable initial state is thermally populated. This activation energy increases with increasing gap and as m_c^*/m_v^* approaches 1, making the rate very sensitive to temperature, gap energy and band structure.

As the energy gap grows, the theoretical "pure band" process described above becomes orders of magnitude too slow compared to experimental Auger rates, and bulk semiconductors with gaps above $\sim 3000\ \mathrm{cm}^{-1}$ (~ 0.4 eV) exhibit scattering-assisted Auger recombination. Here, an intermediate nonresonant process, usually attributed to scattering from phonons or defects, relaxes the momentum conservation requirement for the carriers in bands. This can be modeled with standard second-order perturbation theory [106, 107, 108, 109, 110] or Green's function methods [111, 112, 113, 114, 115]. Although these interactions are generally much weaker than the first-order Coulomb interaction, the greater number of allowed final states can compensate such that the overall rate is appreciable. Hallmarks of scattering-assisted Auger recombination are rates which are relatively insensitive sensitive to temperature, gap size and band structure. In this regime of larger gaps one also finds that inclusion of excitonic and correlation effects can improve agreement with experiments [115, 116], but this avenue remains relatively unexplored in bulk semiconductors. Overall, however, Auger recombination in the bulk is well understood from both experimental and theoretical perspectives.

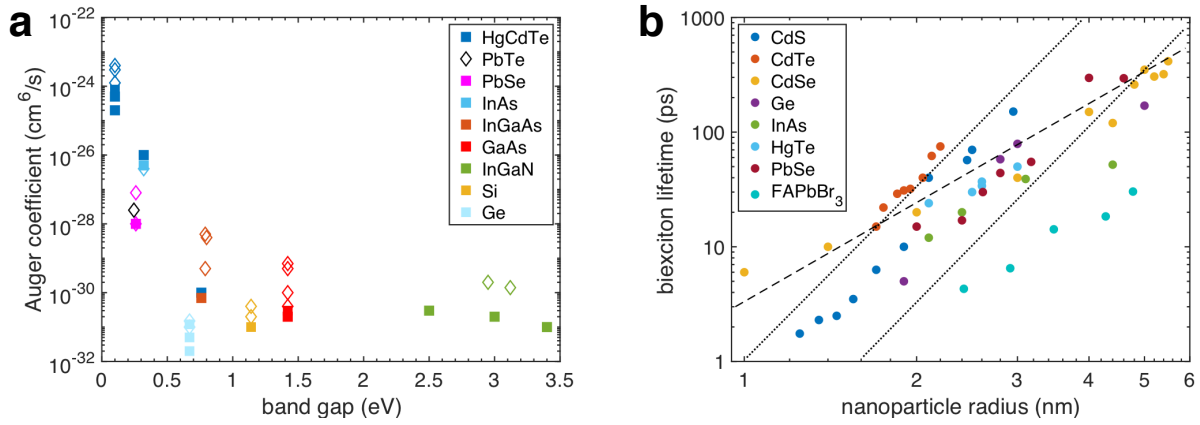

Figure 1.9: Summary of Auger recombination data. (a) Auger coefficients for bulk semiconductors with open diamonds denoting calculated values and filled squares denoting experimental values; (b) Experimental biexciton Auger lifetimes in quantum dots with a generic R^3 curve (dashed lines) and two R^6 curves (dotted lines) corresponding to Auger coefficients of 10^{-29} and 10^{-28} cm^6/s. Adapted with permission from [4].

In quantum dots, Auger recombination may happen as soon as one carrier can interact with an exciton, and it also manifests as a shortened excitonic lifetime. In contrast to bulk semiconductor Auger recombination, however, the mechanisms underlying quantum dot Auger recombination are only partially understood and experiments present a varied and complex phenomenology. The majority of investigations into quantum dot Auger processes have focused on CdSe, with the lead chalcogenides and other systems gaining more recent attention. Most single-component quantum dots display biexciton Auger rates that scale approximately as $1/R^3$ [4], with others scaling as $1/R^6$ [4, 117, 118]. The absolute rates are similar to within an order of magnitude at a given particle size across a variety of materials and gap energies [4, 119], as shown in Figure 1.9b, and the physical origin of this "universal" Auger rate is a central mystery in quantum dot multicarrier dynamics. Biexciton Auger rates are also relatively independent of the gap size as directly tuned through pressure [120]. Experiments also suggest that charge separation, achieved either through hole-extracting ligands or type-II core/shell heterostructures, has relatively small effects on observed Auger rates despite expectations based on wavefunction overlap. The only methods so far which consistently slow Auger rates involve electron delocalization [4].

Although most theories capture the general Auger rate increase in small particles, qualitatively due to the larger Coulomb matrix element, a consistent physical picture of quantum dot Auger recombination remains elusive. One proposed explanation for the R^3 dependence involves viewing the effective biexciton recombination as a two-body process involving an exciton, a single "active" electron or hole, and a spectator charge [4, 121], while another views the processes as involving an uncorrelated pair of true (correlated) excitons [4, 122]. Both imply two-body kinetics, compared to the bulk three-body kinetics, and true excitons were recently invoked to produce the first instance of a cubic trend and quantitative experimental agreement [122]. This calculation, however, utilized an unscreened Coulomb interaction which emphasizes matrix elements occurring near the nanoparticle surface [123] and evidence for surface effects remains varied. Bulk-like analytical models of quantum dot Auger ionization imply surface involvement because high-momentum wavefunction Fourier components are maximized at the sharp particle-matrix interface [124, 125], yet other atomistic studies which explicitly project the states that produce large matrix elements indicate that Auger recombination is an interior process [126]. The insensitivity to charge separation has appeared in simulations [127], but the underlying physics of this effect remains elusive. The general situation in both experiment and theory is one where broad strategies to control Auger rates have been identified, but the mechanisms underlying the observed behaviors have not.

All studies of quantum dot Auger recombination prior to this thesis examined interband transitions and gaps of 5000 cm^{-1} (0.6 eV) or greater, corresponding to the strong scattering-assisted regime in bulk semiconductors and large bulk-like densities of states at $2E_g$ in the nanoparticles. The small-gap mercury chalcogenides allow access to the low energy scales of the bulk pure-band regime where any potential effects of quantum confinement should be even more pronounced. The experiments described in Chapters 2 and 3 introduce quantum dot multicarrier spectroscopy at the lowest energies probed to date, focusing on the interband Auger in HgTe and intraband Auger in n-type HgSe.

1.4 Photophysics in a Device Context

Beyond the interesting fundamental questions surrounding the nonradiative processes discussed above, nonradiative processes determine the intrinsic performance limits of an optoelectronic device when engineering aspects have been optimized. This is particularly relevant in infrared photodetection because HgCdTe already operates at the fundamental limits imposed by its Auger recombination rate [10, 11]. In this section we discuss some device performance metrics in terms of radiative and nonradiative recombination. More detailed treatments of device fundamentals may be found in the texts by Rosencher [33], Sze [34] and Grundmann [128]. Optoelectronic devices may be broadly classified into light collectors, for example solar cells and photodetectors, and light emitters, such as lasers and LEDs. We will focus on detectors here because they are particularly affected by nonradiative processes, but most concepts are broadly applicable and other device categories are briefly discussed as well.

1.4.1 Photodetectors

A photodetector converts light impinging upon the device into charges which are collected at electrodes and read as signal. The overall conversion between the incident optical power P_{in} and the collected photocurrent i_p is quantified by the responsivity $\Re$ with units of amp/W. For a device with no intrinsic gain, it is

$$\Re = \frac{i_p}{P_{in}} = \eta \frac{e}{\hbar\omega} \tag{1.8}$$

where η is the external quantum efficiency.

The external quantum efficiency is a product of the light absorption efficiency η_a, the exciton dissociation efficiency η_d, and the charge collection efficiency η_c. The absorption efficiency depends on the thickness of the absorbing layer and on any photonic enhancement methods which may be used. The dissociation and collection efficiencies are related to the carrier recombination rate. η_d depends on the exciton recombination rate $\gamma_x = \gamma_r + \gamma_{nr}$ and the hopping rate γ_h as

$\eta_d = \gamma_h/(\gamma_h + \gamma_x)$. In mercury chalcogenide quantum dots, $\gamma_x \approx \gamma_{nr}$ and may outpace hopping, especially at lower temperatures [46, 129, 130, 23]. One can increase the dissociation efficiency by increasing the hopping rate, for example by modifying the interfacial chemistry [3, 5, 131, 132], or by reducing the nonradiative rate.

When the exciton dissociates, the free electrons and holes are collected at electrodes with an efficiency η_c that depends on the electrode contact resistance and the average distance traveled by the carriers in comparison to the distance to the electrodes. The average traveled distance can be associated with a diffusion length L_D in the drift-diffusion picture, and it is

$$L_D = \sqrt{\frac{\mu k_B T}{e\gamma_{th}}} \tag{1.9}$$

where μ is the carrier mobility (cm^2/Vs) and γ_{th} is the thermal carrier recombination rate. Thermal recombination rates, discussed at length in Chapter 4, are macroscopic recombination rates that describe a photocarrier interacting with thermally-generated carriers of the opposite sign. γ_{th} therefore depends on the thermal carrier concentration in addition to the fundamental intraparticle recombination rates. It will also contain contributions from both excitonic and multicarrier Auger processes because even at low illumination where no quantum dots are doubly-excited, the exciton dissociation and transport creates a finite probability that some particles will contain more than two carriers. As before, reducing the excitonic and Auger nonradiative rates will benefit device operation until η_c is contact resistance-limited.

The hypothetical perfect detector should not only convert every incident photon into a collected charge, corresponding to $\eta = 1$, but it should also display a minimal level of background noise signal. This is quantified by the specific detectivity D^*

$$D^* = \frac{\Re\sqrt{A\Delta f}}{i_n} \tag{1.10}$$

where A is the sensing area, Δf is the electrical bandwidth, and i_n is the root-mean-square noise

current. The unit of D^*, cm $\sqrt{\text{Hz}}$/W, is known as Jones, and D^* may be viewed as the signal-to-noise ratio normalized to a reference area of 1 cm^2 and an incident optical power of 1 W.

Noise in photodetectors may take the form of photon shot noise, $1/f$ or flicker noise, and Johnson noise [133, 134]. Photon shot noise arises from the Poisson statistics of impinging photons. $1/f$ noise is an unavoidable feature of biased granular conductors [135, 136] and can be a major noise source in photoconductors [137], while it is nominally absent in photovoltaics. The microscopic origins of $1/f$ noise remain poorly understood but it tends to decrease with increasing conductivity, such that it may be indirectly related to nonradiative processes. The Johnson noise is

$$i_n = \sqrt{\frac{4k_BT\Delta f}{R}} \tag{1.11}$$

where R is the resistance. Johnson noise is a generic feature of any conductor even at zero bias. In a detector context, R is the resistance in the absence of external illumination and depends on many factors such as the presence of cracks and voids, the presence of residual ions or other conduction channels which are not quantum dot states, and thermal generation-recombination processes. The first two may be fixed through improved device processing, but thermal generation and recombination is a more basic material property. The thermal generation rate at equilibrium is the thermal recombination rate γ_{th} by the principle of detailed balance, and the associated resistance is

$$R_{g-r} = \frac{2k_BT}{e^2\gamma_{th}} \tag{1.12}$$

γ_{th} therefore sets the fundamental lower limit on the Johnson noise, and by extension, the maximum attainable D^*. Thermal generation-recombination processes depend on the ambient thermal radiation such that overall, when generation-recombination noise dominates, the detectivity becomes

$$D^* = \frac{1}{2\hbar\omega}\sqrt{\frac{\eta\phi_{th}}{\varphi_D}} \tag{1.13}$$

ϕ_{th} is the quantum yield of thermal recombination and φ_D is the 2π blackbody photon flux at the

detector temperature integrated above the gap energy [23]. This formulation of D^* is extensively discussed in Chapter 4.

1.4.2 Solar cells

A solar cell operates according to the same principles as a photovoltaic photodetector, converting incident photons into collected current. In contrast to the detector, however, the goal is simply to maximize the generated electrical power. The open-circuit voltage V_{oc} of a solar cell is a key efficiency metric because it is the largest possible voltage which can be applied by the cell to an external circuit. It will in general experience a reduction from the theoretical maximum E_g/e due to a number of factors including incomplete absorption, below-gap absorption, incomplete charge collection, and nonradiative effects [23, 138, 139, 140, 141]. The magnitude of this open-circuit voltage deficit ΔV_{oc} is therefore one indicator of the overall diode quality, and the nonradiative contribution is

$$\Delta V_{oc,nr} \approx \frac{k_B T}{e} \ln(\phi_{th}) \tag{1.14}$$

This logarithmic dependence on the quantum yield contrasts with the square-root dependence of D^*, indicating that solar cells arguably present a greater tolerance for nonradiative recombination.

1.4.3 LEDs and Lasers

LEDs and electrically-pumped lasers operate through the injection of charges as detectors in "reverse," and the purpose of the device is to promote charge recombination and light extraction. It is clearly advantageous to have ϕ be as large as possible in this case, and indeed, the external quantum efficiency of an LED is simply the product of photoluminescence yield ϕ, the recombination efficiency, and the light extraction efficiency [25]. These can be affected by excitonic and Auger nonradiative processes in the same manner as solar cells and detectors. Auger is particularly relevant at high injection power where it not only reduces carrier lifetimes, but chemically degrades

transport layers via hot carrier generation [4, 142, 143, 144]. Electrically-pumped lasers extend the LED idea to optical amplification but the general ideas remain the same. The exact manifestation of nonradiative processes depends on the energy level structure and pumping scheme, but nonradiative processes generally decrease the lasing efficiency and increase the gain threshold.

1.5 Outline of the Thesis

This thesis describes some of the first transient spectroscopy studies on mercury chalcogenide quantum dots, and the relevance of these studies to infrared photodetection. Chapter 2 introduces the transient absorption and photoluminescence spectroscopy of HgTe quantum dots with an emphasis on size-dependent Auger recombination lifetimes. The Auger rates are found to be remarkably similar to all other quantum dots despite energy gaps that are an order of magnitude smaller, and the mechanistic implications of this observation are discussed alongside the relevance for infrared photodetection. Chapter 3 describes the absorption and photoluminescence spectroscopy of intrinsic and *n*-type HgSe and HgSe/CdS core/shell quantum dots. The mid-infrared transient photoluminescence from *n*-type particles exhibits a rich behavior including a strongly suppressed Auger recombination, near-field energy transfer, and phonon-mediated intersublevel relaxation. The data are discussed in the context of multiphonon relaxation mechanisms. Chapter 4 introduces a simple statistical model that connects the intraparticle recombination rates which are typically measured to the macroscopic thermal rates which are relevant in photodetectors. Using the data from Chapter 2, it is found that the fundamental Auger-limited detectivity of HgTe quantum dot detectors is an order of magnitude higher than the equivalent limit in bulk HgCdTe, the current state-of-the-art. The model further predicts a thermodynamic limit for materials with additional non-Auger nonradiative recombination which is comparable to HgCdTe, indicating that engineering improvements alone may be sufficient to create competitive devices. Avenues for future work are discussed in Chapter 5, and some concluding remarks are offered in Chapter 6. The thesis concludes with three appendices on the topics of nanocrystal electronic structure, infrared nonlinear

optics, and practical optical apparatuses. The first two are included to provide pedagogical, self-contained introductions to these important topics in quantum dot spectroscopy. The final appendix describes the design and operation of the spectroscopic devices used in the experiments of this thesis, with an eye towards future optimizations and advances in instrumentation.

REFERENCES

[1] A. L. Efros and L. E. Brus, "Nanocrystal Quantum Dots: From Discovery to Modern Development," *ACS Nano*, vol. 15, no. 4, pp. 6192–6210, 2021.

[2] D. V. Talapin, J. S. Lee, M. V. Kovalenko, and E. V. Shevchenko, "Prospects of colloidal nanocrystals for electronic and optoelectronic applications," *Chem. Rev.*, vol. 110, no. 1, pp. 389–458, 2010.

[3] P. Guyot-Sionnest, "Electrical Transport in Colloidal Quantum Dot Films," *J. Phys. Chem. Lett.*, vol. 3, no. 9, pp. 1169–1175, 2012.

[4] C. Melnychuk and P. Guyot-Sionnest, "Multicarrier Dynamics in Quantum Dots," *Chem. Rev.*, vol. 121, no. 4, pp. 2325–2372, 2021.

[5] X. Lan, M. Chen, M. H. Hudson, V. Kamysbayev, Y. Wang, P. Guyot-Sionnest, and D. V. Talapin, "Quantum dot solids showing state-resolved band-like transport," *Nat. Mater.*, vol. 19, no. March, pp. 323–330, 2020.

[6] C. R. Kagan, E. Lifshitz, E. H. Sargent, and D. V. Talapin, "Building devices from colloidal quantum dots," *Science (80-.).*, vol. 353, no. 6302, pp. aac5523–aac5523, 2016.

[7] A. Rogalski, *Infrared Detectors*. Boca Raton: CRC Press, 2 ed., 2010.

[8] A. Rogalski, P. Martyniuk, M. Kopytko, P. Madejczyk, and S. Krishna, "InAsSb-based Infrared Photodetectors: Thirty Years Later On," *Sensors*, vol. 20, no. 24, 2020.

[9] A. Rogalski, P. Martyniuk, M. Kopytko, and W. Hu, "Trends in performance limits of the hot infrared photodetectors," *Appl. Sci.*, vol. 11, no. 501, 2021.

[10] W. E. Tennant, ""Rule 07" revisited: Still a good heuristic predictor of p/n HgCdTe photodiode performance?," *J. Electron. Mater.*, vol. 39, no. 7, pp. 1030–1035, 2010.

[11] D. L. Lee, P. Dreiske, J. Ellsworth, R. Cottier, A. Chen, S. Tallaricao, A. Yulius, M. Carmody, E. Piquette, M. Zandian, and S. Douglas, "Law 19: The ultimate photodiode performance metric," in *Infrared Technol. Appl. XLVI*, no. 11407, p. 114040X, 2020.

[12] D. Jung, S. Bank, M. L. Lee, and D. Wasserman, "Next-generation mid-infrared sources," *J. Opt.*, vol. 19, no. 12, p. 123001, 2017.

[13] A. Afonenko, D. Ushakov, A. Dubinov, V. Aleshkin, S. Morozov, and V. Gavrilenko, "Hot phonon effects and Auger recombination on 3 micron room temperature lasing in HgTe-based multiple quantum well diodes," *J. Appl. Phys.*, vol. 132, no. 7, p. 073103, 2022.

[14] K. E. Kudryavtsev, V. V. Rumyantsev, V. Y. Aleshkin, A. A. Dubinov, V. V. Utochkin, M. A. Fadeev, N. N. Ikhailov, G. Alymov, D. Svintsov, V. I. Gavrilenko, and S. V. Morozov, "Temperature limitations for stimulated emission in 3 – 4 μm range due to threshold and non-threshold Auger recombination in HgTe/CdHgTe quantum wells," *Appl. Phys. Lett.*, vol. 117, p. 083103, 2020.

[15] A. J. Muhowski, A. M. Muellerleile, J. T. Olesberg, and J. P. Prineas, "Internal quantum efficiency in 6.1 Å superlattices of 77infrared emitters," *Appl. Phys. Lett.*, vol. 117, no. 6, p. 061101, 2020.

[16] E. Sousa, R. Vardasca, S. Teixeira, A. Seixas, J. Mendes, and A. Costa-Ferreira, "A review on the application of medical infrared thermal imaging in hands," *Infrared Phys. Technol.*, vol. 85, pp. 315–323, 2017.

[17] M. M. Ackerman, "Bringing colloidal quantum dots to detector technologies," *Inf. Disp. (1975).*, vol. 36, no. 6, pp. 19–23, 2020.

[18] H. E. John, V. Niumsawatt, W. M. Rozen, and I. S. Whitaker, "Clinical applications of dynamic infrared thermography in plastic surgery: A systematic review," *Gland Surg.*, vol. 5, no. 2, pp. 122–132, 2016.

[19] B. F. Jones, "A reappraisal of the use of infrared thermal image analysis in medicine," *IEEE Trans. Med. Imaging*, vol. 17, no. 6, pp. 1019–1027, 1998.

[20] C. Livache, B. Martinez, N. Goubet, J. Ramade, and E. Lhuillier, "Road Map for Nanocrystal Based Infrared Photodetectors," *Front. Chem.*, vol. 6, no. 575, 2018.

[21] C. Livache, B. Martinez, N. Goubet, C. Gréboval, J. Qu, A. Chu, S. Royer, S. Ithurria, M. G. Silly, B. Dubertret, and E. Lhuillier, "A colloidal quantum dot infrared photodetector and its use for intraband detection," *Nat. Commun.*, vol. 10, no. 1, p. 2125, 2019.

[22] M. Chen, Q. Hao, Y. Luo, and X. Tang, "Mid-Infrared Intraband Photodetector via High Carrier Mobility HgSe Colloidal Quantum Dots," *ACS Nano*, vol. 16, no. 7, pp. 11027–11035, 2022.

[23] P. Guyot-Sionnest, M. M. Ackerman, and X. Tang, "Colloidal quantum dots for infrared detection beyond silicon," *J. Chem. Phys.*, vol. 151, no. 6, p. 060901, 2019.

[24] M. Ackerman, X. Tang, and P. Guyot-Sionnest, "Fast and Sensitive Colloidal Quantum Dot Mid-Wave Infrared Photodetectors," *ACS Nano*, vol. 12, no. 7, pp. 7264–7271, 2018.

[25] X. Shen, J. C. Peterson, and P. Guyot-Sionnest, "Mid-infrared HgTe Colloidal Quantum Dot LEDs," *ACS Nano*, vol. 16, no. 5, pp. 7301–7308, 2022.

[26] J. Qu, M. Weis, E. Izquierdo, S. G. Mizrahi, A. Chu, C. Dabard, C. Gréboval, E. Bossavit, Y. Prado, E. Péronne, S. Ithurria, G. Patriarche, M. G. Silly, G. Vincent, D. Boschetto, and E. Lhuillier, "Electroluminescence from nanocrystals above 2 μm," *Nat. Photonics*, vol. 16, no. 1, pp. 38–44, 2022.

[27] M. M. Ackerman, M. Chen, and P. Guyot-Sionnest, "HgTe colloidal quantum dot photodiodes for extended short-wave infrared detection," *Appl. Phys. Lett.*, vol. 116, no. 8, p. 083502, 2020.

[28] X. Tang, M. M. Ackerman, and P. Guyot-Sionnest, "Thermal Imaging with Plasmon Resonance Enhanced HgTe Colloidal Quantum Dot Photovoltaic Devices," *ACS Nano*, vol. 12, no. 7, pp. 7362–7370, 2018.

[29] X. Tang, M. Chen, M. M. Ackerman, C. Melnychuk, and P. Guyot-Sionnest, "Direct Imprinting of Quasi-3D Nanophotonic Structures into Colloidal Quantum-Dot Devices," *Adv. Mater.*, vol. 32, no. 9, p. 1906590, 2020.

[30] S. Zhang, G. Mu, J. Cao, Y. Luo, Q. Hao, M. Chen, Y. Tan, P. Zhao, and X. Tang, "Single-/fused-band dual-mode mid-infrared imaging with colloidal quantum-dot triple-junctions," *Photonics Res.*, vol. 10, no. 8, pp. 1987–1995, 2022.

[31] X. Tang, M. M. Ackerman, G. Shen, and P. Guyot-Sionnest, "Towards Infrared Electronic Eyes: Flexible Colloidal Quantum Dot Photovoltaic Detectors Enhanced by Resonant Cavity," *Small*, vol. 15, no. 12, p. 1804920, 2019.

[32] X. Tang, M. M. Ackerman, M. Chen, and P. Guyot-Sionnest, "Dual-band infrared imaging using stacked colloidal quantum dot photodiodes," *Nat. Photonics*, vol. 13, no. 4, pp. 277–282, 2019.

[33] E. Rosencher and B. Vinter, *Optoelectronics*. Cambridge University Press, 2002.

[34] S. Sze and K. N. Kwok, *Physics of Semiconductor Devices*. Hoboken: John Wiley Sons, 3 ed., 2007.

[35] N. W. Ashcroft and N. D. Mermin, *Solid State Physics*. Brooks/Cole, 1976.

[36] A. Svane, N. E. Christensen, M. Cardona, A. N. Chantis, M. Van Schilfgaarde, and T. Kotani, "Quasiparticle band structures of β-HgS, HgSe, and HgTe," *Phys. Rev. B*, vol. 84, no. 20, p. 205205, 2011.

[37] M. Cardona, R. K. Kremer, R. Lauck, G. Siegle, A. Muñoz, and A. H. Romero, "Electronic, vibrational, and thermodynamic properties of metacinnabar β-HgS, HgSe, and HgTe," *Phys. Rev. B*, vol. 80, no. 19, p. 195204, 2009.

[38] G. Allan and C. Delerue, "Tight-binding calculations of the optical properties of HgTe nanocrystals," *Phys. Rev. B*, vol. 86, no. 16, p. 165437, 2012.

[39] F. Virot, R. Hayn, M. Richter, and J. Van Den Brink, "Engineering topological surface states: HgS, HgSe, and HgTe," *Phys. Rev. Lett.*, vol. 111, no. 14, p. 146803, 2013.

[40] M. Chen and P. Guyot-Sionnest, "Reversible Electrochemistry of Mercury Chalcogenide Colloidal Quantum Dot Films," *ACS Nano*, vol. 11, no. 4, pp. 4165–4173, 2017.

[41] S. Keuleyan, E. Lhuillier, and P. Guyot-Sionnest, "Synthesis of colloidal HgTe quantum dots for narrow mid-IR emission and detection," *J. Am. Chem. Soc.*, vol. 133, no. 41, pp. 16422–16424, 2011.

[42] S. E. Keuleyan, P. Guyot-Sionnest, C. Delerue, and G. Allan, "Mercury telluride colloidal quantum dots: Electronic structure, size-dependent spectra, and photocurrent detection up to 12 μm," *ACS Nano*, vol. 8, no. 8, pp. 8676–8682, 2014.

[43] G. Shen, M. Chen, and P. Guyot-Sionnest, "Synthesis of Nonaggregating HgTe Colloidal Quantum Dots and the Emergence of Air-Stable n-Doping," *J. Phys. Chem. Lett.*, vol. 8, no. 10, pp. 2224–2228, 2017.

[44] N. Goubet, A. Jagtap, C. Livache, B. Martinez, H. Portalès, X. Z. Xu, R. P. Lobo, B. Dubertret, and E. Lhuillier, "Terahertz HgTe Nanocrystals: Beyond Confinement," *J. Am. Chem. Soc.*, vol. 140, no. 15, pp. 5033–5036, 2018.

[45] T. Apretna, S. Massabeau, C. Gréboval, N. Goubet, J. Tignon, S. Dhillon, F. Carosella, R. Ferreira, E. Lhuillier, and J. Mangeney, "Few picosecond dynamics of intraband transitions in THz HgTe nanocrystals," *Nanophotonics*, vol. 10, no. 10, pp. 2753–2763, 2021.

[46] S. Keuleyan, J. Kohler, and P. Guyot-Sionnest, "Photoluminescence of mid-infrared HgTe colloidal quantum dots," *J. Phys. Chem. C*, vol. 118, no. 5, pp. 2749–2753, 2014.

[47] K. S. Jeong, Z. Deng, S. Keuleyan, H. Liu, and P. Guyot-Sionnest, "Air-Stable n-Doped Colloidal HgS Quantum Dots," *J. Phys. Chem. Lett.*, vol. 5, no. 7, pp. 1139–1143, 2014.

[48] A. Kamath, C. Melnychuk, and P. Guyot-Sionnest, "Toward Bright Mid-Infrared Emitters: Thick-Shell n-Type HgSe/CdS Nanocrystals," *J. Am. Chem. Soc.*, vol. 143, no. 46, pp. 19567–19575, 2021.

[49] E. Lhuillier, S. Keuleyan, and P. Guyot-Sionnest, "Optical properties of HgTe colloidal quantum dots," *Nanotechnology*, vol. 23, no. 17, p. 175705, 2012.

[50] D. M. Kroupa, M. Vörös, N. P. Brawand, B. W. McNichols, E. M. Miller, J. Gu, A. J. Nozik, A. Sellinger, G. Galli, and M. C. Beard, "Tuning colloidal quantum dot band edge positions through solution-phase surface chemistry modification," *Nat. Commun.*, vol. 8, no. May, 2017.

[51] A. Stavrinadis and G. Konstantatos, "Strategies for the Controlled Electronic Doping of Colloidal Quantum Dot Solids," *ChemPhysChem*, vol. 17, no. 5, pp. 632–644, 2016.

[52] G. Shen and P. Guyot-Sionnest, "HgS and HgS/CdS Colloidal Quantum Dots with Infrared Intraband Transitions and Emergence of a Surface Plasmon," *J. Phys. Chem. C*, vol. 120, no. 21, pp. 11744–11753, 2016.

[53] M. H. Hudson, M. Chen, V. Kamysbayev, E. M. Janke, X. Lan, G. Allan, C. Delerue, B. Lee, P. Guyot-Sionnest, and D. V. Talapin, "Conduction Band Fine Structure in Colloidal HgTe Quantum Dots," *ACS Nano*, vol. 12, no. 9, pp. 9397–9401, 2018.

[54] H. Zhang and P. Guyot-Sionnest, "Shape-Controlled HgTe Colloidal Quantum Dots and Reduced Spin-Orbit Splitting in the Tetrahedral Shape," *J. Phys. Chem. Lett.*, vol. 11, no. 16, pp. 6860–6866, 2020.

[55] V. I. Klimov, D. W. McBranch, C. A. Leatherdale, and M. G. Bawendi, "Electron and hole relaxation pathways in semiconductor quantum dots," *Phys. Rev. B*, vol. 60, no. 19, pp. 740–749, 1999.

[56] P. Guyot-Sionnest, M. Shim, C. Matranga, and M. Hines, "Intraband relaxation in CdSe quantum dots," *Phys. Rev. B*, vol. 60, no. 4, pp. R2181–R2184, 1999.

[57] V. I. Klimov, A. A. Mikhailovsky, D. W. McBranch, C. A. Leatherdale, and M. G. Bawendi, "Mechanisms for intraband energy relaxation in semiconductor quantum dots: The role of electron-hole interactions," *Phys. Rev. B*, vol. 61, no. 20, pp. R13349–R13352, 2000.

[58] P. Guyot-Sionnest, B. Wehrenberg, and D. Yu, "Intraband relaxation in CdSe nanocrystals and the strong influence of the surface ligands," *J. Chem. Phys.*, vol. 123, no. 7, p. 074709, 2005.

[59] A. Pandey and P. Guyot-Sionnest, "Slow Electron Cooling in Colloidal Quantum Dots," *Science (80-.).*, vol. 322, no. 5903, pp. 929–932, 2008.

[60] P. Kambhampati, "Hot exciton relaxation dynamics in semiconductor quantum dots: Radiationless transitions on the nanoscale," *J. Phys. Chem. C*, vol. 115, no. 45, pp. 22089–22109, 2011.

[61] A. E. Siegman, *Lasers*. Sausalito: University Science Books, 1986.

[62] P. W. Milonni and J. H. Eberly, *Laser Physics*. Hoboken: John Wiley Sons, 2010.

[63] R. C. Hilborn, "Einstein coefficients, cross sections, f values, dipole moments, and all that," *Am. J. Phys.*, vol. 50, no. 11, pp. 982–986, 1982.

[64] H. Liu and P. Guyot-Sionnest, "Photoluminescence lifetime of lead selenide colloidal quantum dots," *J. Phys. Chem. C*, vol. 114, no. 35, pp. 14860–14863, 2010.

[65] A. Aharoni, D. Oron, U. Banin, E. Rabani, and J. Jortner, "Long-range electronic-to-vibrational energy transfer from nanocrystals to their surrounding matrix environment," *Phys. Rev. Lett.*, vol. 100, no. 5, p. 057404, 2008.

[66] J. M. Pietryga, R. D. Schaller, D. Werder, M. H. Stewart, V. I. Klimov, and J. A. Hollingsworth, "Pushing the band gap envelope: Mid-infrared emitting colloidal PbSe quantum dots," *J. Am. Chem. Soc.*, vol. 126, no. 38, pp. 11752–11753, 2004.

[67] M. D. Peterson, L. C. Cass, R. D. Harris, K. Edme, K. Sung, and E. A. Weiss, "The Role of Ligands in Determining the Exciton Relaxation Dynamics in Semiconductor Quantum Dots," *Annu. Rev. Phys. Chem.*, vol. 65, no. 1, pp. 317–339, 2014.

[68] B. K. Ridley, *Quantum Processes in Semiconductors*. Oxford: Oxford University Press, 5 ed., 2013.

[69] A. Nitzan, *Chemical Dynamics in Condensed Phases*. Oxford: Oxford University Press, 2006.

[70] X.-Q. Li, H. Nakayama, and Y. Arakawa, "Phonon bottleneck in quantum dots: Role of lifetime of the confined optical phonons," *Phys. Rev. B*, vol. 59, no. 7, pp. 5069–5073, 1999.

[71] T. Grange, R. Ferreira, and G. Bastard, "Polaron relaxation in self-assembled quantum dots: Breakdown of the semiclassical model," *Phys. Rev. B*, vol. 76, no. 24, p. 241304(R), 2007.

[72] S. H. Lin, "Rate of interconversion of electronic and vibrational energy," *J. Chem. Phys.*, vol. 44, no. 10, pp. 3759–3767, 1966.

[73] S. H. Lin and R. Bersohn, "Effect of partial deuteration on triplet-state lifetimes," *J. Chem. Phys.*, vol. 48, no. 6, pp. 2732–2736, 1968.

[74] M. Bixon and J. Jortner, "Intramolecular Radiationless Transitions," *J. Chem. Phys.*, vol. 48, no. 2, pp. 715–726, 1968.

[75] R. Englman and J. Jortner, "The energy gap law for radiationless transitions in large molecules," *Mol. Phys.*, vol. 18, no. 2, pp. 285–287, 1970.

[76] K. F. Freed and J. Jortner, "Multiphonon processes in the nonradiative decay of large molecules," *J. Chem. Phys.*, vol. 52, no. 12, pp. 6272–6291, 1970.

[77] R. Kubo, "Thermal ionization of trapped electrons," *Phys. Rev.*, vol. 86, no. 6, pp. 929–937, 1952.

[78] T. Miyakawa and D. L. Dexter, "Phonon sidebands, multiphonon relaxation of excited states, and phonon-assisted energy transfer between ions in solids," *Phys. Rev. B*, vol. 1, no. 7, pp. 2961–2969, 1970.

[79] B. K. Ridley, "On the multiphonon capture rate in semiconductors," *Solid State Electron.*, vol. 21, no. 11-12, pp. 1319–1323, 1978.

[80] B. K. Ridley, "Multiphonon, non-radiative transition rate for electrons in semiconductors and insulators," *J. Phys. C Solid State Phys.*, vol. 11, no. 11, pp. 2323–2341, 1978.

[81] E. A. Zibik, L. R. Wilson, R. P. Green, G. Bastard, R. Ferreira, P. J. Phillips, D. A. Carder, J. P. R. Wells, J. W. Cockburn, M. S. Skolnick, M. J. Steer, and M. Hopkinson, "Intraband relaxation via polaron decay in InAs self-assembled quantum dots," *Phys. Rev. B*, vol. 70, no. 16, p. 161305(R), 2004.

[82] E. A. Zibik, T. Grange, B. A. Carpenter, N. E. Porter, R. Ferreira, G. Bastard, D. Stehr, S. Winnerl, M. Helm, H. Y. Liu, M. S. Skolnick, and L. R. Wilson, "Long lifetimes of quantum-dot intersublevel transitions in the terahertz range," *Nat. Mater.*, vol. 8, no. 10, pp. 803–807, 2009.

[83] B. Kopainsky, P. Qiu, W. Kaiser, B. Sens, and K. H. Drexhage, "Lifetime, photostability, and chemical structure of IR heptamethine cyanine dyes absorbing beyond 1 μm," *Appl. Phys. B Photophysics Laser Chem.*, vol. 29, no. 1, pp. 15–18, 1982.

[84] L. E. McNamara, J.-N. Boyn, C. Melnychuk, S. W. Anferov, D. A. Mazziotti, R. D. Schaller, and J. S. Anderson, "Bright, Modular, and Switchable Near-Infrared II Emission from Compact Tetrathiafulvalene-Based Diradicaloid Complexes," *J. Am. Chem. Soc.*, vol. 144, no. 36, pp. 16447–16455, 2022.

[85] S. J. Jang, "A simple generalization of the energy gap law for nonradiative processes," *J. Chem. Phys.*, vol. 155, no. 16, p. 164106, 2021.

[86] S. Egorov and J. Skinner, "On the theory of multiphonon relaxation rates in solids," *J. Chem. Phys.*, vol. 103, no. 4, pp. 1533–1549, 1995.

[87] S. A. Egorov and J. L. Skinner, "An improved theory of multiphonon relaxation in solids," *J. Chem. Phys.*, vol. 105, no. 22, pp. 10153–10155, 1996.

[88] S. A. Egorov, E. Rabani, and B. J. Berne, "Nonradiative relaxation processes in condensed phases: Quantum versus classical baths," *J. Chem. Phys.*, vol. 110, no. 11, pp. 5238–5248, 1999.

[89] I. A. Dmitriev and R. A. Suris, "Anharmonicity-assisted multiphonon transitions between distant levels in semiconductor quantum dots," *Phys. Rev. B*, vol. 90, no. 15, p. 155431, 2014.

[90] P. Han and G. Bester, "Carrier relaxation in colloidal nanocrystals: Bridging large electronic energy gaps by low-energy vibrations," *Phys. Rev. B*, vol. 91, no. 8, p. 085305, 2015.

[91] G. Zhou, G. Lu, and O. V. Prezhdo, "Modeling Auger Processes with Nonadiabatic Molecular Dynamics," *Nano Lett.*, vol. 21, no. 1, pp. 756–761, 2021.

[92] N. Yazdani, D. Bozyigit, K. Vuttivorakulchai, M. Luisier, I. Infante, and V. Wood, "Tuning Electron-Phonon Interactions in Nanocrystals through Surface Termination," *Nano Lett.*, vol. 18, no. 4, pp. 2233–2242, 2018.

[93] D. Jasrasaria and E. Rabani, "Interplay of Surface and Interior Modes in Exciton-Phonon Coupling at the Nanoscale," *Nano Lett.*, vol. 21, no. 20, pp. 8741–8748, 2021.

[94] D. Bozyigit, N. Yazdani, M. Yarema, O. Yarema, W. M. M. Lin, S. Volk, K. Vuttivorakulchai, M. Luisier, F. Juranyi, and V. Wood, "Soft surfaces of nanomaterials enable strong phonon interactions," *Nature*, vol. 531, no. 7596, pp. 618–622, 2016.

[95] T. G. Mack, L. Jethi, M. Andrews, and P. Kambhampati, "Direct Observation of Vibronic Coupling between Excitonic States of CdSe Nanocrystals and Their Passivating Ligands," *J. Phys. Chem. C*, vol. 123, no. 8, pp. 5084–5091, 2019.

[96] T. G. Mack, J. Spinelli, M. P. Andrews, and P. Kambhampati, "Resonance Raman Vibrational Mode Enhancement of Adsorbed Benzenethiols on CdSe Is Predominantly Franck-Condon in Nature and Governed by Symmetry," *J. Phys. Chem. Lett.*, vol. 12, no. 33, pp. 7935–7941, 2021.

[97] G. Shen and P. Guyot-Sionnest, "HgTe/CdTe and HgSe/CdX (X = S, Se, and Te) Core/Shell Mid-Infrared Quantum Dots," *Chem. Mater.*, vol. 31, no. 1, pp. 286–293, 2019.

[98] C. Delerue and M. Lannoo, *Nanostructures: Theory and Modeling*. Heidelberg: Springer-Verlag, 2004.

[99] V. Grigel, L. K. Sagar, K. De Nolf, Q. Zhao, A. Vantomme, J. De Roo, I. Infante, and Z. Hens, "The Surface Chemistry of Colloidal HgSe Nanocrystals, toward Stoichiometric Quantum Dots by Design," *Chem. Mater.*, vol. 30, no. 21, pp. 7637–7647, 2018.

[100] A. J. Houtepen, Z. Hens, J. S. Owen, and I. Infante, "On the Origin of Surface Traps in Colloidal II-VI Semiconductor Nanocrystals," *Chem. Mater.*, vol. 29, no. 2, pp. 752–761, 2017.

[101] M. A. Hines and P. Guyot-Sionnest, "Synthesis and Characterization of Strongly Luminescing ZnS-Capped CdSe Nanocrystals," *J. Phys. Chem.*, vol. 100, no. 2, pp. 468–471, 1996.

[102] A. R. Beattie and P. T. Landsberg, "Auger effect in semiconductors," *Proc. R. Soc. A*, vol. 249, no. 1256, pp. 16–29, 1959.

[103] N. Baier, O. Gravrand, C. Lobre, O. Boulade, A. Kerlain, and N. Péré-Laperne, "HgCdTe Diode Dark Current Modeling: Rule 07 Revisited for LW and VLW," *J. Electron. Mater.*, vol. 48, no. 8, pp. 5233–5240, 2019.

[104] P. Roussignol, M. Kull, D. Ricard, F. De Rougemont, R. Frey, and C. Flytzanis, "Time-resolved direct observation of Auger recombination in semiconductor-doped glasses," *Appl. Phys. Lett.*, vol. 51, no. 23, pp. 1882–1884, 1987.

[105] F. De Rougemont, R. Frey, P. Roussignol, D. Ricard, and C. Flytzanis, "Evidence of strong Auger recombination in semiconductor-doped glasses," *Appl. Phys. Lett.*, vol. 50, no. 23, pp. 1619–1621, 1987.

[106] W. Lochmann, "Scattering mechanisms in phonon-assisted Auger recombination," *Phys. Status Solidi*, vol. 42, no. 1, pp. 181–185, 1977.

[107] W. Lochmann, "Phonon-assisted auger recombination in semiconductors," *Phys. Status Solidi*, vol. 40, no. 1, pp. 285–292, 1977.

[108] W. Lochmann, "Phonon-Assisted Auger Recombination in Indirect Gap Semiconductors," *Phys. Status Solidi*, vol. 45, pp. 354–356, 1978.

[109] E. Kioupakis, P. Rinke, K. T. Delaney, and C. G. Van De Walle, "Indirect Auger recombination as a cause of efficiency droop in nitride light-emitting diodes," *Appl. Phys. Lett.*, vol. 98, no. 16, pp. 2009–2012, 2011.

[110] D. Steiauf, E. Kioupakis, and C. G. Van De Walle, "Auger Recombination in GaAs from First Principles," *ACS Photonics*, vol. 1, no. 8, pp. 643–646, 2014.

[111] H. Wen, B. Pinkie, and E. Bellotti, "Direct and phonon-assisted indirect Auger and radiative recombination lifetime in HgCdTe, InAsSb, and InGaAs computed using Green's function formalism," *J. Appl. Phys.*, vol. 118, no. 1, p. 015702, 2015.

[112] M. Takeshima, "Theory of phonon-assisted Auger recombination in semiconductors," *Phys. Rev. B*, vol. 23, no. 12, pp. 6625–6637, 1981.

[113] M. Takeshima, "Green's-function formalism of band-to-band Auger recombination in semiconductors. Correlation effect," *Phys. Rev. B*, vol. 26, no. 2, pp. 917–930, 1982.

[114] M. Takeshima, "Unified theory of the impurity and phonon scattering effects on Auger recombination in semiconductors," *Phys. Rev. B*, vol. 25, no. 8, pp. 5390–5414, 1982.

[115] M. Takeshima, "Enhancement of Auger recombination in semiconductors by electron-hole plasma interactions," *Phys. Rev. B*, vol. 28, no. 4, pp. 2039–2048, 1983.

[116] A. Hangleiter and R. Häcker, "Enhancement of Band-to-Band Auger Recombination by Electron-Hole Correlations," *Phys. Rev. Lett.*, vol. 65, no. 2, pp. 215–218, 1990.

[117] Y. Kobayashi, L. Pan, and N. Tamai, "Effects of size and capping reagents on biexciton auger recombination dynamics of CdTe quantum dots," *J. Phys. Chem. C*, vol. 113, no. 27, pp. 11783–11789, 2009.

[118] Y. Kobayashi, T. Nishimura, H. Yamaguchi, and N. Tamai, "Effect of Surface Defects on Auger Recombination in Colloidal CdS Quantum Dots," *J. Phys. Chem. Lett.*, vol. 2, no. 9, pp. 1051–1055, 2011.

[119] I. Robel, R. Gresback, U. Kortshagen, R. D. Schaller, and V. I. Klimov, "Universal Size-Dependent Trend in Auger Recombination in Direct-gap and Indirect-gap Semiconductor Nanocrystals," *Phys. Rev. Lett.*, vol. 102, no. 17, p. 177404, 2009.

[120] J. M. Pietryga, K. K. Zhuravlev, M. Whitehead, V. I. Klimov, and R. D. Schaller, "Evidence for barrierless auger recombination in PbSe nanocrystals: A pressure-dependent study of transient optical absorption," *Phys. Rev. Lett.*, vol. 101, no. 21, p. 21740, 2008.

[121] A. Hangleiter, "Nonradiative recombination via deep impurity levels in semiconductors: The excitonic Auger mechanism," *Phys. Rev. B*, vol. 37, no. 5, pp. 2594–2604, 1988.

[122] J. P. Philbin and E. Rabani, "Electron-hole correlations govern Auger recombination in nanostructures," *Nano Lett.*, vol. 18, no. 12, pp. 7889–7895, 2018.

[123] L.-W. Wang, M. Califano, A. Zunger, and A. Franceschetti, "Pseudopotential Theory of Auger Processes in CdSe Quantum Dots," *Phys. Rev. Lett.*, vol. 91, no. 5, p. 056404, 2003.

[124] D. I. Chepic, A. L. Efros, A. I. Ekimov, M. G. Ivanov, V. A. Kharchenko, I. A. Kudriavtsev, and T. V. Yazeva, "Auger ionization of semiconductor quantum drops in a glass matrix," *J. Lumin.*, vol. 47, no. 3, pp. 113–127, 1990.

[125] G. E. Cragg and A. L. Efros, "Suppression of Auger Processes in Confined Structures," *Nano Lett.*, vol. 10, no. 1, pp. 313–317, 2010.

[126] A. Jain, O. Voznyy, S. Hoogland, M. Korkusinski, P. Hawrylak, and E. H. Sargent, "Atomistic Design of CdSe/CdS Core-Shell Quantum Dots with Suppressed Auger Recombination," *Nano Lett.*, vol. 16, no. 10, pp. 6491–6496, 2016.

[127] M. Califano, "Photoinduced surface trapping and the observed carrier multiplication yields in static CdSe nanocrystal samples," *ACS Nano*, vol. 5, no. 5, pp. 3614–3621, 2011.

[128] M. Grundmann, *The Physics of Semiconductors*. Heidelberg: Springer-Verlag, 2 ed., 2010.

[129] C. Melnychuk and P. Guyot-Sionnest, "Slow Auger Relaxation in HgTe Colloidal Quantum Dots," *J. Phys. Chem. Lett.*, vol. 9, no. 9, pp. 2208–2211, 2018.

[130] C. Melnychuk and P. Guyot-Sionnest, "Auger Suppression in n-Type HgSe Colloidal Quantum Dots," *ACS Nano*, vol. 13, no. 9, pp. 10512–10519, 2019.

[131] D. Yu, C. Wang, and P. Guyot-Sionnest, "n-Type Conducting CdSe Nanocrystal Solids," *Science (80-.).*, vol. 300, no. May, 2003.

[132] P. Guyot-Sionnest and C. Wang, "Fast voltammetric and electrochromic response of semiconductor nanocrystal thin films," *J. Phys. Chem. B*, vol. 107, no. 30, pp. 7355–7359, 2003.

[133] J. Cohen, "Introduction to Noise in Solid State Devices," *Natl. Bur. Stand.*, p. Technical Note 1169, 1982.

[134] J. Cohen, "Three Guises of Generation-Recombination Noise," *Natl. Bur. Stand.*, p. Technical Note 1173, 1983.

[135] H. Liu, E. Lhuillier, and P. Guyot-Sionnest, "1/f noise in semiconductor and metal nanocrystal solids," *J. Appl. Phys.*, vol. 115, no. 15, p. 154309, 2014.

[136] Y. Lai, H. Li, D. K. Kim, B. T. Diroll, C. B. Murray, and C. R. Kagan, "Low-Frequency (1/f) Noise in Nanocrystal Field-Effect Transistors," *ACS Nano*, vol. 8, no. 9, pp. 9664–9672, 2014.

[137] M. Chen, X. Lan, X. Tang, Y. Wang, M. H. Hudson, D. V. Talapin, and P. Guyot-Sionnest, "High Carrier Mobility in HgTe Quantum Dot Solids Improves Mid-IR Photodetectors," *ACS Photonics*, vol. 6, no. 9, pp. 2358–2365, 2019.

[138] W. Shockley and H. J. Queisser, "Detailed balance limit of efficiency of p-n junction solar cells," *J. Appl. Phys.*, vol. 32, no. 3, pp. 510–519, 1961.

[139] D. A. Evans and P. T. Landsberg, "Recombination statistics for Auger effects with applications to p-n junctions," *Solid State Electron.*, vol. 6, no. 2, pp. 169–181, 1963.

[140] U. Rau, "Reciprocity relation between photovoltaic quantum efficiency and electroluminescent emission of solar cells," *Phys. Rev. B*, vol. 76, no. 8, p. 085303, 2007.

[141] U. Rau, U. W. Paetzold, and T. Kirchartz, "Thermodynamics of light management in photovoltaic devices," *Phys. Rev. B*, vol. 90, no. 3, p. 035211, 2014.

[142] T. Davidson-Hall and H. Aziz, "The role of excitons within the hole transporting layer in quantum dot light emitting device degradation," *Nanoscale*, vol. 11, no. 17, pp. 8310–8318, 2019.

[143] T. Davidson-Hall and H. Aziz, "Perspective: Toward highly stable electroluminescent quantum dot light-emitting devices in the visible range," *Appl. Phys. Lett.*, vol. 116, no. 1, p. 010502, 2020.

[144] J. Lim, Y. S. Park, K. Wu, H. J. Yun, and V. I. Klimov, "Droop-Free Colloidal Quantum Dot Light-Emitting Diodes," *Nano Lett.*, vol. 18, no. 10, pp. 6645–6653, 2018.

CHAPTER 2

INTERBAND RECOMBINATION IN MERCURY TELLURIDE QUANTUM DOTS

The following material is adapted from [1] and [2].

2.1 Introduction

Nonradiative recombination in HgTe nanocrystals is of fundamental interest as a testbed for established models of quantum dot recombination mechanisms. In particular, small-gap quantum dots such as HgTe should highlight the differences between quantum dot and bulk semiconductor multicarrier Auger recombination. Auger recombination in bulk semiconductors is a three-body carrier-carrier scattering which provides the dominant nonradiative pathway at high carrier densities and small gap energies [3, 2]. It is accurately modeled in small-gap systems by considering the screened Coulomb interactions between four states under the conservation of energy and crystal momentum. At larger gap energies, simultaneous energy and momentum conservation becomes increasingly difficult and the Auger rate in bulk semiconductors drops by many orders of magnitude [2, 3, 4, 5].

Auger recombination in quantum dots can occur as soon as one carrier interacts with an exciton, and it is easily observed in kinetic experiments as a shortened exciton lifetime under strong photoexcitation. Investigations of visible and near-infrared gap quantum dots produced the striking observation that many different materials showed similar Auger rates despite vast differences in the corresponding bulk rates [6, 2]. Epitaxial quantum well structures also show similar differences between the nanoscale and bulk rates [7]. Relaxation of momentum conservation requirements has been qualitatively proposed to account for these observations [6], but there remains no quantitative theory that explains the similar biexciton lifetimes in quantum dots of different materials or their deviations from bulk behavior. The degree to which these trends hold at small gaps has substantial

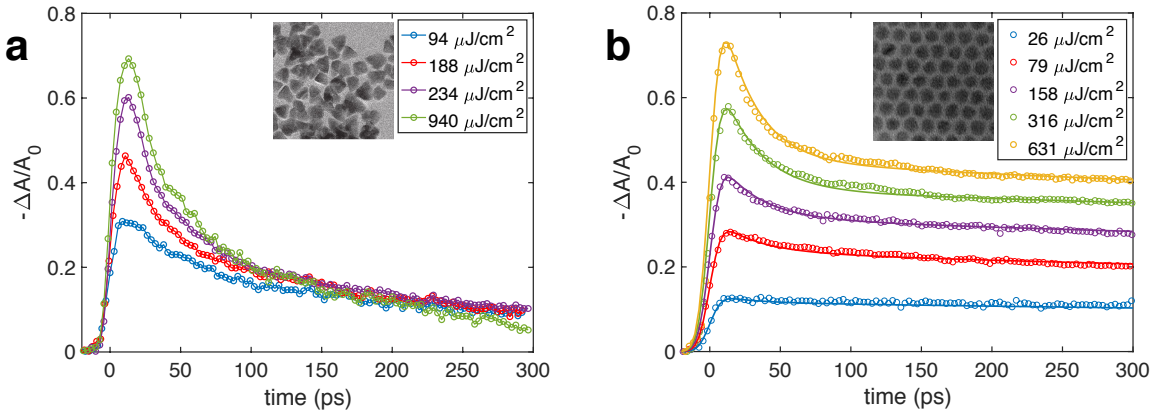

Figure 2.1: Representative transient absorption data plotted as normalized absorbance changes $-\Delta A/A_0$ for (a) partially-aggregated particles with 3950 cm^{-1} band edge, (b) well-dispersed particles with 4200 cm^{-1} band edge. Representative TEM images for the particle types are inset. The band-edge absorbances A_0 were 0.18 in (a) and 0.14 in (b). Not shown in (b) are further data extending to 600 ps and 890 μJ/cm^2.

mechanistic implications, and such fundamental understanding can in turn motivate targeted improvements to nanoparticle synthesis or device fabrication. This chapter focuses on the interband recombination of excitons and biexcitons in HgTe quantum dots, and the fundamental implications for quantum dot photophysics.

2.2 Results and discussion

Figure 2.1 shows representative transient bleaching data for partially-aggregated and well-dispersed HgTe particles. Auger recombination is apparent in sample types as as the faster early-time bleach decay whose magnitude grows with the optical fluence. Also apparent in the data, however, are quantitative differences in the fluence-dependence relaxation. Figure 2.1a in particular shows that the dynamics for partially-aggregated particles display features which are uncharacteristic of Auger recombination in an insulating colloidal suspension. This comes from considering the absolute bleach magnitudes and the corresponding average number of absorbed pump photons per particle.

The average number of pump photons absorbed per particle is the product of the incident optical photon fluence J and the absorption cross section σ_p at the pump wavelength. J is obtained

from the Planck relation and beam size while σ_p is calculated from the particle size in terms of the known cross section per Hg atom in an HgTe nanocrystal at 415 nm refrence wavelength, $\sigma_{415}^{Hg} = 2.6 \pm 0.4 \times 10^{-17}$ cm^2 [8]. σ_p is obtained from the ensemble nanocrystal absorbance A^{NC} as $\sigma_p = \frac{A_p^{NC}}{A_{415}^{NC}} \times N^{Hg} \times \sigma_{415}^{Hg}$ where N^{Hg} is the number of Hg atoms in the nanocrystal. We find that Figure 2.1a shows the fast bleach decay characteristic of multicarrier recombination even when $J\sigma_p \ll 1$, in conflict with the typical picture of the Auger process. Furthermore, the corresponding absolute bleach magnitudes in Figure 2.1a do not support the typical situation of a fast-decaying biexciton bleach and a slow-decaying exciton bleach. Due to the doubly-degenerate nature of the lowest electron state $1S_e$, the creation of one exciton reduces the band-edge absorbance by $\Delta A = -A_0/2$ and the creation of a second exciton results in a complete bleach, $\Delta A = -A_0$, where A_0 denotes the band-edge absorbance in the absence of optical pumping. The saturation of the long-time bleach magnitudes to a constant value much less than $A_0/2$ indicates that distinct exciton and biexciton lifetimes are not resolved in the transient absorption, and it further implies that multicarrier recombination occurs at low excitation levels. We rationalize this observation by invoking the partially aggregated nature of the particles studied, which is apparent in the inset TEM images. If the interparticle electron/hole transfer within aggregates is sufficiently rapid, multicarrier recombination could occur with less than one exciton per quantum dot on average. Although investigating the recombination dynamics in partially aggregated particles may be of practical relevance, the observed behavior prevents a reliable determination of the underlying biexciton Auger rate.

Representative data for well-dispersed HgTe particles with similar gap energies are shown in Figure 2.1b. In these samples, the magnitude of the long-time bleach increases with pump fluence, as one expects from an increasing population of singly-excited particles. At a low pump fluence of 26 μJ/cm^2, we observe almost no relaxation on the time scale of the measurement. Larger optical fluence induces a fast relaxation component, while the slow relaxation rate remains unchanged. At high fluence, the long-time bleach is approximately $A_0/2$ and the early time bleach

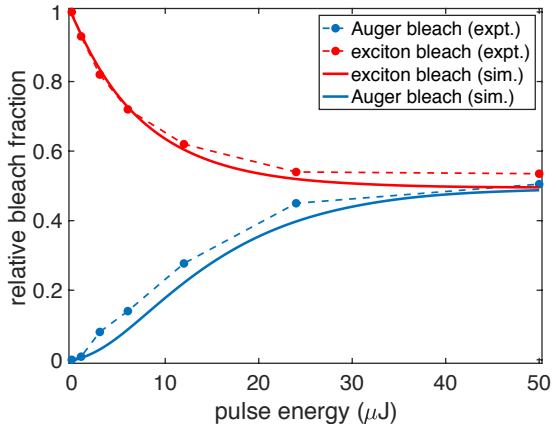

Figure 2.2: Experimental (points) and simulated (solid lines) bleaching ratios for the Auger bleach a_2 and exciton bleach $1 - a_1$. Experimental data were taken from the set shown in Figure 2.1b. Simulations used $\sigma_p = 1.5 \times 10^{-15}$ cm^2.

is almost 80% of A_0. This is the expected behavior and we therefore assign the fast relaxation to biexciton Auger recombination. The data in Figure 2.1b are described well by the convolution of a Gaussian function (15 ps full width at half-maximum) and a biexponential decay of the form $a_1 e^{-t/\tau_X} + a_2 e^{-t/\tau_{BX}}$. Fitting gives $\tau_X = 3100$ ps for the exciton lifetime and $\tau_{BX} = 30$ ps for the biexciton lifetime. As we discuss later, this biexciton lifetime is much longer than implied by the Auger coefficient of comparable bulk HgCdTe. One concern, then, is that the laser pulses used in this experiment do not resolve a much faster Auger recombination. Although this is unlikely given the well-resolved fluence-dependent decay, we further rule this out through a quantitative analysis of the bleach amplitudes. Figure 2.2 shows how the exciton bleach $1 - a_1$ and Auger bleach a_2 vary with the pump energy.

To model these amplitudes as a function of the pump energy, we again begin with σ_p. A dot with an interband transition at 4200 cm^{-1}, for example, has $\sigma_p = 1.9 \pm 0.3 \times 10^{-15}$ cm^2 with the uncertainty due to σ_{415}^{Hg}. The nanocrystal concentration c and the incident photon fluence J then give the average number of excitations per particle as a function of position z in the sample cell as $\sigma_p J e^{-\sigma_p c z}$. Taking a Poisson distribution of excitation levels, appropriate for above-gap pumping, we obtain the local concentration of quantum dots in the ground state, $c_0(z, J)$, with one exciton,

$c_1(z, J)$, and two or more excitons, $c_2(z, J)$, with $\int_0^L (c_0(z, J) + c_1(z, J) + c_2(z, J))dz = c$. Before the pump pulse, the absorbance at the band edge is

$$A_0 = \frac{1}{\ln(10)} \int_0^L \sigma_b c dz \tag{2.1}$$

where σ_b denotes the nanocrystal band-edge cross section and $L = 1.3$ mm is the sample cell thickness. Right after the pump pulse, the absorbance should reduce to

$$A_{\text{early}}(J) = \frac{1}{\ln(10)} \int_0^L \sigma_b \left(c_0(z, J) + \frac{c_1(z, J)}{2} \right) dz \tag{2.2}$$

At later times, when all multicarrier states have relaxed to single-exciton states but before the exciton population has appreciably decayed, the absorbance should then recover as

$$A_{\text{late}}(J) = \frac{1}{\ln(10)} \int_0^L \sigma_b \left(c_0(z, J) + \frac{c_1(z, J)}{2} + \frac{c_2(z, J)}{2} \right) dz \tag{2.3}$$

To connect with the experimental data, we have

$$1 - a_1 = \frac{A_{\text{late}}(J)}{A_0} = 1 - \frac{\langle c_1(J) + c_2(J) \rangle}{c} \tag{2.4}$$

and

$$a_2 = \frac{A_{\text{late}}(J) - A_{\text{early}}(J)}{A_0} = \frac{\langle c_2(J) \rangle}{c} \tag{2.5}$$

where $\langle - \rangle$ denotes a spatial average across the sample cell thickness. As shown in Figure 2.2, $1 - a_1$ decreases from one at low energy to one-half at high energy in both simulation and experiment. This represents the fractional contribution of single excitons to the early-time bleach. a_2 represents the early-time bleach fraction due to multiply-excited particles and increases from zero to one-half in both simulation and experiment. We further note the induction time for the growth of a_2 in comparison to the fall of $1 - a_1$; this arises from the exclusive creation of singly-excited particles

Summary of Transient Absorption Data			
PL peak (cm^{-1})	R (nm)	τ_{BX} (ps)	τ_X (ps)
2500 (800)	4.4	> 80	790
3600 (600)	3.0	49 (56, 45)	1300
3750 (800)	2.9	46 (50, 39)	3000
3950 (800)	2.7	37 (40, 33)	> 6000
4075 (800)	2.6	34 (39, 31)	3000
4200 (700)	2.5	30 (33, 28)	3100
4700 (900)	2.1	24 (28, 19)	5000

Table 2.1: Photoluminescence (PL) peaks have full-widths at half-maxima (fwhm) in parentheses. Particle radii were estimated by fitting the PL-diameter data of Shen *et al.*, giving $R = 10.225 \exp\left(3.38m \times 10^{-4}\right)$ for the PL peak value m in cm^{-1} and particle radius R in nm. Biexciton lifetimes with limits reflecting 95 % confidence intervals were obtained by fitting the data to biexponential decays, and exciton lifetimes were also obtained from the fits.

at low pulse energies and, although correct, is not reproduced by other models [9]. The good overall agreement between the simulation and experiment further supports our assignment of the fluence-dependent bleach decay to Auger recombination and allows us to rule out the presence of faster, unresolved recombination processes.

We obtained transient bleach data for particles with band edges ranging from 2500 to 4700 cm^{-1}, and the results are shown in Table 2.1 and Figure 2.4. The exciton lifetimes generally shorten with increasing particle size, consistent with decreased photoluminescence efficiencies as the gap approaches the mid-infrared [10]. In contrast, the biexciton lifetimes consistently lengthen with increasing particle size. We find the biexciton lifetime to be reasonably linear in R^3, where R is the particle radius, corroborating the findings of Robel and coworkers [6]. Fitting the data to $\tau_{BX} = pR^3$ gives a scaling coefficient p of 1.9 ps/nm^3 (Figure 2.4). Also shown in Figure 2.4 is the corresponding curve for CdSe, for which p = 5.5 ps/nm^3 has been reported [6, 11]. This indicates that for the same particle size, biexciton lifetimes are only three times shorter in HgTe than in CdSe. This result is remarkable considering that the Auger rates differ by many orders of magnitude in the respective bulk materials [6, 2]. As discussed below and at length in [2], this strongly suggests mechanistic changes in the evolution from bulk to nanoscale Auger recombination.

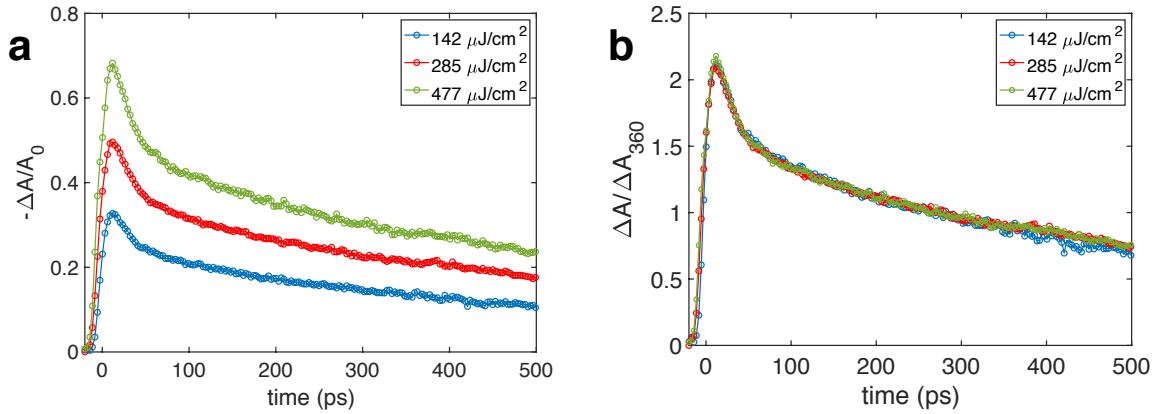

Figure 2.3: Transient data for a well-dispersed sample displaying a 2500 cm^{-1} band edge. Panel (b) displays the data from panel (a) normalized to the bleach magnitude at 360 ps.

When performing measurements on larger particles, we no longer obtained fluence-dependent decay curves. Figure 2.3 shows data for a sample with a photoluminescence peak at 2500 cm^{-1}. The bleach increases with pump power, as seen in Figure 2.3a, but Figure 2.3b clearly shows that the relative amplitudes of the fast and slow decays do not depend on the excitation level. The maximum bleach exceeds half the sample optical density, however, supporting the absence of an Auger processes much faster than the pulse resolution. The exponential decays are well-characterized by two unchanged time constants of 22 and 790 ps, both attributable to nonradiative pathways. Although partial *n*-doping in small-gap materials and thus negative trion decay is possible, it is unlikely to explain the fast decay in this sample because the photogeneration of trions would still produce decay curves that change with pump power [12]. We therefore conclude that the biexciton recombination is not resolved in large HgTe quantum dots because it is too slow, and possibly on the order of the excitonic lifetime. We estimate a lower bound for the Auger lifetime by fitting the data to a triple exponential decay, and such a fit implies a biexciton Auger lifetime longer than 80 ps. This is consistent with the R^3 trend shown in Figure 2.4 and would indeed be difficult to observe on the time scale of our measurements given the presence of the other non-Auger recombination processes.

Figure 2.5 shows transient photoluminescence data for well-dispersed samples similar to those

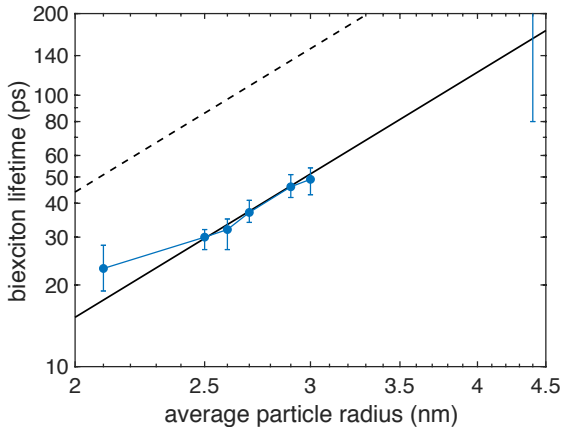

Figure 2.4: Summary of transient absorption Auger data. The solid line is the R^3 fit noted in the text and the dashed line is the corresponding curve for CdSe.

examined by transient absorption. In small particles with photoluminescence peaks at 4300 cm^{-1}, Figure 2.5a, the data display the typical signature of Auger recombination at high fluence and a slower excitonic relaxation at low fluence. The decays in Figure 2.5a are fit well by a fast time constant of 24 ± 3 ps and a slow time constant of 2400 ± 400 ps. This is similar to the transient absorption time constants for comparable particles. The larger particles in Figure 2.5b show photoluminescence decays which are also similar to or slightly faster than those obtained through transient absorption. The slow component displays a time constant of 570 ± 40 ps and the fast component may be fit with a 19 ± 1 ps time constant. The latter comprises about 30% of the time-integrated photoluminescence in qualitative agreement with the contributions of the fast decay to the overall absorption bleach in Figure 2.3. The somewhat faster relaxation observed here is consistent with the smaller gap and previous observations of a monotonously decreasing photoluminescence quantum yield with decreasing gap energy [10]. The broad similarities between the photoluminescence and transient absorption lifetimes suggest that hole trapping effects are small because the absorption measurement primarily probes electron relaxation, while the photoluminescence measurement is equally sensitive to the lifetimes of electrons and holes.

We now compare the Auger recombination rates in HgTe quantum dots to those of bulk HgCdTe. In bulk semiconductors, the Auger carrier loss is cubic in the carrier density and characterized by

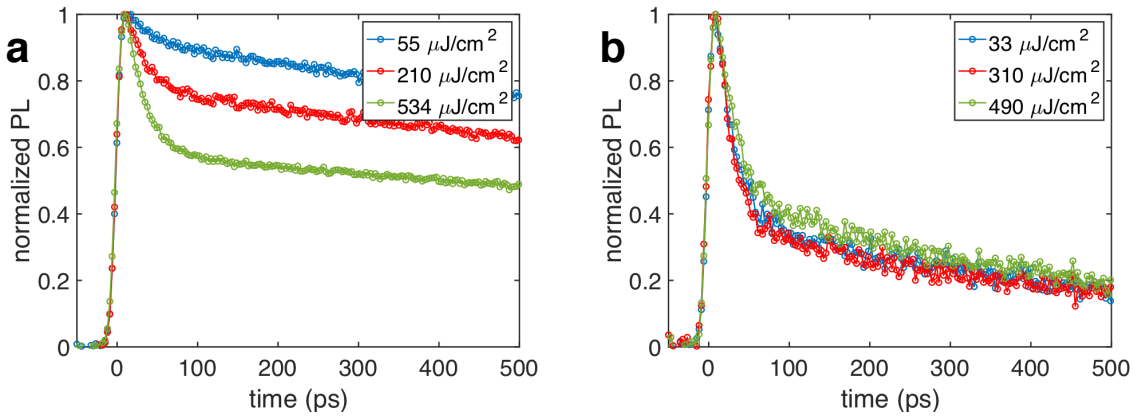

Figure 2.5: Normalized transient photoluminescence (PL) data for well-dispersed samples displaying (a) 4300 cm^{-1} and (b) 2050 cm^{-1} photoluminescence peaks.

Auger coefficients C_A associated with different possible combinations of electrons and holes. In nanoparticles, C_A has been proposed to relate the biexciton lifetime to the particle volume V by $C_A = V^2/8\tau_{BX}$ [2, 13]. Although such a quantum dot Auger coefficient is not rigorously justified, as discussed in the appendix to this chapter, it nevertheless provides a crude comparison metric for Auger rates in quantum dots and bulk semiconductors. For a variety of quantum dot materials, C_A was observed to scale as $C_A = \gamma R^3$ [6]. The data in Figure 2.4 correspond to $\gamma = 1.2 \times 10^{-9}\,cm^3/s$ and Auger coefficients from $0.7 \times 10^{-29}\,cm^6/s$ at 2.1 nm radius to $3 \times 10^{-29}\,cm^6/s$ at 3.0 nm radius. Using the value of γ and extrapolating to 0.12 eV bandgap ($R \approx 7.2$ nm), where bulk HgCdTe is well characterized, gives $C_A = 4 \times 10^{-28}\,cm^6/s$ for an HgTe nanoparticle. This is three orders of magnitude smaller than for bulk HgCdTe with the same gap, 10^{-25} cm^6/s [2]. We therefore find that Auger recombination is strongly suppressed in HgTe quantum dots relative to bulk HgCdTe. For applications in mid-infrared detection, the slower Auger recombination is an intrinsic advantage of the HgTe quantum dots that should allow higher operating temperatures than bulk HgCdTe.

These results imply that the mechanism of Auger recombination in quantum dots differs from the standard Auger mechanism which is active in small-gap bulk semiconductors. To date, the many observations of similar Auger rates across a variety of quantum dot systems have been

limited to large gap energies. Auger recombination in bulk semiconductors involves additional scattering from phonons or defects in this regime because the theoretical pure-band process is too slow. The rates of these scattering-assisted Auger recombination processes typically display a weak dependence on the material gap, just as observed in quantum dots. At smaller gaps, however, bulk Auger recombination is a pure-band process with a rate that increases exponentially with decreasing gap size [2]. The similarities between Auger recombination in HgTe quantum dots and in systems with gaps an order of magnitude larger indicate a lack of crossover between pure-band and scattering-assisted Auger recombination above 0.25 eV, and suggests that a mechanism akin to scattering assistance may be active in all quantum dots. In a bulk-like picture, the scattering of confined charges from the nanocrystal boundaries could randomize the effective wavevectors to relax momentum conservation requirements [14, 15, 16]. Although these ideas have been introduced before, they have not been interpreted or analyzed in the context of gap-insensitive quantum dot Auger rates. In an atomistic picture, the notion of surface scattering has less meaning but momentum must still be conserved. It would manifest in the symmetries of the states which produce large Auger matrix elements, and these may or may not be surface-derived.

A complementary viewpoint is to consider that the Auger rate, as calculated with perturbation theory, depends on the density of states at twice the gap energy and the Coulomb matrix element. The matrix element is generally accepted to be larger in quantum dots than in bulk materials due to the spatial charge confinement, yet the density of states is smaller. Although the faster Auger recombination in wide-gap quantum dots relative to the corresponding bulk materials was proposed to arise from a "universal enhancement" of quantum dot Auger recombination [6, 13], the much slower Auger recombination in HgTe quantum dots relative to HgCdTe of equivalent gap is at odds with this perspective. Instead, the present data suggest that in the small-gap quantum dot regime, the smaller density of states sufficiently compensates for the larger matrix element such that the overall rate is reduced.

2.3 Conclusions

In summary, we presented an experimental study of Auger recombination in HgTe quantum dots. Time-resolved bleaching experiments revealed conspicuously different recombination dynamics between partially aggregated and well-dispersed HgTe, attributed to rapid intra-aggregate charge transfer and recombination. This behavior precludes straightforward quantitative examination of Auger rates by transient bleaching. Measurements on well-dispersed particles allowed us to determine the Auger and exciton lifetimes as functions of particle size. The excitonic lifetimes are broadly consistent with the model of near-field energy transfer previously applied by Keuleyan *et al.* [10], while the similar excitonic lifetimes measured by transient bleaching and photoluminescence indicate that trapping effects are small. The magnitude and scaling of the Auger lifetimes agree with trends observed in other quantum dot systems, and our measurements extend these trends to the mid-infrared. We showed that Auger recombination in HgTe nanoparticles is significantly suppressed relative to bulk HgCdTe. This could imply that the confinement-induced reduction in the density of states overcomes the confinement-induced enhancement of the Auger matrix element to reduce the overall rate. The slower Auger recombination in HgTe quantum dots versus bulk infrared materials is a fundamental benefit for infrared detection and lasing.

2.4 Methods

Synthesis of HgTe nanoparticles: Quasi-tetrahedral, partially-aggregated particles were synthesized by adapting the protocol of Keuleyan *et al.* [17]. Briefly, 30 mg of $HgCl_2$ was mixed with 4 ml of oleylamine, placed in a N_2-purged glovebox, stirred, and heated for 1 hour to a final temperature of 100° C. This produced a clear, light-yellow solution which was heated or cooled to the reaction temperature, with higher temperatures furnishing larger particles. Upon reaching the target reaction temperature, 130 μl of 1 molar trioctylphosphine telluride was quickly injected via micropipette and the mixture was allowed to react while stirring for 10 - 40 minutes, with longer

times resulting in larger particles. The reaction was quenched by pouring the mixture into 4 ml of -5° C chlorobenzene. Outside the glovebox, the particles were cleaned of excess organics and unreacted material by precipitation with isopropanol, and redispersed in tetrachloroethylene with the addition of approximately 60 μl of 1-dodecanethiol. Quasi-spherical, well-dispersed particles were synthesized following Shen's method [18]. $HgCl_2$ was dissolved in oleylamine as above, adjusted to the desired reaction temperature, and reacted with 15 μl of bis-(trimethylsilyl)telluride for 5 minutes while stirring. After reaction quenching as above, the particles were precipitated with a mixture of acetone and ethanol and redispersed in tetrachloroethylene. The steady-state spectroscopy was consistent with prior reports [17, 18].

Transient absorption: Transient absorption data were acquired using the near-infrared pump, mid-infrared probe apparatus described in Appendix C. In brief, a Nd:YLF regenerative amplifier producing 8 ps full-width at half-maximum pulses at 1053 nm and 1 kHz was used to generate pulses tunable from 1.4 - 4.5 μm by type-II parametric amplification in a KTA crystal. Unconverted 1053 nm light was split off from the beam path by a CaF_2 1053 nm mirror and used to pump the sample after variable attenuation and optical delay. The idler waves were selected as probes by a germanium plate oriented at Brewster's angle, split into reference and sample beams, and attenuated by a NiCr-coated CaF_2 window to below 22 $\mu J/cm^2$ at the sample after focusing. Pump and probe beam radii ($1/e^2$ intensity) were respectively 1.3 and 0.12 mm at the sample. Probe beams were detected by a pair of amplified PbSe photoconductors and discriminated from the background by a gated integrator. The samples were contained in a cell consisting of two CaF_2 windows separated by a 1.3 mm thick PTFE spacer in a stainless steel housing.

Transient photoluminescence: Transient photoluminescence upconversion data were acquired using the upconversion apparatus described in Appendix C. The 1053 nm beam was split into two paths by a 20% reflector. The weak path pumped the sample in the transverse geometry after attenuation, variable optical delay, and weak focusing by a cylindrical lens. The strong path was brought collinear with the sample photoluminescence by a CaF_2 1053 nm mirror and mixing in KTA gener-

ated a pulse at the sum-frequency. Filters and a monochromator discriminated the sum-frequency pulse from background and weak frequency-doubled laser light, and the pulse was detected with a silicon photomultiplier and windowed with a gated integrator. The samples were contained in a CaF_2 cuvette.

Photoluminescence spectroscopy: Photoluminescence spectra were obtained using a home-built Michelson interferometer operating in step-scan mode. An 808 nm laser diode of 150 mW average power modulated as a sine wave at 100 kHz excited the sample. The fluorescence was collimated by a parabolic mirror and sent through the interferometer to a cooled HgCdTe detector with a 900 cm^{-1} cutoff frequency. A silicon wafer filtered out scattered laser light. The detector output was sent through a lock-in amplifier, and one of the interferometer arm lengths was scanned for a distance corresponding to 50 cm^{-1} spectral resolution after Fourier transformation of the interferogram.

2.5 Appendix

In the following we discuss the kinetics of Auger recombination for three-body and two-body mechanisms in the bulk and microscopic limits. Auger coefficients for quantum dots are also examined in this context.

2.5.1 Auger kinetics in bulk semiconductors

Auger recombination in the bulk free-carrier (plasma) model is described by the kinetics

$$\frac{dn}{dt} = -C_A n^3 \equiv -C_A \langle n \rangle^3 = \frac{d\langle n \rangle}{dt} \tag{2.6}$$

where n is the carrier density, $\langle n \rangle$ is the ensemble average carrier density and C_A is the Auger coefficient. In terms of the carrier number N, the Auger recombination is described by

$$\frac{dN}{dt} = -\gamma N^3 \equiv -\gamma \langle N \rangle^3 = \frac{d\langle N \rangle}{dt} \tag{2.7}$$

where γ is the reciprocal Auger lifetime. The underlying assumption in both formulations is the equivalence of macroscopic and local carrier densities or numbers. This neglect of counting statistics is a good assumption in homogeneous bulk semiconductors, where N is always large.

2.5.2 Discrete kinetic models

In solutions of quantum dots or molecules, the local variations in excitation (carrier) number are not negligible compared to the ensemble average at typical excitation levels. One must therefore explicitly consider the populations of single, double, triple etc. excitations and treat the ensemble average as a derived quantity. For the probability P_N that a dot has N excitations, the average is defined

$$\langle N \rangle = \sum_{N=1} N P_N \tag{2.8}$$

and the kinetics may generically be written in terms of P_N as

$$\frac{dP_N}{dt} = \frac{P_{N+1}}{\tau_{N+1}} - \frac{P_N}{\tau_N} \tag{2.9}$$

where τ_N is the time constant for the decay $N \rightarrow (N-1)$. The specific dependence of τ on N is determined by the kinetic model. In the following, we assume the linear recombination is slow compared to the Auger recombinations so that the latter are the only relevant processes.

2.5.3 *Discrete kinetic model: free-carrier Auger recombination*

If the Auger process involves free electrons and holes, then τ_N depends on the joint probability of choosing two electrons from N electrons and one hole from N holes, plus the probability of the opposite configuration. These two configurations have the same probability in an intrinsic system, so the total rate is proportional to twice the probability of two-electron one-hole recombination:

$$\tau_N^{-1} \propto 2 \times \left(\frac{N!}{2!\,(N-2)!} \times \frac{N!}{1!\,(N-1)!} \right) = N^2(N-1) \tag{2.10}$$

Therefore we have

$$\tau_N^{-1} = \frac{N^2(N-1)}{\tau_{A,F}} \tag{2.11}$$

where $\tau_{A,F}$ is the Auger lifetime for recombination in a free carrier model. The ensemble average kinetics are given by $\frac{d\langle N \rangle}{dt} = \sum N \frac{dP_N}{dt}$. Plugging in the above formulation of τ_N^{-1} into the generic discrete kinetic model and using the definition of the average, this gives

$$\frac{d\langle N \rangle}{dt} = \frac{1}{\tau_{A,F}} \sum_{N=1} N\Big(N(N+1)^2 P_{N+1} - N^2(N-1) P_N \Big) \tag{2.12}$$

This formulation can be evaluated directly by summing over a suitable distribution for P, typically a Poisson distribution. To obtain a more transparent equation, we can first rewrite the P_{N+1} term using $N' = N + 1$ to give

$$\begin{aligned} \sum_{N=1} N^2(N+1)^2 P_{N+1} &= \sum_{N'=2} (N'-1)^2 N'^2 P_{N'} \\ &= \sum_{N'=1} (N'-1)^2 N'^2 P_{N'} - (1-1)^2 (1^2) P_1 \\ &= \sum_{N=1} (N-1)^2 N^2 P_N \end{aligned} \tag{2.13}$$

so that

$$\frac{d\langle N\rangle}{dt} = \frac{1}{\tau_{A,F}} \sum_{F=1} (N-1)^2 N^2 - N^3(N-1))P_N$$
$$= \frac{1}{\tau_{A,F}} \sum_{N=1} -N^2(N-1)P_N \tag{2.14}$$

Using the definition of the average, we then have the kinetics as

$$\frac{d\langle N\rangle}{dt} = -\frac{1}{\tau_{A,F}}\langle N^2(N-1)\rangle \tag{2.15}$$

This displays the gross cubic kinetics one expects from a free carrier model, but due to counting statistics, it only approaches the bulk formula $d\langle N\rangle/dt = \tau_{A,F}^{-1}\langle N^3\rangle$ in the large-N limit.

2.5.4 Discrete kinetic model: excitonic Auger recombination

If the Auger recombination involves two excitons, τ_N is related to the probability of choosing two excitons from N excitons:

$$\tau_N^{-1} \propto \frac{N!}{2!\,(N-2)!} = \frac{N(N-1)}{2} \tag{2.16}$$

If $N = 2$ then τ_N should be the biexciton lifetime $\tau_{A,X}$, so we have for this model

$$\tau_N^{-1} = \frac{N(N-1)}{2\tau_{A,X}} \tag{2.17}$$

Going through a similar procedure as for the free carrier model gives

$$\frac{d\langle N\rangle}{dt} = -\frac{1}{2\tau_{A,X}}\langle N(N-1)\rangle \tag{2.18}$$

For a given N, the solution to this equation will never be similar to either the discrete plasma model or the bulk plasma model unless there is a fortuitous relationship between $\tau_{A,X}$ and $\tau_{A,F}$.

2.5.5 *Auger coefficients for quantum dots*

We now re-derive the Auger coefficient proposed by Klimov and co-workers using the bulk model $dn/dt = -C_A n^3$ and an effective macroscopic carrier density $\langle n \rangle = \langle N \rangle / V$, where V is the dot volume. Rewriting the bulk kinetics in terms of $\langle N \rangle$,

$$\frac{d}{dt}\frac{\langle N \rangle}{V} = -C_A\left(\frac{\langle N \rangle}{V}\right)^3 \longrightarrow \frac{d\langle N \rangle}{dt} = \frac{-C_A \langle N \rangle^3}{V^2} \tag{2.19}$$

we obtain the lifetime using the bulk definition $\tau^{-1} \equiv n^{-1} dn/dt$:

$$\frac{1}{\tau^*} \equiv \frac{d\langle N \rangle}{dt}\frac{1}{\langle N \rangle} = -\frac{C_A \langle N \rangle^2}{V^2} \tag{2.20}$$

Here τ^* is the lifetime of the ensemble average carrier number per nanoparticle. The Auger coefficient is then obtained by making an equivalence between the bulk and discrete formulations of $d\langle N \rangle/dt$. The discrete kinetics are

$$\begin{aligned} \frac{d\langle N \rangle}{dt} &= \sum_N \left(\frac{N P_{N+1}}{\tau_{N+1}} - \frac{N P_N}{\tau_N} \right) \\ &= -\sum_N \frac{P_N}{\tau_N} \\ &= \frac{1}{\langle \tau_N \rangle} \end{aligned} \tag{2.21}$$

As before, τ_N is the lifetime of the $N \rightarrow (N-1)$ process in a single particle. The last part defines the average single-particle lifetime for a given N value. This is equivalent to the procedure used before, but remains agnostic on the dependence of τ_N on N. By substitution we then obtain the relationships between τ^*, $\langle \tau_N \rangle$ and $d\langle N \rangle/dt$:

$$\frac{d\langle N \rangle}{dt} = \frac{\langle N \rangle}{\tau^*} = \frac{1}{\langle \tau_N \rangle} \tag{2.22}$$

Writing the bulk $d\langle N\rangle/dt$ in terms of $\langle\tau_N\rangle$ as derived from the discrete model, we finally obtain the Auger coefficient

$$C_A = \frac{V^2}{\langle N\rangle^3\langle\tau_N\rangle} = \frac{V^2}{8\langle\tau_{BX}\rangle} \tag{2.23}$$

as described by Klimov and co-workers [13].

Formulating a quantum dot Auger coefficient therefore requires two basic assumptions: the assumption of third-order kinetics, and the equivalence between discrete and continuous (free carrier) kinetics. As discussed in [2], a two-body (excitonic) mechanism is more consistent with the linear volume scaling of the biexciton recombination rate observed in most quantum dots. The assumed equivalence between discrete and bulk third-order models implies the large-N limit which is not valid the the majority of spectroscopic situations in which τ_{BX} is measured. In a device situation involving a conducting quantum dot solid and $\langle N\rangle \ll 1$, however, the numerical accuracy of C_A as formulated above is likely reasonable because charge transport makes the intraparticle counting statistics less relevant. This situation is briefly discussed in the appendix to Chapter 4.

REFERENCES

[1] C. Melnychuk and P. Guyot-Sionnest, "Slow Auger Relaxation in HgTe Colloidal Quantum Dots," *J. Phys. Chem. Lett.*, vol. 9, no. 9, pp. 2208–2211, 2018.

[2] C. Melnychuk and P. Guyot-Sionnest, "Multicarrier Dynamics in Quantum Dots," *Chem. Rev.*, vol. 121, no. 4, pp. 2325–2372, 2021.

[3] P. T. Landsberg, *Recombination in Semiconductors*. Cambridge: Cambridge University Press, 1991.

[4] E. Kioupakis, P. Rinke, K. T. Delaney, and C. G. Van De Walle, "Indirect Auger recombination as a cause of efficiency droop in nitride light-emitting diodes," *Appl. Phys. Lett.*, vol. 98, no. 16, pp. 2009–2012, 2011.

[5] D. Steiauf, E. Kioupakis, and C. G. Van De Walle, "Auger Recombination in GaAs from First Principles," *ACS Photonics*, vol. 1, no. 8, pp. 643–646, 2014.

[6] I. Robel, R. Gresback, U. Kortshagen, R. D. Schaller, and V. I. Klimov, "Universal Size-Dependent Trend in Auger Recombination in Direct-gap and Indirect-gap Semiconductor Nanocrystals," *Phys. Rev. Lett.*, vol. 102, no. 17, p. 177404, 2009.

[7] J. R. Meyer, C. L. Felix, W. W. Bewley, I. Vurgaftman, E. H. Aifer, L. J. Olafsen, J. R. Lindle, C. A. Hoffman, M. J. Yang, B. R. Bennett, B. V. Shanabrook, H. Lee, C. Lin, S. S. Pei, and R. H. Miles, "Auger coefficients in type-II InAs / Ga 1x In x Sb quantum wells," *Appl. Phys. Lett.*, vol. 73, no. 20, pp. 2857–2859, 1998.

[8] E. Lhuillier, S. Keuleyan, and P. Guyot-Sionnest, "Optical properties of HgTe colloidal quantum dots," *Nanotechnology*, vol. 23, no. 17, p. 175705, 2012.

[9] C. Liu, J. J. Peterson, and T. D. Krauss, "Uncovering hot hole dynamics in CdSe nanocrystals," *J. Phys. Chem. Lett.*, vol. 5, no. 17, pp. 3032–3036, 2014.

[10] S. Keuleyan, J. Kohler, and P. Guyot-Sionnest, "Photoluminescence of mid-infrared HgTe colloidal quantum dots," *J. Phys. Chem. C*, vol. 118, no. 5, pp. 2749–2753, 2014.

[11] V. I. Klimov, A. A. Mikhailovsky, D. W. McBranch, C. A. Leatherdale, and M. G. Bawendi, "Quantization of Multiparticle Auger Rates in Semiconductor Quantum Dots," *Science (80-.).*, vol. 287, no. 5455, pp. 1011–1013, 2000.

[12] P. P. Jha and P. Guyot-Sionnest, "Trion decay in colloidal quantum dots," *ACS Nano*, vol. 3, no. 4, pp. 1011–1015, 2009.

[13] V. I. Klimov, J. A. McGuire, R. D. Schaller, and V. I. Rupasov, "Scaling of multiexciton lifetimes in semiconductor nanocrystals," *Phys. Rev. B*, vol. 77, no. 19, p. 195324, 2008.

[14] G. G. Zegrya and D. M. Samosvat, "Mechanisms of Auger recombination in semiconducting quantum dots," *J. Exp. Theor. Phys.*, vol. 104, no. 6, pp. 951–965, 2007.

[15] V. A. Kharchenko and M. Rosen, "Auger relaxation processes in semiconductor nanocrystals and quantum wells," *J. Lumin.*, vol. 70, no. 1-6 SPEC. ISS., pp. 158–169, 1996.

[16] D. I. Chepic, A. L. Efros, A. I. Ekimov, M. G. Ivanov, V. A. Kharchenko, I. A. Kudriavtsev, and T. V. Yazeva, "Auger ionization of semiconductor quantum drops in a glass matrix," *J. Lumin.*, vol. 47, no. 3, pp. 113–127, 1990.

[17] S. Keuleyan, E. Lhuillier, and P. Guyot-Sionnest, "Synthesis of colloidal HgTe quantum dots for narrow mid-IR emission and detection," *J. Am. Chem. Soc.*, vol. 133, no. 41, pp. 16422–16424, 2011.

[18] G. Shen, M. Chen, and P. Guyot-Sionnest, "Synthesis of Nonaggregating HgTe Colloidal Quantum Dots and the Emergence of Air-Stable n-Doping," *J. Phys. Chem. Lett.*, vol. 8, no. 10, pp. 2224–2228, 2017.

CHAPTER 3

INTERBAND AND INTRABAND RECOMBINATION IN MERCURY SELENIDE QUANTUM DOTS

The following material is adapted from [1] and [2].

3.1 Introduction

Nonradiative recombination is a fundamental limitation for many semiconductor technologies. Specific effects include reduced lasing efficiencies [3], lowered specific detectivities in photodetectors [4, 5] and efficiency droop in high-power LEDs [6]. The mechanisms are generally quite well understood in bulk crystalline semiconductors. At low carrier densities in extremely clean specimens, multiphonon recombination presents the slowest achievable nonradiative rate. More typically, however, various mechanisms associated with material defects dominate in this carrier density regime. The generic mechanism of defect-mediated nonradiative relaxation involves localization of a carrier at the defect center followed by rapid multiphonon relaxation of the bound state, the latter promoted by defects' localized nature and resultant strong coupling to phonons [7, 8]. Near-field energy transfer may also be active in any situation where a suitable absorber exists. At high carrier densities, nonradiative recombination is typically attributed to carrier-carrier scattering such as Auger recombination, a process by which an exciton transfers its gap energy to a nearby electron or hole. It is often modeled by considering the screened Coulomb interactions between carriers under energy and momentum conservation within the framework of perturbation theory [9, 8, 10, 11, 7]. For small-gap materials it is a straightforward and purely electronic process [9, 8, 10, 12], while excitonic effects and phonons or other "assisting" scattering modes are often implicated at larger energies [9, 6, 12, 13]. The purely electronic mechanism is a thermally-activated process due momentum conservation requirements, and the Auger rate grows rapidly in bulk materials as the energy gap decreases.

In contrast to the developed understanding of nonradiative recombination in bulk semiconductors, the mechanisms in colloidal quantum dots are less codified. Auger processes in a quantum dot may occur when a trion or biexciton forms within the particle. The first observations fluence-dependent exciton lifetimes in nanocrystal-doped glasses [14, 15] lead to the attribution of this signature to Auger ionization of trions[16]. The majority of quantum dots have displayed an inverse-cubic scaling of the Auger rate with particle radius and a strong similarity between the Auger rates for very different materials of the same particle size [17, 18]. The scaling has been recently attributed to the combined effects of the density of states and modified Coulomb couplings for hot carriers [19], but there has been no quantitative theoretical explanation for the similarities between observed Auger rates across a wide range of materials and gap sizes. This motivates further study of the Auger recombination in quantum dots, especially for small- and negative-gap materials where the dissimilarity between bulk and nanoparticle rates should be greatest.

In the regime of low carrier densities, the dominant nonradiative recombination pathway depends strongly on the energy gap and remains a topic of uncertainty in small-gap systems. The intraband $1S_e - 1P_e$ transition around 2000 cm^{-1} is the most widely studied low-energy transition in quantum dots because of the traditional focus on excited state relaxation in intrinsic wide-gap systems. It was initially believed that $1S_e - 1P_e$ relaxation should be very slow because of the low expected multiphonon emission rate at these gap energies, an effect known as the "phonon bottleneck" [9]. Electronic phonon bottlenecks are rarely observed in practice, however, because electrons can undergo subpicosecond relaxation by coupling to a valence hole in a process known as Auger electron cooling [9, 20, 21, 22, 23]. Relaxation in the tens to hundreds of picoseconds is observed when Auger electron cooling is inhibited, either by hole localization [24, 25, 26] or by *n*-doping, and these lifetimes are often attributed to near-field energy transfer involving surface ligand vibrations. Further reduction of the nonradiative energy transfer via thick shell growth has led to intraband lifetimes around 1.5 ns in very large CdSe/ZnS/ZnSe/CdSe quantum dot heterostructures [25].

Recent atomistic simulations using a semiclassical electron-phonon coupling framework [27] predict that lifetimes around 1 ns are the fundamental upper limit due to phonon processes intrinsic to all nanocrystals. Fully quantum mechanical models, however, imply that microsecond lifetimes are attainable when electronphonon coupling and lattice anharmonicity are small, as in II-VI semiconductors [28, 29]. Furthermore, molecular dynamics simulations and neutron scattering experiments have suggested the presence of surface-derived anharmonicities which could fundamentally limit intraband lifetimes to subnanosecond levels [30, 31]. There is consequently a substantial uncertainty regarding the basic limits on maximum achievable intraband lifetimes. A natural experimental test would be to examine the intraband lifetime in a strongly confined quantum dot where Auger cooling, nonradiative energy transfer, and other nonphonon relaxation mechanisms are minimized.

HgSe quantum dots are an attractive system for the study of nonradiative processes in confined semiconductors. A negative-gap semimetal in the bulk, quantum confinement in HgSe nanoparticles opens a size-tunable gap in the near-infrared. The low energy of the conduction band with respect to typical environmental Fermi levels renders HgSe quantum dots naturally *n*-doped [32], inducing an additional mid-infrared intraband transition as also observed in HgS [33, 34], HgTe [35], and Ag_2Se quantum dots [36]. This allows interband and intraband transitions at different energy scales to be easily investigated in the same material. The carrier dynamics in HgSe nanocrystals are also of practical interest due to applications in mid-infrared photodetection [5, 37, 38] and light emission [39].

Prior spectroscopic studies on HgSe quantum dots were limited to static measurements focusing on the spectral response of particles to alterations of their electrochemical environment [32] and surface chemistry [5, 39, 40, 41, 42]. Here, we investigate the carrier dynamics in HgSe and HgSe/CdS core/shell structures by transient photoluminescence upconversion, a nonlinear optical technique that circumvents the lack of fast infrared detectors. Auger recombination is examined in HgSe by comparing photoluminescence optical lifetimes between *n*-type and intrinsic particles

as a function of optical fluence, while the excitonic nonradiative relaxation mechanisms are examined through the effects of the CdS shell on the quantum yield and nonradiative lifetime. We also observe the emergence of surface plasmon transitions at large HgSe particle sizes, and spectral and dynamical evidence of fine structure in $1P_e$.

3.2 Results and discussion

3.2.1 Steady-state spectroscopy

Intraband absorption and emission spectra for *n*-type HgSe quantum dots are shown in Figure 3.1a. The quantum dots show size-tunable transitions in absorption and emission across the 2000 3000 cm^{-1} region. Figure 3.1b shows the size-dependence of the $1S_e - 1P_e$ absorption calculated from the electron dispersion within a two-band $k \cdot p$ approximation with diagonal matrix elements 0 and $-E_g$. For a particle of radius R, intraband transition energy is then given by

$$E(k) = \frac{1}{2}\left(\frac{\hbar^2 k^2}{m} - E_g\right) + \sqrt{\frac{\hbar^2 k^2}{2m} E_p + \frac{E_g^2}{4}} + E_b \tag{3.1}$$

with free electron mass m, bulk gap E_g, $k_{1S_e} = \pi/R$, $k_{1P_e} = 4.49/R$ and a $1S_e - 1P_e$ excitonic binding energy $E_b = -1.6e^2/\epsilon_1 R$ (gaussian units). The material parameters used may be found in the supporting information of [1].

The measurements are consistent with the $k \cdot p$ prediction at small particle sizes, but at larger sizes the intraband frequencies are significantly blueshifted from expectations and saturate at a value around 1900 cm^{-1}. The fluorescence also weakens and is not detected in the largest particles. The blueshift from the single-electron calculation, saturation at a finite energy, narrowing absorption, and quenching of fluorescence are all consistent with the emergence of surface plasmon transitions at large sizes due to further conduction band filling. Such behavior has previously been observed in ZnO [43, 44, 45] and HgS quantum dots [34]. These effects arise as the local

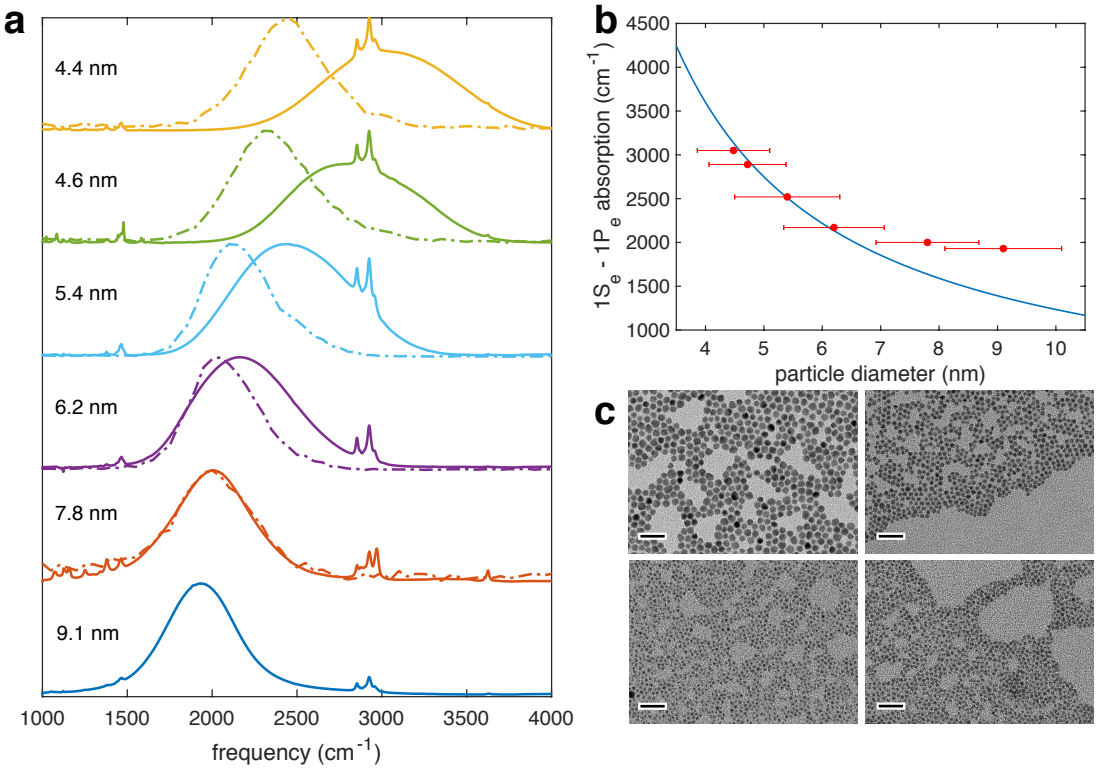

Figure 3.1: (a) Normalized intraband absorption (solid lines) and emission (dashed lines) spectra for HgSe particles of the indicated diameters. (b) Particle sizes and corresponding absorption frequencies shown with the $k \cdot p$ prediction. (c) Representative TEM images of the HgSe particles, with 40 nm scale bars. Sharp features in the absorption spectra around 2900 cm^{-1} are C-H stretch vibrations of the surface ligands. Error bars in (b) indicate standard deviations. In (a), the relative magnitude of the CH resonance decreases in large particles because the doping and resulting absorption increase.

fields produced by carriers blueshift the collective resonance. In the semiclassical picture of local field effects, a free carrier density ρ modifies the resonance angular frequency to

$$\omega = \sqrt{\omega_0^2 + \omega_{sp}^2} \tag{3.2}$$

where

$$\omega_{sp}^2 = \frac{4\pi e^2 \rho}{m^*(\epsilon_{IB} + 2\epsilon_2)} \tag{3.3}$$

defines the surface plasmon frequency ω_{sp} and ω_0 is the one-electron resonance frequency [34].

e is the electron charge, m^* is the electron effective mass, c is the vacuum light speed, and ϵ_{IB} and ϵ_2 are respectively the particle interband and matrix optical dielectric constants. We note that in contrast to most semiconductors, $\epsilon_{IB} \neq \epsilon_\infty$ in HgSe due to the negative bulk gap [46, 47]. Plasmonic effects arise from the collective excitation of many quasi-degenerate optical transitions, which in the present case may arise from $1P_e - 1D_e$, $1D_e - 1F_e$ and $1F_e - 1G_e$ transitions which are nearly degenerate at the $k \cdot p$ level of theory. Calculating ω_0 in the absence of excitonic binding and noting that $m^* \approx m$ at the wavevectors considered here, we find $\omega_{sp}/2\pi c = 960$ cm^{-1} for the 9.1 nm particles. This corresponds to a carrier density of 9.8×10^{19} cm^{-3} and 38 "excess" electrons per particle. The typical physical picture of doping in mercury chalcogenide quantum dots is one of a surface dipole lowering the quantum dot state energies relative to a fixed environmental Fermi level [33]. The heavy doping achieved here would require a very strong counterion presence in the standard picture, and possibly suggests contributions from other doping mechanisms such as chalcogen deficiency in the particle itself.

The remainder of this work focuses exclusively on the spectroscopy of smaller particles where plasmonic effects should be negligible. For these sizes, notable features in Figure 3.1 are the Stokes shift and spectral narrowing of the emission with respect to the absorption. These arise in part from the level splitting of $1P_e$ due to spin-orbit coupling and aspheric particle shape, as in HgTe quantum dots [48]. Electron-phonon coupling may also play a role. In a simple configuration coordinate picture, for example, the 200 cm^{-1} Stokes shift with respect to the lower $1S_e - 1P_{e1/2}$ transition implies a Huang-Rhys parameter of order unity in the smallest particles measured here. The intraband lineshapes are discussed further in a dedicated section.

3.2.2 Auger recombination

Figure 3.2 shows steady-state spectra and photoluminescence dynamics for the interband and intraband transitions in a sample of 5 nm diameter HgSe quantum dots. The presence of both intraband transitions around 2000 cm^{-1} and interband transitions around 6000 cm^{-1} reflects the presence

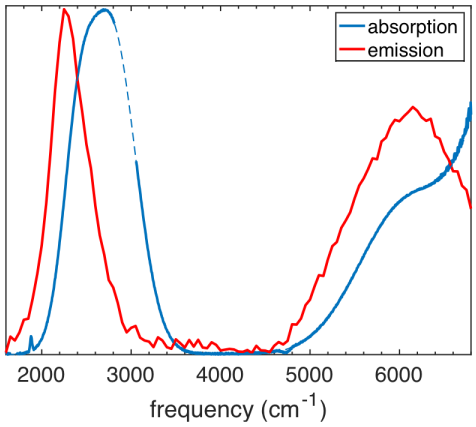

Figure 3.2: Absorption and emission spectra of 5 nm diameter HgSe nanoparticles in arbitrary units. The C-H stretch resonances have been removed from the absorption spectrum for clarity.

of separate n-doped and intrinsic populations in this sample. As shown in Figure 3.3a, at a low pump fluence of 66 μJ/cm^2 we observe a single decay for the interband photoluminescence. As the pump fluence increases, an additional fast decay becomes apparent. The decay dynamics in Figure 3.3 are accurately described by functions of the form $a_1 \exp(-t/\tau_1) + a_1 \exp(-t/\tau_2)$. For the data in Figure 3.3a, fitting gives $\tau_1 = 2600 \pm 550$ ps and $\tau_2 = 20 \pm 3$ ps. We assign the slow decay component to the exciton lifetime. Prior work has shown the interband quantum yield to strongly increase with decreasing temperature; along with the beneficial effect of shell growth, this suggested the presence of surface traps [40, 41]. Based on a calculated radiative lifetime, the exciton lifetime observed here is consistent with previously measured quantum yields of order 10^{-2} [41]. The relative amplitude of the short lifetime component increases with fluence, and this behavior is assigned to the Auger recombination of multiexcitons [15, 18, 49, 50]. Further support for this assignment, including analysis of the excitation densities and absolute photoluminescence magnitudes, may be found in the appendix to this chapter. We further note that the normalized amplitude of the fast component significantly exceeds 0.5 at high fluence, indicating that the radiative rate of the multicarrier state exceeds that of the excitonic state. This is consistent with statistical effects and, as discussed in the appendix to this chapter, possibly indicates a quadratic dependence of the interband radiative rate on the excitation number.

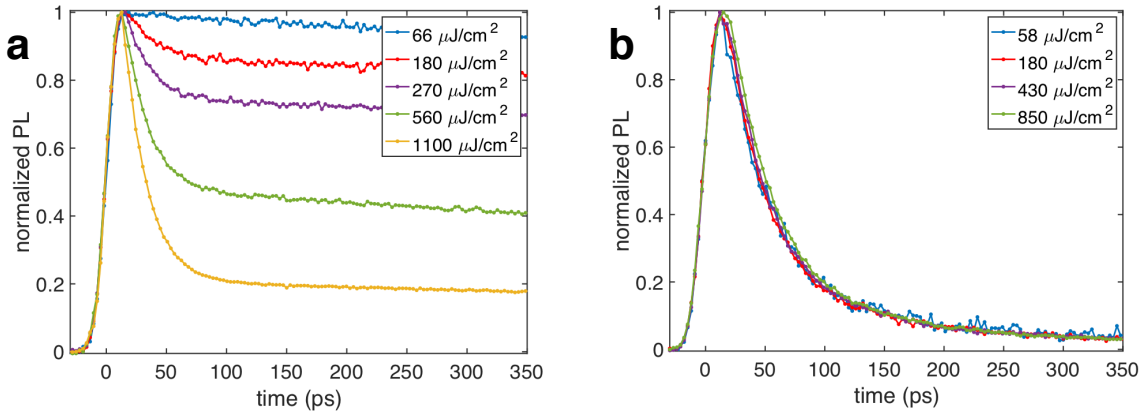

Figure 3.3: (a) Interband fluorescence decay at 5600 cm^{-1}. (b) Intraband fluorescence decay at 2100 cm^{-1} in the same sample.

As discussed in Chapter 2, it has been proposed that Auger recombination in quantum dots can be characterized by an Auger coefficient C_A defined as $C_A = V^2/8\tau_{XX}$ for the Auger decay of a biexciton with a lifetime τ_{XX} in a particle of volume V [51]. This allows direct comparisons between nanoparticle and bulk Auger recombination rates. The interband Auger coefficients are 2.6×10^{-29} cm^6/s at 5 nm diameter and 6.1×10^{-29} cm^6/s at 6 nm diameter. The Auger coefficient for bulk HgSe is not known, but these values are more consistent with those of larger gap bulk semiconductors [9]. This corroborates our previous observation of slower Auger recombination in small-gap quantum dots versus the corresponding bulk materials discussed in Chapter 2 [18].

Figure 3.3b shows the fluorescence decay for the intraband transition under similar pumping conditions. The difference is striking, as there is no longer any notable fluence-dependence. The data exhibit two decay constants of 35 ± 5 ps and 210 ± 40 ps that are nearly unchanged over the range of pump fluences, and the slow decay always constitutes approximately 60% of the time-integrated fluorescence. The absolute time-integrated photoluminescence intensities also display no clear saturation effects as shown in the appendix to this chapter. This indicates that Auger recombination is strongly suppressed in HgSe quantum dots doped with one or two electrons. The different carrier dynamics in intrinsic and weakly *n*-type HgSe may be qualitatively understood by considering that the Auger recombination rate is affected by the density of states, as determined by

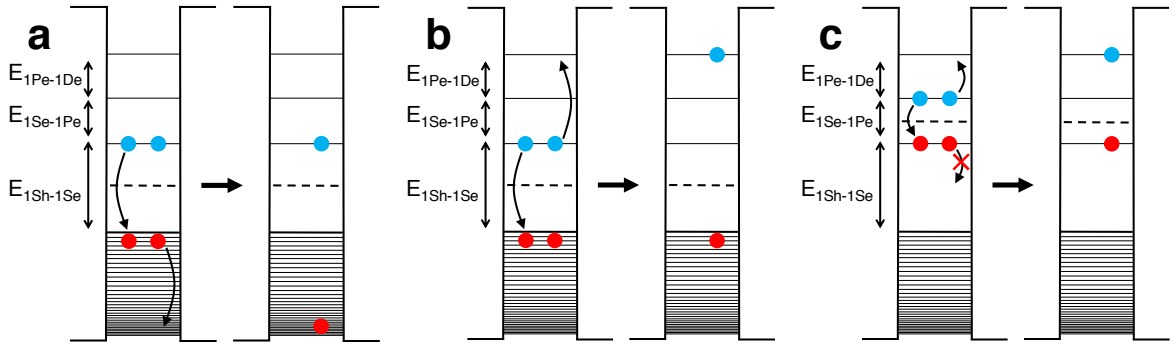

Figure 3.4: Schematics for biexciton Auger recombination in HgSe quantum dots. Blue circles are electrons and red circles are holes: (a) intrinsic particle, hot Auger hole; (b) intrinsic particle, hot Auger electrons; (c) n-type particle, hot Auger electron with no energy-conserving hot Auger hole. Dashed lines denote Fermi level positions.

Fermi's golden rule:

$$\gamma = \frac{2\pi}{\hbar}\left|\langle f|\,\hat{V}\,|i\rangle\right|^2 \rho_f \tag{3.4}$$

γ is the Auger transition rate, $\langle f|$ is a high-energy exciton final state, $|i\rangle$ is a band-edge biexciton or trion, $\hat{V}$ is a screened Coulomb operator, and ρ_f is the density of resonant final states [9]. In HgSe, the density of valence states is far greater than the density of conduction states because the hole is much heavier than the electron [47]. For interband Auger recombination, the final state is a valence-conduction exciton and there are a large number of these states resonant with the biexciton. In contrast, Auger recombination in n-type quantum dots involves conduction states exclusively and the number of exciton states resonant with a $1S_e - 1P_e$ biexciton is very low. This situation is summarized in Figure 3.4. We note that even if the lifetime under strong pumping was due to Auger recombination, a $\sim$ 200 ps Auger lifetime for a particle of 2.5 nm radius gives $C_A = 2.6 \times 10^{-30}$ cm^6/s. This upper bound on C_A is already a factor of $10^2 - 10^3$ smaller than for bulk materials of similar gap [8, 9], and similar to Auger coefficients in quantum dot systems of 10$\times$ greater gap [9, 17].

Although this suppression of Auger recombination should be a general phenomenon in weakly n-type quantum dots with a sparse conduction level structure, it does not necessarily remain at

higher doping levels. The absence of photoluminescence for the larger and more heavily doped HgSe may indeed be attributed to a very fast relaxation arising from electron-electron scattering across a large number of electron configurations.

3.2.3 Excitonic nonradiative recombination

Although intraband Auger recombination in weakly *n*-type HgSe quantum dots is absent or slow, the intraband fluorescence decay is still fast. A prior study of the intraband photoluminescence from HgSe quantum dots showed the quantum yield to be relatively independent of temperature. This indicated that trapping contributions are minor and instead suggested an activation-less process.24 Near-field energy transfer via dipolar coupling between the exciton and ligand molecular vibrations is one such mechanism [24, 25, 52, 53]. The nonradiative relaxation rate γ_{nr} for this process is derived by considering the energy dissipated by a spherical dipole of radius R into a thin absorbing coating of thickness ΔR and imaginary dielectric function ϵ'', as discussed in the supporting information of [53]. It is

$$\gamma_{nr} = \frac{\Delta R \epsilon''}{R^4} \times \frac{p^2}{\hbar} \tag{3.5}$$

where p is the transition dipole moment.

We use this formula to quantitatively model the intraband photoluminescence. The electric field within a spherical dipole of optical dielectric constant ϵ_1 embedded in a host of optical dielectric constant ϵ_2 is screened such that $p = p_0(3\epsilon_2)/(\epsilon_1 + 2\epsilon_2)$, where $p_0 = e\langle 1S_e|z|1P_e\rangle \approx 0.3eR$ for the $1S_e - 1P_e$ transition. It is calculated from the spherical Bessel solutions to a spherical potential well of radius R and infinite depth [54]. The transition dipole moment is calculated for a given transition energy from the electron dispersion including exciton binding, and a size-dependent Stokes shift is taken from an empirical fit to the data in Figure 3.1a. ϵ'' is determined from the measured absorption spectrum of the aliphatic ligands through the relation $\alpha = 2\pi\epsilon''/n\lambda$

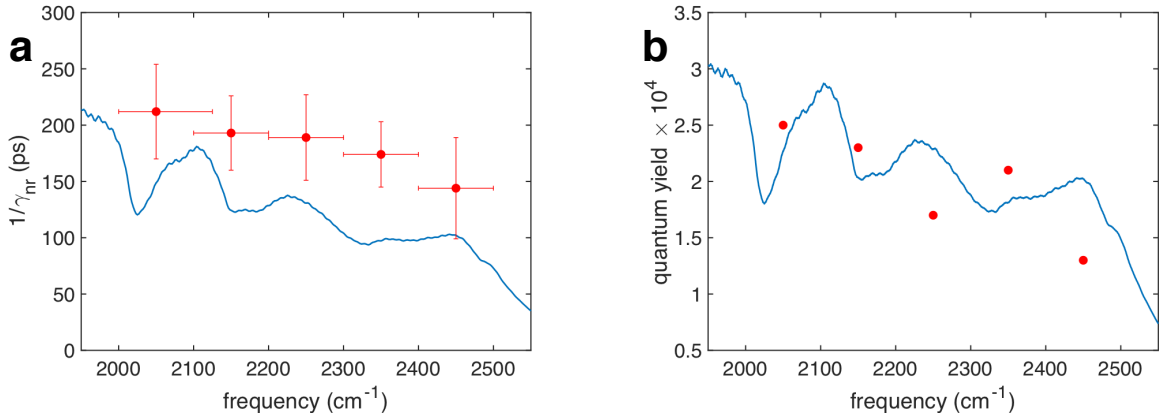

Figure 3.5: (a) Nonradiative lifetime calculated from eq 5 (line) and slow lifetime components (points); (b) quantum yields calculated from eq 6 (line) and data (points). The calculations assume a negligible width for the electronic transition. Error bars on the lifetime reflect 95% confidence bounds from fitting and error bars on the frequency reflect the measurement resolution.

where α is the absorption coefficient, λ is the vacuum wavelength of the radiation, and n is the real refractive index of the ligand. The ligand absorption between 2000 and 2500 cm^{-1} is due to a weak background of overtone and combination modes with molecular cross sections around 10^{-20} cm^2, and α ranges from 10 to 20 cm^{-1} in this region. ΔR is estimated to be approximately 1 nm from the relation $R + \Delta R = \left(R^3 + 3V_S/4\pi\right)^{1/3}$ with a ligand shell volume $V_S = 1.5 \times 10^{-19}$ cm^3, calculated assuming dense close ligand packing of 4 nm^{-2} and $R = 2.5$ nm. With these numbers we obtain a lower bound on the lifetime $1/\gamma_{nr}$, shown in Figure 3.5a. The structure in the calculations reflects structure in the measured absorption spectrum. The lifetimes are in the 100 - 200 ps range, and it is notable that a coating with an absorption coefficient as low as 10 cm^{-1} is sufficient to induce such lifetimes.

In a static measurement, the nonradiative lifetime should manifest in the photoluminescence quantum yield ϕ. When γ_{nr} is much larger than the radiative rate γ_r, $\phi \approx \gamma_r/\gamma_{nr}$. This ratio for near-field energy transfer is

$$\frac{\gamma_r}{\gamma_{nr}} = \frac{4\omega^3\sqrt{\epsilon_2}}{3c^3} \times \frac{R^4}{\epsilon'' \Delta R} \tag{3.6}$$

where ω and c are the angular frequency and vacuum speed of light, respectively. The predicted

and measured quantum yields are shown in Figure 3.5b. The overall agreement between the data and theory is reasonable considering the simplicity of the model. We note that this model does not account for the short lifetime component, which comprises approximately 40% of the fluorescence and may be due to a minority population exhibiting defects or increased doping. Transient fluorescence and quantum yield measurements were performed on samples with intraband emission across the 2000 - 2500 cm^{-1} region, and the results are summarized in Table 3.1.

Summary of Intraband Photoluminescence Data			
PL frequency (cm^{-1})	τ_1 (ps)	τ_2 (ps)	ϕ
2050	44 ± 2	210 ± 40	2.5×10^{-4}
2150	35 ± 2	200 ± 30	2.3×10^{-4}
2250	38 ± 2	190 ± 30	1.7×10^{-4}
2350	25 ± 2	170 ± 30	2.2×10^{-4}
2450	34 ± 2	140 ± 40	1.4×10^{-4}

Table 3.1: Summary of HgSe intraband photoluminescence data. Uncertainties represent the maximum variations in time constants across all measured pump powers for a given sample.

3.2.4 Excitonic nonradiative recombination: shell effects

The near-field energy transfer model of nonradiative relaxation implies that, given a fixed transition frequency and absorbing environment, γ_{nr} should scale inversely with the total nanocrystal size. In a single-component system, however, this behavior is difficult to verify because p and possibly ϵ'' (via the changing transition frequency) are also affected. One may decouple these fundamental radiative properties from the nanocrystal radius by growth of a core/shell heterostructure with a type-I band alignment, which confines both carriers to the core. Energy transfer to surface ligands should exhibit an polynomial scaling as noted previously, while mechanisms involving bulk phonons should not be affected by a shell. Localized surface vibrations associated with mechanical softness and undercoordinated atoms should be strongly reduced even with thin shells, provided that they are highly lattice-matched. Although the rate of surface trapping ideally exhibits an expo-

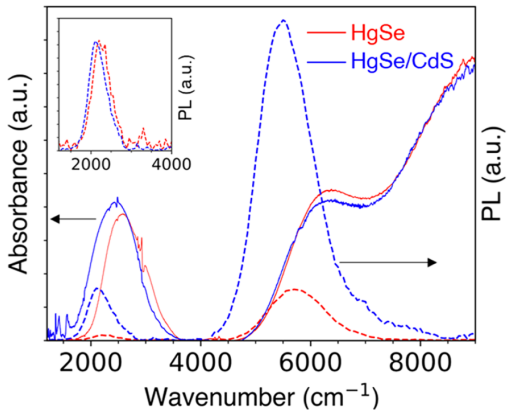

Figure 3.6: Absolute absorption (solid lines) and emission (dashed lines) spectra for 2.4 nm radius HgSe and the same particles with a 2.9 nm thick shell. The inset shows the normalized intraband emission.

nential decrease with increasing shell thickness due to the distance-dependence of tunneling, this could be modified if the shell is sufficiently defective.

To investigate the underlying relaxation mechanisms, we examined the influence of CdS shell thickness for HgSe/CdS at low doping levels. Representative absorption and emission spectra of 2.4 nm radius HgSe with a 2.9 nm CdS shell are shown below in Figure 3.6. Shell growth produces negligible shifts in the interband and intraband transition energies in accordance with the expectation of strong type-I band alignment in HgSe/CdS. We also see that the shell increases the absolute interband and intraband photoluminescence with a stronger effect in the latter. This suggests a reduced nonradiative relaxation rate which should manifest in quantum yield and lifetime measurements.

Such data are shown in Figure 3.7. Growth of a thick shell leads to a small increase in the interband quantum yield, with the exception of the thin-shell HgSe/CdS sample. These QDs display a relatively low interband quantum yield of 0.5% due to the low temperature shell synthesis, which increases to $> 2\%$ upon annealing [2]. The mild increase of interband quantum yield with shell thickness is qualitatively similar to prior works which reported saturation of interband HgSe/CdS quantum yield at moderate shell thicknesses [41, 40]. In contrast, the intraband quantum yield exhibits a 30-fold increase over the same shell thickness range. The intraband radiative rate γ_r of

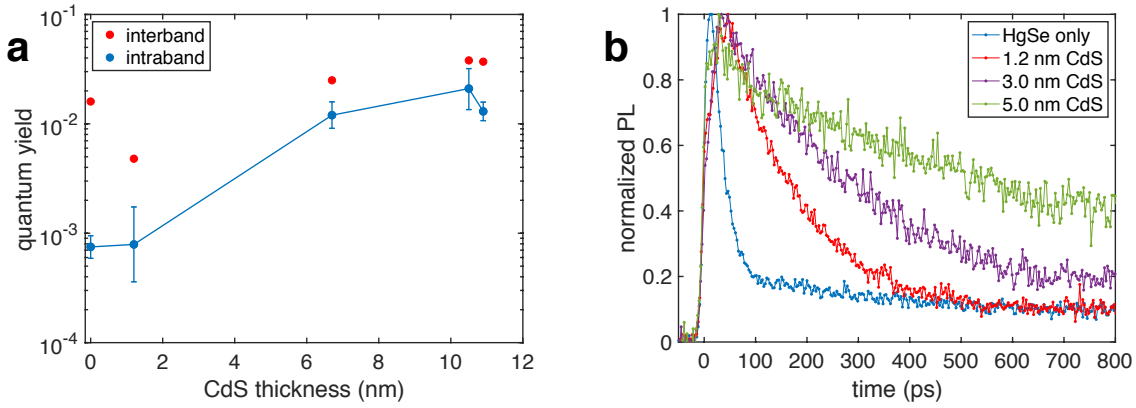

Figure 3.7: (a) Interband and intraband photoluminescence quantum yields versus CdS shell thickness for 2.4 nm radius HgSe particles; (b) Normalized intraband photoluminescence decays for different CdS thicknesses in similar samples.

HgSe QDs is

$$\gamma_r = \frac{4\omega^3 p^2 \sqrt{\epsilon_2}}{3\hbar c^3} \tag{3.7}$$

With the material parameters from the supporting information of [2], the intraband radiative lifetime $1/\gamma_r$ for HgSe QDs emitting at 2050 cm^{-1} is calculated to be 900 ns. Growth of a CdS shell slightly changes the dielectric screening [2], leading to a radiative lifetime of 700 ns for HgSe with a thick CdS shell.

With the measured quantum yields and calculated radiative lifetimes, the average nonradiative lifetimes are calculated to vary from 700 ps in the HgSe core to 15 ns in HgSe/CdS with a 15 nm thick shell. This increasing trend is supported by the lifetime measurements, although they exhibit multiexponential behavior. The HgSe cores exhibit two nonradiative relaxation times of 26 ± 1 and 1030 ± 35 ps, and about 90% of the time-integrated signal comes from the slower decay. This relaxation component is about three times as long as those shown earlier, which might be due to modified synthetic and cleaning procedures leading to a smaller surface ligand density. Shell growth leads to a 25-fold lengthening of the fast lifetime component, while expected lengthening of the slow component is not resolved on the timescale of these measurements. Overall, the photoluminescence data indicate that thick CdS shells substantially lengthen average intraband

nonradiative lifetimes into the nanosecond regime.

The intraband lifetime derived from the quantum yield is at least an order of magnitude longer than the $\sim$ 1 ns phonon-mediated lifetime limit predicted by semiclassical simulations [27]. Although the rate of surface trapping should be slow at the larger shell thicknesses considered here, it is still possible that stacking faults in CdS related to lattice strain can allow carriers to reach the surface [55]. The present data therefore do not definitively rule out a trapping mechanism. Overall, the weak but positive scaling of lifetimes and quantum yields with shell thickness suggests that energy transfer remains the dominant nonradiative mechanism and that anharmonicity or intrinsic phonon effects are relatively small.

The 2% intraband quantum yields achieved in thick-shell HgSe/CdS makes them the brightest reported solution-phase chromophores in the 2000 cm^{-1} (5 μm) infrared region at room temperature. This quantum yield is also close to the room temperature record of $\sim$ 4% recently observed in epitaxial III-V superlattices, which are limited by Auger recombination [56]. Long lifetimes and large quantum yields are beneficial for mid-infrared light detection and emission as discussed at length elsewhere in this thesis. The present results indicate that decoupling the quantum dot excitation from the infrared-absorbing environment remains a crucial component of this goal.

3.2.5 Intraband lineshapes and intersublevel relaxation

We now consider the lineshapes of the intraband transitions and the corresponding dynamics in HgSe. Careful inspection of the intraband absorption for weakly doped particles reveals that it does not consist of a single inhomogeneously broadened line. Instead, as shown in Figure 3.8, it is better described as a sum of two Gaussian distributions. This fitting is motivated by the spin-orbit splitting of the $1P_e$ manifold into $1P_{e1/2}$ and $1P_{e3/2}$ sublevels as previously reported for HgTe quantum dots [48]. Although the spin-orbit coupling is smaller in HgSe, it should still produce a sizable splitting [57]. The emission nearly overlaps with the lower absorption feature and its 480 cm^{-1} full-width at half-maximum (fwhm) matches the line width of the fitted $1S_e$ -

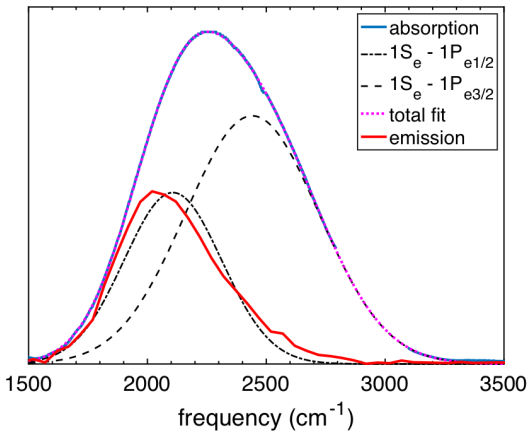

Figure 3.8: Measured absorption and emission spectra for the intraband transition in HgSe along with fits of the absorption lines. The $1S_e - 1P_{e1/2}$ transition fit has a 2100 cm^{-1} center frequency and 480 cm^{-1} fwhm, and the $1S_e - 1P_{e3/2}$ transition fit has a 2450 cm^{-1} center frequency and 650 cm^{-1} fwhm. C-H stretching resonances in the absorption have been removed for clarity.

$1P_{e1/2}$ transition. This indicates electron relaxation to $1P_{e1/2}$ within picoseconds and subsequent emission from that state. There is also a weak high-energy tail which may be emission from the short-lived $1P_{e3/2}$ population. This assignment is supported by time-resolved fluorescence measurements which show spectrally structured photoluminescence decays. To enable collection of transient data over the entire emission band, a sample with an emission peak around 2300 cm^{-1} was synthesized.

Its spectra are shown in Figure 3.9a, and relaxation dynamics across the emission line are shown in Figure 3.9b. To the red, the dynamics similar to those shown earlier. Slow relaxation constitutes the majority of the time-integrated fluorescence and displays a time constant of approximately 170 ps, in agreement with the near-field energy transfer model. To the blue, a fluorescence transient of 15 ps width grows in magnitude and constitutes $> 60\%$ of the time-integrated fluorescence at 2750 cm^{-1}, consistent with emission from $1P_{e3/2}$. The slow relaxation also becomes faster, with a time constant of about 100 ps, likely due to stronger ligand absorption as one approaches the ligand C-H stretch modes around 2900 cm^{-1}. At intermediate frequencies, the dynamics are more complex. Both prompt and slow emission are apparent, but a secondary

rise in emission is also observed. At these frequencies, the measurement simultaneously probes red ($1P_{e1/2}$) emission from small particles and blue ($1P_{e3/2}$) emission from large particles. If the $1P_{e3/2} - 1P_{e1/2}$ transition rate is slower for smaller particles, this would account for the observed behavior. The physical basis for a size-dependent rate could be due to phonon-mediated relaxation, leading to slower relaxation for larger splitting. Although such a "phonon bottleneck" effect is not observed in intrinsic particles due to a subpicosecond Auger process [9, 58], it may be active here. Indeed, a nonradiative $1P_{e3/2} - 1P_{e1/2}$ transition should only be possible via phonon emission because the dense manifold of valence states is not accessible, and the observation of slow intersublevel relaxation is therefore consistent with the lack of measurable Auger recombination in this system.

We modeled the transient data using a four-level relaxation scheme shown in Figure 3.9c. To simulate the photoluminescence, the population N at each simulation time t_i with time step $\Delta = 0.5$ ps was calculated according to equations 3.8, where $I(t_i)$ is the instantaneous pump pulse fluence at time step t_i and σ is the nanocrystal cross section. The levels 1, 2, 3 and 4 respectively correspond to the pump state, $1P_{e3/2}$, $1P_{e1/2}$ and $1S_e$ states in Figure 3.9c, and the instantaneous photoluminescence signal is taken to be the weighted sum of N_2 and N_3.

$$
\begin{aligned}
N_1(t_i) &= N_1(t_{i-1})I(t_i)\sigma N_4(t_{i-1}) - \frac{N_1(t_{i-1})}{\tau_1}\Delta \\
N_2(t_i) &= N_2(t_{i-1}) + \left(\frac{N_1(t_{i-1})}{\tau_1} - \frac{N_2(t_{i-1})}{\tau_2} - \frac{N_2(t_{i-1})}{\tau_3}\right)\Delta \\
N_3(t_i) &= N_3(t_{i-1}) + \left(\frac{N_2(t_{i-1})}{\tau_2} - \frac{N_3(t_{i-1})}{\tau_4}\right)\Delta \\
N_4(t_i) &= 1 - N_1(t_i) - N_2(t_i) - N_3(t_i)
\end{aligned}
\tag{3.8}
$$

Simulated fluorescence decays used $\tau_{\text{pump}} = 10$ ps (fwhm) centered at $t = 0$, corresponding to $I(t)$ in equation 7, $\tau_1 = 1$ ps, $\tau_3 = \tau_4 = 100$ ps, $\tau_{\text{hole}} = 0$ ps and $\Delta = 0.1$ ps. τ_2 was taken to be 5 ps for large particles and 30 ps for small particles, a realistic range based on reported phonon-mediated relaxation across similar energy gaps [59, 28]. The relative weights of the $1P_{e3/2}$ state for the

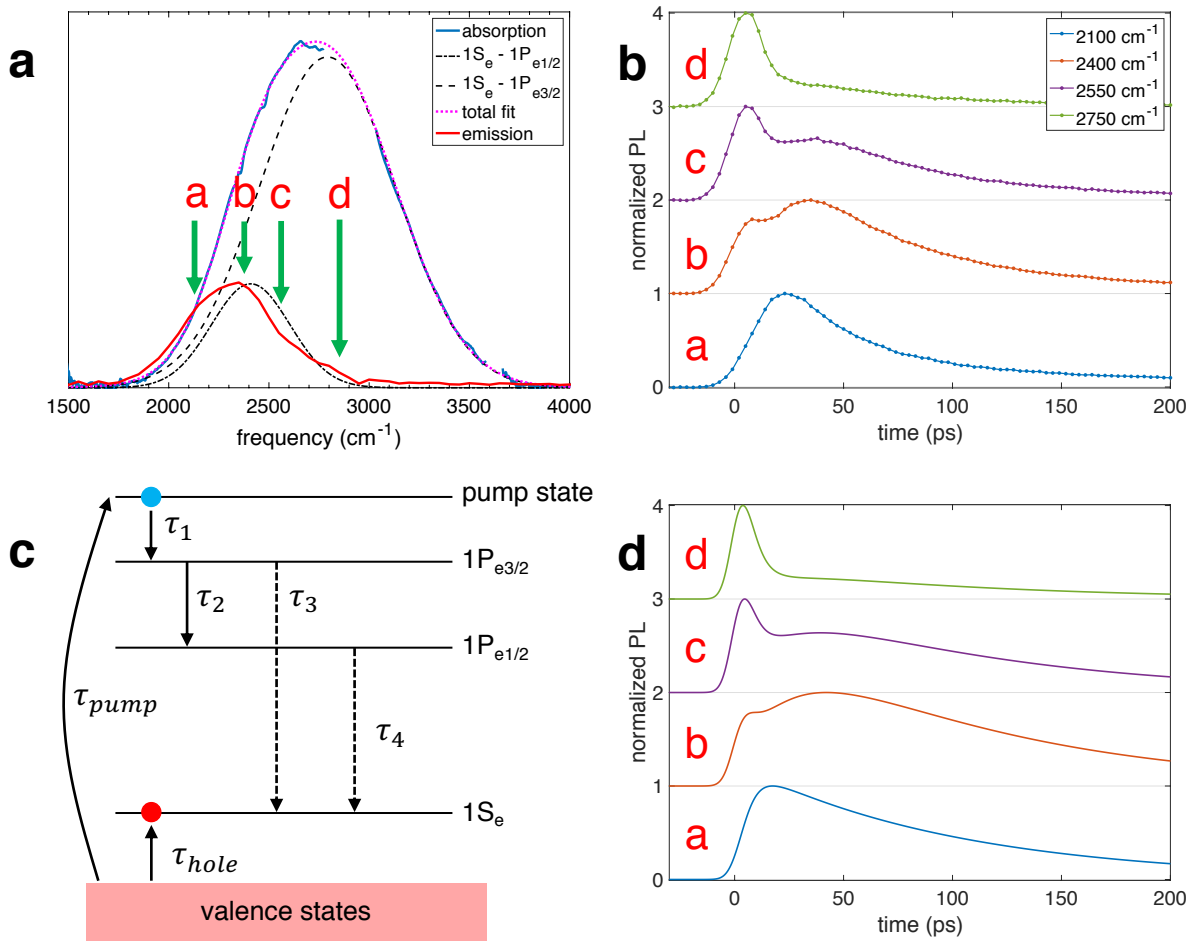

Figure 3.9: (a) Measured absorption and photoluminescence in arbitrary units (solid lines) with organic vibrations removed for clarity and fits to the absorption spectrum (dashed lines). (b) Transient fluorescence at the indicated frequencies. (c) Four-level model with radiative transitions shown as dashed lines. (d) Simulated transient fluorescence using the model shown in (c).

simulated curves were 0%, 30%, 60%, and 90% from bottom to top. The model reproduces gross features of the intraband dynamics, supporting the proposition of distinct emission dynamics from individual $1P_e$ sublevels.

3.3 Conclusions

We studied the photophysics in intrinsic and *n*-type HgSe quantum dots using steady-state absorption and photoluminescence, and transient infrared photoluminescence upconversion. With

intrinsic quantum dots, the interband transition emitting around 2 μm displays nanosecond exciton lifetimes and biexciton Auger lifetimes of 20 - 30 ps. This behavior is similar to that observed in other interband quantum dots without alloyed shells. In *n*-type quantum dots, the mid-infrared absorption evolves from the intraband $1S_e - 1P_e$ transition in small particles to a transition with increased plasmonic character at large sizes. In the weakly *n*-type quantum dots, intraband transitions emit around 5 μm. Measurements of the intraband photoluminescence lifetime revealed an absent or dramatically reduced Auger recombination rate, assigned to the sparse density of states in *n*-type quantum dots. This effect is expected to generalize beyond HgSe to all weakly *n*-type quantum dots where the density of states in the conduction band is small. Auger coefficients for the intraband transition in HgSe quantum dots are at least three orders of magnitude smaller than for bulk materials of similar gaps. In addition, spectrally resolved dynamical measurements revealed slow phonon-mediated intersublevel relaxation assigned again to the sparse density of states. The suppressed Auger recombination in weakly *n*-type quantum dots is a significant motivation to pursue mid-infrared lasers and detectors utilizing intraband transitions.

3.4 Methods

Synthesis of HgSe nanocrystals: 45 mg of $HgCl_2$ was dissolved in 5 ml of oleylamine by stirring and heating at 100 °C for 50 min in an N_2-purged glovebox. The clear solution was then cooled or heated to the reaction temperature, determined by the desired particle size. 20 μl of bis(trimethylsilyl)selenide (TMSSe) diluted into 0.45 ml of dry oleylamine was then injected into the $HgCl_2$ solution, which immediately turned black. The reaction was typically allowed to progress for 4 min, after which it was quenched by pouring the reaction mixture into 5 ml of cold chlorobenzene. Higher temperatures and longer reaction times furnished larger particles. Outside the glovebox, the particles were precipitated by addition of 1.2 ml of a 0.1 molar didodecyldimethylammonium bromide (DDAB)/isopropanol solution and additional ethanol as needed. After centrifugation, the supernatant was discarded, and the particles were dispersed

in 2 ml of tetrachloroethylene (TCE). The particles were then cleaned a second time. 0.6 ml of DDAB/isopropanol was added to the cleaned solution along with additional isopropanol as needed for precipitation. After centrifugation and drying, the particles were dispersed in TCE for measurements.

Synthesis of HgSe cores for HgSe/CdS: HgSe cores were synthesized following a modified version of the above procedure. 108 mg of $HgCl_2$ was added to a 3-neck flask on a heating mantle with 10 mL of oleylamine and a stir bar. The flask was equipped with rubber sleeve stoppers and a thermocouple, and connected to a Schlenk line manifold. Three vacuum - Argon flush cycles were performed at room temperature, and the flask was heated at 100 °C for 45 minutes. The temperature was then reduced to 90 °C. A solution comprised of 50 μL TMSSe and 0.95 mL oleylamine was prepared in a N_2 glovebox and injected into the flask. The temperature dropped to 88 °C and was kept at this temperature for 2 minutes. The flask was then removed from the mantle, cooled to room temperature using compressed air, and 10 mL octane was added. In air, the reaction mixture was centrifuged to remove excess unreacted Hg complex as a grey pellet. The supernatant containing the nanocrystals was collected, cleaned by addition of ethanol and centrifugation, and dispersed in 0.1 mL of oleylamine and 4 mL of TCE. A second cleaning was done by addition of 0.8 mL of 0.1M DDAB/TCE and isopropanol precipitation. After centrifugation, the precipitate was dispersed in 0.1 mL of oleylamine and 2 mL of TCE, and stored as a stock solution at -10 °C. This procedure produces about 30 mg of cleaned HgSe nanocrystals.

Growth of CdS shells: CdS shells were grown by a two-step procedure involving growth of a thin shell at low temperature, cleaning, and a final high-temperature thick shell growth. A more detailed discussion may be found in [2]. 30 mg of purified HgSe nanocrystals were added to a 3-neck flask with 15 mL of a 4:1 oleylamine:hexadecane solution, and three vacuum - Argon cycles were performed at room temperature. The temperature was then set to 80 °C. When the temperature reached 40 °C, 1.17 mL of 0.1 molar cadmium bis(phenyldithiocarbamate) (CdPDTC) solution was injected. This corresponds to 2 monolayer-equivalents (MLs) of CdS shell. The

solution was kept at 80 °C for 5 minutes then cooled to 50 °C. 0.82 mL of 0.1 molar CdPDTC solution (1 ML of CdS) was then injected and the solution was heated at 80 °C for 5 minutes. The flask was then connected to vacuum at 80 °C to remove H_2S gas evolved during the reaction. When the pressure dropped below 1 torr, the flask was returned to Argon flow and cooled to room temperature. These thin-shell HgSe/CdS particles were then precipitated using methyl acetate and redispersed in 2 mL of TCE. They may be stored at this stage as a stock solution at -10 °C. TEM imaging showed that the nanoparticle diameter to increase from 4.8 nm to 6.1 nm after this shell growth with no obvious homogeneous nucleation.

Thick CdS shells were then overgrown on the thin-shell HgSe/CdS using cadmium bis (diethyldithiocarbamate) (CdDEDTC) as a single-source precursor, with amines and cadmium oleate as ligands. A 1:5 molar ratio of cadmium oleate to CdDEDTC prevented the formation of wurtzite arms during shell growth while avoiding homogenous nucleation of CdS. The reaction solvent was a 2:2:1 mixture of hexadecane, dodecylamine and hexadecylamine served as the solvent. A 0.02 molar CdS shell precursor solution was first prepared by adding 2 mL of 0.024 molar cadmium oleate solution to 10 mL of 0.024 molar cadmium bis(diethyldithiocarbamate) solution (98 mg CdDEDTC in 10 mL of reaction solvent). The mixture was sonicated at room temperature to dissolve, and gently warmed before loading into an automated syringe pump. Thin shell HgSe/CdS nanocrystals grown from 8 mg of HgSe cores were precipitated with methyl acetate, dispersed in 4 mL of warmed solvent solution, and 1.35 mL of 0.024 molar cadmium oleate solution (1.5 MLs) was added. The mixture was placed in a 3-neck flask on the Schlenk line with vacuum - Argon cycling and then heated rapidly to 220 °C at about 50 °C/minute. When the temperature reached 215 °, the CdS precursor solution was injected at rate 0.396 mL/minute for 10 minutes. This is equivalent to 3MLs of CdS. The temperature during this time was maintained at 220 °C but did not exceed 225 °C to minimize alloying. The solution was then cooled to 120 °C and evacuated to remove the H_2S. Evacuation is necessary to prevent homogeneous nucleation of CdS during subsequent growth cycles or post-synthetic doping. For further CdS growth cycles in 3 ML units,

the flask was heated again to 220 °C and CdS precursor injected at 0.650 mL/minute for 10 minutes. After the injection is complete, the flask was then cooled and evacuated. The cooled reaction mixture was cleaned by centrifugation to form a thick precipitate, with remaining particles in the supernatant precipitated by methyl acetate acetate addition and further centrifugation. The final precipitate was then dispersed in 4 mL of 10:1 TCE:oleylamine, boiled at for a few seconds to dissolve the saturated amine solvent, and allowed to cool. The solution was then cleaned twice by precipitation with methyl acetate and dispersion in TCE. After the second precipitation, the pellet was dried under vacuum and dispersed in TCE for measurements.

Electron microscopy: Transmission electron microscopy images were collected using an FEI Tecnai Spirit electron microscope operating at 120 kV. Particle sizes were determined manually as the longest distance across the particle using ImageJ software.

Absorption spectroscopy: Absorption spectra were collected using a Nicolet Magna 550 FTIR instrument with a DTGS detector, scanning at 4 cm^{-1} resolution.

Transient photoluminescence spectroscopy Transient data were obtained by the technique of gated sum-frequency generation (upconversion), described in more detail in Appendix C. The beam from a home-built Nd:YLF regenerative amplifier producing 10 ps, 1053 nm pulses at 1 kHz was split into two paths by an 80:20 beamsplitter. The weak path pumped the sample in the transverse geometry after attenuation, variable optical delay, and weak focusing by a cylindrical lens. The strong path was brought collinear with the fluorescence by a CaF_2 beamsplitter and parametric mixing in a KTA crystal generated light at the sum-frequency. Filters removed the fundamental and weak second harmonic of the laser. The sum-frequency pulse then passed through a monochromator to a silicon photomultiplier (Hamamatsu C14193-1325SA) and a gated integrator discriminated it from the background. The spectral resolution of the measurement was 80 - 140 cm^{-1} , governed by either the phasematching bandwidth or the monochromator depending on the spectral region. The spectral range of the measurement was 6500 - 2000 cm^{-1}, limited on the red side by crystal absorption and on the blue side by the crystal cut angle.

Photoluminescence spectroscopy: Photoluminescence spectra were obtained using a home-built Michelson interferometer operating in step-scan mode. An 808 nm laser diode of 150 mW average power modulated as a sine wave at 100 kHz excited the sample. The fluorescence was collimated by a parabolic mirror and sent through the interferometer to a cooled HgCdTe detector with a 900 cm^{-1} cutoff frequency. A silicon wafer filtered out scattered laser light. The detector output was sent through a lock-in amplifier, and one of the interferometer arm lengths was scanned for a distance corresponding to 50 cm^{-1} spectral resolution after Fourier transformation of the interferogram. To correct for the detector responsivity and atmospheric absorption, the measured spectrum was divided by the ratio of a measured and calculated blackbody photon flux.

Quantum yield determination: The quantum yield was determined by making an absolute quantum yield measurement on a reference near-infrared sample in an integrating sphere and calibrating subsequent photoluminescence measurements to this reference. An HgTe sample with a photoluminescence peak at 3800 cm^{-1} (2630 nm) was prepared as the reference according to a prior report.14 It was dispersed in TCE and contained in a CaF_2 cuvette for the measurement. In a gold integrating sphere with an amplified PbSe detector on one port, the sample was excited by an 808 nm diode laser modulated as a square wave at 1 kHz. The detector signal S, with and without a silicon window on the detector port, was recorded with the sample and with a TCE blank. 808 nm light is completely blocked by the silicon window within the sensitivity of the measurement. The reference photoluminescence quantum yield ϕ_r under these conditions is therefore $\phi_r = S_{S,Si}/(S_B - S_S) \times (\Re_{808}/\Re_{2630}) \times T^{-1}$ where the subscripts S, B and Si respectively denote the sample, TCE blank, and silicon window. $\Re$ is the wavelength-dependent PbSe detector responsivity and $T = 0.6$ is the transmission of the silicon window. The detector responsivity is linear with wavelength in this spectral range so that $\Re_{808}/\Re_{2630} = 808/2630$. To obtain the quantum yield of an arbitrary sample from its emission spectrum, the quantum yield of the reference sample was correlated to its measured emission spectrum. The spectrum was normalized to the blackbody as described above and integrated. The integral of the reference sample emission is Δ_r.

The quantum yield of an arbitrary sample with integrated emission Δ could then be calculated as $\phi = (\Delta/\Delta_r) \times \phi_r$.

3.5 Appendix

3.5.1 Photoluminescence saturation behavior

Additional support for the assignment of the fast interband photoluminescence decay to Auger recombination, and the absence of detectable Auger recombination in intraband photoluminescence, comes from the fluence-dependence of the absolute signal magnitudes. Shown below are the integrated and early-time signals for the interband data presented in the main text, determined using the biexponential fits, along with the absolute decays. The integrated signal shows clear satura-

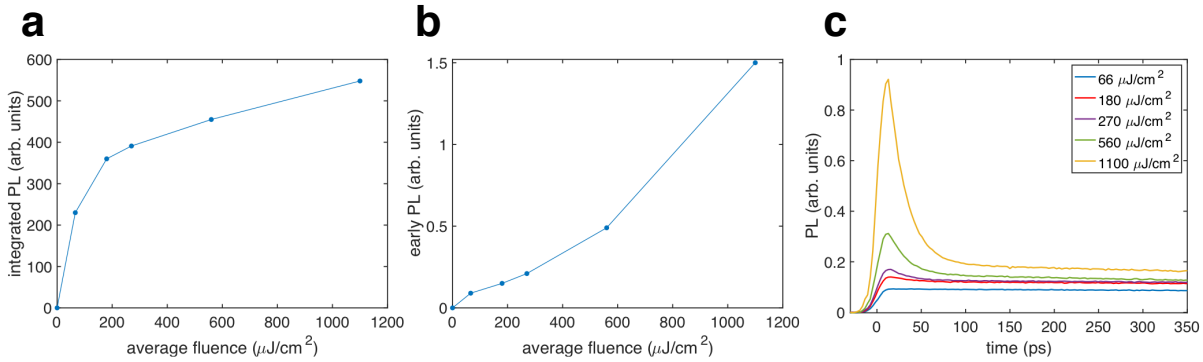

Figure 3.10: (a) Interband time-integrated photoluminescence signal; (b) Interband early-time peak photoluminescence signal; (c) Absolute interband photoluminescence decays presented in the main text.

tion while the early-time signal grows steadily with the pump fluence. This is consistent with an Auger decay of multicarrier states. The lack of complete saturation in the integrated PL and the superlinear early-time signal are likely due to bleaching effects, which limits reabsorption of the fluorescence and allows more of the sample to be excited. Statistical effects could also contribute to superlinear behavior, as described later in this appendix.

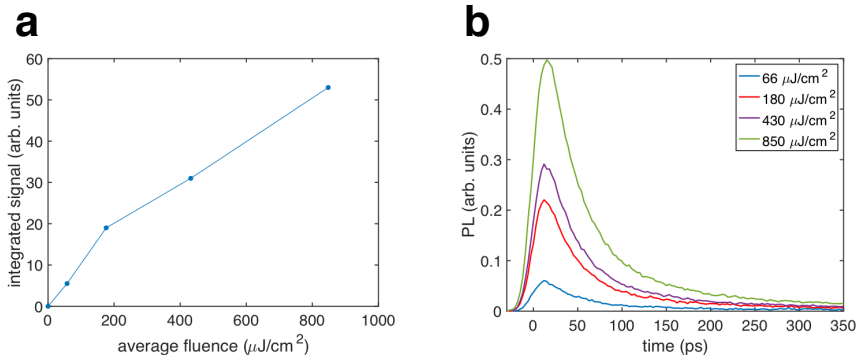

Figure 3.11: (a) Intraband time-integrated photoluminescence signal; (b) Absolute intraband photoluminescence decays presented in the main text.

Shown above are equivalent data for the intraband decays presented in the main text. As discussed earlier, they do not change with pump fluence. The early-time and time-integrated signals are therefore equivalent. The signal does not display an obvious saturation, consistent with our determination that Auger recombination is not detectable in this system.

3.5.2 Multicarrier decay kinetics without Auger processes

Manifestation of Auger decay in photoluminescence lifetime measurements depends on the emission rate of N-exciton (multicarrier) states in the ensemble average. In the case of noninteracting bound excitons, the emission rate scales as N and the decay remains exponential with a constant exciton lifetime. In the plasma picture used to describe recombination in bulk semiconductors, all electrons and holes are uncorrelated and all may recombine with each other equally. The decay is hyperbolic, and the emission rate scales as N^2. These scalings are examined below.

Linear scaling: For N noninteracting excitons, the exciton decay kinetics are given by

$$\frac{dN}{dt} = -kN \tag{3.9}$$

and exponential behavior is observed. If one considers a multiexciton simply as a noninteracting

collection of n excitons, then $N(t) = \sum_n P_n(t)n$ where $P_n(t)$ is the time-dependent occupation probability of the n-exciton. This decays due to the recombination of a single constituent exciton and creates an $(n-1)$-exciton at a rate k_n. Therefore, the change in average exciton number is

$$\Delta N = \sum_n (-nk_nP_n(t) + (n-1)k_nP_n(t))\Delta t = -\sum_n k_nP_n(t)\Delta t \tag{3.10}$$

Discretizing the kinetic equation above and multiplying both sides by Δt allows one to compare the two equations for ΔN, implying that

$$k_{X,n} = nk \tag{3.11}$$

where X denotes the exciton picture. Thus, although the overall decay of the average exciton number has a fixed rate k, the decay of an n-exciton is n times faster. This does not imply that an n-exciton is more strongly coupled to radiation, only that it may decay in n more ways. We refer to this as a "trivial" factor in later discussions, and k remains the relevant rate for an energy transfer mechanism based on the dipole interaction.

Quadratic scaling: In the free carrier or plasma picture, all electrons and holes may recombine with each other equally. The relevant model in this case is

$$\frac{dN}{dt} = -gNP \tag{3.12}$$

where N and P now respectively denote the electron and hole numbers. For intrinsic systems, $N = P$ and the decay is hyperbolic:

$$\frac{dN}{dt} = -gN^2 \tag{3.13}$$

Applying the same procedure as above and taking the recombination coefficient g to be independent

of n, as is conventional in bulk semiconductors, we find

$$k_{F,n} = gn^2 \tag{3.14}$$

where F denotes the free carrier picture. One factor of n here is the trivial scaling noted above, and the other factor of n reflects the n equivalent recombination pathways between all electrons and holes.

The relevant scaling in a quantum dot might vary. The quadratic scaling could apply in the case of interband transitions where the hole density of states is large and bulk-like. Indeed, quantum mechanical calculations by Wimmer *et al.* [60] show the interband biexciton radiative rate to vary between 1× and 2× the exciton radiative rate, not counting the trivial n factor, depending on the particle size and correlation strength. Only the factor of 2× is consistent with the bulk free carrier picture. For intraband transitions, the "holes" have a nominal multiplicity of 2, and an intraband biexciton can only relax by recombining an electron with a hole of appropriate spin. The quadratic scaling is unlikely in this case.

3.5.3 Simulations of multicarrier decay kinetics with Auger processes

If one takes the Auger recombination mechanism to involve pairs of true bound excitons, and that any exciton pair may recombine equivalently, the nonraditive Auger rate will scale according to the probability of choosing 2 excitons from n excitons. This

$$k_{AX,n} = k_{XX}\frac{n(n-1)}{2} \tag{3.15}$$

where k_{XX} is the biexction Auger recombination rate. In the plasma or free carrier picture for bulk semiconductors, the kinetics for Auger recombination are

$$\frac{dN}{dt} = -\gamma N^3 \tag{3.16}$$

and, by the same procedure used earlier, one obtains

$$k_{AF,n} = \gamma n^3 \rightarrow \gamma(n-1)^3 \tag{3.17}$$

The rightmost expression is a necessary modification for quantum dots, where Auger recombination requires $n \geq 2$ and the "biexciton" Auger rate follows $k_{AF,2} \leftrightarrow k_{XX,2}$ by convention.

To simulate the photoluminescence decays associated with the excitonic and plasma models, the initial excitation levels are obtained from the Poisson distribution as

$$N_n(t_0) = \frac{e^{-\langle n \rangle}\langle n \rangle^n}{n!} \tag{3.18}$$

$N_n(t_0)$ is the number of quantum dots with n excitations as a function of the average $\langle n \rangle$ at time $t_0 = 0$. In the excitonic picture, the populations N_n evolve according to

$$\begin{aligned}
N_5(t_i) &= N_5(t_{i-1}) - \left(\frac{N_5(t_{i-1})}{\tau_{AX,5}} + \frac{N_5(t_{i-1})}{\tau_{X,5}}\right)\Delta \\
N_4(t_i) &= N_4(t_{i-1}) + \left(\frac{N_5(t_{i-1})}{\tau_{X,5}} + \frac{N_5(t_{i-1})}{\tau_{AX,5}} - \frac{N_4(t_{i-1})}{\tau_{X,4}} - \frac{N_4(t_{i-1})}{\tau_{AX,4}}\right)\Delta \\
N_3(t_i) &= N_3(t_{i-1}) + \left(\frac{N_4(t_{i-1})}{\tau_{X,4}} + \frac{N_4(t_{i-1})}{\tau_{AX,4}} - \frac{N_3(t_{i-1})}{\tau_{X,3}} - \frac{N_3(t_{i-1})}{\tau_{AX,3}}\right)\Delta \\
N_1(t_i) &= N_1(t_{i-1}) + \left(\frac{N_2(t_{i-1})}{\tau_{X,2}} + \frac{N_2(t_{i-1})}{\tau_{AX,2}} - \frac{N_1(t_{i-1})}{\tau_{X,1}}\right)\Delta
\end{aligned} \tag{3.19}$$

where $\tau = 1/k$ in all cases. Populations in the free carrier picture evolve analogously with $X \rightarrow F$ and $k \rightarrow g$ or γ. If all multicarrier states have equal dipole coupling to the ground state, the two models of photoluminescence are

$$PL_X(t_i) = \frac{1}{\tau_R}\left(\sum_n n N_n(t_i)\right)\Delta \tag{3.20}$$

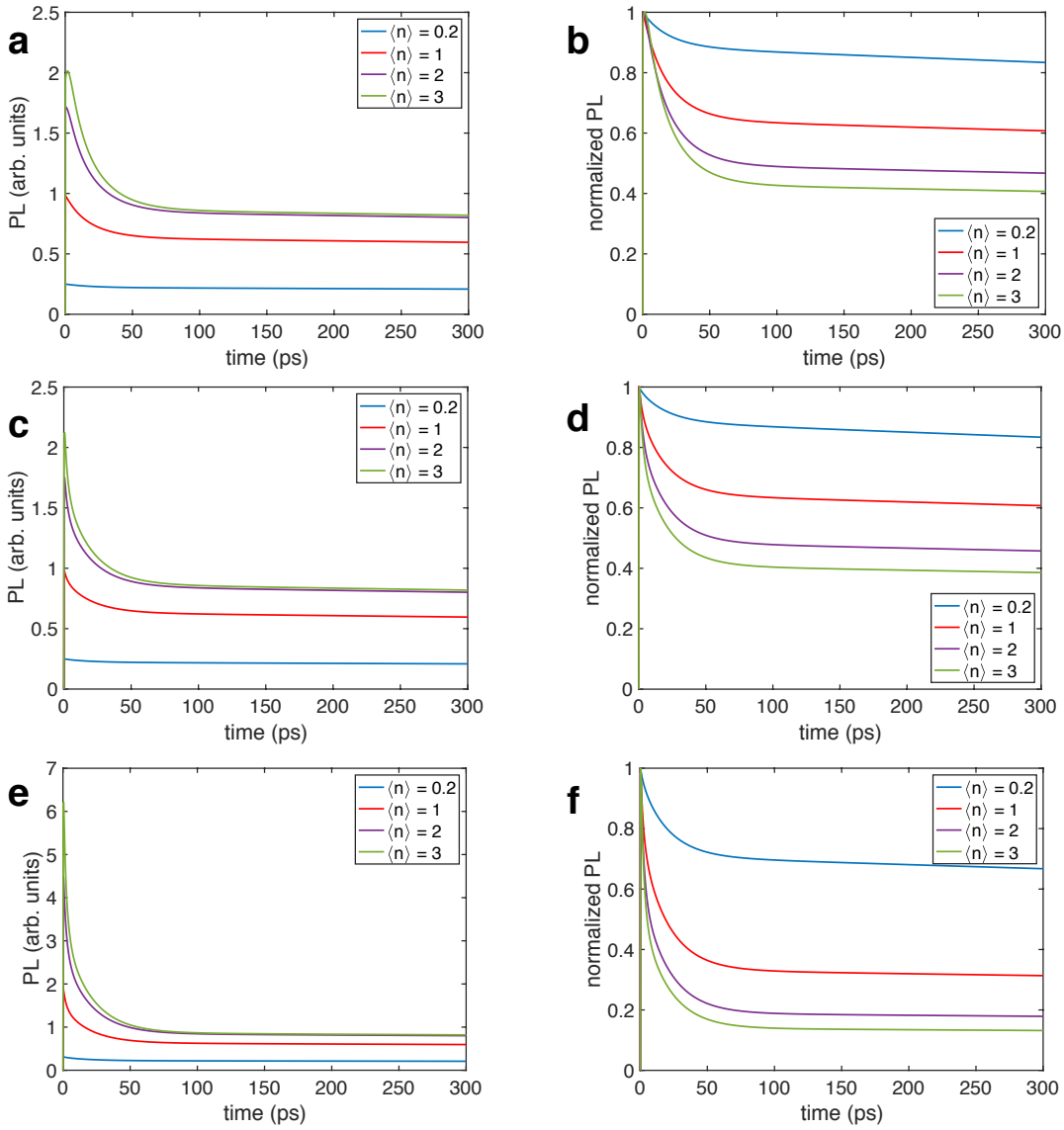

Figure 3.12: Simulated photoluminescence using (a, b) excitonic populations and linear radiative scaling; (c, d) free carrier populations and linear radiative scaling; (e, f) free carrier populations and quadratic radiative scaling.

and

$$PL_F(t_i) = \frac{1}{\tau_R}\left(\sum_n n^2 N_n(t_i)\right)\Delta \tag{3.21}$$

where R denotes the radiative decay. Shown below are simulated photoluminescence decays taking either excitonic or free carrier transient populations and the two options for photon emission. The combination of excitonic population transients and free carrier photoluminescence is not consid-

ered. Simulations used $\Delta = 0.1$ ps, $1/k_X = 1/g = 5$ ns, $1/k_{XX} = 1/\gamma = 20$ ps, and $1/k_R = 100$ ns.

Absolute and normalized simulated photoluminescence decays are shown in Figure 3.12. Differences between excitonic (a, b) and free carrier (c, d) population relaxation with linear radiative scaling are subtle, being most apparent at early times as a faster Auger decay. This effect may not be apparent in experiments where the instrument response is of comparable or slower timescale to the earliest-time relaxation. The late-time signals are similar with a slightly lower level in the free carrier case. The situation of quadratic radiative scaling (e, f) dramatically increases the absolute early-time signal and the overall early-time decay rate, while the absolute signal saturates at a similar long-time value compared to the other cases. This manifests in the normalized decays as a saturation of the long-time signal at a value much less than 0.5.

3.5.4 Absorption cross sections and excitation densities for HgSe

The cross section per Hg atom in an HgSe quantum dot is required for calculations of excitation numbers, as noted in Chapter 2. This can be obtained through method utilizing acid digestion of the particles coupled with inductively-coupled plasma optical emission spectroscopy (ICPOES) and optical absorption, or from an assumed or known reaction yield and the optical absorption.

For the ICPOES determination, particles are precipitated from 0.2 mL of a 4 mL cleaned solution, dried under N_2, digested in 0.5 mL each of HCl and HNO_3 for 3 hours, and diluted to 25 mL in deionized water. 1 mL of aqueous 400 ppm $AuCl_3 \cdot 3H_2O$ and 1 mL of 70% HNO_3 are added to 3 mL of the diluted digest for the ICPOES measurement. The Au complex prevents Hg reduction. The ICPOES spectra are compared to those for a series of Hg standards for quantitative analysis. The data for a variety of samples are shown below along with the optical absorption and 415 and 1053 nm. These data give the per-Hg nanocrystal cross section as $\sigma_{415}^{Hg} = 1.35 \pm 0.2 \times 10^{-17}$ cm^2.

Optical absorption and assumption of 80% reaction yield, reasonable for the highly-reactive TMSSe precursor, gives $\sigma_{415}^{Hg} = 1.5 \pm 0.4 \times 10^{-17}$ cm^2. Both this value and the ICPOES value

ICPOES and Absorption Data			
ICPOES concentration (ppm)	A_{415}	A_{1053}	A_{1053}/A_{415}
9.47	1.44	0.161	0.11
9.68	1.52	0.165	0.11
12.14	1.71	0.181	0.11
11.88	1.67	0.175	0.10
13.13	1.86	0.196	0.11
12.42	1.85	0.194	0.10
7.47	1.06	0.111	0.10
7.91	1.08	0.112	0.10

Table 3.2: ICPOES and optical data for HgSe cross section determination.

Excitation Levels for HgSe		
average fluence ($\mu J/\text{cm}^2$)	$\langle n \rangle$	$P(n \geq 2)$
66	0.2	0.01
180	0.56	0.11
270	0.86	0.21
560	1.8	0.53
1100	3.5	0.87

Table 3.3: Excitation levels for HgSe calculated using the absorption cross section at 1053 nm.

are smaller than the $2.6 \pm 0.4 \times 10^{-17}$ cm^2 for an Hg atom in an HgTe quantum dot [61]. Using the larger HgSe value as a conservative estimate in the context of Auger analysis, we obtain the nanocrystal cross section at the experimental pump wavelength of 1053 nm as $\sigma^{NC}_{1053} = N_{Hg} \times \sigma^{Hg}_{415} \times A_{1053}/A_{415} = 6 \pm 2 \times 10^{-16}$ cm^2 for a spherical particle of 2.5 ± 0.25 nm radius. From this cross section we calculate the average number of excitations $\langle n \rangle$ and the population fraction with $n \geq 2$ from Poisson statistics. This is shown in Table 3.3 below at the fluences used in the interband experiment.

REFERENCES

[1] C. Melnychuk and P. Guyot-Sionnest, "Auger Suppression in n-Type HgSe Colloidal Quantum Dots," *ACS Nano*, vol. 13, no. 9, pp. 10512–10519, 2019.

[2] A. Kamath, C. Melnychuk, and P. Guyot-Sionnest, "Toward Bright Mid-Infrared Emitters: Thick-Shell n-Type HgSe/CdS Nanocrystals," *J. Am. Chem. Soc.*, vol. 143, no. 46, pp. 19567–19575, 2021.

[3] A. E. Siegman, *Lasers*. Sausalito: University Science Books, 1986.

[4] P. Martyniuk, S. Krishna, and A. Rogalski, "Assessment of quantum dot infrared photodetectors for high temperature operation," *J. Appl. Phys.*, vol. 104, no. 3, p. 034314, 2008.

[5] Z. Deng, K. S. Jeong, and P. Guyot-Sionnest, "Colloidal quantum dots intraband photodetectors," *ACS Nano*, vol. 8, no. 11, pp. 11707–11714, 2014.

[6] E. Kioupakis, P. Rinke, K. T. Delaney, and C. G. Van De Walle, "Indirect Auger recombination as a cause of efficiency droop in nitride light-emitting diodes," *Appl. Phys. Lett.*, vol. 98, no. 16, pp. 2009–2012, 2011.

[7] B. K. Ridley, *Quantum Processes in Semiconductors*. Oxford: Oxford University Press, 5 ed., 2013.

[8] P. T. Landsberg, *Recombination in Semiconductors*. Cambridge: Cambridge University Press, 1991.

[9] C. Melnychuk and P. Guyot-Sionnest, "Multicarrier Dynamics in Quantum Dots," *Chem. Rev.*, vol. 121, no. 4, pp. 2325–2372, 2021.

[10] A. R. Beattie, "Auger transitions in semiconductors and their computation," *J. Phys. C Solid State Phys.*, vol. 18, no. 35, pp. 6501–6515, 1985.

[11] A. R. Beattie and P. T. Landsberg, "Auger effect in semiconductors," *Proc. R. Soc. A*, vol. 249, no. 1256, pp. 16–29, 1959.

[12] H. Wen, B. Pinkie, and E. Bellotti, "Direct and phonon-assisted indirect Auger and radiative recombination lifetime in HgCdTe, InAsSb, and InGaAs computed using Green's function formalism," *J. Appl. Phys.*, vol. 118, no. 1, p. 015702, 2015.

[13] K. W. Williams, N. R. Monahan, T. J. Evans, and X. Y. Zhu, "Direct Time-Domain View of Auger Recombination in a Semiconductor," *Phys. Rev. Lett.*, vol. 118, no. 8, p. 087402, 2017.

[14] F. De Rougemont, R. Frey, P. Roussignol, D. Ricard, and C. Flytzanis, "Evidence of strong Auger recombination in semiconductor-doped glasses," *Appl. Phys. Lett.*, vol. 50, no. 23, pp. 1619–1621, 1987.

[15] P. Roussignol, M. Kull, D. Ricard, F. De Rougemont, R. Frey, and C. Flytzanis, "Time-resolved direct observation of Auger recombination in semiconductor-doped glasses," *Appl. Phys. Lett.*, vol. 51, no. 23, pp. 1882–1884, 1987.

[16] D. I. Chepic, A. L. Efros, A. I. Ekimov, M. G. Ivanov, V. A. Kharchenko, I. A. Kudriavtsev, and T. V. Yazeva, "Auger ionization of semiconductor quantum drops in a glass matrix," *J. Lumin.*, vol. 47, no. 3, pp. 113–127, 1990.

[17] I. Robel, R. Gresback, U. Kortshagen, R. D. Schaller, and V. I. Klimov, "Universal Size-Dependent Trend in Auger Recombination in Direct-gap and Indirect-gap Semiconductor Nanocrystals," *Phys. Rev. Lett.*, vol. 102, no. 17, p. 177404, 2009.

[18] C. Melnychuk and P. Guyot-Sionnest, "Slow Auger Relaxation in HgTe Colloidal Quantum Dots," *J. Phys. Chem. Lett.*, vol. 9, no. 9, pp. 2208–2211, 2018.

[19] J. P. Philbin and E. Rabani, "Electron-hole correlations govern Auger recombination in nanostructures," *Nano Lett.*, vol. 18, no. 12, pp. 7889–7895, 2018.

[20] I. Vurgaftman and J. Singh, "Effect of spectral broadening and electron-hole scattering on carrier relaxation in GaAs quantum dots," *Appl. Phys. Lett.*, vol. 64, no. 2, pp. 232–234, 1994.

[21] A. L. Efros, V. A. Kharchenko, and M. Rosen, "Breaking the phonon bottleneck in nanometer quantum dots: Role of Auger-like processes," *Solid State Commun.*, vol. 93, no. 4, pp. 281–284, 1995.

[22] V. I. Klimov, D. W. McBranch, C. A. Leatherdale, and M. G. Bawendi, "Electron and hole relaxation pathways in semiconductor quantum dots," *Phys. Rev. B*, vol. 60, no. 19, pp. 740–749, 1999.

[23] R. Cooney, S. Sewall, E. Dias, D. Sagar, K. Anderson, and P. Kambhampati, "Unified Picture of Electron and Hole Relaxation Pathways in Semiconductor Quantum Dots," *Phys. Rev. B*, vol. 75, no. 24, p. 245311, 2007.

[24] P. Guyot-Sionnest, B. Wehrenberg, and D. Yu, "Intraband relaxation in CdSe nanocrystals and the strong influence of the surface ligands," *J. Chem. Phys.*, vol. 123, no. 7, p. 074709, 2005.

[25] A. Pandey and P. Guyot-Sionnest, "Slow Electron Cooling in Colloidal Quantum Dots," *Science (80-.).*, vol. 322, no. 5903, pp. 929–932, 2008.

[26] L. Wang, Z. Chen, G. Liang, Y. Li, R. Lai, T. Ding, and K. Wu, "Observation of a phonon bottleneck in copper-doped colloidal quantum dots," *Nat. Commun.*, vol. 10, p. 4532, 2019.

[27] P. Han and G. Bester, "Carrier relaxation in colloidal nanocrystals: Bridging large electronic energy gaps by low-energy vibrations," *Phys. Rev. B*, vol. 91, no. 8, p. 085305, 2015.

[28] T. Grange, R. Ferreira, and G. Bastard, "Polaron relaxation in self-assembled quantum dots: Breakdown of the semiclassical model," *Phys. Rev. B*, vol. 76, no. 24, p. 241304(R), 2007.

[29] I. A. Dmitriev and R. A. Suris, "Anharmonicity-assisted multiphonon transitions between distant levels in semiconductor quantum dots," *Phys. Rev. B*, vol. 90, no. 15, p. 155431, 2014.

[30] D. Bozyigit, N. Yazdani, M. Yarema, O. Yarema, W. M. M. Lin, S. Volk, K. Vuttivorakulchai, M. Luisier, F. Juranyi, and V. Wood, "Soft surfaces of nanomaterials enable strong phonon interactions," *Nature*, vol. 531, no. 7596, pp. 618–622, 2016.

[31] N. Yazdani, D. Bozyigit, K. Vuttivorakulchai, M. Luisier, I. Infante, and V. Wood, "Tuning Electron-Phonon Interactions in Nanocrystals through Surface Termination," *Nano Lett.*, vol. 18, no. 4, pp. 2233–2242, 2018.

[32] M. Chen and P. Guyot-Sionnest, "Reversible Electrochemistry of Mercury Chalcogenide Colloidal Quantum Dot Films," *ACS Nano*, vol. 11, no. 4, pp. 4165–4173, 2017.

[33] K. S. Jeong, Z. Deng, S. Keuleyan, H. Liu, and P. Guyot-Sionnest, "Air-Stable n-Doped Colloidal HgS Quantum Dots," *J. Phys. Chem. Lett.*, vol. 5, no. 7, pp. 1139–1143, 2014.

[34] G. Shen and P. Guyot-Sionnest, "HgS and HgS/CdS Colloidal Quantum Dots with Infrared Intraband Transitions and Emergence of a Surface Plasmon," *J. Phys. Chem. C*, vol. 120, no. 21, pp. 11744–11753, 2016.

[35] G. Shen, M. Chen, and P. Guyot-Sionnest, "Synthesis of Nonaggregating HgTe Colloidal Quantum Dots and the Emergence of Air-Stable n-Doping," *J. Phys. Chem. Lett.*, vol. 8, no. 10, pp. 2224–2228, 2017.

[36] M. Park, D. Choi, Y. Choi, H. B. Shin, and K. S. Jeong, "Mid-Infrared Intraband Transition of Metal Excess Colloidal Ag2Se Nanocrystals," *ACS Photonics*, vol. 5, no. 5, pp. 1907–1911, 2018.

[37] E. Lhuillier, M. Scarafagio, P. Hease, B. Nadal, H. Aubin, X. Z. Xu, N. Lequeux, G. Patriarche, S. Ithurria, and B. Dubertret, "Infrared Photodetection Based on Colloidal Quantum-

Dot Films with High Mobility and Optical Absorption up to THz," *Nano Lett.*, vol. 16, no. 2, pp. 1282–1286, 2016.

[38] C. Livache, B. Martinez, N. Goubet, C. Gréboval, J. Qu, A. Chu, S. Royer, S. Ithurria, M. G. Silly, B. Dubertret, and E. Lhuillier, "A colloidal quantum dot infrared photodetector and its use for intraband detection," *Nat. Commun.*, vol. 10, no. 1, p. 2125, 2019.

[39] Z. Deng and P. Guyot-Sionnest, "Intraband Luminescence from HgSe/CdS Core/Shell Quantum Dots," *ACS Nano*, vol. 10, no. 2, pp. 2121–2127, 2016.

[40] G. Shen and P. Guyot-Sionnest, "HgTe/CdTe and HgSe/CdX (X = S, Se, and Te) Core/Shell Mid-Infrared Quantum Dots," *Chem. Mater.*, vol. 31, no. 1, pp. 286–293, 2019.

[41] L. K. Sagar, W. Walravens, J. Maes, P. Geiregat, and Z. Hens, "HgSe/CdE (E = S, Se) Core/Shell Nanocrystals by Colloidal Atomic Layer Deposition," *J. Phys. Chem. C*, vol. 121, no. 25, pp. 13816–13822, 2017.

[42] V. Grigel, L. K. Sagar, K. De Nolf, Q. Zhao, A. Vantomme, J. De Roo, I. Infante, and Z. Hens, "The Surface Chemistry of Colloidal HgSe Nanocrystals, toward Stoichiometric Quantum Dots by Design," *Chem. Mater.*, vol. 30, no. 21, pp. 7637–7647, 2018.

[43] M. Shim and P. Guyot-Sionnest, "Organic-capped ZnO nanocrystals: Synthesis and n-type character," *J. Am. Chem. Soc.*, vol. 123, no. 47, pp. 11651–11654, 2001.

[44] A. M. Schimpf, N. Thakkar, C. E. Gunthardt, D. J. Masiello, and D. R. Gamelin, "Charge-Tunable Quantum Plasmons in Colloidal Semiconductor Nanocrystals," *ACS Nano*, vol. 8, no. 1, pp. 1065–1072, 2014.

[45] J. A. Faucheaux and P. K. Jain, "Plasmons in photocharged ZnO nanocrystals revealing the nature of charge dynamics," *J. Phys. Chem. Lett.*, vol. 4, no. 18, pp. 3024–3030, 2013.

[46] W. Szuszkiewicz, A. M. Witowski, and M. Grynberg, "The Dynamic Dielectric Function in HgSe and HgTe," *Phys. Status Solidi B*, vol. 87, pp. 637–645, 1978.

[47] S. Einfeldt, F. Goschenhofer, C. Becker, and G. Landwehr, "Optical properties of HgSe," *Phys. Rev. B*, vol. 51, no. 8, pp. 4915–4925, 1995.

[48] M. H. Hudson, M. Chen, V. Kamysbayev, E. M. Janke, X. Lan, G. Allan, C. Delerue, B. Lee, P. Guyot-Sionnest, and D. V. Talapin, "Conduction Band Fine Structure in Colloidal HgTe Quantum Dots," *ACS Nano*, vol. 12, no. 9, pp. 9397–9401, 2018.

[49] Y. Kobayashi, T. Nishimura, H. Yamaguchi, and N. Tamai, "Effect of Surface Defects on Auger Recombination in Colloidal CdS Quantum Dots," *J. Phys. Chem. Lett.*, vol. 2, no. 9, pp. 1051–1055, 2011.

[50] Y. Kobayashi, L. Pan, and N. Tamai, "Effects of size and capping reagents on biexciton auger recombination dynamics of CdTe quantum dots," *J. Phys. Chem. C*, vol. 113, no. 27, pp. 11783–11789, 2009.

[51] V. I. Klimov, J. A. McGuire, R. D. Schaller, and V. I. Rupasov, "Scaling of multiexciton lifetimes in semiconductor nanocrystals," *Phys. Rev. B*, vol. 77, no. 19, p. 195324, 2008.

[52] S. Keuleyan, J. Kohler, and P. Guyot-Sionnest, "Photoluminescence of mid-infrared HgTe colloidal quantum dots," *J. Phys. Chem. C*, vol. 118, no. 5, pp. 2749–2753, 2014.

[53] H. Liu and P. Guyot-Sionnest, "Photoluminescence lifetime of lead selenide colloidal quantum dots," *J. Phys. Chem. C*, vol. 114, no. 35, pp. 14860–14863, 2010.

[54] P. Guyot-Sionnest and M. A. Hines, "Intraband transitions in semiconductor nanocrystals," *Appl. Phys. Lett.*, vol. 72, no. 6, pp. 686–688, 1998.

[55] N. J. Orfield, J. R. McBride, J. D. Keene, L. M. Davis, and S. J. Rosenthal, "Correlation of

atomic structure and photoluminescence of the same quantum dot: Pinpointing surface and internal defects that inhibit photoluminescence," *ACS Nano*, vol. 9, no. 1, pp. 831–839, 2015.

[56] A. J. Muhowski, A. M. Muellerleile, J. T. Olesberg, and J. P. Prineas, "Internal quantum efficiency in 6.1 Å superlattices of 77infrared emitters," *Appl. Phys. Lett.*, vol. 117, no. 6, p. 061101, 2020.

[57] C. Delerue, "Private Communication," 2019.

[58] V. I. Klimov and D. W. McBranch, "Femtosecond 1P-to-1S electron relaxation in strongly confined semiconductor nanocrystals," *Phys. Rev. Lett.*, vol. 80, no. 18, pp. 4028–4031, 1998.

[59] E. A. Zibik, L. R. Wilson, R. P. Green, G. Bastard, R. Ferreira, P. J. Phillips, D. A. Carder, J. P. R. Wells, J. W. Cockburn, M. S. Skolnick, M. J. Steer, and M. Hopkinson, "Intraband relaxation via polaron decay in InAs self-assembled quantum dots," *Phys. Rev. B*, vol. 70, no. 16, p. 161305(R), 2004.

[60] M. Wimmer, S. V. Nair, and J. Shumway, "Biexciton recombination rates in self-assembled quantum dots," *Phys. Rev. B*, vol. 73, no. 16, p. 165305, 2006.

[61] E. Lhuillier, S. Keuleyan, and P. Guyot-Sionnest, "Optical properties of HgTe colloidal quantum dots," *Nanotechnology*, vol. 23, no. 17, p. 175705, 2012.

CHAPTER 4

DETAILED-BALANCE LIMITS FOR MERCURY TELLURIDE QUANTUM DOT INFRARED PHOTODETECTORS

The following material is adapted from [1].

4.1 Introduction

Photodetection in the mid- and long-wave infrared (MWIR and LWIR) relies primarily on epitaxially-grown semiconductor crystals with small band gaps, such as InSb and Hg-rich HgCdTe alloys. The performances of optimized devices are usually limited by the Auger nonradiative recombination of thermally-generated carriers, and as a result, MWIR and LWIR photodetectors function best under cryogenic conditions [2, 3, 4]. The Auger rate provides the fundamental performance limitation because it is a basic material property of bulk semiconductors, and efforts to further raise performances therefore require nonequilibrium schemes which reduce the effective carrier density in the active region [4, 5, 6]. Auger suppression is also one of the motivations behind the development of type-II superlattice detectors [7, 8]. Cooling requirements, alongside difficulties associated with growing epitaxial materials and interfacing them with silicon electronics, make high-performance MWIR and LWIR photodetection extremely costly. This generally limits present uses to defense and research applications. Yet, there are many commercial situations such as autonomous driving, agricultural analysis, and product sorting which would greatly benefit from affordable, high-performance photodetection in the MWIR and LWIR.

Solids of nanocrystal quantum dots are increasingly being investigated as promising alternatives to conventional epitaxial materials [9, 10, 11, 12, 13, 14, 15, 9, 16, 17] with the performances of MWIR and short-wave infrared (SWIR) HgTe quantum dot detectors most closely approaching those of existing technologies [12, 17]. In addition to the very low material costs and simple interfacing with silicon electronics, the solution-processability of nanocrystal quantum dots readily

enables modalities such as dual-band [15] and hyperspectral [14] detectors, polarization-sensitive detectors [9] and curved detectors [16, 13] which are difficult or impossible to realize with crystalline systems.

Beyond exploring such practical advantages of nanocrystal quantum dots for infrared detection, it is important to examine the basic performance limits of the material system and the possible benefits of future optimizations. The initial works along these lines focused on epitaxial quantum dots and employed bulk semiconductor models to evaluate detectivity limits [18, 19]. Such analyses do not capture the important modifications to radiative and Auger recombination which are induced by strong quantum confinement, and they also may not be appropriate for conducting granular systems such as nanocrystal solids. In this chapter, we develop a simple statistical recombination model which connects microscopic intraparticle recombination rates, which are easily calculated or measured, to the macroscopic thermal recombination rates which are relevant to infrared photodetection. The model is then applied to HgTe nanocrystal quantum dots, and the fundamental detectivity limits are determined by applying the principle of detailed balance. We conclude the chapter with a discussion of the results' implications for quantum dot infrared detector performance.

4.2 Thermal recombination model

We begin with a parameterization, based on prior experimental data, of the HgTe quantum dot energy gap as a function of temperature and nanocrystal size. The gap is taken to be the lowest-energy excitonic transition between quantized valence and conduction states, and it is obtained at 300 K from the polynomial fit reported by Hudson *et al.* for absorption spectra of quasi-spherical particles [20]. The temperature-dependence is added via a linear correction based on an average across three sets of photoluminescence data reported by Keuleyan *et al.* [21]. This gives the overall parameterized gap as

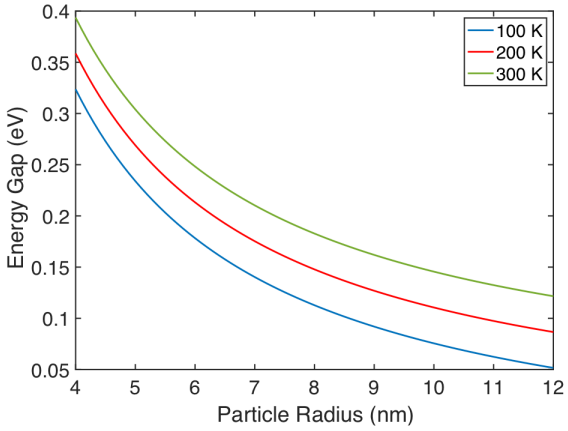

Figure 4.1: Energy gaps calculated from Equation 4.1

$$E_g(R,T) = \frac{1}{-0.0056R^2 + 0.80R - 0.57} - \left(3.5 \times 10^{-4}\right) \times (300 - T) \tag{4.1}$$

with E_g in eV, R in nm, and T in Kelvins. Here, we consider particles with 4 to 12 nm radii for MWIR and LWIR photodetection across the temperature range 100 - 300 K. Radius- and temperature-dependent energy gaps are shown below in Figure 4.1. Equation 4.1 produces energies similar to those obtained using a Kane conduction band, parabolic heavy hole band, and temperature-dependent bulk gap with $k = \pi/R$.

The energy gaps given by equation 4.1 are then used to determine thermal carrier populations assuming that the particles are intrinsic. Measurements on MWIR *p-i-n* HgTe quantum dot photodiodes indeed show low residual doping [11], and this should also be the optimum situation in a photoconductor [22]. Although very precise doping control remains a general challenge with nanocrystal quantum dots [23], it is reasonably tunable in HgTe via the nanocrystal surface chemistry [15, 24, 25, 26]. As shown in the appendix to this chapter, the average number of thermal electrons or holes per quantum dot, N_i, is given in the intrinsic limit by

$$N_i = \sqrt{Z_c Z_v e^{-\beta E_g}} \tag{4.2}$$

where Z_c and Z_v respectively denote the conduction and valence partition functions, and $\beta = 1/k_B T$ with k_B denoting Boltzmann's constant. Equation 4.2 is valid when N_i is small and excitonic effects are weak; these conditions will usually be satisfied in HgTe quantum dot solids [11, 24, 26, 27]. Effects related to particle size inhomogeneity are not considered in the present treatment.

At the particle sizes considered here, the two lowest conduction levels are separated by 100 meV or more due to the light electron effective mass. We therefore expect only one conduction level to contribute in equation 4.2 so that, including spin degeneracy, $Z_c = 2$ at all temperatures. The valence levels are more closely spaced, by 30 meV or less due to the heavy hole effective mass, and Z_v varies more strongly with particle size and temperature. It is

$$Z_v = \sum_{n,l} g_l e^{-\beta E_{n,l}} \tag{4.3}$$

where n is the principal quantum number, l is the orbital angular momentum quantum number, g_l is the valence state degeneracy, and $E_{n,l}$ is the valence state energy. Since the valence level structure is not directly resolved in experiments, in contrast to the excitonic energy gap E_g, we evaluate Z_v in the parabolic approximation assuming hole confinement to a spherical potential well of radius R and infinite depth. This gives $g_l = 2(2l + 1)$ including spin, and $E_{n,l} = \hbar^2 \xi_{n,l}^2 / 2 m_v R^2$ where $\xi_{n,l}$ is the n^{th} root of the l^{th} order spherical Bessel function, m_v is the heavy hole effective mass, and $\xi_{n,l}/R = k_{n,l}$ is the quantized wavevector. Values of m_v between 0.3 and 0.8 free electron mass units have been reported in the literature [28, 29] and we employ an intermediate value of 0.5. $E_{1,0}$ is the zero of energy and we neglect light hole and spin-orbit split-off states because they lie much deeper in the valence band at all $k_{n,l}$ considered here [27, 29, 30]. Plots of Z_v are shown in the appendix to this chapter. Alternative choices of m_v within the range specified above can change $\sqrt{Z_v}$ by at most 40%, occurring in the largest particles at 300 K. The macroscopic thermal carrier density n_i can then be approximated as $n_i = 0.63 N_i / V$ where V is the spherical particle volume and 0.63 is the random close packing fraction for spheres. Densities and carrier numbers for two sizes of particle are shown in Figure 4.2, and the densities are comparable to those

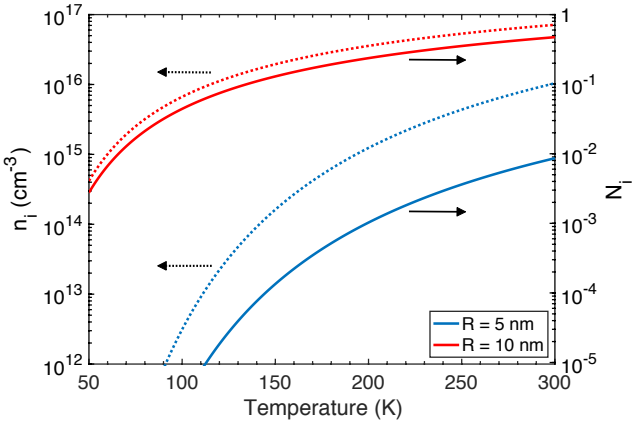

Figure 4.2: Average thermal carrier numbers per particle (solid lines, right axis) and thermal carrier densities (dotted lines, left axis) calculated for 5 nm and 10 nm radius particles.

in intrinsic HgCdTe at similar gap energies [31]. Although the strong confinement approximation employed for the calculation of Z_v is not rigorously valid for holes, it nevertheless presents a good estimate as discussed in the appendix to this chapter. We further note that although N_i remains of order 0.01 or less in the MWIR, it can reach much higher levels in the largest LWIR particles at higher temperatures. Below 0.14 eV gap and above 200 K, for example, N_i is of order unity. Fermi–Dirac statistics are more appropriate in this regime and the corresponding carrier numbers would be smaller than modeled here.

The carrier number data are then used to calculate thermal recombination rates in the conducting nanocrystal solid. Charge transfer in the system of close-packed particles occurs via activated hopping whereby individual carriers thermalize to their band edges before tunneling to a neighboring nanocrystal [32], When hopping outpaces the intraparticle (excitonic) recombination, as will occur in high-mobility HgTe quantum dot solids at moderate temperatures [21, 24, 26, 33], carriers will sample many particles before recombining. The effective thermal recombination rate τ_{th}^{-1} can then be calculated from the product of the intraparticle recombination rate τ^{-1} and the probability N_i that a particle contains a thermal carrier, giving

$$\frac{1}{\tau_{th}} = S\frac{N_i^{\gamma}}{\tau} \tag{4.4}$$

where γ is an integer exponent that depends on the kinetic order of the recombination process. This equation is derived under the assumption of Poisson statistics at small N_i, and violation of this condition would motivate considerations of blockade-type correlated transport effects. When the hopping time is long or the intraparticle lifetime is short, the thermal recombination rate will instead be governed by the hopping time as shown in the appendix to this chapter.

For radiative recombination we may take $S = \gamma = 1$, and equation 4.4 then gives the thermal radiative rate as the simple product of N_i and the intraparticle excitonic radiative rate τ_R^{-1}. Using the standard description of dipole spontaneous emission [34] with a local-field modification in the empty-cavity approximation [35, 36], this gives in cgs units

$$\frac{1}{\tau_{R,th}} = N_i \frac{2\omega_g^2 e^2 f \sqrt{\epsilon_2}}{m_0 c^3} \left(\frac{3\epsilon_2}{2\epsilon_2 + \epsilon_1} \right)^2 \tag{4.5}$$

where e is now the unit charge, c is the vacuum speed of light, m_0 is the free electron mass, f is the effective interband oscillator strength, $\omega_g = E_g/\hbar$ is the radiation angular frequency, and ϵ_1 and ϵ_2 are, respectively, the real optical dielectric constants of the nanocrystal and its environment. We approximate the effective interband oscillator strength as $f = f_0/Z_c Z_v$, where f_0 is the oscillator strength of the band-edge transition between quantized heavy hole and conduction states. f_0 is calculated from $k \cdot p$ Bloch functions [37] using a Kane parameter of 14 eV, intermediate within the reported range [29, 38, 39, 40, 41]. The $Z_c Z_v$ factor arises because the band-edge transition carries most of the total oscillator strength, and the effective interband oscillator strength is reduced upon thermal population of other states. ϵ_1 is taken as 10, the optical dielectric constant of bulk HgTe [42, 43], which should be close to the true nanoparticle value [44, 45]. ϵ_2 is taken as 6 based on the measured refractive indices of HgTe nanocrystal films [11, 37, 46]. Examples of thermal radiative lifetimes calculated from equation 4.5 are shown by solid lines in Figure 4.3, and they are considerably shorter than in doped and intrinsic HgCdTe of similar gap energies [47]. We note that τ_R^{-1} and $\tau_{R,th}^{-1}$ exhibit opposing dependencies on E_g due to the presence or absence of the N_i factor. Although radiative lifetimes could in principle be longer than calculated here due to valence fine

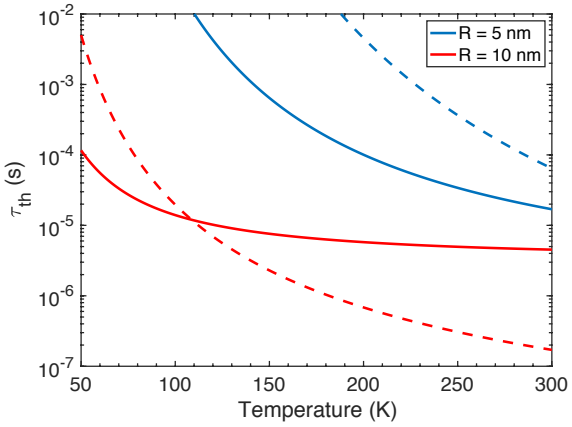

Figure 4.3: Thermal radiative (solid lines) and Auger (dashed lines) recombination lifetimes calculated for 5 nm and 10 nm radius particles.

structure [48], exchange interactions should be weak in the HgTe particles presently considered and we therefore neglect such effects.

The competition between nonradiative and radiative recombination will determine the maximum achievable detector performance. Following the situation in bulk crystalline semiconductors, we first suppose that Auger recombination is the only nonradiative process which can occur in a defect-free material. Within the model of equation 4.4, the Auger recombination rate of mobile thermal carriers $\tau_{A,th}$ can be calculated from standard bulk recombination statistics [49, 50] as

$$\frac{1}{\tau_{A,th}} = C_A n_i^2 \tag{4.6}$$

Here C_A is the Auger coefficient, a third-order rate constant which in quantum dots takes the approximate form $C_A = V^2/8\tau_A$ where τ_A denotes the intraparticle biexciton Auger lifetime [51]. The assumptions underlying this C_A are nuanced, as described in [49] and the appendix to Chapter 2, but this quantity should reasonably describe the recombination of mobile charges in the intrinsic thermal limit. τ_A depends weakly on the gap energy in quantum dots and instead usually scales approximately as R^3 in the regime of strong quantum confinement [49]. Its scaling with particle radius has been measured by transient absorption spectroscopy to be approximately 2 ps/nm^3 in

small HgTe nanocrystals and we employ this scaling here [33]. Although the cubic scaling results in slower intraparticle Auger recombination at larger particle sizes, larger particles (smaller gaps) increase the thermal carrier numbers such that $\tau_{A,th}$ decreases with decreasing gap, just as in bulk semiconductors. The dashed lines in Figure 4.3 show examples of calculated thermal Auger lifetimes. They are one to two orders of magnitude longer than in intrinsic HgCdTe [50, 52] and in InSb/InAsSb superlattices [7, 8] of similar gaps. They are also substantially longer than in *n*-type HgCdTe with $\sim 10^{15}$ donors/cm^3, the material which constitutes most of the device thickness in good commercial photodiodes [2, 52, 53, 54]. Figure 4.3 shows that thermal Auger lifetimes are generally much longer than radiative lifetimes for MWIR HgTe, and that they are only about ten times shorter than radiative lifetimes in the LWIR. This situation can lead to large upper limits on device performances as discussed below.

4.3 Detectivity model

An ideal photodetector maximizes the signal while minimizing the noise. This is quantified by the detectivity D^*, given here as $D^* = \Re\sqrt{A\Delta\nu}/i_n$ where i_n is the root-mean-square noise current (amp), $\Delta\nu$ is the electrical bandwidth (Hz) over which i_n is measured, $\Re$ is the responsivity (amp/W), and A is the sensing area of the device (cm^2). Its unit, cm $\sqrt{\text{Hz}}$/W, is known as Jones and describes the bandwidth- and area-normalized signal-to-noise ratio. Noise currents may come from many sources, but in good photodiodes at small bias they are dominated by the shot noise associated with thermal generation and recombination [19, 55, 56]. A material at equilibrium with its own thermal photon flux has a thermal excitation rate which equals the recombination rate. Maintaining this equilibrium in the presence of nonradiative recombination necessitates faster generation than in the radiative limit, and the lowest achievable noise level is therefore determined by the relative rates of radiative and nonradiative recombination. To emphasize this relationship, D^*

can be recast through a detailed balance analysis as

$$D^* = \frac{1}{\hbar\omega_g}\sqrt{\frac{\eta f_r}{4\phi_D}} \tag{4.7}$$

where η is the external quantum efficiency, f_r is the fractional of the total recombination which is radiative, and ϕ_D is the blackbody photon flux at the detector temperature integrated over frequencies greater than ω_g. Equation 4.7 is derived in the appendix to this chapter. It assumes the conventional 1 Hz electrical bandwidth for $\Delta\nu$ and for calculations we employ the approximation $\phi_D = \left(\omega_g/2\pi c\sqrt{\beta\hbar}\right)^2 \exp\left(-\beta\hbar\omega_g\right)$ which is valid when $\beta\hbar\omega_g \gg 1$. Equation 4.7 is thermodynamically-equivalent to the Shockley–Queisser limit for solar cell efficiency [57], and f_r and η respectively relate to i_n and $\Re$ in the typical detectivity formula. So-called photon recycling effects [58] are subsumed in the external quantum efficiency and their absence would manifest as $\eta < 1$. Although we do not account for the $1/f$ noise which may be prominent in biased granular conductors [59], HgTe photodiodes usually exhibit a white noise spectrum [11, 12, 15] and equation 4.7 should therefore be a good description of their underlying performance limits.

The radiative recombination fraction is

$$f_r = \frac{\tau_{R,th}^{-1}}{\tau_{R,th}^{-1} + \tau_{A,th}^{-1} + \tau_{N,th}^{-1}} \tag{4.8}$$

where $\tau_{N,th}^{-1}$ represents the sum of all non-Auger nonradiative rates. In HgTe nanocrystals, transient absorption [33] and photoluminescence [21, 60] measurements on particles with gaps across the 0.15 - 0.85 eV range suggest that intraparticle nonradiative lifetimes τ_N range from several nanoseconds in the MWIR to a few hundred picoseconds in the LWIR. The experimental ratio τ_N/τ_R decreases with the gap energy [21] and is only weakly dependent on temperature [60]. This behavior in infrared nanocrystals is typically attributed to near-field energy transfer between the exciton and infrared-absorbing species such as organic surface ligands [21, 61, 62]. The thermal rate of such a near-field mechanism would be $\tau_{N,th}^{-1} = N_i/Z_c Z_v \tau_N^0$ where τ_N^0 is a low tempera-

ture reference value. $\tau_{N,th}^{-1}$ will significantly exceed $\tau_{R,th}^{-1}$ and $\tau_{A,th}^{-1}$ at all temperatures and particle sizes considered here, and it is consequently the present fundamental detectivity limitation. This is somewhat analogous to a Shockley-Read-Hall rate in bulk semiconductors.

4.4 Detectivity results and device implications

Figure 4.4 displays the maximum achievable equilibrium detectivities as determined by radiative and Auger recombination (blue lines) and an additional 100 ps base nonradiative recombination (red lines) with $\eta = 1$. Also shown are the detectivities given by the semiempirical "Rule 07" (blue dotted lines) describing the Auger limit of *p*-on-*n* HgCdTe photodiodes under small biases [2]. They are calculated from the Johnson noise as $D^* = \eta e \sqrt{\beta R_0 A}/2\hbar\omega_g$ with $\eta = 1$ and the resistance-area products R_0A given in [2]. We see that even with the rapid nonradiative recombination typical of present materials, the underlying performance limits of HgTe quantum dot detectors are comparable to those of Auger-limited HgCdTe. These detectivities also substantially exceed those of standard commercial HgCdTe photodiodes, as shown in the supplementary information of [1]. The Auger-limited HgTe quantum dot detectivities exceed those of Auger-limited commercial HgCdTe photodiodes [2, 3, 4], representing a fundamental advantage of HgTe quantum dots for MWIR and LWIR photodetection. More extended versions of the data shown in Figure 4.4 may be found in the supplementary information of [1]. It is notable that other material systems such as *n*-type HgSe quantum dots display much slower intraparticle Auger recombination than HgTe at comparable gaps [63], and the further engineering of slow Auger recombination is possible in many nanocrystal quantum dot systems [49]. Due to the sparse conduction level structure, intraparticle radiative rates in *n*-type quantum dots should also be relatively independent of temperature, and this could further benefit high temperature operation. These and other directions might eventually allow greater performances with quantum dots than predicted here.

The best quantum dot MWIR detectors are presently *p*-*i*-*n* HgTe photodiodes, and as shown by the purple data in Figure 4.4a, these devices exhibit detectivities which are below the fundamental

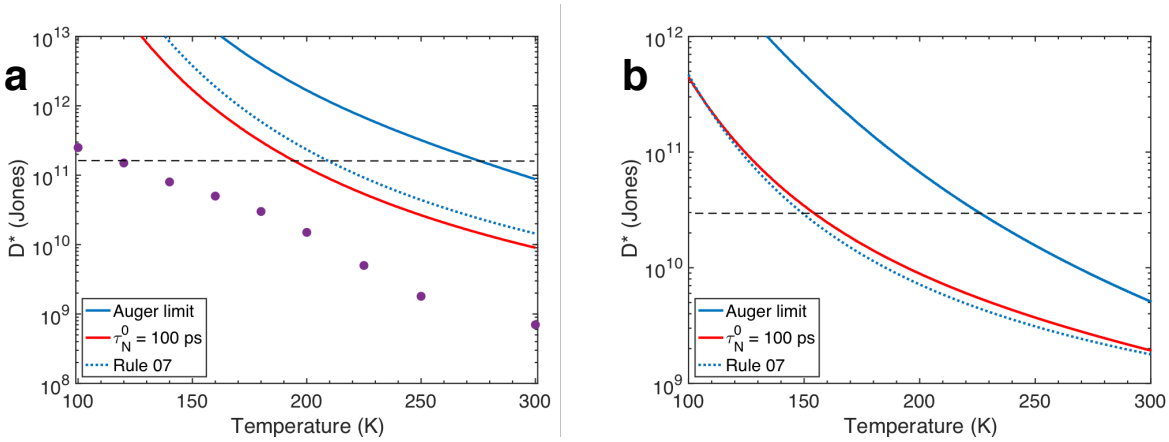

Figure 4.4: (a) Detectivities calculated at 0.25 eV ($\lambda = 5\mu$m gap; (b) detectivities calculated at 0.12 eV ($\lambda = 10\mu$m) gap with $\eta = 1$. Black dashed lines denote 300 K background-limited (BLIP) detectivities which are given by $D^*_{BLIP} = 1/\hbar\omega\sqrt{2\phi}$ when $\eta = 1$. The curves in (a) are calculated using radii of 5 - 6 nm and the curves in (b) are calculated using radii of 8 - 12 nm. Purple data are for a fixed particle size displaying 0.26 eV gap at 100 K [12].

material limits. This illustrates several routes for progress. First, η does not yet reach unity in MWIR HgTe photodiodes, but instead lies in the approximate range 0.01 - 0.5, decreasing with increasing temperature [11, 12, 15]. This comes from several sources. As shown in the supplementary material to [1], nanocrystal films with thicknesses of several microns would be required for near-unity light absorption with the particle sizes considered here; present devices utilize thinner films, and this immediately limits the maximum value of η. This situation can be addressed with embedded photonic structures which enhance the light absorption [64, 12] so that η is not absorption-limited. More consequential detectivity improvements will come from reducing noise currents and raising carrier diffusion lengths. At low temperatures, i_n is presently dominated by the Johnson noise associated with small shunt resistances instead of the generation–recombination noise calculated here [11, 12, 15]. Shunt resistances can in principle be increased through improved film deposition techniques that minimize cracks and voids, and by chemistries which minimize conduction through gap and surface states. At higher temperatures, η at present is likely limited by short diffusion lengths and large series resistances [11, 12, 15]. In the limit of fast charge hopping and weak external illumination, the diffusion length L_D is $\sqrt{\mu\tau_{th}/e\beta}$ where μ is the carrier

mobility. L_D must exceed the device thickness to ensure complete extraction of photogenerated charges, and this condition is not currently satisfied at higher temperatures due to nonradiative recombination and modest carrier mobilities. HgTe photodiodes have so far utilized nanocrystal solids with mobilities around 10^{-2} cm^2/Vs, but mobilities up to 10 cm^2/Vs have recently been achieved through improved interparticle coupling [26]. This has indeed raised the detectivities of HgTe photoconductors [22] and should also improve photodiodes. Reduced nonradiative recombination will also increase diffusion lengths. Combined with the photonic enhancements noted before, these improvements could enable $\eta \sim 1$ and lifetime-limited D^* over a broad temperature range [65].

Figure 4.4 shows that another effect of nonradiative recombination is to dramatically lower the temperatures at which detectivities are limited by 300 K thermal background radiation, known as the BLIP condition (dashed black lines). This performance degradation will be present even in a device with optimized engineering ($\eta = 1$). As noted earlier, nonradiative recombination in infrared nanocrystal quantum dots is usually attributed to near-field energy transfer processes. It has also been proposed that broadband vibrations associated with the mechanically-soft nanocrystal surface might be involved [66]. The relative importance of each process remains a topic of investigation, but both mechanisms should be addressable using established colloidal chemistries. The rate of nonradiative energy transfer scales as $\tau_N^{-1} \propto \epsilon''/R^4$ where ϵ'' is the imaginary dielectric constant of the local environment at the gap energy and R is now the physical radius of the nanocrystal. ϵ'' may be reduced by utilizing inorganic ligands and embedding the nanocrystals in matrices of low infrared absorbance. The physical radius may be engineered to substantially exceed the electronic radius by growing upon the nanocrystal a think shell displaying type-I band alignment, and this strategy has successfully reduced nonradiative recombination in other infrared nanocrystal systems [61, 67]. If the soft nanocrystal surface is involved in the recombination, thin lattice-matched shells with type-I band alignment should be sufficient to substantially reduce the nonradiative recombination. When the above processes are addressed, the ultimate viability of

Auger-limited HgTe quantum dot detector performance will be determined by the intrinsic rate of phonon-mediated carrier relaxation across the gap. Experiments suggest that intraparticle phonon-mediated lifetimes exceed several nanoseconds [67], as discussed in Chapter 3, but the true upper limits remain unknown.

4.5 Conclusions

In summary, we developed a simple statistical model of mobile thermal carrier recombination in HgTe nanocrystal films, and applied it to calculations of MWIR and LWIR detectivities in the limit that device noise arises from generation-recombination fluctuations. We find that if HgTe nanocrystal photodetectors can achieve Auger-limited performance, they will substantially outperform most MWIR and LWIR technologies. We further show that although HgTe quantum dots presently display additional non-Auger nonradiative recombination, this does not fundamentally limit the ability of HgTe quantum dots to achieve performances close to those of commercial Auger-limited HgCdTe photodiodes. Future work could extend the present model to address complexities introduced by particle size inhomogeneity and large thermal carrier densities on the carrier lifetimes and transport [65]. The potential for superior detector performance with HgTe quantum dots should motivate improvements to device architectures and fabrication processes, and continued investigations of the nonradiative lifetimes and mechanisms.

4.6 Appendix

4.6.1 Thermal carrier numbers

At thermal equilibrium, the average number of electrons per quantum dot N_j with absolute energy E_j is given by the Fermi-Dirac distribution as

$$N_j = \frac{g_j}{e^{\beta\left(E_j - E_f\right)} + 1} \approx g_j e^{-\beta E_j} e^{\beta E_f} \tag{4.9}$$

where $\beta = 1/k_B T$, E_f is the Fermi level and g_j is the degeneracy of level j. In the second step we have taken $E_j - E_f \gg 1$, corresponding to low doping and the Boltzmann approximation. The average total number of thermal electrons per quantum dot N_e in the Boltzmann limit is then

$$N_e = \sum_j g_j N_j = e^{\beta E_f} \sum_j g_j e^{-\beta E_j} \tag{4.10}$$

Similarly, the average total number of holes N_h is

$$N_h = e^{-\beta E_f} \sum_{j'} g_{j'} e^{\beta E_{j'}} \tag{4.11}$$

and the intrinsic average carrier number N_i defined through $N_i^2 = N_e N_h$ is then

$$N_i^2 = \sum_{j,j'} g_j g_{j'} e^{-\beta\left(E_j - E_{j'}\right)} \tag{4.12}$$

We now define the absolute energies in terms of the quantum dot energy gap E_g and the quantized state energies ε so that $E_j = E_g + \varepsilon_j$ and $E_{j'} = \varepsilon_{j'}$ with $\varepsilon_j > 0$ and $\varepsilon_{j'} \leq 0$. This corresponds to taking the band-edge quantized valence level as the local zero of energy and gives

$$\begin{aligned} N_i^2 &= e^{-\beta E_g} \sum_{j,j'} g_j g_{j'} e^{-\beta\left(\varepsilon_j + \varepsilon_{j'}\right)} \\ &= Z_c Z_v e^{-\beta E_g} \end{aligned} \tag{4.13}$$

where in the last step we have denoted the valence and conduction partition functions as Z_v and Z_c, respectively. We note the close correspondence between the above equation and the standard textbook expression for the intrinsic carrier density in a semiconductor, discussed below.

Due to the large hole effective mass in HgTe, at large particle sizes the hole states will not be strongly quantized and the model of a free particle confined to a spherical potential of infinite depth is not rigorously valid. Indeed, strong hole confinement requires a particle radius $R \lesssim$

$\epsilon_0\hbar^2/m_v e^2 = 2$ nm for a hole effective mass $m_v = 0.5m_0$ and static dielectric constant $\epsilon_0 = 20$. The HgTe particles relevant for MWIR and LWIR applications are much larger, and thermal carrier numbers calculated assuming strong hole quantization would therefore be an underestimate. An upper limit would be to assume bulk hole behavior. The standard equation for the carrier density in a bulk intrinsic semiconductor is

$$n_i^2 = \gamma_v \gamma_c e^{-\beta E_g} \tag{4.14}$$

where

$$\gamma_{c(v)} = \frac{1}{4}\left(\frac{2m_{c(v)}}{\pi\beta\hbar^2}\right)^{3/2} \tag{4.15}$$

is the number of states per unit volume near the band extrema [68]. To obtain a "bulk" model for N_i we may take $Z = \gamma V$ where V is the nanocrystal volume and Z is an effective bulk value of the partition function. A reasonable model for HgTe quantum dots would be to treat the hole levels in this manner while keeping $Z_c = 2$ as in the main text, and this provides an upper limit on the thermal carrier number. Results for the limiting cases of bulk and strongly confined hole levels are shown below. Both models produce similar results, except at low temperature where the bulk value of Z_v unphysically trends to zero in small particles. These small differences in Z_v produce negligible effects on N_i due to the square-root dependence. The chosen value of m_v will have a stronger effect on Z_v and N_i in both models.

4.6.2 Thermal carrier lifetimes

We wish to examine the average lifetime of a small photogenerated carrier population interacting with a larger thermal carrier population. When N is small, the probability that a single quantum dot has N_0 thermal excitations, $\Pr(N_0)$, will follow the Poisson distribution:

$$\Pr(N_0) = \frac{N^{N_0} e^{-N}}{N_0!} \tag{4.16}$$

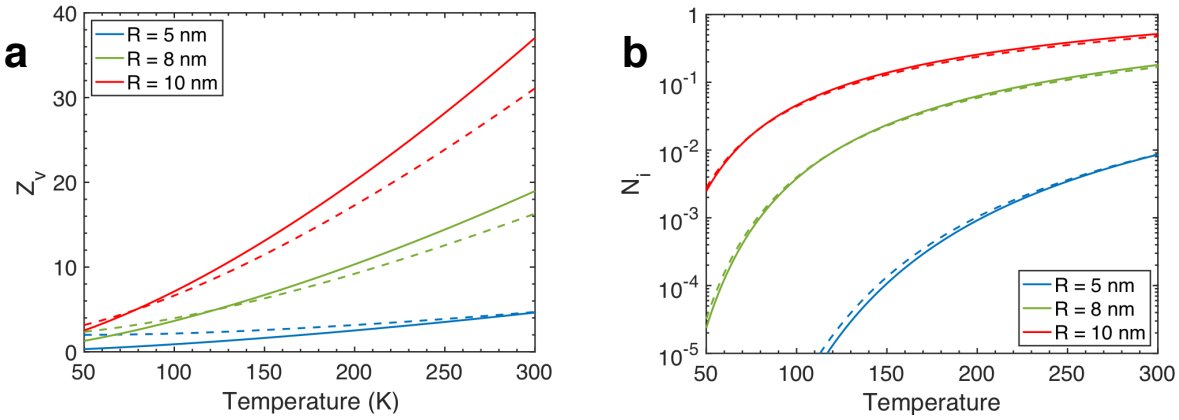

Figure 4.5: (a) Valence partition functions; (b) Thermal carrier numbers. Solid and dashed lines respectively denote calculations employing bulk and confined models for the hole levels. All calculations use $m_v = 0.5m_0$ and $E_g(R,T)$ from the main text.

Taking the conduction mechanism to be carrier hopping, we suppose that at every hopping time interval τ_h the electrons and holes occupy new quantum dots. The probability that a carrier undergoes excitonic recombination, P_1, is the probability that the dot has one carrier of opposite sign multiplied by the probability of recombination during the hopping time interval. This is

$$P_1 = \Pr(1) \times \left(1 - e^{-\tau_h/\tau_1}\right) \approx N\left(1 - e^{-\tau_h/\tau_1}\right) \tag{4.17}$$

where τ_1 is the intraparticle exciton lifetime and in the second step we have used the assumption of small N to take $e^{-N} \approx 1 - N$ and $N - N^2 \approx N$. When $\tau_h \ll \tau_1$, one has $1 - e^{-\tau_h/\tau_1} \approx \tau_h/\tau_1$. This approximation is accurate to within about 20% or better when $\tau_h/\tau_1 \leq 0.5$. Defining the thermal exciton lifetime $\tau_{1,th}$ as the recombination probability in a unit time τ_h, this gives

$$\frac{1}{\tau_{1,th}} \equiv \frac{P_1}{\tau_h} \approx \frac{N}{\tau_1} \tag{4.18}$$

For higher-order recombination processes, we assume that the dominant recombination pathway will be Auger recombination. Considering the probability that multiple thermal carriers reside in

a single particle, we have

$$\Pr(N_0 \geq 2) = 1 - \Pr(0) - \Pr(1) = 1 - e^{-N} - Ne^{-N} \tag{4.19}$$

Again taking $e^{-N} \approx 1 - N$,

$$\Pr(N_0 \geq 2) \approx N^2 \tag{4.20}$$

This approximation is also accurate to within about 20% or better when $N \leq 0.5$. Following the reasoning presented before, the total thermal Auger probability P_2 is

$$\mathrm{P}_2 \approx N^2 \frac{\tau_h}{\tau_A} \tag{4.21}$$

where we have again taken τ_h to be much less than the intraparticle Auger lifetime τ_A. The thermal Auger lifetime is then

$$\frac{1}{\tau_{A,th}} \equiv \frac{\mathrm{P}_2}{\tau_h} \approx \frac{N^2}{\tau_A} \tag{4.22}$$

One may also consider the limit $\tau \ll \tau_h$. In this case $1 - e^{-\tau_h/\tau} \approx 1$ so that the thermal lifetime then depends only on the hopping time as $\tau_{A,th}^{-1} = N^2/\tau_h$ and $\tau_{1,th}^{-1} = N/\tau_h$. This regime is likely relevant at low temperatures and large particle sizes, where τ_h may be large.

The above considerations give the nominal dependence of the thermal recombination lifetime on the thermal carrier number per particle. For Auger recombination, one must consider that the recombination requires, at minimum, two electrons and one hole or two holes and one electron per particle. This leads to an additional combinatorial factor S which depends on the details of the quantum dot Auger mechanism, as discussed in [51, 49] and the appendix to Chapter 2. The more general thermal lifetime is therefore

$$\frac{1}{\tau_{th}} = S \frac{N^\gamma}{\tau} \tag{4.23}$$

γ is an integer exponent. This equation bears a close resemblance to bulk recombination statistics,

in which the lifetime is defined

$$\frac{1}{\tau} \equiv \frac{1}{N}\frac{dN}{dt} \tag{4.24}$$

as discussed in the appendix to Chapter 2. With the assumptions leading to the above thermal recombination lifetime, counting statistics issues discussed in Chapter 2 do not appear because charge transport makes quantum dot solid behave like a homogeneous macroscopic semiconductor.

4.6.3 Shot noise and the detailed balance formulation of D^*

As noted in the main text, the detectivity D^* is defined

$$D^* = \frac{\Re\sqrt{A\Delta\nu}}{i_n} \tag{4.25}$$

and the detailed balance formulation requires a microscopic interpretation of the noise current i_n. Here we examine the case of a device operating in the shot noise limit, relevant to mobile charge generation by a thermal or optical photon flux. Shot noise is derived from a Fourier analysis of the current associated with a random distribution of electron arrival times, and the detailed balance D^* follows from assigning the random current to thermal carrier generation and recombination.

Consider a device consisting of a semiconductor with thickness d sandwiched between a pair of electrodes. Following Cohen [55], we define $\overline{I}$ as the average collected current and $\overline{n}$ as the average number of collected electrons per unit time. Associated with these quantities are the average electron velocity $\overline{v}$, average electron transit time $\tau_{tr} = d/\overline{v}$, and the instantaneous time-dependent counterparts $I(t)$, $n(t)$ and $v(t)$. The mean-squared current fluctuations $\overline{i^2}$ are by convention defined through

$$\overline{\left(I - \overline{I}\right)^2} \equiv \overline{i^2} \tag{4.26}$$

and from statistics we know that

$$\overline{(n - \overline{n})^2} = \overline{n} \tag{4.27}$$

We may relate these quantities through Campbell's theorem. It states that for a signal s defined $s = \sum_{i=1}^{N} f(t - t_r)$ where $f(t)$ is the response function, N is the number of signal-generating events, and t_r are random times, $\overline{s} = N \int_{-\infty}^{\infty} f(t)dt$ and $\overline{(s - \overline{s})^2} = N \int_{-\infty}^{\infty} f^2(t)dt$. Applied to the present situation of an average current generated by discrete electrons, we find

$$\overline{I} = \overline{n} \int_{-\infty}^{\infty} I(t)dt \tag{4.28}$$

and

$$\overline{i^2} = \overline{n} \int_{-\infty}^{\infty} I^2(t)dt \tag{4.29}$$

The associated Fourier transform relationships are

$$I(t) = \frac{1}{\sqrt{2\pi}} \int_{-\infty}^{\infty} \iota(\omega) e^{i\omega t} d\omega \tag{4.30}$$

$$\iota(\omega) = \frac{1}{\sqrt{2\pi}} \int_{-\infty}^{\infty} I(t) e^{-i\omega t} dt \tag{4.31}$$

$$\int_{-\infty}^{\infty} I^2(t)dt = \int_{-\infty}^{\infty} \iota(\omega)\iota^*(\omega)d\omega \tag{4.32}$$

where $\iota^*(\omega)$ is the complex conjugate of $\iota(\omega)$. Since $\iota(\omega)\iota^*(\omega)$ is an even function when $I(t)$ follows Poisson statistics [55], we may write

$$\overline{i^2} = \frac{2I(t)}{e} \int_{0}^{\infty} \iota(\omega)\iota^*(\omega)d\omega \tag{4.33}$$

where e is the unit charge. We now require an explicit equation for $I(t)$. If the electron experiences a constant acceleration, its final velocity v_f is twice the average, $v_f = 2d/\tau_{tr}$, and the instantaneous velocity may be written as $v(t) = tv_f/\tau_{tr} = 2td/\tau_{tr}^2$. The instantaneous current is thus $I(t) =$

$ev(t)/d = 2et/\tau_{tr}^2$. Plugging in to $\iota(\omega)$, we have

$$\iota(\omega) = \frac{2e}{\tau_{tr}^2\sqrt{2\pi}} \int_0^{\tau_{tr}} te^{-i\omega t} dt \tag{4.34}$$

so that

$$\iota(\omega)\iota^*(\omega) = \frac{2e^2}{\pi\omega^4\tau_{tr}^4}\Big(\omega^2\tau_{tr}^2 + 2\Big(1 - \cos(\omega\tau_{tr}) - \omega\tau_{tr}\sin(\omega\tau_{tr})\Big)\Big) \tag{4.35}$$

When the product $\omega\tau_{tr}$ is small, $\iota(\omega)\iota^*(\omega) = e^2/2\pi$ and integrating across the bandwidth $\Delta\nu = \Delta\omega/2\pi$ gives the mean-square shot noise current as

$$\overline{i^2} = 2eI\Delta\nu \tag{4.36}$$

The root-mean-square shot noise current is

$$i_n \equiv \sqrt{\overline{i^2}} = \sqrt{2eI\Delta\nu} \tag{4.37}$$

The explicit time-dependence of $I(t)$ has been dropped because t may be loosely considered as modulo τ in the present context, and I is then a quantity that fluctuates about a quasi-static value.

When the fluctuations in I are dominated by thermal fluctuations in the number of mobile charges, characterized by a generation-recombination rate G_{th}, we may associate I with a thermal current eG_{th} so that

$$i_n = e\sqrt{2G_{th}\Delta\nu} \tag{4.38}$$

The best possible detectivity will occur when G_{th} is dominated by the 2π background thermal photon flux ϕ_B from a scene at finite temperature. ϕ_B is integrated above the detector cutoff energy and one assumes that above-gap thermal photons create excitations which rapidly relax to the cutoff energy. In this case, $G_{th} = A\eta\phi_B$ where A is the device absorbing area and η is the external quantum efficiency characterizing the light absorption fraction and electrical transport efficiency.

The corresponding noise current is then $i_n = e\sqrt{2A\eta\phi_B\Delta\nu}$ and

$$D^*_{BLIP} = \frac{1}{\hbar\omega}\sqrt{\frac{\eta}{2\phi_B}} \tag{4.39}$$

where we have used $\Re = \eta e/\hbar\omega$. This is known as the background-limited infrared photodetection (BLIP) limit.

For a detector at finite temperature, one must also consider thermal radiation from the detector itself. The thermal emission rate must exactly balance the excitation rate arising from the detector's own radiation; when all recombination is radiative, one has $G_{th,r} = 2A\eta\phi_D$ where ϕ_D is the 2π thermal photon flux at the detector temperature. The factor of 2 arises because, neglecting boundary effects, the radiation now comes from all directions (4π). When nonradiative recombination competes effectively with radiative recombination, the thermal excitation rate must increase to maintain equilibrium and $G_{th} = 2A\eta\phi_D/f_r$ where $f_r \leq 1$ is the fraction of the total recombination which is radiative. The maximum possible detectivity for a real detector is therefore [69]

$$D^* = \frac{1}{\hbar\omega}\sqrt{\frac{\eta f_r}{4\phi_D}} \tag{4.40}$$

REFERENCES

[1] C. Melnychuk and P. Guyot-Sionnest, "Thermodynamic Limits to HgTe Quantum Dot Infrared Detector Performance," *J. Electron. Mater.*, vol. 51, no. 3, pp. 1428–1435, 2022.

[2] W. E. Tennant, ""Rule 07" revisited: Still a good heuristic predictor of p/n HgCdTe photodiode performance?," *J. Electron. Mater.*, vol. 39, no. 7, pp. 1030–1035, 2010.

[3] N. Baier, O. Gravrand, C. Lobre, O. Boulade, A. Kerlain, and N. Péré-Laperne, "HgCdTe Diode Dark Current Modeling: Rule 07 Revisited for LW and VLW," *J. Electron. Mater.*, vol. 48, no. 8, pp. 5233–5240, 2019.

[4] A. Rogalski, *Infrared Detectors*. Boca Raton: CRC Press, 2 ed., 2010.

[5] D. Lee, M. Carmody, E. Piquette, P. Dreiske, A. Chen, A. Yulius, D. Edwall, S. Bhargava, M. Zandian, and W. E. Tennant, "High-Operating Temperature HgCdTe: A Vision for the Near Future," *J. Electron. Mater.*, vol. 45, no. 9, pp. 4587–4595, 2016.

[6] D. L. Lee, P. Dreiske, J. Ellsworth, R. Cottier, A. Chen, S. Tallaricao, A. Yulius, M. Carmody, E. Piquette, M. Zandian, and S. Douglas, "Law 19: The ultimate photodiode performance metric," in *Infrared Technol. Appl. XLVI*, no. 11407, p. 114040X, 2020.

[7] B. V. Olson, E. A. Shaner, J. K. Kim, J. F. Klem, S. D. Hawkins, M. E. Flatté, and T. F. Boggess, "Identification of dominant recombination mechanisms in narrow-bandgap InAs/InAsSb type-II superlattices and InAsSb alloys," *Appl. Phys. Lett.*, vol. 103, no. 5, p. 052106, 2013.

[8] B. V. Olson, C. H. Grein, J. K. Kim, E. A. Kadlec, J. F. Klem, S. D. Hawkins, and E. A. Shaner, "Auger recombination in long-wave infrared InAs/InAsSb type-II superlattices," *Appl. Phys. Lett.*, vol. 107, no. 26, p. 261104, 2015.

[9] X. Tang, M. Chen, M. M. Ackerman, C. Melnychuk, and P. Guyot-Sionnest, "Direct Imprinting of Quasi-3D Nanophotonic Structures into Colloidal Quantum-Dot Devices," *Adv. Mater.*, vol. 32, no. 9, p. 1906590, 2020.

[10] I. Ramiro, O. Özdemir, S. Christodoulou, S. Gupta, M. Dalmases, I. Torre, and G. Konstantatos, "Mid- and Long-Wave Infrared Optoelectronics via Intraband Transitions in PbS Colloidal Quantum Dots," *Nano Lett.*, vol. 20, no. 2, pp. 1003–1008, 2020.

[11] M. Ackerman, X. Tang, and P. Guyot-Sionnest, "Fast and Sensitive Colloidal Quantum Dot Mid-Wave Infrared Photodetectors," *ACS Nano*, vol. 12, no. 7, pp. 7264–7271, 2018.

[12] X. Tang, M. M. Ackerman, and P. Guyot-Sionnest, "Thermal Imaging with Plasmon Resonance Enhanced HgTe Colloidal Quantum Dot Photovoltaic Devices," *ACS Nano*, vol. 12, no. 7, pp. 7362–7370, 2018.

[13] X. Tang, M. M. Ackerman, G. Shen, and P. Guyot-Sionnest, "Towards Infrared Electronic Eyes: Flexible Colloidal Quantum Dot Photovoltaic Detectors Enhanced by Resonant Cavity," *Small*, vol. 15, no. 12, p. 1804920, 2019.

[14] X. Tang, M. M. Ackerman, and P. Guyot-Sionnest, "Acquisition of Hyperspectral Data with Colloidal Quantum Dots," *Laser Photonics Rev.*, vol. 13, no. 11, p. 1900165, 2019.

[15] X. Tang, M. M. Ackerman, M. Chen, and P. Guyot-Sionnest, "Dual-band infrared imaging using stacked colloidal quantum dot photodiodes," *Nat. Photonics*, vol. 13, no. 4, pp. 277–282, 2019.

[16] Q. Hao, X. Tang, Y. Cheng, and Y. Hu, "Development of flexible and curved infrared detectors with HgTe colloidal quantum dots," *Infrared Phys. Technol.*, vol. 108, no. March, p. 103344, 2020.

[17] M. M. Ackerman, M. Chen, and P. Guyot-Sionnest, "HgTe colloidal quantum dot photodiodes

for extended short-wave infrared detection," *Appl. Phys. Lett.*, vol. 116, no. 8, p. 083502, 2020.

[18] P. Martyniuk, S. Krishna, and A. Rogalski, "Assessment of quantum dot infrared photodetectors for high temperature operation," *J. Appl. Phys.*, vol. 104, no. 3, p. 034314, 2008.

[19] J. Phillips, "Evaluation of the fundamental properties of quantum dot infrared detectors," *J. Appl. Phys.*, vol. 91, no. 7, pp. 4590–4594, 2002.

[20] M. H. Hudson, M. Chen, V. Kamysbayev, E. M. Janke, X. Lan, G. Allan, C. Delerue, B. Lee, P. Guyot-Sionnest, and D. V. Talapin, "Conduction Band Fine Structure in Colloidal HgTe Quantum Dots," *ACS Nano*, vol. 12, no. 9, pp. 9397–9401, 2018.

[21] S. Keuleyan, J. Kohler, and P. Guyot-Sionnest, "Photoluminescence of mid-infrared HgTe colloidal quantum dots," *J. Phys. Chem. C*, vol. 118, no. 5, pp. 2749–2753, 2014.

[22] M. Chen, X. Lan, X. Tang, Y. Wang, M. H. Hudson, D. V. Talapin, and P. Guyot-Sionnest, "High Carrier Mobility in HgTe Quantum Dot Solids Improves Mid-IR Photodetectors," *ACS Photonics*, vol. 6, no. 9, pp. 2358–2365, 2019.

[23] A. Stavrinadis and G. Konstantatos, "Strategies for the Controlled Electronic Doping of Colloidal Quantum Dot Solids," *ChemPhysChem*, vol. 17, no. 5, pp. 632–644, 2016.

[24] M. Chen and P. Guyot-Sionnest, "Reversible Electrochemistry of Mercury Chalcogenide Colloidal Quantum Dot Films," *ACS Nano*, vol. 11, no. 4, pp. 4165–4173, 2017.

[25] G. Shen, M. Chen, and P. Guyot-Sionnest, "Synthesis of Nonaggregating HgTe Colloidal Quantum Dots and the Emergence of Air-Stable n-Doping," *J. Phys. Chem. Lett.*, vol. 8, no. 10, pp. 2224–2228, 2017.

[26] X. Lan, M. Chen, M. H. Hudson, V. Kamysbayev, Y. Wang, P. Guyot-Sionnest, and D. V. Ta-

lapin, “Quantum dot solids showing state-resolved band-like transport,” *Nat. Mater.*, vol. 19, no. March, pp. 323–330, 2020.

[27] G. Allan and C. Delerue, “Tight-binding calculations of the optical properties of HgTe nanocrystals,” *Phys. Rev. B*, vol. 86, no. 16, p. 165437, 2012.

[28] M. Weiler, R. Aggarwal, and B. Lax, “Interband magnetoreflectance in semiconducting HgCdTe alloys,” *Phys. Rev. B*, vol. 16, no. 8, pp. 3603–3607, 1977.

[29] M. T. Czyżyk and M. Podgórny, “Energy Bands and Optical Properties of HgTe and CdTe Calculated on the Basis of the Tight-Binding Model with Spin–Orbit Interaction,” *Phys. Status Solidi*, vol. 98, no. 2, pp. 507–516, 1980.

[30] A. Svane, N. E. Christensen, M. Cardona, A. N. Chantis, M. Van Schilfgaarde, and T. Kotani, “Quasiparticle band structures of β-HgS, HgSe, and HgTe,” *Phys. Rev. B*, vol. 84, no. 20, p. 205205, 2011.

[31] G. L. Hansen and J. L. Schmit, “Calculation of intrinsic carrier concentration in Hg1-xCdxTe,” *J. Appl. Phys.*, vol. 54, no. 3, pp. 1639–1640, 1983.

[32] P. Guyot-Sionnest, “Electrical Transport in Colloidal Quantum Dot Films,” *J. Phys. Chem. Lett.*, vol. 3, no. 9, pp. 1169–1175, 2012.

[33] C. Melnychuk and P. Guyot-Sionnest, “Slow Auger Relaxation in HgTe Colloidal Quantum Dots,” *J. Phys. Chem. Lett.*, vol. 9, no. 9, pp. 2208–2211, 2018.

[34] R. C. Hilborn, “Einstein coefficients, cross sections, f values, dipole moments, and all that,” *Am. J. Phys.*, vol. 50, no. 11, pp. 982–986, 1982.

[35] E. Yablonovitch, T. J. Gmitter, and R. Bhat, “Inhibited and enhanced spontaneous emission from optically thin AlGaAs/GaAs Double Heterostructures,” *Phys. Rev. Lett.*, vol. 61, no. 22, pp. 2546–2549, 1988.

[36] P. de Vries and A. Lagendijk, "Resonant scattering and spontaneous emission in dielectrics: Microscopic derivation of local-field effects," *Phys. Rev. Lett.*, vol. 81, no. 7, pp. 1381–1384, 1998.

[37] E. Lhuillier, S. Keuleyan, and P. Guyot-Sionnest, "Optical properties of HgTe colloidal quantum dots," *Nanotechnology*, vol. 23, no. 17, p. 175705, 2012.

[38] S. H. Groves, R. N. Brown, and C. R. Pidgeon, "Interband magnetoreflection and band structure of HgTe," *Phys. Rev.*, vol. 161, no. 3, pp. 779–793, 1967.

[39] R. A. Stradling, "A millimetre microwave determination of the conduction band effective mass of HgTe," *Proc. Phys. Soc.*, vol. 90, pp. 175–180, 1967.

[40] Y. Guldner, C. Rigaux, A. Mycielski, and Y. Couder, "Magnetooptical Investigation of HgCdTe Mixed Crystals. II. Semiconducting Configuration and Semimetal to Semiconductor Transition," *Phys. Status Solidi*, vol. 82, pp. 149–158, 1977.

[41] P. Man and D. S. Pan, "Infrared absorption in HgTe," *Phys. Rev. B*, vol. 44, no. 16, pp. 8745–8758, 1991.

[42] W. Szuszkiewicz, A. M. Witowski, and M. Grynberg, "The Dynamic Dielectric Function in HgSe and HgTe," *Phys. Status Solidi B*, vol. 87, pp. 637–645, 1978.

[43] M. Grynberg, R. Le Toullec, and M. Balkanski, "Dielectric function in HgTe between 8 and 300°K," *Phys. Rev. B*, vol. 9, no. 2, pp. 517–526, 1974.

[44] C. Delerue, G. Allan, and M. Lannoo, "Concept of dielectric constant for nanosized systems," *Phys. Rev. B*, vol. 68, no. 11, p. 115411, 2003.

[45] X. Cartoixà and L. W. Wang, "Microscopic dielectric response functions in semiconductor quantum dots," *Phys. Rev. Lett.*, vol. 94, no. 23, p. 236804, 2005.

[46] P. Rastogi, A. Chu, T. H. Dang, Y. Prado, C. Gréboval, J. Qu, C. Dabard, A. Khalili, E. Dandeu, B. Fix, X. Z. Xu, S. Ithurria, G. Vincent, B. Gallas, and E. Lhuillier, "Complex Optical Index of HgTe Nanocrystal Infrared Thin Films and Its Use for Short Wave Infrared Photodiode Design," *Adv. Opt. Mater.*, p. 2002066, 2021.

[47] S. E. Schacham and E. Finkman, "Recombination mechanisms in p-type HgCdTe: Freezeout and background flux effects," *J. Appl. Phys.*, vol. 57, no. 6, pp. 2001–2009, 1985.

[48] P. C. Sercel and A. L. Efros, "Band-Edge Exciton in CdSe and Other II-VI and III-V Compound Semiconductor Nanocrystals - Revisited," *Nano Lett.*, vol. 18, no. 7, pp. 4061–4068, 2018.

[49] C. Melnychuk and P. Guyot-Sionnest, "Multicarrier Dynamics in Quantum Dots," *Chem. Rev.*, vol. 121, no. 4, pp. 2325–2372, 2021.

[50] P. T. Landsberg, *Recombination in Semiconductors*. Cambridge: Cambridge University Press, 1991.

[51] V. I. Klimov, J. A. McGuire, R. D. Schaller, and V. I. Rupasov, "Scaling of multiexciton lifetimes in semiconductor nanocrystals," *Phys. Rev. B*, vol. 77, no. 19, p. 195324, 2008.

[52] H. Wen, B. Pinkie, and E. Bellotti, "Direct and phonon-assisted indirect Auger and radiative recombination lifetime in HgCdTe, InAsSb, and InGaAs computed using Green's function formalism," *J. Appl. Phys.*, vol. 118, no. 1, p. 015702, 2015.

[53] C. H. Grein, M. E. Flatté, and Y. Chang, "Modeling of recombination in HgCdTe," *J. Electron. Mater.*, vol. 37, no. 9, pp. 1415–1419, 2008.

[54] R. R. Gerhardts, R. Dornhaus, and G. Nimtz, "The Auger-effect in Hg1-xCdxTe," *Solid State Electron.*, vol. 21, no. 11-12, pp. 1467–1470, 1978.

[55] J. Cohen, "Introduction to Noise in Solid State Devices," *Natl. Bur. Stand.*, p. Technical Note 1169, 1982.

[56] J. Cohen, "Three Guises of Generation-Recombination Noise," *Natl. Bur. Stand.*, p. Technical Note 1173, 1983.

[57] W. Shockley and W. Read, "Statistics of the Recombination of Holes and Electrons," *Phys. Rev.*, vol. 87, no. 5, pp. 835–842, 1952.

[58] P. Asbeck, "Self-absorption effects on the radiative lifetime in GaAs-GaAlAs double heterostructures," *J. Appl. Phys.*, vol. 48, no. 2, pp. 820–822, 1977.

[59] H. Liu, E. Lhuillier, and P. Guyot-Sionnest, "1/f noise in semiconductor and metal nanocrystal solids," *J. Appl. Phys.*, vol. 115, no. 15, p. 154309, 2014.

[60] G. Shen and P. Guyot-Sionnest, "HgTe/CdTe and HgSe/CdX (X = S, Se, and Te) Core/Shell Mid-Infrared Quantum Dots," *Chem. Mater.*, vol. 31, no. 1, pp. 286–293, 2019.

[61] A. Pandey and P. Guyot-Sionnest, "Slow Electron Cooling in Colloidal Quantum Dots," *Science (80-.).*, vol. 322, no. 5903, pp. 929–932, 2008.

[62] H. Liu and P. Guyot-Sionnest, "Photoluminescence lifetime of lead selenide colloidal quantum dots," *J. Phys. Chem. C*, vol. 114, no. 35, pp. 14860–14863, 2010.

[63] C. Melnychuk and P. Guyot-Sionnest, "Auger Suppression in n-Type HgSe Colloidal Quantum Dots," *ACS Nano*, vol. 13, no. 9, pp. 10512–10519, 2019.

[64] A. Chu, C. Gréboval, N. Goubet, B. Martinez, C. Livache, J. Qu, P. Rastogi, F. A. Bresciani, Y. Prado, S. Suffit, S. Ithurria, G. Vincent, and E. Lhuillier, "Near Unity Absorption in Nanocrystal Based Short Wave Infrared Photodetectors Using Guided Mode Resonators," *ACS Photonics*, vol. 6, no. 10, pp. 2553–2561, 2019.

[65] P. Guyot-Sionnest, J. C. Peterson, and C. Melnychuk, "Extracting Bulk-like Semiconductor Parameters from the Characterization of Colloidal Quantum Dot Film Photoconductors," *J. Phys. Chem. C*, p. ASAP, 2022.

[66] D. Bozyigit, N. Yazdani, M. Yarema, O. Yarema, W. M. M. Lin, S. Volk, K. Vuttivorakulchai, M. Luisier, F. Juranyi, and V. Wood, "Soft surfaces of nanomaterials enable strong phonon interactions," *Nature*, vol. 531, no. 7596, pp. 618–622, 2016.

[67] A. Kamath, C. Melnychuk, and P. Guyot-Sionnest, "Toward Bright Mid-Infrared Emitters: Thick-Shell n-Type HgSe/CdS Nanocrystals," *J. Am. Chem. Soc.*, vol. 143, no. 46, pp. 19567–19575, 2021.

[68] N. W. Ashcroft and N. D. Mermin, *Solid State Physics*. Brooks/Cole, 1976.

[69] P. Guyot-Sionnest, M. M. Ackerman, and X. Tang, "Colloidal quantum dots for infrared detection beyond silicon," *J. Chem. Phys.*, vol. 151, no. 6, p. 060901, 2019.

CHAPTER 5

FUTURE DIRECTIONS

The results and discussions of preceding chapters motivate many new avenues for research. In the following sections, these research directions are introduced with preliminary comments on practical aspects and possible observations.

5.1 Intraband Intersublevel Relaxation

In Chapter 3, $1P_e$ intersublevel relaxation times of 5 - 30 ps in *n*-type HgSe were inferred by simulating spectrally-resolved photoluminescence transients. These relaxation times are broadly consistent with the anharmonic polaron decay mechanism [1, 2], and it would be significant if they could be measured more precisely and compared to theoretical predictions. This can be done using several flavors of mid-infrared pump-probe experiments. The most straightforward option is to pump the $1S_e - 1P_{e3/2}$ transition, and to use degenerate and $1S_e - 1P_{e1/2}$ probes to obtain the $1P_{e3/2} - 1P_{e1/2}$ lifetime from a concomitant $1P_{e3/2}$ bleach decay and $1P_{e1/2}$ bleach risetime. This would require two OPAs such as the LBO-LGS apparatus described in Appendix C, and no additional line-narrowing elements should be necessary.

At these energy scales, around 300 cm^{-1} in HgSe, the anharmonic polaron decay should be reasonably straightforward to calculate and compare with data. Calculations require parameters such as the optical phonon frequency, sound velocity and Grüneisen parameter which are all reasonably well-characterized for bulk materials, and the polaronic coupling will be the major unknown quantity. Hallmarks of the polaronic mechanism are the strong temperature-dependence and nonmonotonic energy-dependence of the rate that comes from resonance effects, and these traits should be clearly resolvable in experiments. Measurements on *n*-type HgTe quantum dots with even larger $\sim$ 500 cm^{-1} splittings and additional fine structure [3] would be natural complements to these studies. Beyond the unique information on excited state quantum dot dynamics

obtained from these studies, the polaron coupling which might be obtained could place useful constraints on mid-infrared nonradiative relaxation mechanisms.

5.2 Doping-dependent Homogeneous Intraband Linewidths

Although surface plasmons are traditionally associated with metals and metal nanoparticles, there has been enormous recent interest in "low density" plasmonic nanoparticles made of very highly doped semiconducting material [4]. The physical nature of low-density nanoparticle plasmons, and particularly the smooth evolution between one-electron and plasmon-like (metallic) optics, is a debated topic [5, 6, 7, 8] that remains only partly understood [9, 6, 10, 11]. Measurements of temperature-dependent homogeneous linewidths as a function of doping could in principle provide a wealth of information on this topic because metals and semiconductors should display rather different behaviors in such experiments. The homogeneous linewdith in semiconducting quantum dots is dominated by acoustic phonons with a smaller optical phonon contribution [12, 13]. This leads to a reasonably strong and linear temperature-dependence of the linewidth with a particle size-dependence that depends on the coupling mechanism [14]. The linewidth in metal nanoparticles is dominated by electron-electron and electron-surface scattering with a smaller phonon contribution such that the linewidth is only weakly temperature-dependent [15], and the size-dependence is dominated by the surface scattering term.

There are some practical challenges that prevent the kind of study described above, and they are both addressable with dynamic hole burning measurements on HgSe or HgS quantum dots. The plasmon homogeneous linewidth is usually obtained through single-particle microscopy experiments and this is only possible in the visible due to the limitations of diffraction and detector sensitivity. However, the carrier densities required to sustain visible plasmons are so large that tuning the doping between intraband and plasmonic regimes is not feasible. With infrared transitions in HgSe or HgS, however, the entire range of behavior from intraband to plasmon-like is accessible due to the lower carrier densities and facile doping, and a picosecond hole-burning experiment [14]

can provide the linewidth directly.

This will require a pair of tunable narrowband pulses utilizing a scheme along the lines of the LBO-LGS OPA described in Appendix C. The LBO seed and overall output, however, will need to be narrowed to produce the approximately 10 cm^{-1} resolution required for these measurements at low temperature.

5.3 Dephasing and State Mixing in Isoenergetic Interband and Intraband Transitions

Although there have been many studies of the homogeneous width and dephasing dynamics in quantum dots [16, 17, 18, 19] and nanomaterials more broadly [20], nearly all concern interband transitions which invariably involve valence hole states. The close level spacing of the valence levels leads to a congested hole level structure arising from a variety of known and unknown perturbations such that the hole states are poorly understood. In contrast, the conduction levels in quantum dots are widely separated leading to a much cleaner level structure. An early study of the CdSe intraband homogeneous width showed a narrower relative width $\Delta\omega/\omega$ than commonly reported for the CdSe interband transition [14]. This may have been due to contributions from the dense valence structure, although interpretation of that early study is complicated by the rapid $1S_e$ hole trapping. Investigating the dephasing caused by a dense level structure would be much more straightforward using the interband HgTe transition and the intraband HgSe transition. Comparing these homogeneous widths should more cleanly reveal any effects of the dense valence level structure, and their temperature-dependencies will inform on any differences in electron-phonon coupling. The experiment would use the same hole-burning scheme as noted above. Echo spectroscopy might also be an option for the potentially narrower intraband lines, especially at low temperature.

A different perspective on these same questions could come from two-photon absorption spectroscopy [21, 22, 23]. Two-photon absorption is nominally forbidden for strongly-allowed one-

electron transitions due to parity, but perturbations can relax these restrictions. In CdSe, for example, the interband two-photon absorption has been attributed to valence state mixing [23]. Here, a long-wave infrared pulse tuned to the two-photon resonances of $1S_e - 1P_e$ or $1S_h - 1S_e$ would be used. If the beam quality is sufficiently good, a z-scan measurement could provide the two-photon cross sections directly. Otherwise, the ratio of the one-photon and two-photon absorption or the relative integrated peak areas in an excitation spectrum could also inform on the degree of level mixing.

5.4 Upconverted Resonance Fluorescence

Resonance fluorescence experiments are often used to obtain the homogeneous width, and can also be used to obtain an excitation spectrum. Such data can be used to identify defects or fine structure and assign state-specific kinetics to them. Indeed, as shown in Chapters 2 and 3, photoluminescence decays are typically bi-exponential in mercury chalcogenides, indicating the presence of at least two distinct populations with rather different lifetimes. The origins of these populations are entirely unknown at this time and efforts to reduce nonradiative relaxation should benefit from this understanding. The photoluminescence upconversion apparatus described in Appendix C could be modified in a straightforward way for such an experiment by replacing the 1053 nm sample pump pulse with a tunable mid-infrared pulse derived from an OPA. The gated nature of the measurement will naturally minimize background signals at small delay times, and choosing a pump polarization which is not phasematched in the mixing crystal might allow reliable quasi-zero time data as well. One may then obtain line-narrowed spectra and state-specific photoluminescence decays.

5.5 Electronic and Excitonic g-factors

The g-factor is a critical parameter in the interpretation of many experiments involving magnetic fields. Free electrons and those bound in atoms or molecules display g-factors around 2, while

values ranging from 4 to -60 are observed in bulk and confined semiconductors due to the effects of band structure [24, 25]. Recent work on temperature-dependent charge transport in HgTe quantum dot solids has opened the exciting possibility of observing delocalized (coherent) charge transport, but with nuances and uncertainties in the experimental interpretations [26]. Subsequent studies aiming to elucidate the degree of delocalization showed a large negative magnetoresistance, in principle a signature of weak localization, but this was instead attributed to a large g-factor derived from modeling [27]. Although the model-derived value around -50 is consistent with broad trends in semiconductors, it is rather different from calculated values [28]. Future investigations aiming to more precisely examine the conduction mechanisms will likely benefit from independent g-factor measurements, and the influences of particle size and shape upon it.

g-factors can be measured optically through transient Faraday rotation experiments [29, 30, 31, 32]. This involves a degenerate pump-probe laser pulse pair which is resonant with the optical transition to be studied. The pump pulse is circularly-polarized, the probe pulse is linearly-polarized, and a magnetic field is applied to the sample. In this configuration the pump creates a spin-polarized population of excitons and the macroscopic magnetization rotates the polarization angle of the probe pulse. This rotation is known as the Faraday effect and can detected using a bridge apparatus consisting of a half-wave plate, polarizing beamsplitter, and a pair of detectors for the exiting beam pair. 45° polarization at the polarizer leads to equal signals at both detectors, and the pump-induced rotation produces a small differential signal. The differential signal magnitude, in terms of the polarization rotation angle θ per sample unit length z, is $d\theta/dz = 2\pi e^2 N B_0/m^{*2}\omega^2 c$ where N is the number density of excited particles, B_0 is the applied magnetic field, e is the unit charge, and m^* is the effective mass. The inverse-quadratic dependence on ω should promote good differential signal levels in the infrared with close-packed film samples. Interferometric [33] and/or lock-in schemes should further facilitate sensitive detection.

In the Faraday geometry the signal decays with the total macroscopic magnetization, which in most cases is just the exciton lifetime. In the Voigt geometry, however, Larmor precession

about the field axis creates a transient signal in the form of a decaying sinusoid with a frequency $\omega_L = -g\frac{e}{2m^*}B$ and lifetime T_2^*. With a g-factor around -50 [27], only moderate B-fields would be required to produce a Larmor precession measurable with picosecond pulses. It would be interesting to perform these measurements as a function of particle size on interband and intraband transitions in HgSe and HgTe quantum dots to asses the effects of the dense valence band, spin-orbit splitting, and additional shape-derived fine structure [3].

5.6 Intraband Distributed Feedback Lasing

A quantum dot mid-infrared laser would be a milestone achievement because quantum dot lasing has only been observed in the visible region where traditional semiconductors are already successful and inexpensive. Infrared lasers, on the other hand, face all of the same significant challenges as infrared detectors [34]. The suppressed Auger recombination in n-type HgSe is a fundamental benefit to lasing applications because the gain lifetime is nominally the biexciton lifetime, and intraband lasing from HgSe or core/shell derivatives should be possible from liquids and solids, each with their own benefits and drawbacks.

In a liquid sample, traditional distributed feedback designs [35, 36, 37, 38] could be adapted in a straightforward manner. Illuminating the liquid sample with a pair of crossed pump beams creates a gain grating, and the stimulated emission preferentially occurs in a narrow bandwidth and direction due to the interference of counterpropagating modes [39, 40]. The lasing wavelength λ_l in a distributed feedback laser is $\lambda_l = 2n_l a_p$ where n_l is the refractive index at λ_l and a_p is the period of the pump grating. The grating period is determined by the pump beam crossing angle 2θ and wavelength λ_p as $a_p = \lambda_p/2\sin\theta$ so that $\lambda_l = \lambda_p n_l/\sin\theta$. For lasing at 4.5 μm and pumping at 1053 nm in a liquid of index of 1.5, one has $\theta \approx 20°$ and a pump grating period of about 1.5 μm. This could be easily achieved by sending the pump beam on a lithographically-defined transmission grating, blocking the 0^{th} order, and imaging the ± 1 diffracted modes onto the sample. The transmission grating period would be $a_t = \lambda_p/\sin\theta \approx 3\mu$m such that $a_t/2 = a_p$. For liquid

solutions of index around 1.5, the 20° angles involved will require numerical apertures greater than 0.35. Lasing in a close-packed quantum dot film with $n_l \approx 2$ would require even larger numerical aperture which might be challenging. Films could instead use a patterned substrate as typically done with organic and quantum dot lasers in the visible [41, 42, 43].

An advantage of the liquid approach is the automatic high optical quality of all interfaces, and the easy achievement of "thick" samples. A quantum dot film would need to act as a slab waveguide with a thickness around half the wavelength for strong waveguiding at $n = 2$ [44, 45]. Creating such a thick film with good optical quality is a substantial practical challenge. The tradeoff, however, is a much larger gain in the film than in the liquid. The small-signal gain is $g = N\sigma$ where N is the excitation density and σ is the emission cross section. Although σ is not known for HgSe quantum dots, it can be calculated from the radiative rate γ_r as $\sigma = \lambda^2\gamma_r^2/2\pi\Delta\omega n^2$, giving 2×10^{-16} cm^2 in solution and 3×10^{-16} cm^2 in films for a 500 cm^{-1} linewidth [46]. This should enable $g \sim 10^4$ cm^{-1} in films and a few orders of magnitude less in concentrated solutions. Films also enable more sophisticated schemes such as surface plasmon amplification [47, 48, 49, 50] and various photonic waveguides [51, 52]. Incorporating mercury chalcogenide quantum dots into solution-processable and extrudable inorganic hosts such as chalcogenide glasses [53, 54, 55, 56] or perovskites [57] might lead to the exciting prospect of direct mid-infrared fiber lasers.

REFERENCES

[1] E. A. Zibik, T. Grange, B. A. Carpenter, N. E. Porter, R. Ferreira, G. Bastard, D. Stehr, S. Winnerl, M. Helm, H. Y. Liu, M. S. Skolnick, and L. R. Wilson, "Long lifetimes of quantum-dot intersublevel transitions in the terahertz range," *Nat. Mater.*, vol. 8, no. 10, pp. 803–807, 2009.

[2] T. Grange, R. Ferreira, and G. Bastard, "Polaron relaxation in self-assembled quantum dots: Breakdown of the semiclassical model," *Phys. Rev. B*, vol. 76, no. 24, p. 241304(R), 2007.

[3] M. H. Hudson, M. Chen, V. Kamysbayev, E. M. Janke, X. Lan, G. Allan, C. Delerue, B. Lee, P. Guyot-Sionnest, and D. V. Talapin, "Conduction Band Fine Structure in Colloidal HgTe Quantum Dots," *ACS Nano*, vol. 12, no. 9, pp. 9397–9401, 2018.

[4] A. Agrawal, S. H. Cho, O. Zandi, S. Ghosh, R. W. Johns, and D. J. Milliron, "Localized Surface Plasmon Resonance in Semiconductor Nanocrystals," *Chem. Rev.*, vol. 118, no. 6, pp. 3121–3207, 2018.

[5] A. M. Schimpf, N. Thakkar, C. E. Gunthardt, D. J. Masiello, and D. R. Gamelin, "Charge-tunable quantum plasmons in colloidal semiconductor nanocrystals," *ACS Nano*, vol. 8, no. 1, pp. 1065–1072, 2014.

[6] G. Shen and P. Guyot-Sionnest, "HgS and HgS/CdS Colloidal Quantum Dots with Infrared Intraband Transitions and Emergence of a Surface Plasmon," *J. Phys. Chem. C*, vol. 120, no. 21, pp. 11744–11753, 2016.

[7] G. Shen and P. Guyot-Sionnest, "Reply to "Comment on 'HgS and HgS/CdS Colloidal Quantum Dots with Infrared Intraband Transitions and Emergence of a Surface Plasmon'"," *J. Phys. Chem. C*, vol. 120, no. 50, pp. 28903–28904, 2016.

[8] N. Thakkar, A. M. Schimpf, C. E. Gunthardt, D. R. Gamelin, and D. J. Masiello, "Comment on "HgS and HgS/CdS Colloidal Quantum Dots with Infrared Intraband Transitions and

Emergence of a Surface Plasmon"," *J. Phys. Chem. C*, vol. 120, no. 50, pp. 28900–28902, 2016.

[9] E. B. Guidez and C. M. Aikens, "Quantum mechanical origin of the plasmon: from molecular systems to nanoparticles.," *Nanoscale*, vol. 6, no. 20, pp. 11512–11527, 2014.

[10] B. T. Lau and T. C. Berkelbach, "Quantum plasmons and intraband excitons in doped nanoparticles: Insights from quantum chemistry," *J. Chem. Phys.*, vol. 152, no. 22, p. 224704, 2020.

[11] P. K. Jain, "Plasmon-in-a-box: On the physical nature of few-carrier plasmon resonances," *J. Phys. Chem. Lett.*, vol. 5, no. 18, pp. 3112–3119, 2014.

[12] M. A. Stroscio and M. Dutta, *Phonons in Nanostructures*. Cambridge: Cambridge University Press, 2001.

[13] B. K. Ridley, *Quantum Processes in Semiconductors*. Oxford: Oxford University Press, 5 ed., 2013.

[14] M. Shim and P. Guyot-Sionnest, "Intraband hole burning of colloidal quantum dots," *Phys. Rev. B*, vol. 64, no. 24, p. 245342, 2001.

[15] M. Liu, M. Pelton, and P. Guyot-Sionnest, "Reduced damping of surface plasmons at low temperatures," *Phys. Rev. B*, vol. 79, no. 3, p. 035418, 2009.

[16] S. B. Block, L. A. Yurs, A. V. Pakoulev, R. S. Selinsky, S. Jin, and J. C. Wright, "Multiresonant multidimensional spectroscopy of surface-trapped excitons in PbSe quantum dots," *J. Phys. Chem. Lett.*, vol. 3, no. 18, pp. 2707–2712, 2012.

[17] T. A. Gellen, J. Lem, and D. B. Turner, "Probing Homogeneous Line Broadening in CdSe Nanocrystals Using Multidimensional Electronic Spectroscopy," *Nano Lett.*, vol. 17, no. 5, pp. 2809–2815, 2017.

[18] C. Y. Wong and G. D. Scholes, "Biexcitonic fine structure of CdSe nanocrystals probed by polarization-dependent two-dimensional photon echo spectroscopy," *J. Phys. Chem. A*, vol. 115, no. 16, pp. 3797–3806, 2011.

[19] H. Seiler, S. Palato, C. Sonnichsen, H. Baker, and P. Kambhampati, "Seeing Multiexcitons through Sample Inhomogeneity: Band-Edge Biexciton Structure in CdSe Nanocrystals Revealed by Two-Dimensional Electronic Spectroscopy," *Nano Lett.*, vol. 18, no. 5, pp. 2999–3006, 2018.

[20] L. T. Lloyd, *Resolving Exciton Dynamics and Couplings in Atomically Thin Semiconductors with Multidimensional Spectroscopy*. PhD thesis, University of Chicago, 2022.

[21] S. A. Blanton, A. Dehestani, P. C. Lin, and P. Guyot-Sionnest, "Photoluminescence of single semiconductor nanocrystallites by two-photon excitation microscopy," *Chem. Phys. Lett.*, vol. 229, no. 3, pp. 317–322, 1994.

[22] M. E. Schmidt, S. A. Blanton, M. A. Hines, and P. Guyot-Sionnest, "Size-dependent two-photon excitation spectroscopy of CdSe nanocrystals," *Phys. Rev. B*, vol. 53, no. 19, pp. 12629–12632, 1996.

[23] M. E. Schmidt, S. A. Blanton, M. A. Hines, and P. Guyot-Sionnest, "Polar CdSe nanocrystals: Implications for electronic structure," *J. Chem. Phys.*, vol. 106, no. 12, pp. 5254–5259, 1997.

[24] A. Kiselev, E. Ivchenko, and U. Rössler, "Electron g factor in one- and zero-dimensional semiconductor nanostructures," *Phys. Rev. B*, vol. 58, no. 24, pp. 16353–16359, 1998.

[25] A. Tadjine, Y. M. Niquet, and C. Delerue, "Universal behavior of electron g -factors in semiconductor nanostructures," *Phys. Rev. B*, vol. 95, no. 23, p. 235437, 2017.

[26] X. Lan, M. Chen, M. H. Hudson, V. Kamysbayev, Y. Wang, P. Guyot-Sionnest, and D. V. Talapin, "Quantum dot solids showing state-resolved band-like transport," *Nat. Mater.*, vol. 19, no. March, pp. 323–330, 2020.

[27] M. Chen, X. Lan, M. H. Hudson, G. Shen, P. B. Littlewood, D. V. Talapin, and P. Guyot-Sionnest, "Magnetoresistance of high mobility HgTe quantum dot films with controlled charging," *J. Mater. Chem. C*, 2022.

[28] X. W. Zhang and J. B. Xia, "Electronic structure and electron g factors of HgTe quantum dots," *J. Phys. D. Appl. Phys.*, vol. 39, no. 9, pp. 1815–1820, 2006.

[29] S. A. Crooker, D. D. Awschalom, and N. Samarth, "Time-Resolved Faraday Rotation Spectroscopy of Spin Dynamics in Digital Magnetic Heterostructures," *IEEE J. Sel. Top. Quantum Electron.*, vol. 1, no. 4, pp. 1082–1092, 1995.

[30] J. A. Gupta, D. D. Awschalom, A. L. Efros, and A. V. Rodina, "Spin dynamics in semiconductor nanocrystals," *Phys. Rev. B*, vol. 66, no. 12, p. 125307, 2002.

[31] D. Feng, D. R. Yakovlev, V. V. Pavlov, A. V. Rodina, E. V. Shornikova, J. Mund, and M. Bayer, "Dynamic Evolution from Negative to Positive Photocharging in Colloidal CdS Quantum Dots," *Nano Lett.*, vol. 17, no. 5, pp. 2844–2851, 2017.

[32] E. V. Shornikova, L. Biadala, D. R. Yakovlev, D. Feng, V. F. Sapega, N. Flipo, A. A. Golovatenko, M. A. Semina, A. V. Rodina, A. A. Mitioglu, M. V. Ballottin, P. C. Christianen, Y. G. Kusrayev, M. Nasilowski, B. Dubertret, and M. Bayer, "Electron and Hole g-Factors and Spin Dynamics of Negatively Charged Excitons in CdSe/CdS Colloidal Nanoplatelets with Thick Shells," *Nano Lett.*, vol. 18, no. 1, pp. 373–380, 2018.

[33] A. C. Rowe, I. Zhaksylykova, G. Dilasser, Y. Lassailly, and J. Peretti, "Polarizers, optical bridges, and Sagnac interferometers for nanoradian polarization rotation measurements," *Rev. Sci. Instrum.*, vol. 88, no. 4, 2017.

[34] K. E. Kudryavtsev, V. V. Rumyantsev, V. Y. Aleshkin, A. A. Dubinov, V. V. Utochkin, M. A. Fadeev, N. N. Ikhailov, G. Alymov, D. Svintsov, V. I. Gavrilenko, and S. V. Morozov, "Temperature limitations for stimulated emission in 3 – 4 μm range due to threshold and non-

threshold Auger recombination in HgTe/CdHgTe quantum wells," *Appl. Phys. Lett.*, vol. 117, p. 083103, 2020.

[35] H. Kogelnik and C. V. Shank, "Stimulated emission in a periodic structure," *Appl. Phys. Lett.*, vol. 18, no. 4, pp. 152–154, 1971.

[36] Y. Aoyagi, T. Aoyagi, K. Toyoda, and S. Namba, "Tunable distributed-feedback dye laser," *Appl. Phys. Lett.*, vol. 27, no. 12, pp. 687–688, 1975.

[37] Z. Bor and A. Müller, "Picosecond Distributed Feedback Dye Lasers," *IEEE J. Quantum Electron.*, vol. 22, no. 8, pp. 1524–1533, 1986.

[38] G. M. Gale, P. Ranson, and M. Denariez-Roberge, "Coherent Spectroscopy with a Distributed Feedback Dye Laser," *Appl. Phys. B Photophysics Laser Chem.*, vol. 44, no. 4, pp. 221–223, 1987.

[39] H. Kogelnik and C. V. Shank, "Coupled-wave theory of distributed feedback lasers," *J. Appl. Phys.*, vol. 43, no. 5, pp. 2327–2335, 1972.

[40] M. Sargent, W. Swantner, and J. Thomas, "Theory of a distributed feedback laser," *IEEE J. Quantum Electron.*, vol. 16, no. 4, pp. 465–472, 1980.

[41] I. D. Samuel and G. A. Turnbull, "Organic semiconductor lasers," *Chem. Rev.*, vol. 107, no. 4, pp. 1272–1295, 2007.

[42] J. M. Pietryga, Y. S. Park, J. Lim, A. F. Fidler, W. K. Bae, S. Brovelli, and V. I. Klimov, "Spectroscopic and device aspects of nanocrystal quantum dots," *Chem. Rev.*, vol. 116, no. 18, pp. 10513–10622, 2016.

[43] M. M. Adachi, F. Fan, D. P. Sellan, S. Hoogland, O. Voznyy, A. J. Houtepen, K. D. Parrish, P. Kanjanaboos, J. A. Malen, and E. H. Sargent, "Microsecond-sustained lasing from colloidal quantum dot solids," *Nat. Commun.*, vol. 6, p. 8694, 2015.

[44] A. Yariv, *Quantum Electronics*. John Wiley Sons, 3 ed., 1989.

[45] J. F. Lotspeich, "Explicit General Eigenvalue Solutions for Dielectric Slab Waveguides," *Appl. Opt.*, vol. 14, no. 2, p. 327, 1975.

[46] A. E. Siegman, *Lasers*. Sausalito: University Science Books, 1986.

[47] I. De Leon and P. Berini, "Theory of surface plasmon-polariton amplification in planar structures incorporating dipolar gain media," *Phys. Rev. B*, vol. 78, no. 16, p. 161401, 2008.

[48] I. De Leon and P. Berini, "Amplification of long-range surface plasmons by a dipolar gain medium," *Nat. Photonics*, vol. 4, no. 6, pp. 382–387, 2010.

[49] P. Berini and I. De Leon, "Surface plasmon-polariton amplifiers and lasers," *Nat. Photonics*, vol. 6, no. 1, pp. 16–24, 2012.

[50] P. Bolger, W. Dickson, A. Krasavin, L. Liebscher, S. Hickey, D. Skryabin, and A. Zayats, "Amplified spontaneous emission of surface plasmon polaritons and limitations on the increase of their propagation length," *Opt. Lett.*, vol. 35, no. 8, p. 1197, 2010.

[51] C. Grivas, "Optically pumped planar waveguide lasers, Part I: Fundamentals and fabrication techniques," *Prog. Quantum Electron.*, vol. 35, no. 6, pp. 159–239, 2011.

[52] C. Grivas, "Optically pumped planar waveguide lasers: Part II: Gain media, laser systems, and applications," *Prog. Quantum Electron.*, vol. 45-46, pp. 3–160, 2016.

[53] G. C. Chern and I. Lauks, "Spin-coated amorphous chalcogenide films," *J. Appl. Phys.*, vol. 53, no. 10, pp. 6979–6982, 1982.

[54] G. C. Chern and I. Lauks, "Spin coated amorphous chalcogenide films: Structural characterization," *J. Appl. Phys.*, vol. 54, no. 5, pp. 2701–2705, 1983.

[55] J. Nishii, S. Morimoto, I. Inagawa, R. Iizuka, T. Yamashita, and T. Yamagishi, "Recent advances and trends in chalcogenide glass fiber technology: a review," *J. Non. Cryst. Solids*, vol. 140, no. C, pp. 199–208, 1992.

[56] M. V. Kovalenko, R. D. Schaller, D. Jarzab, M. A. Loi, and D. V. Talapin, "Inorganically functionalized PbS-CdS colloidal nanocrystals: Integration into amorphous chalcogenide glass and luminescent properties," *J. Am. Chem. Soc.*, vol. 134, no. 5, pp. 2457–2460, 2012.

[57] D. N. Dirin, S. Dreyfuss, M. I. Bodnarchuk, G. Nedelcu, P. Papagiorgis, G. Itskos, and M. V. Kovalenko, "Lead halide perovskites and other metal halide complexes as inorganic capping ligands for colloidal nanocrystals," *J. Am. Chem. Soc.*, vol. 136, no. 18, pp. 6550–6553, 2014.

CHAPTER 6

SUMMARY AND CONCLUDING REMARKS

The recent development of HgTe and HgSe colloidal quantum dots covering the entire infrared spectrum opens the door to broad commercial adoption of infrared technologies. Currently limited by excessive costs to military and advanced research applications, infrared detectors and light sources might one day find applications in autonomous vehicles, medical diagnostics, manufacturing, and emissions testing if inexpensive yet high-performing devices are developed. The successful development of mercury chalcogenide quantum dots as competitive infrared materials will depend not only on advances in synthesis and device engineering, but also on the fundamental carrier dynamics and transport properties. In this thesis I have described time-resolved spectroscopic studies of infrared carrier dynamics in HgTe and HgSe quantum dots, and the manner in which these dynamics manifest in devices.

In Chapter 1, I introduced the present state of infrared technologies and the potential improvements afforded by mercury chalcogenide quantum dot devices. Motivated by the connection between basic photophysics and device performance, I reviewed the photophysical phenomenology of infrared systems with emphases on nonradiative mechanisms and their manifestations in quantum dot devices.

Chapter 2 discusses the transient spectroscopy of HgTe quantum dots synthesized following two different protocols. Conspicuously different transient absorption dynamics are observed in partially-aggregated and well-dispersed colloids, attributed to intra-aggregate charge transfer and sub-threshold Auger recombination. Measured biexciton Auger lifetimes in well-dispersed samples are found to be far slower than in bulk materials of similar gaps, in contrast to the conventional notions of Auger enhancement in nanostructures. The Auger lifetimes are rather similar to those in quantum dots with much wider gaps, such as CdSe, supporting the viewpoint that quantum dot Auger recombination may occur through a scattering-assisted mechanism. Yet, the origin and physical interpretation of this scattering remains an open question of great general relevance in the

study of quantum dot Auger processes.

In Chapter 3, I describe a systematic investigation of particle size and doping effects on the steady-state and time-resolved spectroscopy in HgSe quantum dots. In the steady-state, intraband absorption HgSe is consistent with a simple $k \cdot p$ picture at small particle sizes, while larger particles display evidence of surface plasmon resonances and heavy n-doping. The amount of implied doping goes beyond what is easily rationalized in the typical electrostatic model, and this might motivate more detailed investigations of doping mechanisms and plasmonic behavior in mercury chalcogenides. Time-resolved photoluminescence upconversion measurements revealed an absence of measurable Auger recombination in n-type particles while intrinsic particles exhibited typical quantum dot Auger behavior. I attributed this phenomenon to the vastly different density of states available to an Auger-excited hole in the two doping situations. In the single-exciton regime, the nonradiative relaxation is consistent with near-field energy transfer and growth of thick CdS shells lengthens nonradiative lifetimes into the nanosecond regime. Such long mid-infrared lifetimes challenge the results of recent atomistic simulations, leading to important questions about the basic nature of quantum dot electron-vibration coupling. Finally, a careful examination of the intraband lineshape and early-time photoluminescence dynamics revealed spectral and dynamic evidence of $1P_e$ spin-orbit fine structure, including the first observations of direct intersublevel relaxation.

The time-resolved data of Chapter 2 are connected to the upper limits on achievable device performances in Chapter 4. From a simple statistical model, macroscopic thermal generation-recombination rates are calculated from microscopic intraparticle Auger and exciton recombination rates. The quantum dot solid behaves as a bulk homogeneous semiconductor in the regime of fast charge hopping, and the thermodynamic detectivity limits are then easily obtained by applying the principle of detailed balance. The confluence of slow Auger recombination and fast radiative recombination leads to thermodynamic limits which exceed those of bulk HgCdTe by an order of magnitude. In the limit of optimized device design and fabrication, HgTe quantum dot detectors

will therefore be capable of lower noise, higher temperature operation than unbiased HgCdTe photovoltaics. Coupled with the vastly reduced costs associated with quantum dot optoelectronics, this presents a strong fundamental advantage of infrared quantum dots in photodetection applications.

Chapter 5 describes several experiments which are natural outgrowths of those described previously. The proposed projects are fundamental in nature and focus on multiphonon relaxation, homogeneous broadening and magnetic interactions. These studies might constitute foundational contributions to quantum dot science due to the uniquely low energy scales which are accessible in mercury chalcogenide quantum dots, and these measurements will also directly benefit our practical understanding of carrier relaxation and transport in functioning devices.

The past six years have seen tremendous practical and fundamental advances in our understanding of infrared mercury chalcogenide quantum dot behavior. Fast and sensitive photodiodes, band-like transport, conduction fine structure, THz photoresponse, and LEDs have all been discovered or demonstrated during this time, both in Chicago and elsewhere. As infrared quantum dot device engineering continues to improve, the spectroscopy described in this thesis will become increasingly relevant as the ultimate performance limitation and goal. The fundamental motivations for continued spectroscopic studies are equally compelling. Outstanding questions in electron-vibration interactions, many-body dynamics, charging effects and dephasing are all uniquely addressable in mercury chalcogenide quantum dots due to their small energy gaps. These avenues of study directly impact functional devices through their effects on spectra and nonradiative recombination, and they are also important aspects of basic quantum dot photophysics which remain sparsely explored even in conventional wide-gap systems. With the present work as a foundation, future researchers should be well-positioned to tackle these questions and make exciting contributions to our understanding of semiconductor nanostructures.

APPENDIX A

ELECTRONIC STRUCTURE OF NANOCRYSTAL QUANTUM DOTS

A.1 Introduction

This section provides a brief and generalized overview of nanocrystal quantum dot electronic structure. We begin by providing the simplest realistic treatment of the energies and wavefunctions for perfect infinite crystals by solving the $k \cdot p$ equation. The quantum dot particle-in-a-sphere model and envelope function approximation are then introduced, and electron-hole interactions are finally described briefly as simple perturbative corrections.

Good general references on electron bands in solids are the texts by Simon [1] and Ashcroft and Mermin [2], and the introductory yet very insightful works of Hoffmann [3, 4, 5]. More detailed references focusing on semiconductor optical and transport properties of are the texts by Klingshirn [6], Yu and Cardona [7], and Ridley [8]. Various flavors of $k \cdot p$ theory are discussed in several texts [7, 9, 10] and the early papers of Kane [11, 12]. Nice introductory discussions of quantum dot electronic structure have been given by Norris [13] and Brus [14], while more thorough treatments of electronic structure, optics and dynamics may be found in the text by Delerue and Lannoo [15].

A.2 Bulk Crystals: k·p Equation and the Kane Model

In this section we will derive the $k \cdot p$ equation and use it to obtain realistic nonparabolic dispersion relations for the conduction bands of semiconductors. We begin with the Hamiltonian of a single electron of mass m moving in a potential $V(r)$. The Schrodinger equation is

$$\left(\frac{p^2}{2m} + V(r)\right)\psi(r) = E\psi(r) \tag{A.1}$$

and when $V(r)$ is periodic, the wavefunctions are given by Bloch's theorem. In the reduced zone scheme, Bloch's theorem states that the wavefuncions will always take the form

$$\psi_{n,k}(r) = u_{n,k}(r)e^{ik\cdot r} \tag{A.2}$$

The $u_{n,k}(r)$ are known as Bloch or cellular functions and they satisfy the condition $u_{n,k}(r) = u_{n,k}(r+qa)$, where a is the period of $V(r)$ and q is any integer. In the tight-binding picture they can be constructed as symmetry-adapted linear combinations of atomic orbitals. The complex exponential part takes the form of a plane wave of wavelength $\lambda = 2\pi/k$. It is known as the envelope function and at small k depends weakly on r compared to $u(r)$. The basic equation of $k\cdot p$ theory is obtained by substituting the total wavefunction into the Schrodinger equation. We find upon substitution that one can eliminate the complex exponential factors to produce a new Schrodinger equation for the Bloch functions:

$$\left(\frac{p^2}{2m} + \frac{\hbar}{m}k\cdot p + \frac{\hbar^2k^2}{2m} + V(r)\right)u_{n,k} = E_{n,k}\,u_{n,k} \tag{A.3}$$

This is known as the $k\cdot p$ equation. Note that here and throughout this section, p is an operator, $\hbar k$ is the crystal momentum, and $p \neq \hbar k$.

The Hamiltonian in parentheses can be grouped into a free electron-type Hamiltonian H_0 which does not depend on k and a k-dependent crystal Hamiltonian H':

$$H_0 = \frac{p^2}{2m} + V(r) \tag{A.4}$$

$$H' = \frac{\hbar}{m}k\cdot p + \frac{\hbar^2k^2}{2m} \tag{A.5}$$

Physically, H' may be thought of as the potential arising from local interactions between the electron and the lattice, and it ultimately gives rise to the effective mass. When the states of interest are not too far from the Brillouin zone center, H' can be treated with perturbation theory. The presence of both k-linear and k-quadratic terms means that H' would be formally addressed by subsequent

applications of first- and second-order perturbation theory. This approach is most useful when k is small and the basis set is large. An alternative approach is to directly diagonalize $H_0 + H'$. This is known as the Kane model and is especially useful when working analytically in a small basis.

A.2.1 Two bands: eigenvalues

A simple example of $k \cdot p$ theory is the two-band Kane model. In our version we assume the system to be comprised of bands a and b with extrema at $\pm E_g/2$ located at $k = 0$. The total Hamiltonian in the orthonormal basis of zone-center Bloch functions is

$$H = H_0 + H' = \begin{pmatrix} \langle u_{a,0}|H_0|u_{a,0}\rangle & \langle u_{a,0}|H_0|u_{b,0}\rangle \\ \langle u_{b,0}|H_0|u_{a,0}\rangle & \langle u_{b,0}|H_0|u_{b,0}\rangle \end{pmatrix} + \begin{pmatrix} \langle u_{a,0}|H'|u_{a,0}\rangle & \langle u_{a,0}|H'|u_{b,0}\rangle \\ \langle u_{b,0}|H'|u_{a,0}\rangle & \langle u_{b,0}|H'|u_{b,0}\rangle \end{pmatrix} \tag{A.6}$$

$$= \begin{pmatrix} \frac{E_g}{2} & 0 \\ 0 & -\frac{E_g}{2} \end{pmatrix} + \begin{pmatrix} \langle u_{a,0}|H'|u_{a,0}\rangle & \langle u_{a,0}|H'|u_{b,0}\rangle \\ \langle u_{b,0}|H'|u_{a,0}\rangle & \langle u_{b,0}|H'|u_{b,0}\rangle \end{pmatrix} \tag{A.7}$$

The energies $\pm E_g/2$ may be physically interpreted as those of the atomic-like $u_{a,0}$ and $u_{b,0}$ in a hypothetical crystal made of noninteracting atoms. To obtain the total energies at $k \neq 0$ we must determine the matrix elements of H'. Working for simplicity in 1D so that $r \to x$ and $p = -i\hbar\frac{d}{dx}$, we have for the diagonal elements

$$\begin{aligned} \langle u_{a,0}|H'|u_{a,0}\rangle = \langle u_{b,0}|H'|u_{b,0}\rangle &= \frac{\hbar}{m}k\langle u_{b,0}|p|u_{b,0}\rangle + \langle u_{b,0}|u_{b,0}\rangle\frac{\hbar^2k^2}{2m} \\ &= -i\frac{\hbar^2}{m}k\langle u_{b,0}|\frac{d}{dx}|u_{b,0}\rangle + \frac{\hbar^2k^2}{2m} \\ &= \frac{\hbar^2k^2}{2m} \end{aligned} \tag{A.8}$$

Note that we have taken $|\frac{d}{dx}u_{b,0}\rangle$ and $|u_{b,0}\rangle$ to be orthogonal. This is the case for crystals in which the unit cell possesses inversion symmetry or, as assumed here, when $k = 0$ corresponds to an energy extremum. One can equivalently say that within $k \cdot p$ theory, the above conditions cause the

energy correction to vanish at first order. For the off-diagonal elements we have

$$\begin{aligned}\langle u_{a,0}|H'|u_{b,0}\rangle = \langle u_{b,0}|H'|u_{a,0}\rangle &= \frac{\hbar k}{m}\langle u_{b,0}|p|u_{a,0}\rangle \\ &= \frac{\hbar}{m}kP \end{aligned} \tag{A.9}$$

where we have defined $P = -i\langle u_{b,0}|p|u_{a,0}\rangle$. P has units of momentum and its magnitude quantifies the coupling strength between the zone-center Bloch functions. Typically in II-VI and III-V semiconductors, the relevant Bloch functions are s orbital-like for the cation and p orbital-like for the anion.

To obtain the energies E we diagonalize the total Hamiltonian matrix

$$H = \begin{pmatrix} \frac{E_g}{2} + \frac{\hbar^2 k^2}{2m} & \frac{\hbar}{m}kP \\ \frac{\hbar}{m}kP & -\frac{E_g}{2} + \frac{\hbar^2 k^2}{2m} \end{pmatrix} \tag{A.10}$$

by solving the determinental equation

$$\begin{vmatrix} \frac{E_g}{2} + \frac{\hbar^2 k^2}{2m} - E & \frac{\hbar}{m}kP \\ \frac{\hbar}{m}kP & -\frac{E_g}{2} + \frac{\hbar^2 k^2}{2m} - E \end{vmatrix} = 0 \tag{A.11}$$

The energies are therefore

$$\begin{aligned} E &= \frac{\hbar^2 k^2}{2m} \pm \sqrt{\left(\frac{E_g}{2}\right)^2 + \left(\frac{\hbar k P}{m}\right)^2} \\ &= \frac{\hbar^2 k^2}{2m} \pm \sqrt{\left(\frac{E_g}{2}\right)^2 + \frac{\hbar^2 k^2}{2m}E_p} \end{aligned} \tag{A.12}$$

where in the second line we have expressed the coupling through the so-called Kane parameter or Kane energy E_p. This avoids potential confusion related to other definitions of P such as $P = -i\frac{\hbar}{m}\langle u_{a,0}|p|u_{b,0}\rangle$ and $P = -\frac{i}{m}\langle u_{a,0}|p|u_{b,0}\rangle$ which are frequently encountered in the literature; equations written in terms of E_p are unaffected by such differences. Shown below are examples of

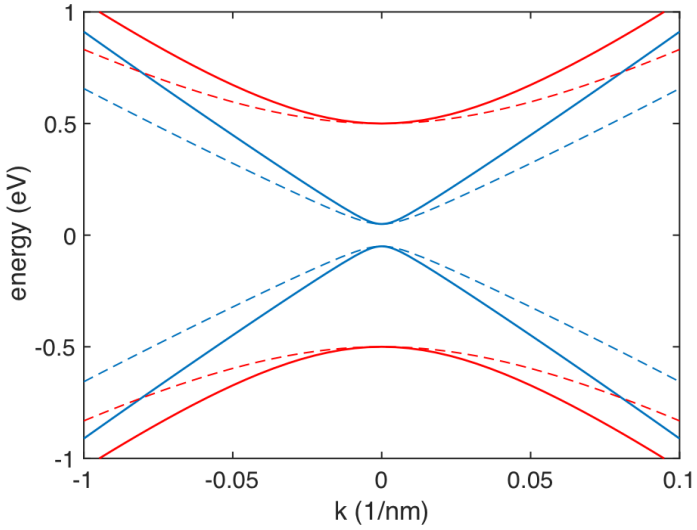

Figure A.1: Dispersion given by the two-band $k \cdot p$ model for energy gaps of 0.1 eV (blue) and 1 eV (red), and Kane parameters of 10 eV (dashed) and 20 eV (solid).

dispersion relations predicted by the two-band $k \cdot p$ model.

The upper branch represents the conduction band and the lower branch represents the light hole band. As shown above, the two major outcomes of the $k \cdot p$ terms are to make both dispersion relations asymptotically linear and to invert the curvature of the lower band, relative to the free-electron result. Although deviation from parabolic behavior at $k \neq 0$ is particularly prominent in small-gap systems, quantitative calculations usually require nonparabolicity to be accounted for even at moderate wavevectors.

A.2.2 Two bands: effective masses

It is useful to consider the effective mass in the context of $k \cdot p$ theory. In general, the effective mass m^* of a charge carrier is defined as

$$\frac{1}{m^*} = \frac{1}{\hbar^2}\left(\frac{d^2E}{dk^2}\right) \tag{A.13}$$

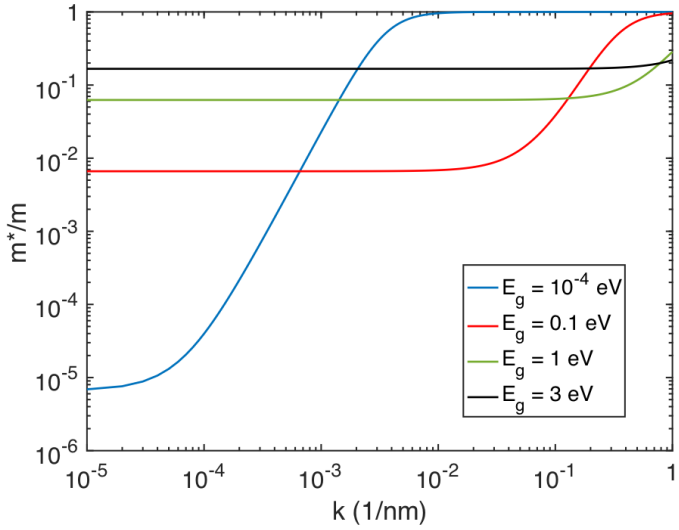

Figure A.2: $k-$dependent effective masses given by the two-band $k \cdot p$ model.

If $E(k)$ is the upper (electron) energy branch, for example, then the electron effective mass is

$$\frac{1}{m^*(k)} = \frac{1}{m} + \frac{E_g^2 E_p}{8m}\left(\frac{E_g^2}{4} + \frac{\hbar^2 k^2}{2m}E_p\right)^{-3/2} \tag{A.14}$$

From this expression we see that for fixed material parameters E_g and E_p, the effective mass increases with increasing k. This reflects the increasing deviation of the Kane dispersion from the quadratic dispersion associated with a k-invariant m^*. We also find that the physical origin of $m^* \neq m$ is the coupling between Bloch functions. This can be seen by considering the limits $E_g \to \infty$ or $E_p \to 0$ and is more obvious in the expression for the zone-center effective mass:

$$\frac{1}{m^*(0)} = \frac{1}{m}\left(1 + \frac{E_p}{E_g}\right) \tag{A.15}$$

Both limits produce vanishing coupling and m^* consequently approaches m. In the opposite limit, we see that small-gap systems will typically display small zone-center effective masses and rapid effective mass variations with k. This behavior is illustrated below, and is indeed observed in nearly every semiconductor system.

A.2.3 Two bands: eigenvectors

The theory developed above also gives the Bloch functions in perturbed and exact forms. We will first examine the perturbative solution. For a system of two unperturbed states $|n^{(0)}\rangle$ and $|m^{(0)}\rangle$, the first-order wavefunction correction $|n^{(1)}\rangle$ due to a small perturbation V is generically

$$|n^{(1)}\rangle = \frac{\langle m^{(0)}|V|n^{(0)}\rangle}{E_n^{(0)} - E_m^{(0)}}|m^{(0)}\rangle \tag{A.16}$$

In our two-band $k \cdot p$ theory, one may take $V = \hbar k p/m$ so that the (non-normalized) Bloch functions are

$$\begin{aligned} |u_{a(b),k}\rangle &= |u_{a(b),0}\rangle + \frac{\hbar k P}{E_g m}|u_{b(a),0}\rangle \\ &= |u_{a(b),0}\rangle + \frac{\hbar k}{E_g}\sqrt{\frac{E_p}{2m}}|u_{b(a),0}\rangle \end{aligned} \tag{A.17}$$

Even at a moderate wavevector of 1 nm^{-1}, this first order wavefunction correction remains truly perturbative only for large values E_g, and small E_p and/or k. The above formulation will therefore only be useful very close to the zone center. Pertrubative treatments are more widely useful when the basis is larger, and in such cases the wavefunction is obtained by summing over many different states $|m^{(0)}\rangle$ so that the expansion converges. The perturbation approach is the one most commonly shown in general solid state physics textbooks, and it has been popular historically because it guarantees an analytical expression.

The other approach is to directly obtain the eigenvectors from the Hamiltonian matrix. Although analytical solutions are not guaranteed for an arbitrary basis size, they are simple to obtain in a two-state basis. Writing the wavefunctions as, for example,

$$|u_{a,k}\rangle = c_1|u_{a,0}\rangle + c_2|u_{b,0}\rangle \tag{A.18}$$

we must solve a matrix equation of the form

$$\begin{pmatrix} \frac{E_g}{2} + \frac{\hbar^2 k^2}{2m} & \frac{\hbar}{m} kP \\ \frac{\hbar}{m} kP & -\frac{E_g}{2} + \frac{\hbar^2 k^2}{2m} \end{pmatrix} \begin{pmatrix} c_1 \\ c_2 \end{pmatrix} = E \begin{pmatrix} c_1 \\ c_2 \end{pmatrix} \tag{A.19}$$

where E is an eigenvalue calculated previously (A.12). Choosing $c_2 = 1$ as an arbitrary constant, this gives

$$c_1 = \frac{m\left(E - \frac{\hbar^2 k^2}{2m} + \frac{E_g}{2}\right)}{\hbar k P} \times \frac{1}{N} \tag{A.20}$$

where $N^2 = c_1^2 + c_2^2$ is a normalization factor. In the limit of large k, $c_1 \to 1$ so that the wavefunction has equal contributions from both basis states. $c_1 \to 0$ as k approaches 0, and the wavefunction is pure at the zone center.

Overall, $k \cdot p$ models are very useful because the input parameters E_p and E_g can be determined from experiments. From these two parameters one obtains improved dispersion relations and $k-$dependent wavefunctions from which many important properties can be calculated. E_p is typically around 20 eV for most II-VI and III-V semiconductors, and closer to 10 eV for systems with very small gaps and stronger coupling to bands not considered in the two-band model. It is much smaller, about 3 eV, in IV-VI systems such as PbSe. Although precise experimental determination of E_p can be challenging, its error is rarely more than about 30 %, corresponding to about 15 % error in energies and wavefunction mixing. It can alternatively be determined by fitting an accurate *ab initio* band structure, if one exists, but in the end it is often simply treated as an adjustable parameter.

A.2.4 Eight bands: eigenvalues

The two-band Kane model is a good description of the conduction band and optical absorption in most semiconductors, but it neither captures the most important features of the valence band nor their effects on the conduction band. This is typically done using six- and eight-band models

which include spin. The main complications compared to the two-band case arise in the evaluation of the matrix elements and in the choice of a convenient basis. This is assuaged with the aid of group theory, and here we assume the Γ point of the diamond/zincblende crystal structure with tetrahedral symmetry. The six-band model treats interactions within the valence band and the eight-band model adds the effects of a coupled conduction band.

Our starting point remains the $k \cdot p$ equation but we now include spin-orbit coupling in the underlying Hamiltonian. This introduces a pair of spin-orbit terms H_{so} to the $k \cdot p$ Hamiltonian:

$$H_{so} = \frac{\hbar}{(2mc)^2}((\sigma \times \nabla V) \cdot p + (\sigma \times \nabla V) \cdot k) \tag{A.21}$$

Here c is the vacuum speed of light and σ is a vector of Pauli spin matrices. The first term in H_{so} is the atom-like spin-orbit coupling and the second term is the spin-orbit coupling involving crystal momentum. We will ignore the latter because crystal momentum is usually very small compared to the orbital momentum in core levels where atomic spin-orbit coupling is strongest. We therefore wish to diagonalize the Hamiltonian

$$H = \frac{p^2}{2m} + V(r) + \frac{\hbar}{m}k \cdot p + \frac{\hbar^2 k^2}{2m} + \frac{\hbar}{(2mc)^2}(\sigma \times \nabla V) \cdot p \tag{A.22}$$

in a basis of Bloch functions. The Bloch functions will be constructed from the spatial functions $|S\rangle, |X\rangle, |Y\rangle$ and $|Z\rangle$. The S designation indicates that this function has the symmetry properties of s atomic orbitals under operations of the tetrahedral group. Likewise, the other designations indicate that those functions transform like $p_{x,y,z}$ atomic orbitals. $|S\rangle$ is typically associated with the conduction band and the others are associated with the valence band.

To address the spin-orbit interaction, it is first convenient to rewrite the vector part of H_{so} as $(\sigma \times \nabla V) \cdot p = (\nabla V \times p) \cdot \sigma$. One can then show that the only nonzero matrix elements of H_{so} will be those involving $\langle X|(\nabla V \times p)_z|Y\rangle$ and its permutations because $(\nabla V \times p)$ is an axial vector. This

is the foundation for the quantity Δ, which is defined as

$$\begin{aligned}\Delta &= i\frac{3\hbar}{(2mc)^2}\langle X|\frac{\partial V}{\partial x}p_y - \frac{\partial V}{\partial y}p_x|Y\rangle \\ &= i\frac{3\hbar}{(2mc)^2}\langle Y|\frac{\partial V}{\partial y}p_z - \frac{\partial V}{\partial z}p_y|Z\rangle \\ &= i\frac{3\hbar}{(2mc)^2}\langle Z|\frac{\partial V}{\partial z}p_x - \frac{\partial V}{\partial x}p_z|X\rangle \end{aligned} \tag{A.23}$$

It quantifies the spin-orbit splitting between bands at the zone center. To proceed further, we must now construct the Bloch basis functions. There are two general approaches to the choice of basis - the $|jm_j\rangle$ basis and the $|ls\rangle$ basis. The former are the eigenfunctions of H_{so} and the conserved quantities are the total angular momentum j and its z projection m_j. The Hamiltonian is somewhat simplified in this basis. The $|ls\rangle$ basis is essentially comprised of atomic orbitals in which orbital angular momentum l and spin angular momentum s are conserved. Although H_{so} is not diagonal in this representation, $|ls\rangle$ highlights more clearly the physical effects of the $k \cdot p$ and Δ terms. We will work in this basis here and show how the $|jm_j\rangle$ basis arises naturally from the solutions. Both approaches give the same results up to a phase factor.

It is customary to write the $|ls\rangle$ basis states as $|iS\ \downarrow\rangle$, $|\frac{1}{\sqrt{2}}(X - iY)\ \uparrow\rangle$, $|Z\ \downarrow\rangle$, $|\frac{1}{\sqrt{2}}(X + iY)\ \uparrow\rangle$, $|iS\ \uparrow\rangle$, $|\frac{1}{\sqrt{2}}(-X - iY)\ \downarrow\rangle$, $|Z\ \uparrow\rangle$ and $|\frac{1}{\sqrt{2}}(X - iY)\ \downarrow\rangle$. The first set of four are orthogonal to the second set of four due to the spin component. The matrix elements of H_{so} are calculated, for example, as

$$\begin{aligned}\langle (X + iY)\uparrow |H_{so}|(X + iY)\uparrow\rangle &= \frac{\hbar}{2(2mc)^2}\langle (X + iY)\uparrow |(\nabla V \times p)\cdot\sigma|(X + iY)\uparrow\rangle \\ &= \frac{i\hbar}{(2mc)^2}\langle X|(\nabla V \times p)_z|Y\rangle \cdot \langle\uparrow |\sigma|\uparrow\rangle \\ &= \frac{\Delta}{3}\end{aligned} \tag{A.24}$$

and the original $k \cdot p$ matrix elements are calculated as described in the two-band treatment. By symmetry, they obey

$$P = -i\langle S|p_x|X\rangle = -i\langle S|p_y|Y\rangle = -i\langle S|p_z|Z\rangle \tag{A.25}$$

Taking the basis state ordering listed above, the total Hamiltonian takes the block-diagonal form

$$H = \begin{pmatrix} \mathcal{M} & 0 \\ 0 & \mathcal{M} \end{pmatrix} \tag{A.26}$$

with

$$\mathcal{M} = \begin{pmatrix} E_s + \varepsilon & 0 & \frac{\hbar}{m}kP & 0 \\ 0 & E_{xyz} - \frac{\Delta}{3} + \varepsilon & \frac{\Delta\sqrt{2}}{3} & 0 \\ \frac{\hbar}{m}kP & \frac{\Delta\sqrt{2}}{3} & E_{xyz} + \varepsilon & 0 \\ 0 & 0 & 0 & E_{xyz} + \frac{\Delta}{3} + \varepsilon \end{pmatrix} \tag{A.27}$$

and $\varepsilon = \hbar^2 k^2/2m$. The energies E_s and E_{xyz} are the energies of the basis states at the zone center. By inspection we can already see that spin-orbit coupling narrows the energy gap by $\Delta/3$ and also splits the $p-$like states at the zone center. We can also see that only certain states will couple to produce nonparabolic bands due to the presence or absence of terms involving P. In writing the matrix M we have taken k to be in the z direction. If k lies along another direction, M may still be written in the form above if the basis states are rotated appropriately. We may diagonalize H using the method of minors and co-factors, so that the secular equations are

$$0 = E_{xyz} + \frac{\Delta}{3} - E + \varepsilon \tag{A.28}$$

and

$$\begin{aligned} 0 = (E_s - E + \varepsilon)\left(E_{xyz} - \frac{\Delta}{3} - E + \varepsilon\right)\left(E_{xyz} - E + \varepsilon\right) - (E_s - E + \varepsilon)\left(\frac{\Delta\sqrt{2}}{3}\right)^2 \\ - \left(\frac{\hbar}{m}kP\right)^2\left(E_{xyz} - \frac{2\Delta}{3} - E + \varepsilon\right) \end{aligned} \tag{A.29}$$

Although these equations give a total of four double roots without convenient closed forms, analytical solutions do exist for certain limiting cases. Near the zone center the parabolic approxi-

mation is valid, and these solutions are obtained by only retaining terms to order k^2. This gives

$$\begin{aligned}
E_{hh} &= \frac{\hbar^2 k^2}{2m} \\
E_c &= E_g + \frac{\hbar^2 k^2}{2m}\left(1 + \frac{2E_p}{3E_g} + \frac{E_p}{E_g + \Delta}\right) \\
E_{lh} &= \frac{\hbar^2 k^2}{2m}\left(1 - \frac{2E_p}{3E_g}\right) \\
E_{so} &= -\Delta + \frac{\hbar^2 k^2}{2m}\left(1 - \frac{E_p}{3(E_g + \Delta)}\right)
\end{aligned} \tag{A.30}$$

These are the heavy hole, conduction, light hole and spin-orbit split-off bands. The relation $2P^2/m = E_p$ has again been employed, and we have taken $E_s = E_g$ and $E_{xyz} = -\Delta/3$ so that E_g corresponds to the "observed" energy gap. Note that because the state $|(X \pm iY)/\sqrt{2}\rangle$ does not couple to others at this level of theory (see the fourth row/column of $\mathcal{M}$), the resulting heavy hole band retains free electron curvature. It is straightforward to obtain the zone-center effective masses from the above expressions. One interesting outcome of the eight-band model is that the mirror symmetry of the conduction and light hole bands seen in the two-band case is no longer present. One has $m_c^* < |m_{lh}^*|$ when $E_g + \Delta > 1$, a condition which is satisfied in typical semiconductors.

Another set of analytical solutions exists in the limit $\Delta \gg \hbar k P/m = \sqrt{\hbar^2 k^2 E_p/2m}$. They are

$$\begin{aligned}
E_{hh} &= \frac{\hbar^2 k^2}{2m} \\
E_c &= \frac{E_g}{2} + \frac{\hbar^2 k^2}{2m} + \frac{1}{2}\sqrt{E_g^2 + \frac{8}{3}\left(\frac{\hbar^2 k^2}{2m}E_p\right)} \\
E_{lh} &= \frac{E_g}{2} + \frac{\hbar^2 k^2}{2m} - \frac{1}{2}\sqrt{E_g^2 + \frac{8}{3}\left(\frac{\hbar^2 k^2}{2m}E_p\right)} \\
E_{so} &= -\Delta + \frac{\hbar^2 k^2}{2m}\left(1 - \frac{E_p}{3(E_g + \Delta)}\right)
\end{aligned} \tag{A.31}$$

These equations show the nonparabolicity present in the conduction and light-hole bands, as seen earlier in the two-band model. The magnitude of the nonparabolicity is modified compared to the

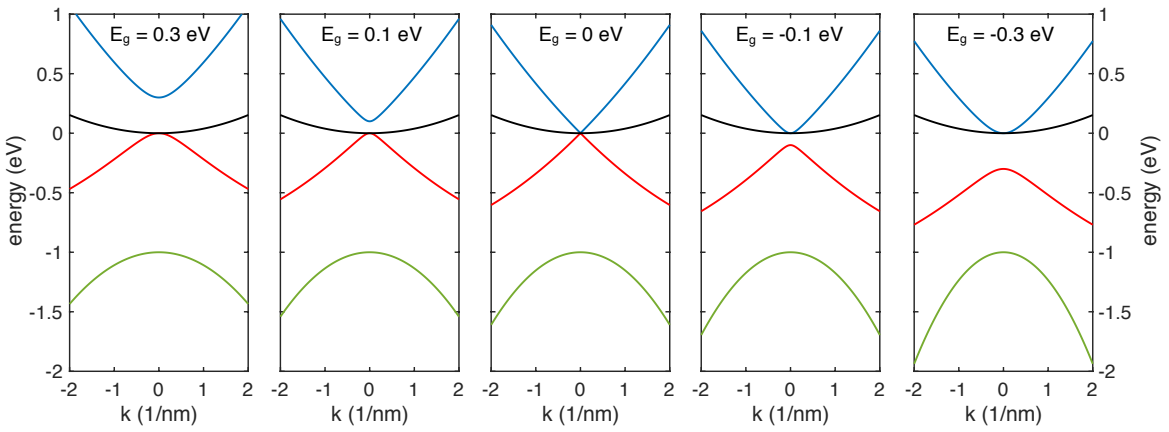

Figure A.3: Band structures given by the eight-band $k \cdot p$ model in the limit $\Delta \gg \hbar kP/m$ using $\Delta = 1$ eV and $E_p = 15$ eV. Blue is the conduction band, black is the heavy hole band, red is the light hole band, and green is the spin-orbit split-off band.

earlier model, however, due to interactions between valence bands. The spin-orbit split-off band exhibits parabolic behavior. Although the heavy hole band still exhibits the wrong curvature, the other dispersion relations are reasonably accurate. The band structure given by these equations is shown below.

The eight-band model nicely illustrates the meaning of a "negative" energy gap. This terminology refers to the situation $E_s < E_{xyz}$ which, according to notational convention, results in $E_g < 0$. A negative gap of any magnitude causes the heavy hole and conduction bands to become degenerate at the zone center, while the light-hole splits from the heavy hole by the amount E_g. As described below, the character of the wavefunctions also changes so that instead of having a $p-$like zone center light hole and $s-$like zone center conduction band, the situation is reversed. This is known as an "inverted" band structure and occurs in systems such as HgTe, HgSe and α-Sn. It is interesting to note that in the HgCdTe alloys, one can tune the gap so that it is exactly zero. The conduction and light hole bands are both degenerate at the zone center and also display linear dispersion. This situation resembles that of the famous Dirac dispersion in graphene and such electrons are sometimes known as "massless Kane electrons." This behavior is shown above and can also be seen in the vanishingly small effective mass as E_g approaches 0, plotted earlier for

two bands.

The issue of the heavy hole band is resolved at a higher level of theory than discussed here. It gives the dispersion in the spherical approximation as

$$E_{hh} = \frac{\hbar^2 k^2}{2m} + Mk^2 \tag{A.32}$$

where

$$M = \frac{\hbar^2}{m^2} \sum_n^{\Gamma_{15}} \frac{|\langle X|p_y|n\rangle|^2}{E_{xyz} - E_n} + \frac{\hbar^2}{m^2} \sum_n^{\Gamma_{25'}} \frac{|\langle X|p_y|n\rangle|^2}{E_{xyz} - E_n} \tag{A.33}$$

The notation Γ_{15} denotes that the sum is over states belonging to the Γ_{15} representation of the tetrahedral group, and the same applies to $\Gamma_{25'}$. The former is the symmetry group of the p orbitals at the Γ point and the basis functions, as implied by the above developments, are x, y and z. Γ_{25} is the symmetry group of d orbitals at Γ with basis $z(x^2 - y^2)$, and the prime specifically denotes the states which transform like d_{xy}, d_{yz} and d_{zx}. The sums run over all states excluding those already considered. Note that if no states of Γ_{15} or $\Gamma_{25'}$ symmetry are used in the calculation, $M = 0$ and the free electron result is obtained. Stronger coupling to remote p and d states corresponds to more negative values of M and lighter effective masses. It is difficult in practice to calculate M from wavefunctions and it is usually deduced from experimental data instead. Typical values are around $-0.5m$.

A.2.5 Eight bands: eigenvectors

In a manner analogous to the earlier two-band model, the perturbed wavefunctions for the conduction, light hole and split-off hole are linear combinations of the basis functions. As already seen,

the heavy hole remains unperturbed and therefore keeps its original character. We therefore have

$$
\begin{aligned}
|u_{n\alpha}\rangle &= a_n|iS\ \downarrow\rangle + b_n|\frac{1}{\sqrt{2}}(X - iY)\ \uparrow\rangle + c_n|Z\ \downarrow\rangle \\
|u_{n\beta}\rangle &= a_n|iS\ \uparrow\rangle + b_n|\frac{1}{\sqrt{2}}(-X - iY)\ \downarrow\rangle + c_n|Z\ \uparrow\rangle \\
|u_{hh\alpha}\rangle &= |\frac{1}{\sqrt{2}}(X + iY)\ \uparrow\rangle \\
|u_{hh\beta}\rangle &= |\frac{1}{\sqrt{2}}(X - iY)\ \downarrow\rangle
\end{aligned}
\tag{A.34}
$$

with n denoting the conduction, light hole and split-off bands, and the α/β designation denoting the total spin character. The coefficients are obtained by solving the equation

$$
\begin{pmatrix}
E_s + \varepsilon & 0 & \frac{\hbar}{m}kP \\
0 & E_{xyz} - \frac{\Delta}{3} + \varepsilon & \frac{\Delta\sqrt{2}}{3} \\
\frac{\hbar}{m}kP & \frac{\Delta\sqrt{2}}{3} & -\frac{\Delta}{3} + \varepsilon
\end{pmatrix}
\begin{pmatrix} a_n \\ b_n \\ c_n \end{pmatrix}
= E_n
\begin{pmatrix} a_n \\ b_n \\ c_n \end{pmatrix}
\tag{A.35}
$$

Again substituting $E_s = E_g$, $E_{xyz} = -\Delta/3$ and $2P^2/m = E_p$ we find

$$
\begin{aligned}
a_n &= \hbar k\sqrt{\frac{E_p}{2m}}\left(E_n - \frac{\hbar^2k^2}{2m} + \frac{2\Delta}{3}\right)\frac{1}{N} \\
b_n &= \frac{\sqrt{2}}{3}\Delta\left(E_n - \frac{\hbar^2k^2}{2m} - E_g\right)\frac{1}{N} \\
c_n &= \left(E_n - \frac{\hbar^2k^2}{2m} - E_g\right)\left(E_n - \frac{\hbar^2k^2}{2m} + \frac{2\Delta}{3}\right)\frac{1}{N}
\end{aligned}
\tag{A.36}
$$

where N is a normalization constant. In the small-k limit the coefficients are

$$\begin{aligned}
&a_c = 1, b_c = c_c = 0 \\
&a_{lh} = 0, b_{lh} = \frac{1}{\sqrt{3}}, c_{lh} = \sqrt{\frac{2}{3}} \\
&a_{so} = 0, b_{so} = \sqrt{\frac{2}{3}}, c_{so} = -\frac{1}{\sqrt{3}}
\end{aligned} \tag{A.37}$$

These small-k coefficients also define the $|jm_j\rangle$ basis because we diagonalized H_{so} in the process of diagonalizing H. These basis states are

$$\begin{aligned}
\left|\frac{1}{2} \quad -\frac{1}{2}\right\rangle &= |u_{c\alpha}\rangle = |iS\ \downarrow\rangle \\
\left|\frac{1}{2} \quad \frac{1}{2}\right\rangle &= |u_{c\beta}\rangle = |iS\ \uparrow\rangle \\
\left|\frac{3}{2} \quad \frac{3}{2}\right\rangle &= |u_{hh\alpha}\rangle = \frac{1}{\sqrt{2}}|(X - iY)\uparrow\rangle \\
\left|\frac{3}{2} \quad \frac{1}{2}\right\rangle &= |u_{lh\beta}\rangle = -\frac{1}{\sqrt{6}}|(X + iY)\downarrow\rangle + \sqrt{\frac{2}{3}}|Z\uparrow\rangle \\
\left|\frac{3}{2} -\frac{1}{2}\right\rangle &= |u_{lh\alpha}\rangle = \frac{1}{\sqrt{6}}|(X - iY)\uparrow\rangle + \sqrt{\frac{2}{3}}|Z\downarrow\rangle \\
\left|\frac{3}{2} -\frac{3}{2}\right\rangle &= |u_{hh\beta}\rangle = \frac{1}{\sqrt{2}}|(-X - iY)\downarrow\rangle \\
\left|\frac{1}{2} \quad \frac{1}{2}\right\rangle &= |u_{so\beta}\rangle = -\frac{1}{\sqrt{3}}|(X + iY)\downarrow\rangle + \frac{1}{\sqrt{3}}|Z\uparrow\rangle \\
\left|\frac{1}{2} -\frac{1}{2}\right\rangle &= |u_{so\alpha}\rangle = \frac{1}{\sqrt{3}}|(X - iY)\uparrow\rangle - \frac{1}{\sqrt{3}}|Z\downarrow\rangle
\end{aligned} \tag{A.38}$$

and they serve as a starting point for more sophisticated $k \cdot p$ treatments. Such calculations address effects such as spin-splitting, correct heavy hole effective masses, and k-linear energy corrections.

A.3 Nanocrystals

A simple model of the electronic structure of a nanocrystal quantum dot is the "particle-in-a-sphere" model. In it we suppose we can map the problem onto that of a free particle confined in an infinitely-deep spherical potential of radius R. This is a reasonable description of the plane-wave envelope function when its natural wavelength is very long compared to R, as is the case when k is small. We further suppose that due to the very local nature of the Bloch functions, to a good approximation they remain unaffected by the boundary conditions.

A.3.1 Particle-in-a-sphere model

A result from quantum mechanics is that the energy eigenfunctions of a particle moving in a spherically-symmetric potential $V(r)$ can always be written in the form $\psi(r,\theta,\phi) = \chi_l(r)Y_{m,l}(\theta,\phi)$ where $Y_{m,l}(\theta,\phi)$ are the spherical harmonics and the $\chi_l(r)$ are radial wavefunctions which depend on the particular form of $V(r)$. For a particle or particle pair of reduced mass μ, the radial Schrodinger equation is generically

$$\left(\frac{\hbar^2}{2\mu}\left(\frac{d^2}{dr^2}+\frac{2d}{rdr}\right)+\frac{l(l+1)\hbar^2}{2\mu r^2}+V(r)\right)\chi_l(r) = E\chi_l(r) \tag{A.39}$$

In the particle-in-a-sphere model the potential is of the form

$$V(r) = \begin{cases} 0 & r < R \\ \infty & r > R \end{cases} \tag{A.40}$$

and the Schrodinger equation becomes

$$\frac{d^2\chi}{dr^2}+\frac{2d\chi}{rdr}-\frac{l(l+1)}{r^2}\chi+k^2\chi = 0 \tag{A.41}$$

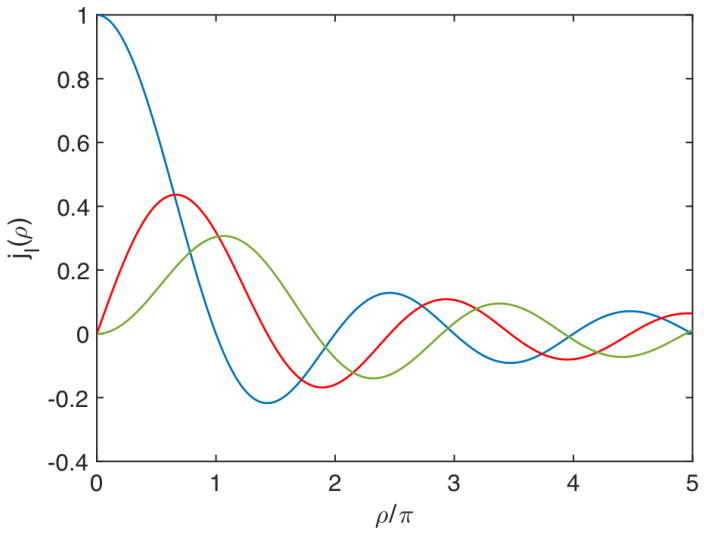

Figure A.4: Plots of spherical Bessel functions j_0 (blue), j_1 (red) and j_2 (green).

where we have utilized the free-particle wavevector $k = \sqrt{2\mu E/\hbar^2}$. If we recast the above equation in terms of a new dimensionless variable $\rho = kr$, it may be rearranged as

$$\frac{d^2\chi}{d\rho^2} + \frac{2d\chi}{\rho d\rho} + \left(1 - \frac{l(l+1)}{\rho^2}\right) = 0 \tag{A.42}$$

Equations of this form are known as spherical Bessel equations and they arise whenever plane waves are expressed in spherical coordinates. There are two classes of solution - the spherical Bessel functions which are regular at the origin, and the spherical Neumann functions which are irregular at the origin. We can eliminate the Neumann functions on physical grounds. The spherical Bessel functions $j_l(\rho)$ are given by

$$j_l(\rho) = (-\rho)^l \left(\frac{d}{\rho d\rho}\right)^l \left(\frac{\sin(\rho)}{\rho}\right) \tag{A.43}$$

and the first few are plotted above.

The wavefunctions $\chi_l(r)$ must satisfy the boundary condition $r\chi_l(r) = 0$ when $r = 0$ and $r \geq R$. The first constraint is automatically satisfied because we have chosen functions which are regular

at the origin. The second condition is satisfied when $\rho = kr$ is a root of $j_l(\rho)$. Indicating the roots as $\rho_{n,l}$, the allowed values of k are then given by

$$k_{n,l} = \frac{\rho_{n,l}}{R} \tag{A.44}$$

When $l = 0$, for example, the roots are obtained by solving

$$j_0(\rho) = \frac{\sin(\rho)}{\rho} = 0 \tag{A.45}$$

which gives $\rho_{n,0} = n\pi$ with $n = 1, 2, 3, ...$ Following the convention for atomic systems, n is known as the principal quantum number (1, 2, 3,...) and l is known as the orbital angular momentum quantum number (*S, P, D,...*) so that the radial wavefunctions are denoted $1S$, $1P$, $1D$, $2S$ etc. The $1S$ radial wavefunction is

$$\chi_{1S}(r) = N\frac{\sin(\pi r/R)}{\pi r/R} \tag{A.46}$$

where N is a normalization constant, and the total $1S$ particle-in-a-sphere wavefunction is

$$\psi_{1S}(r, \theta, \phi) = \chi_{1S}(r)Y_{m,l}(\theta, \phi) \tag{A.47}$$

The first few radial wavefunctions are plotted below. The energies are obtained by substitution of the now-quantized k into the free particle dispersion relation:

$$E_{n,l} = \frac{\hbar^2 k_{n,l}^2}{2\mu} \tag{A.48}$$

When the sphere is comprised of semiconductor, one would use effective masses to calculate μ in the above equation. For a single electron or hole, the kinetic energy given above is known as the confinement energy because it quantifies the additional energy imposed by quantum confinement. Although the particle-in-a-sphere model assumes parabolic dispersion *i.e.* decoupled m^* and k, we

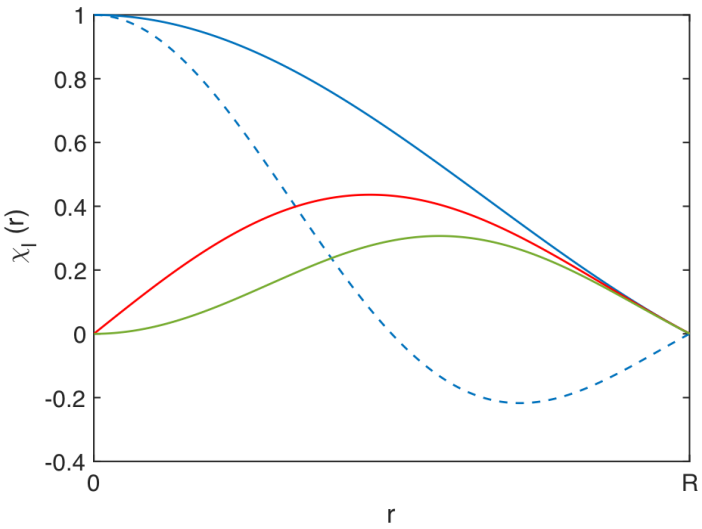

Figure A.5: Plots of unnormalized radial wavefunctions 1S (blue), 1P (red), 1D (green) and 2S (blue dash).

can obtain more accurate quantized energies by using $k_{n,l}$ with a more sophisticated dispersion such as that obtained from $k \cdot p$. In the context of excitons, discussed further in a following subsection, employing the exciton reduced mass is appropriate only when the binding energy is large compared to the confinement energy of the lighter carrier. If the confinement energy is much larger than the binding energy, then it is more appropriate to treat the electron and hole as independent particles confined to the spherical potential and the excitonic binding as a perturbation.

A.3.2 Envelope function approximation

In the envelope function approximation for semiconductor nanostructures, one supposes that the plane-wave envelope function in the wavefunction for an infinite crystal can be replaced by one that matches the boundary conditions of the nanostructure. When the nanocrystal diameter is much larger than the crystal lattice constant, the nanocrystal wavefunctions can be written in the basis of

infinite crystal wavefunctions as

$$\psi_n(r) = \sum_k c_{n,k} u_{n,k}(r) e^{ikr} \tag{A.49}$$

where the $c_{n,k}$ are expansion coefficients. In this section we are working in Cartesian coordinates so that r is the Cartesian vector $x\hat{i} + y\hat{j} + z\hat{k}$, and the spherical radial coordinate is denoted r_s.

For the particular case of spherical quantum dots, we wish to replace the plane wave envelope of the bulk crystal with spherical Bessel functions. Since the spherical Bessel functions can be expressed in the basis of plane waves e^{ikr}, we may write without loss of generality

$$\chi_n(r) = \sum_k c_{n,k} e^{ikr} \tag{A.50}$$

As long as the $u_{n,k}(r)$ have a weak dependence on k in the vicinity of some reference wavevector k_0, by substitution one then has

$$\psi_n(r) \approx u_{n,k_0}(r) \sum_k c_{n,k} e^{ikr} = u_{n,k_0}(r)\chi(r) \tag{A.51}$$

The total wavefunction of an electron would then be, for example,

$$\psi_e(r_s, \theta, \phi) = u_{e,k_0}(r, \theta, \phi)\chi_l(r_s)Y_{m,l}(\theta, \phi) \tag{A.52}$$

Although for notational consistency we should either express the Bloch functions in spherical coordinates or the spherical Bessel functions in Cartesian coordinates, the Bloch function is usually treated as a parameter which is calculated separately at the unit cell level, and the overall wavefunction is expressed in spherical Coordinates.

The envelope function approximation formally requires $k_0 = 0$ and the sum to run from 0 to ∞. The degree to which $u_{n,k}(r)$ differs from $u_{n,0}(r)$ can be calculated using the $k \cdot p$ models developed in the previous sections. One finds that extraction of $u_{n,0}(r)$ out of the sum is usually justified

only at large energy gaps and for large nanostructures, where the wavefunction retains much of its zone-center character. In practice, however, the envelope function approximation is successful over a much wider range of situations than implied above. This is because very small wavevectors will not contribute much to the sum over k in the series expansion of the spherical Bessel functions. To estimate the smallest value of k which contributes, we can note that for $1S$ radial wavefunctions $\lambda = 4R$ so that $k_{\min} = \pi/2R$. For very small nanocrystals of 1 nm radius this corresponds to wavevectors $k_{\min} \approx 1.5$ nm^{-1} while for larger nanocrystals of 5 nm radius, $k_{\min} \approx 0.3$ nm^{-1}. It is common to take $k_0 = k_{n,l}$, and the quality of this approximation degrades at high values of n and l or small values of R.

A.3.3 Confinement regimes, excitons and optical matrix elements

When a quantum dot absorbs light, an electron is excited to a conduction state while a hole is created in a valence state. One must in general consider the Coulombic attraction in such an electron-hole pair when calculating the carrier energies. In bulk materials this attraction produces excitons, hydrogen-like bound states in which the lighter carrier "orbits" the heavier. The manner in which this correlated motion is treated in nanocrystal quantum dots depends on the so-called confinement regime. This is typically estimated from the characteristic particle Bohr radius a, which is given by

$$a = \frac{\epsilon \hbar^2}{\mu e^2} \tag{A.53}$$

where now μ can be the electron effective mass, heavy hole effective mass, or electron-hole effective reduced mass depending on the situation. The strong confinement regime occurs when electron, hole and exciton Bohr radii a_e, a_h, a_x are all much smaller than R. The weak confinement regime occurs when $a_e, a_h < R < a_x$ and the intermediate confinement regime occurs when R is only smaller than either a_e or a_h. In the strong confinement regime the energies of both carriers are strongly quantized and and the internal charge motion is very well described by the particle-in-a-sphere model. This is an appropriate description of small nanocrystal quantum dots made of

II-VI, III-V and IV-VI semiconductors. Coulombic attraction in this case is accurately treated as simple perturbation to an independent electron and hole. The intermediate confinement regime is more appropriate for larger nanocrystals or when only one of the carriers, usually the hole, is rather heavy. In this case, the lighter carrier remains well-described by the particle-in-a-sphere model while a quantitative description of the heavier requires more sophisticaed methods. The Coulombic interaction is more complicated and typically taken for bulk hole interacting with the mean field of a confined electron. In weak confinement, the correct picture is that of a bulk exciton confined to the spherical potential.

Treatment of electron-hole Coulomb attraction is simplest in the strong confinement regime. Since the confinement energy is much greater than the Coulomb energy, perturbation theory and simple electrostatics may be used. Although only strictly valid in a limited set of situations, this treatment nevertheless represents an improvement over the single-particle description over a wide range of particle sizes and compositions. In the strong confinement approximation the excitonic envelope function ψ_x is simply the product of independent electron and hole envelope functions:

$$\psi_x(r_s, \theta, \phi) = \chi_e(r_s)\chi_h(r_s)Y^e_{m,l}(\theta, \phi)Y^h_{m,l}(\theta, \phi) \tag{A.54}$$

The corresponding energy of the electron-hole pair is

$$E^x_{n,l} = E_g + \frac{\hbar^2}{2}\left(\frac{\left(k^e_{n,l}\right)^2}{m^*_e} + \frac{\left(k^h_{n,l}\right)^2}{m^*_h}\right) - \int \psi^2_x(r)V'(r)dr^3 \tag{A.55}$$

where the last term is the first-order perturbative correction to the energy due to the Coulomb interaction $V'(r) = e^2/4\pi\epsilon_0\epsilon|r_e - r_h|$ and n is the principal quantum number. The perturbation is typically evaluated in spherical coordinates using Laplace expansions for the Coulomb potential. We have neglected the Coulomb interactions between Bloch functions here because the Bloch functions oscillate very rapidly compared to the envelope functions, and their contribution to the integration is usually assumed to be small. This approximation is rather good at low energies, but

its quality will decrease as the energy grows and the envelope function gains local character. When both electron and hole occupy $1S$ states, for example, the Coulomb correction is $1.77e^2/4\pi\epsilon_0\epsilon R$. This is typically in the range 10 – 200 meV depending on the screening and particle size.

A common and important application of quantum dot wavefunctions is in the calculation of the oscillator strength and other optical constants which are related to it. The oscillator strength of an optical transition between states $|i\rangle$ and $|j\rangle$ is usually expressed in atoms and molecules directly in the dipole approximation as

$$f_{ij} = \frac{2m\omega_{ij}|\langle i|r|j\rangle|^2}{3\hbar} \tag{A.56}$$

where r is the position operator [16, 17, 18]. The oscillator strength in semiconductors is often expressed as

$$f_{ij} = \frac{2P'^2}{3m\hbar\omega_{ij}} \tag{A.57}$$

where $P' = \langle i|p|j\rangle$ is a generalized momentum matrix element. When $|i\rangle$ and $|j\rangle$ are pure zone-center Bloch functions, P' is the momentum matrix element from $k \cdot p$ theory and $\sum_{j\neq i} f_{ij} = 1 + m/m^*_j$ for the *zone-center* effective mass m^* [8, 7]. In this notation valence effective masses have negative values. This aligns with the physical interpretation of the oscillator strength in terms of real and classical electrons, for a lighter particle will behave as a stronger oscillator in a classical equation of motion.

The situation is slightly more involved when the transition occurs between impure states. This is most clearly illustrated by examining the relationship between position and momentum matrix elements. We begin with the commutation relation

$$\begin{aligned} p &= \frac{m}{i\hbar}[H, r] \\ \langle i|p|j\rangle &= \frac{m}{i\hbar}(\langle i|Hr|j\rangle - \langle i|rH|j\rangle) \end{aligned} \tag{A.58}$$

If $|i\rangle$ and $|j\rangle$ are eigenstates of $H = p^2/2m + V(r)$, then H can act to the left in the first term and to

the right in the second term to give

$$\langle i|p|j\rangle = \frac{m}{i\hbar}\Big(E_i\langle i|r|j\rangle - E_j\langle i|r|j\rangle\Big) \tag{A.59}$$

which defines the relationship between position and momentum matrix elements of eigenstates. If $|i\rangle$ and $|j\rangle$ are instead linear combinations of eigenstates, as in a quantum dot, P' must be calculated from the mixed state at the relevant k. Equation A.57 still applies in this case, but the simple effective mass expression may not be applicable because it is derived under the assumption of parabolic dispersion [8].

REFERENCES

[1] S. E. Simon, *The Oxford Solid State Basics*. Oxford: Oxford University Press, 2013.

[2] N. W. Ashcroft and N. D. Mermin, *Solid State Physics*. Brooks/Cole, 1976.

[3] R. Hoffmann, "How Chemistry and Physics Meet in the Solid State," *Angew. Chemie Int. Ed. English*, vol. 26, no. 9, pp. 846–878, 1987.

[4] R. Hoffmann, "A chemical and theoretical way to look at bonding on surfaces," *Rev. Mod. Phys.*, vol. 60, no. 3, pp. 601–628, 1988.

[5] R. Hoffmann, *Solids and Surfaces: A Chemist's View of Bonding in Extended Structures*. Wiley-VCH, 1991.

[6] C. F. Klingshirn, *Semiconductor Optics*. Springer, 4 ed., 2012.

[7] P. Y. Yu and M. Cardona, *Fundamentals of Semiconductors*. Springer, 4th ed., 2010.

[8] B. K. Ridley, *Quantum Processes in Semiconductors*. Oxford: Oxford University Press, 5 ed., 2013.

[9] J. Chu and A. Sher, *Physics and Properties of Narrow Gap Semiconductors*. New York: Springer, 2008.

[10] L. C. Lew Yan Voon and M. Willatzen, *The kp Method: Electronic Properties of Semiconductors*. Heidelberg: Springer-Verlag, 2009.

[11] E. O. Kane, "Band structure of indium antimonide," *J. Phys. Chem. Solids*, vol. 1, no. 4, pp. 249–261, 1957.

[12] E. O. Kane, "The semi-empirical approach to band structure," *J. Phys. Chem. Solids*, vol. 8, no. C, pp. 38–44, 1959.

[13] D. J. Norris, "Electronic Structure in Semiconductor Nanocrystals: Optical Experiment," in *Nanocrystal Quantum Dots* (V. Klimov, ed.), pp. 63–96, Boca Raton: CRC Press, 2 ed., 2010.

[14] L. E. Brus, "Electronic wave functions in semiconductor clusters: experiment and theory," *J. Phys. Chem.*, vol. 90, no. 12, pp. 2555–2560, 1986.

[15] C. Delerue and M. Lannoo, *Nanostructures: Theory and Modeling*. Heidelberg: Springer-Verlag, 2004.

[16] A. E. Siegman, *Lasers*. Sausalito: University Science Books, 1986.

[17] P. W. Milonni and J. H. Eberly, *Laser Physics*. Hoboken: John Wiley Sons, 2010.

[18] R. C. Hilborn, "Einstein coefficients, cross sections, f values, dipole moments, and all that," *Am. J. Phys.*, vol. 50, no. 11, pp. 982–986, 1982.

APPENDIX B

NONLINEAR OPTICAL FREQUENCY CONVERSION

B.1 Overview and Introduction

Nonlinear optics, and especially its application to altering the frequency of light, is an old and established topic with no shortage of textbooks and references. Yet, it can be challenging to learn and apply in a laboratory setting due to the wide variety of notational conventions and different topical emphases found in the standard texts. Furthermore, while most texts give detailed descriptions of second-harmonic and sum-frequency processes, subtle points related to phases and symmetries are often given a more cursory treatment in the downconversion processes which are most relevant in infrared spectroscopy. My hope here is to present a self-contained introduction emphasizing the topics and conceptual issues which are relevant to the infrared spectroscopy experiments of this thesis. The overall presentation loosely follows Boyd's text [1] with additional topics and insights from the works of Shen [2] and Yariv [3]. The sections on field energy density and parametric fluorescence follow Yariv [3] and the primary literature [4, 5, 6], where more detailed discussions may be found. An excellent discussion of phasematching and crystal optics is given by Dmitriev and co-workers [7], and very useful general optics references are the texts by Guenther [8] and Peatross and Ware [9].

Nonlinear optical phenomena arise when the typical linear relationship between the electric polarization of the material and the electric field strength no longer holds. This is often illustrated by expanding the expression for the electric polarization P in terms of the electric susceptibility χ and the electric field E:

$$P = \epsilon_0\left(\chi^{(1)}E + \chi^{(2)}E^2 + \chi^{(3)}E^3 + ...\right) = P^{(1)} + P^{(2)} + P^{(3)} + ... = P^{(1)} + P^{(NL)} \tag{B.1}$$

The nonlinear $P^{(NL)}$ terms will be much smaller than the linear $P^{(1)}$ term when E is small, and the

linear polarization therefore dominates interactions between the material and the light. For strong fields, however, the higher-order terms grow to appreciable magnitudes and produce nonlinear optical material properties. Before moving further, it is important to note that (B.1) is only valid far from resonances so that population transfer can be neglected. In the case of resonance and appreciable population transfer, a different formalism such as the optical Bloch equations is more appropriate for describing the response of the material to light.

To see how the inclusion of nonlinear polarization can result in optical frequency conversion, let us consider a monochromatic light field $E = \bar{E}e^{-i\omega t} + \text{c.c.}$ ω is the light frequency, t is time, and $\bar{E} = \mathcal{E}e^{ikz}$ is the spatial part of the wave. c.c. denotes the complex conjugate. Plugging in this light field to (B.1) and considering only the quadratic term, the induced second-order nonlinear polarization $P^{(2)}$ is $\epsilon_0\chi^{(2)}\bar{E}\bar{E}^* + \epsilon_0\chi^{(2)}(\bar{E}^2e^{-2i\omega t} + \text{c.c})$. It has two distinct components: a new polarization at zero frequency corresponding to the creation of a DC field across the material, and a new oscillating polarization at 2ω. These processes are called optical rectification and second-harmonic generation, respectively. We can also examine what happens if we apply we apply two different frequencies ω_a and ω_b. In this case $E = \bar{E}_1e^{-i\omega_a t} + \bar{E}_2e^{-i\omega_b t} + \text{c.c.}$ and the polarization is

$$\begin{aligned} P^{(2)} = \epsilon_0\chi^{(2)}\Big(&\bar{E}_a^2e^{-2i\omega_a t} + \bar{E}_b^2e^{-2i\omega_b t} + 2\bar{E}_a\bar{E}_be^{-i(\omega_a+\omega_b)t} + 2\bar{E}_a\bar{E}_b^*e^{-i(\omega_a-\omega_b)t} + \text{c.c}\Big) \\ &+ 2\chi^{(2)}\Big(\bar{E}_a\bar{E}_a^* + \bar{E}_a\bar{E}_b^*\Big) \end{aligned} \tag{B.2}$$

Each of the applied fields generates its second harmonic and a DC field as for the previous case, but we also see two new oscillating polarizations at $(\omega_a + \omega_b)$ and $(\omega_a - \omega_b)$ which produce radiation.

The production of a radiating polarization at $(\omega_a + \omega_b)$ is called sum-frequency generation. For the work described in this thesis, sum-frequency generation was used as a spectroscopic method for detecting mid-infrared photoluminescence with high time resolution. The production of a radiating polarization at $(\omega_a - \omega_b)$ is called difference-frequency generation and was used to generate the tunable mid-infrared beams required for absorption spectroscopies. This processes is also called optical parametric amplification because, as we will see later, it results in amplification of one of

the input fields as well. Both sum-frequency generation and parametric amplification are essentially classical phenomena and can be understood within the framework of Maxwell's equations in media. A process related to parametric amplification, parametric fluorescence, is a quantum mechanical phenomenon and can be thought of as parametric amplification of vacuum fluctuations. For the work described in this thesis, it was used to generate one of the input fields to "seed" parametric amplification. In the following sections, we derive these processes and examine some of their important physical features. Experimental realization of the nonlinear optical devices with an emphasis on practical design principles are described in Appendix C.

B.2 Nonlinear Wave Equation

The wave equation for nonlinear optics is derived in much the same manner as the wave equation for linear optics. The main difference is that we will modify the constitutive relation for the displacement field to allow a nonlinear electronic polarization. We can begin from Maxwell's equations for a nonmagnetic insulator. In SI units they are

$$\nabla \cdot D = 0 \tag{B.3}$$

$$\nabla \cdot B = 0 \tag{B.4}$$

$$\nabla \times E = -\frac{\partial B}{\partial t} \tag{B.5}$$

$$\nabla \times H = \frac{\partial D}{\partial t} \tag{B.6}$$

To start the derivation of the wave equation, we can take the curl of (B.5) and reorder the space and time derivatives, giving $\nabla \times \nabla \times E = -\frac{\partial}{\partial t}(\nabla \times B)$. We then employ two constitutive relations. The first, $B = \mu_0 H$, is a consequence of the fact that we have assumed the magnetic polarization M to be zero. The second, $D = \epsilon_0 E + P$, is responsible for the radiation emitted from the induced electronic polarization in the material. In particular, it will be the nonlinear components of P that act as the source of radiation at the sum or difference frequencies of the driving fields. Substituting

in (B.6) and the two constitutive relations gives a general wave equation:

$$\nabla \times \nabla \times E + \mu_0 \epsilon_0 \frac{\partial^2 E}{\partial t^2} = -\mu_0 \frac{\partial^2 P}{\partial t^2} \tag{B.7}$$

This equation can be simplified if we take the electric fields to be transverse infinite plane waves, which is a good approximation for unfocused or weakly-focused laser beams. Using the identity $\nabla \times \nabla \times E = \nabla(\nabla \cdot E) - \nabla^2 E$ and noting that the first term vanishes for infinite transverse fields, the wave equation is now

$$-\nabla^2 E + \mu_0 \epsilon_0 \frac{\partial^2 E}{\partial t^2} = -\mu_0 \frac{\partial^2 P}{\partial t^2} \tag{B.8}$$

We can now make a series of substitutions to write the wave equation in terms of the nonlinear polarization. Writing the displacement constitutive relation more explicitly as $D = \epsilon_0 E + P^{(1)} + P^{(NL)} = D^{(1)} + P^{(NL)}$ and noting that $\epsilon_0 n^2 E = \epsilon_0 E + P^{(1)}$, where n is the linear real refractive index, we can write the wave equation as

$$-\nabla^2 E + \frac{n^2}{c^2} \frac{\partial^2 E}{\partial t^2} = -\frac{1}{\epsilon_0 c^2} \frac{\partial^2 P^{(NL)}}{\partial t^2} \tag{B.9}$$

We have also made the substitution $c^{-2} = \mu_0 \epsilon_0$. It is useful to compare this equation with the wave equation for linear optics, obtained by simply taking $P^{(NL)} = 0$. In that case, the only frequencies present in the wave equation are the fundamental frequencies of E. In (B.9), the wave equation contains additional frequencies via $P^{(NL)}$. In the following sections, we will use the nonlinear wave equation to derive expressions which quantify the conversion of the input field(s) into the output fields(s).

B.3 Coupled Wave Equations, Parametric Amplification and Phasematching

We begin by discussing the coupled wave equations for nonlinear optical frequency conversion, using the example of parametric amplification (difference-frequency generation). The general procedure shown here will be applicable to the case of sum-frequency generation and other nonresonant nonlinear phenomena as well.

For parametric amplification we will consider application of a strong beam at ω_3 and a weak beam at ω_2 to a material, and the subsequent generation of the difference frequency $\omega_1 = \omega_3 - \omega_2$ from the induced polarization at this frequency. Throughout the rest of this appendix, we will follow the convention that $\omega_3 > \omega_2 > \omega_1$. In one dimension, the solution to the linear wave equation is a plane wave $E(z,t) = \mathcal{E}e^{i(kz-\omega t)}$+ c.c. where $\mathcal{E}$ is a constant. The constant value of $\mathcal{E}$ reflects the fact that the wave does not gain or lose amplitude as it travels through the lossless linear medium. For nonlinear polarizations which are not too large, we can make the approximation that the solution to the nonlinear wave equation will retain this form, but now with a spatially-varying $\mathcal{E}$. This reflects the fact that due to the nonlinear polarization, the field can gain or lose energy. We will first consider the field generated at ω_1. The two applied fields are

$$E_3(z,t) = \mathcal{E}_3 e^{i(k_3 z-\omega_3 t)} + \text{c.c} \tag{B.10}$$

and

$$E_2(z,t) = \mathcal{E}_2 e^{i(k_2 z-\omega_2 t)} + \text{c.c} \tag{B.11}$$

and they generate a polarization in the material given by

$$P_1(z,t) = 2\epsilon_0 \chi^{(2)} \mathcal{E}_3 \mathcal{E}_2^* e^{i(k_3-k_2)z} e^{-i\omega_1 t} + \text{c.c} \tag{B.12}$$

This expression for the polarization is obtained by plugging (B.10) and (B.11) into (B.1) and se-

lecting the terms which oscillate at $\omega_1 = \omega_3 - \omega_2$. The induced polarization will radiate, generating a field

$$E_1(z,t) = \mathcal{E}_1 e^{i(k_1 z - \omega_1 t)} + \text{c.c} \tag{B.13}$$

Now we substitute (B.12) and (B.13) into the nonlinear wave equation (B.9) as $P^{(NL)}$ and E, respectively. After taking the derivatives and cancelling terms, we obtain

$$\frac{d^2\mathcal{E}_1}{dz^2} + 2ik_1\frac{d\mathcal{E}_1}{dz} = \frac{-2\chi^{(2)}\omega_1^2}{c^2}\mathcal{E}_3\mathcal{E}_2^* e^{i(k_3 - k_2 - k_1)z} \tag{B.14}$$

We now make what is known as the slowly-varying amplitude approximation, which states that $|\frac{d^2\mathcal{E}_1}{dz^2}| \ll |2k_1\frac{d\mathcal{E}_1}{dz}|$. This allows us to ignore the leftmost term in (B.14). Physically, this amounts to an assumption that the growth in amplitude of the ω_1 wave is not large over distances of the order $1/k_1$. This is true in practical situations. More fundamentally, as can be shown by solving B.14 directly using Green's functions [2], the slowly-varying amplitude approximation arises from neglecting the electric field traveling in the $-z$ i.e. backwards direction. With this approximation and the substitutions $k = n\omega/c$ and $\Delta k = k_3 - k_2 - k_1$, we can then write (B.14) as

$$\frac{d\mathcal{E}_1}{dz} = i\frac{\chi^{(2)}\omega_1}{n_1 c}\mathcal{E}_3\mathcal{E}_2^* e^{i\Delta k z} \tag{B.15}$$

This is a "coupled wave equation" for the difference-frequency field and it describes how the field amplitude depends on the position in the nonlinear medium and on the applied field strengths. The analogous equations for the other fields are

$$\frac{d\mathcal{E}_2}{dz} = i\frac{\chi^{(2)}\omega_2}{n_2 c}\mathcal{E}_3\mathcal{E}_1^* e^{i\Delta k z} \tag{B.16}$$

and

$$\frac{d\mathcal{E}_3}{dz} = i\frac{\chi^{(2)}\omega_3}{n_3 c}\mathcal{E}_1\mathcal{E}_2 e^{-i\Delta k z} \tag{B.17}$$

These equations, and in particular the choices of conjugation and phase, were derived using the following procedure. In writing out the polarization by substitution of fields into (B.1) we can notice that if we adopt the convention that every polarization oscillates at a sum of frequencies, positive frequencies correspond to $\mathcal{E}e^{ik}$ and negative frequencies correspond to $\mathcal{E}^* e^{-ik}$. We can use this as a shortcut to derive (B.16) and (B.17) from (B.15). As an example, beginning from $P(\omega_1 = \omega_3 - \omega_2)$ we can "solve" for ω_2 in the argument of the polarization and use the convention to associate $P(\omega_2 = \omega_3 - \omega_1)$ with $\mathcal{E}_3\mathcal{E}_1^* e^{i(k_3-k_1)z}$. Indeed, neglecting constants, this matches the right hand side of (B.16) up to the factor of $e^{-ik_2 z}$ contained in Δk. This factor will come from cancelling the $e^{ik_2 z}$ factor which appears on the left hand side in connection with $\mathcal{E}_2$. This procedure physically amounts to an acknowledgement that all fields are present at all times if we take them to be infinite plane waves. We are allowed to permute the argument in the polarization because of the particular symmetry properties of the susceptibility, which are discussed next.

Although $\chi^{(2)}$ is in general a frequency-dependent tensor quantity, far from resonance it has the property that it obeys permutation symmetry. This means that the indices of the susceptibility tensor can be freely permuted as long as the frequency arguments are also appropriately rearranged. For example, it implies that $\chi^{(2)}_{ijk}(\omega_3 = \omega_1 + \omega_2) = \chi^{(2)}_{ikj}(\omega_3 = \omega_2 + \omega_1) = \chi^{(2)}_{kji}(\omega_2 = -\omega_1 + \omega_3) = \chi^{(2)}_{kij}(\omega_2 = \omega_3 - \omega_1) = ...$ Under highly nonresonant conditions, however, the susceptibility can also be approximated as dispersionless, allowing the indices to be permuted without permuting the frequencies and vice versa. This is known as the Kleinman symmetry condition and justifies the procedure we used to obtain (B.16) and (B.17) by inspection. Kleinman symmetry is derived and justified more completely in the next section. The Kleinman symmetry also simplifies the tensorial nature of $\chi^{(2)}$ and leads to the result that an effective, constant value of $\chi^{(2)}$ can be defined for a fixed pair of propagation and polarization directions of the wave. Thus, the $\chi^{(2)}$ in the three coupled wave equations take on the same value for a given experimental geometry. We will address how one determines this effective value of $\chi^{(2)}$ when the experimental devices are discussed in later sections.

In the practical application of optical frequency conversion, we are interested in quantifying the growth of the generated wave(s) as a function of the applied field strengths and other experimental conditions. It is first convenient to examine the effect of Δk on the conversion efficiency process in the limit that the conversion is very small. In this case, we can take the field amplitudes on the right hand side of (B.15) to be constant and integrate directly to give

$$\mathcal{E}_1(L) = i\frac{\chi^{(2)}\omega_1}{n_1 c}\mathcal{E}_3\mathcal{E}_2^* \int_0^L e^{i\Delta k z}dz = i\frac{\chi^{(2)}\omega_1}{n_1 c}\mathcal{E}_3\mathcal{E}_2^*\left(\frac{e^{i\Delta k L}-1}{i\Delta k L}\right) \tag{B.18}$$

where L is the length of the material. We now square this expression to obtain a form which is proportional to the measurable intensity I via $I = 2n\epsilon_0 c|\mathcal{E}|^2$. Using some algebraic substitutions, this gives

$$|\mathcal{E}_1|^2 = \frac{\left(\chi^{(2)}\right)^2\omega_1^2|\mathcal{E}_3|^2|\mathcal{E}_2|^2}{n_1^2 c^2}L^2\mathrm{sinc}^2(\Delta k L/2) \tag{B.19}$$

As shown below, the sinc function is strongly peaked when its argument is zero, and this causes a strong reduction of the radiated intensity for even small values of $\Delta k L$. Ideally, $\Delta k = 0$ and when this condition is satisfied the waves are said to be phase-matched or momentum-matched. This results in the dipoles oscillating in phase at all three frequencies, allowing the coherent radiation generation. The experimental strategy for achieving phase matching utilizes the birefringence of certain crystals and is discussed in the final section of this appendix.

Having established the general principle that $\Delta k = 0$ is desirable, we can now address the efficiency of difference-frequency generation without the approximation that the conversion is very small. We will however make the approximation that $d\mathcal{E}_3/dz = 0$. This is valid in the typical experimental situation where the high-frequency wave is very much stronger than the others, so it is not appreciably depleted by the interaction even when the gain for the lower-frequency waves is considerable. To derive the growth of the difference-frequency wave, we will solve a single differential equation obtained by combining (B.15) and (B.16). We first differentiate (B.15) with respect to z. Then we take the complex conjugate of (B.16) and substitute this into the formula for

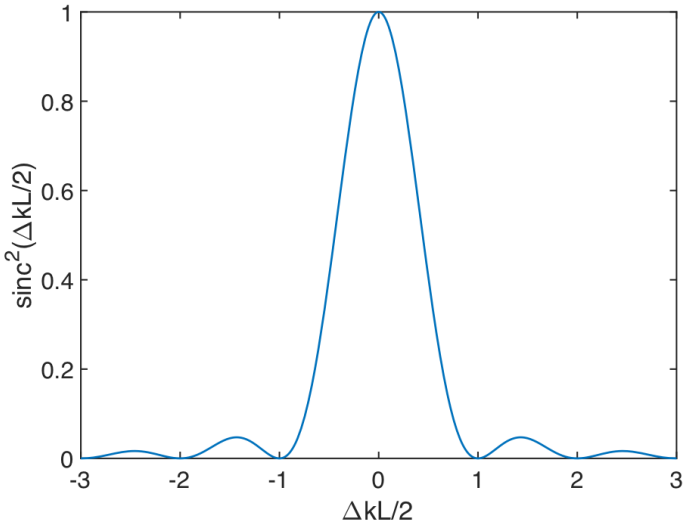

Figure B.1: sinc^2 function illustrating the sensitivity of phasematching to the value of Δk.

$d^2\mathcal{E}_1/dz^2$. Setting $\Delta k = 0$, we obtain

$$\frac{d^2\mathcal{E}_1}{dz^2} = \xi^2\mathcal{E}_1 \tag{B.20}$$

where the coupling constant is defined

$$\xi^2 = \xi_1\xi_2^* = \left(i\frac{\chi^{(2)}\omega_1\mathcal{E}_3}{n_1c}\right)\left(-i\frac{\chi^{(2)}\omega_2\mathcal{E}_3^*}{n_2c}\right) = \frac{\left(\chi^{(2)}\right)^2\omega_1\omega_2}{n_1n_2c^2}\left|\mathcal{E}_3\right|^2 \tag{B.21}$$

ξ characterizes the coupling strength between the undepleted wave at ω_3 and the waves at the lower frequencies. It has units of inverse length and can be interpreted as a gain coefficient for the electric field. The general solution to this equation is

$$\mathcal{E}_1(z) = A\sinh(\xi z) + B\cosh(\xi z) \tag{B.22}$$

where ξ is now $\sqrt{\xi^2}$ and A and B are constants determined from the boundary conditions. With

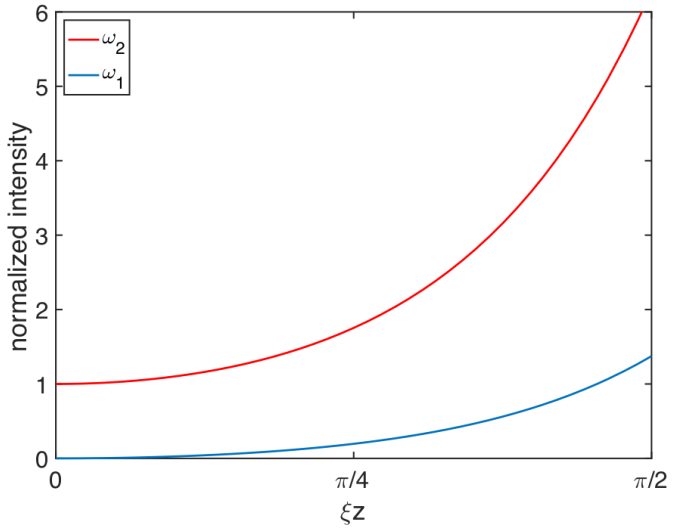

Figure B.2: Parametric amplification solutions plotted as the normalized "intensity" $|\mathcal{E}|^2/|\mathcal{E}_2(0)|^2$ for the case $\omega_1/2\pi c = 2000$ cm^{-1} and $\omega_2/2\pi c = 7496$ cm^{-1}.

the boundary condition $\mathcal{E}_1(0) = 0$, (B.22) can be used to solve (B.15) and (B.16), giving

$$\mathcal{E}_1(z) = i\sqrt{\frac{n_2\omega_1}{n_1\omega_2}}\frac{\mathcal{E}_3}{|\mathcal{E}_3|}\mathcal{E}_2(0)^*\sinh(\xi z) \tag{B.23}$$

$$\mathcal{E}_2(z) = \mathcal{E}_2(0)\cosh(\xi z) \tag{B.24}$$

The behavior of the solutions is shown in Figure B.2.

Both of these equations reduce to exponential growth when when ξz is large. If we wish to maximize the generated field strength for a fixed set of material parameters and interaction length z, the exponential nature of the solutions indicates that we should maximize $\mathcal{E}_3$ subject to constraints imposed by material damage thresholds. It is also noteworthy that the exponential dependence of $\mathcal{E}_{1(2)}$ on ξ and the linear dependence of ξ on $\omega_{1(2)}$ makes the efficient generation of mid- and long-wave infrared light particularly difficult.

B.4 Lorentz Oscillator and Field Energy Density

When we discuss parametric fluorescence in the next section, we will need to write down a Hamiltonian for the interaction between the fields in the medium. This will require an expression for the energy density in a classical field. This is given by Poynting's theorem in linear optics, and in this section we generalize this idea to a nonlinear material. A critical assumption for the derivation will be that far from resonance, the the material is lossless and dispersionless. To see why this is so, we can examine the anharmonic oscillator model of the susceptibility.

The equation of motion for an electron in an asymmetric anharmonic potential is

$$\frac{d^2x}{dt^2} + 2\Gamma\frac{dx}{dt} + \omega_0^2 x + Dx^2 = -\frac{eE}{m} \tag{B.25}$$

where x, e and m are respectively the electron displacement, charge and mass, Γ is the dipole damping rate, ω_0 is the resonance frequency, and D is related to the anharmonic restoring force F_D by $F_D = Dmx^2$. The equation of motion can be solved using perturbation theory. We multiply the right hand size by an expansion parameter λ and take the solution x to be a power series expansion in this parameter *i.e.* $x = \lambda x^{(1)} + \lambda^2 x^{(2)} + ...$ Then, we separately equate terms which are proportional to the various powers of λ. One finds that the first order contribution to the position is, for two input fields at ω_a and ω_b,

$$x^{(1)} = x^{(1)}(\omega_a)e^{-i\omega_a t} + x^{(1)}(\omega_b)e^{-i\omega_b t} + \text{c.c} \tag{B.26}$$

with the displacements given by

$$x^{(1)}(\omega) = \frac{-eE}{m\left(\omega_0^2 - \omega^2 - 2i\omega\Gamma\right)} \tag{B.27}$$

The displacement is related to the material polarization and the susceptibility by $P^{(1)} = \chi^{(1)}E = -Nex^{(1)}$, where N is the density of oscillators. The second order solution involves the quantity

$(x^{(1)})^2$ and as we saw from the introduction, this will create displacements oscillating at the harmonic, sum, difference, and zero frequencies. The second-order displacement associated with the difference-frequency response is

$$x^{(2)}(\omega_a - \omega_b) = \frac{-2De^2E_aE_b^*}{m^2\Big(\omega_0^2 - (\omega_a - \omega_b)^2 - 2i\Gamma(\omega_a - \omega_b)\Big)\Big(\omega_0^2 - \omega_a^2 - 2i\Gamma\omega_a\Big)\Big(\omega_0^2 - \omega_b^2 - 2i\Gamma\omega_b\Big)} \tag{B.28}$$

Analogous to the first-order (linear) case, we can obtain the second-order susceptibility from $P^{(2)}(\omega_a - \omega_b) = -Nex^{(2)}(\omega_a - \omega_b) = 2\epsilon_0\chi^{(2)}E_aE_b^*$. As we would expect, the nonlinear displacement and resulting susceptibility are proportional to the degree of anharmonicity in the potential (characterized by D), and also to the field strengths. It is interesting to note that the nonlinear contribution to the displacement can be written as a product of the linear displacements at the three frequencies. Applied to the resulting susceptibility, this is known as Miller's rule and is one way to estimate the nonlinear susceptibility.

In examining the denominator of (B.28) we note that when all three frequencies are much smaller than ω_0 and the medium is lossless ($\Gamma = 0$), the susceptibility is essentially independent of frequency *i.e.* it is dispersionless. Instead it is governed by the fundamental properties of the material, namely the resonance frequency, anharmonicity and density. We can therefore take the susceptibility and thus the polarization to be single-valued functions of the electric field. This allows us to write

$$\oint d(P \cdot E) = 0 \tag{B.29}$$

where the integral is over a closed path. To see why this is the case, recall that in general $\int_{x_1}^{x_2} df(x) = f(x_2) - f(x_1)$, and $x_1 = x_2$ for a closed path. Since $d(P \cdot E) = dP \cdot E + P \cdot dE$ and the dot product is commutative, it follows that

$$\oint E \cdot dP = -\oint P \cdot dE \tag{B.30}$$

The quantity $\oint E \cdot dP$ is the work done by the field on the polarization. Since we are in the nonresonant and lossless limit, the material does not change its energy and this quantity is zero. We can then apply Stokes theorem to the left hand side:

$$\oint P \cdot dE = 0 \longrightarrow \int_S (\nabla_E \times P) \cdot \hat{n}\, d\mathcal{S}_E = 0 \tag{B.31}$$

From this, we can conclude that $\nabla_E \times P = 0$. The curl of a vector field is zero if the field can be written as the gradient of a scalar field, so we can therefore posit the existence of an energy density function U which satisfies

$$P = \nabla_E U \tag{B.32}$$

We can obtain this function by comparing (B.32) with the polarization we know from (B.1). The U which satisfies this equation is

$$U = \epsilon_0 \left(\frac{1}{2}\chi^{(1)}_{ij} E_i E_j + \frac{1}{3}\chi^{(2)}_{ijk} E_i E_j E_k + \frac{1}{4}\chi^{(3)}_{ijkl} E_i E_j E_k E_l + ... \right) \tag{B.33}$$

so that one has, for example

$$P_i = \frac{\partial U}{\partial E_i} = \epsilon_0 \left(\frac{1}{2}\chi^{(1)}_{ij} E_j + \frac{1}{3}\chi^{(2)}_{ijk} E_j E_k + \frac{1}{4}\chi^{(3)}_{ijkl} E_j E_k E_l + ... \right) \tag{B.34}$$

The equation (B.33) gives the energy density of the field generalized for a nonlinear medium and will form the basis of the Hamiltonian which couples the ω_3 wave to the lower-frequency waves. The preceding material also justifies the Kleinman symmetry mentioned earlier. Summing over the indices brings (B.34) into agreement with (B.1) because at each order, the denominator of the fraction coefficient equals the number of equivalent terms which appear after summing over the fields. In the current context, Kleinman symmetry states the order of multiplication for the electric field components has no physical significance and as a further consequence, all susceptibilities which are related by rearranging the indices must be equal. Note that at the beginning of this

derivation we assumed a lossless material and highly nonresonant fields, which allowed us to write (B.29) and carry out the derivation. (B.29), and therefore Kleinman symmetry, do not apply outside of those conditions.

B.5 Parametric Fluorescence

In contrast to the assertion of equations (B.23) and (B.24) for parametric amplification, a strong wave at ω_3 can generate light at ω_2 and ω_1 even when when no field is present at ω_2. This process is called parametric fluorescence and can be thought of as parametric amplification of the vacuum fluctuations at ω_2 and ω_1. The low-frequency fields are treated quantum-mechanically, while the high-frequency field can be treated classically since its amplitude in practice is very large.

We begin by defining the unperturbed Hamiltonian for photons at ω_1 and ω_2:

$$H_0 = \hbar\omega_1\left(a_1^\dagger a_1 + \frac{1}{2}\right) + \hbar\omega_2\left(a_2^\dagger a_2 + \frac{1}{2}\right) \tag{B.35}$$

where $a^\dagger$ and a are creation and annihilation operators for photons. The product $a^\dagger a = N$ is the photon number. The field interaction Hamiltonian, which is determined by the $\chi^{(2)}$ term in (B.33), is

$$H' = \frac{1}{3}\chi^{(2)}\int_V E_1 E_2 E_3\, dV \tag{B.36}$$

where the integral is taken over the mode volume V. To make use of this equation in the current problem, we need define the operator for one mode of a quantized light field:

$$E = i\hat{e}\sqrt{\frac{\hbar\omega}{2n^2V}}\left(ae^{ikr} - a^\dagger e^{-ikr}\right) \tag{B.37}$$

Here $\hat{e}$ is the polarization unit vector. In all of these equations, the creation and annihilation operators carry the time-dependence, corresponding to the "Heisenberg picture" of quantum mechanics.

Plugging in quantized the light fields E_1 and E_2 and a classical field E_3 in to (B.36) gives

$$H' = \kappa\hbar\cos(\omega_3 t)\left(a_1^\dagger - a_1\right)\left(a_2^\dagger - a_2\right) \tag{B.38}$$

where κ is given by

$$\kappa = \frac{\chi^{(2)}\sqrt{\omega_1\omega_2}}{Cn_1n_2}|\mathcal{E}_3| \tag{B.39}$$

and C is a normalization constant derived from the integration over spatial components of the three fields. κ has units of inverse time and can be thought of as the time-domain version of ξ. It characterizes the strength of coupling between the strong classical field and photons at ω_1 and ω_2.

We are now in a position to solve the quantum mechanical problem of the time-dependent photon numbers at those frequencies. The Hamiltonian is

$$H = H_0 + H' = \hbar\omega_1\left(a_1^\dagger a_1 + \frac{1}{2}\right) + \hbar\omega_2\left(a_2^\dagger a_2 + \frac{1}{2}\right) + \kappa\hbar\cos(\omega_3 t)\left(a_1^\dagger - a_1\right)\left(a_2^\dagger - a_2\right) \tag{B.40}$$

and the generic time-dependence of an operator O is given by the Heisenberg equation of motion:

$$\frac{dO}{dt} = -\frac{i}{\hbar}[O, H] \tag{B.41}$$

In the present case, we are interested in the creation and annihilation operators for the low-frequency photons. For ω_1 we therefore have

$$\begin{aligned}\frac{da_1^\dagger}{dt} &= -\frac{i}{\hbar}[a_1^\dagger, H] = -\frac{i}{\hbar}\left([a_1^\dagger, H_0] + [a_1^\dagger, H']\right) \\ &= -\frac{i}{\hbar}\left(\hbar\omega_1[a_1^\dagger, a_1^\dagger a_1] + \hbar\omega_2[a_1^\dagger, a_2^\dagger a_2] + \hbar\kappa\cos(\omega_3 t)[a_1^\dagger, (a_1^\dagger - a_1)(a_2^\dagger - a_2)]\right)\end{aligned} \tag{B.42}$$

Using the commutation relations $[a_i, a_j] = [a_i^\dagger, a_j^\dagger] = 0$ and $[a_i, a_j^\dagger] = \delta_{ij}$, and converting the

cosine to complex form, this reduces to

$$\frac{da_1^\dagger}{dt} = i\omega_1 a_1^\dagger - \frac{i\kappa}{2}\Big(e^{i\omega_3 t}a_2^\dagger - e^{i\omega_3 t}a_2 + e^{-i\omega_3 t}a_2^\dagger - e^{-i\omega_3 t}a_2\Big) \tag{B.43}$$

In the absence of coupling ($\kappa = 0$) the solution is $a_1^\dagger(t) = a_{10}^\dagger e^{i\omega_1 t}$ where for notational compactness, $a_{10}^\dagger \equiv a_1^\dagger(0)$. This solution gives the natural time-dependence of $a_1^\dagger$ and it will be maintained when $\kappa \ll \omega$. This condition is satisfied in typical nonlinear crystalline media. $a_2^\dagger$ will have an analogous time-dependence and the corresponding lowering operators will have the form $a_k(t) = a_{k0}e^{-i\omega_k t}$. Plugging in the explicitly time-dependent operators into (B.43), we can see that only one term will oscillate in phase with $a_1^\dagger$ if $\omega_3 = \omega_1 + \omega_2$. It is the second term in parentheses, $e^{i\omega_3 t}a_2 = a_{20}e^{i\omega_3 t}e^{-i\omega_2 t} = a_{20}e^{i\omega_1 t}$. The remaining terms oscillate at other frequencies and will not contribute coherently to the photon production. We can therefore take the second term in parentheses to be the major contributor and simplify the nonlinear contribution in (B.43) to

$$\frac{da_1^\dagger}{dt} = ie^{i\omega_1 t}\Big(\omega_1 a_{10}^\dagger + \frac{\kappa}{2}a_{20}\Big) \tag{B.44}$$

From an analogous procedure, we can also write

$$\frac{da_2}{dt} = -ie^{-i\omega_2 t}\Big(\omega_2 a_{20} + \frac{\kappa}{2}a_{10}^\dagger\Big) \tag{B.45}$$

The corresponding solutions are

$$a_1^\dagger(t) = \left(a_{10}^\dagger \cosh\left(\frac{\kappa}{2}t\right) + ia_{20}\sinh\left(\frac{\kappa}{2}t\right)\right)e^{i\omega_1 t} \tag{B.46}$$

$$a_2(t) = \left(a_{20}\cosh\left(\frac{\kappa}{2}t\right) - ia_{10}^\dagger \sinh\left(\frac{\kappa}{2}t\right)\right)e^{-i\omega_2 t} \tag{B.47}$$

The creation and annihilation operators do not represent observables themselves because they are not Hermitian, but the product $a^\dagger a = N$ does. To obtain the number of photons at ω_1 and ω_2,

we multiply the preceding equations by their adjoints. Using $[a_i, a_j^\dagger] = \delta_{ij}$ and the fact that N is Hermitian, this gives

$$\begin{aligned} N_1(t) &\equiv a_1^\dagger(t)a_1(t) \\ &= a_{10}^\dagger a_{10}\cosh^2\left(\frac{\kappa}{2}t\right) + (1 + a_{20}^\dagger a_{20})\sinh^2\left(\frac{\kappa}{2}t\right) - \frac{i}{2}\sinh(\kappa t)\left(a_{10}^\dagger a_{20}^\dagger - a_{10}a_{20}\right) \end{aligned} \tag{B.48}$$

and

$$\begin{aligned} N_2(t) &\equiv a_2^\dagger(t)a_2(t) \\ &= a_{20}^\dagger a_{20}\cosh^2\left(\frac{\kappa}{2}t\right) + (1 + a_{10}^\dagger a_{10})\sinh^2\left(\frac{\kappa}{2}t\right) + \frac{i}{2}\sinh(\kappa t)\left(a_{10}^\dagger a_{20}^\dagger - a_{10}a_{20}\right) \end{aligned} \tag{B.49}$$

We can immediately note the functional similarities between the photon numbers at ω_1 and ω_2 and the intensities, proportional to $|\mathcal{E}|^2$, at ω_1 and ω_2 in parametric amplification. In contrast to parametric amplification, however, it is clear that even without initial photons at ω_1 or ω_2 ($a_{10}^\dagger a_{10} = a_{20}^\dagger a_{20} = 0$), photons at these frequencies can still exist at $t > 0$. Physically, this is due to the strong wave at ω_3 stimulating the amplification of the vacuum fluctuations which are already present due to the terms in H_0. From a more mathematical standpoint, the generation of photons at ω_1 and ω_2 is due to the fact that creation and annihilation operators do not commute.

B.6 Sum-Frequency Generation and Upconversion

For the particular implementation of sum-frequency generation used in this thesis work, the theoretical treatment is very similar to that for parametric amplification discussed previously. In this case, we apply fields at ω_1 and ω_2 to generate light at ($\omega_3 = \omega_1 + \omega_2$). The applied fields are

$$E_1(z,t) = \mathcal{E}_1 e^{i(k_1 z - \omega_1 t)} + \text{c.c} \tag{B.50}$$

$$E_2(z,t) = \mathcal{E}_2 e^{i(k_2 z - \omega_2 t)} + \text{c.c} \tag{B.51}$$

and the induced polarization is

$$P_3(z,t) = 2\epsilon_0 \chi^{(2)} \mathcal{E}_1 \mathcal{E}_2 e^{i(k_1+k_2)z} e^{-i\omega_3 t} + \text{c.c} \tag{B.52}$$

Following the same procedure described in the previous section, the coupled wave equations are

$$\frac{d\mathcal{E}_3}{dz} = i\frac{\chi^{(2)}\omega_3}{n_3 c}\mathcal{E}_1 \mathcal{E}_2 e^{i\Delta k z} \tag{B.53}$$

$$\frac{d\mathcal{E}_2}{dz} = i\frac{\chi^{(2)}\omega_2}{n_2 c}\mathcal{E}_3 \mathcal{E}_1^* e^{i\Delta k z} \tag{B.54}$$

$$\frac{d\mathcal{E}_1}{dz} = i\frac{\chi^{(2)}\omega_1}{n_1 c}\mathcal{E}_3 \mathcal{E}_2^* e^{i\Delta k z} \tag{B.55}$$

For the experiment in which weak mid-infrared light at ω_1 is converted to near-infrared light at ω_3 by a strong laser beam at ω_2, we can take $d\mathcal{E}_2/dz = 0$. This is because for a weak field at ω_1, the strong beam will not be appreciably depleted even if all the light at ω_2 is converted. We can then solve the remaining equations in an analogous way. Similarly to the case of difference-frequency generation, the coupling constant is

$$\xi^2 = -\xi_1 \xi_3 = \left(-i\frac{\chi^{(2)}\omega_1 \mathcal{E}_2^*}{n_1 c}\right)\left(i\frac{\chi^{(2)}\omega_3 \mathcal{E}_2}{n_3 c}\right) = \frac{(\chi^{(2)})^2 \omega_1 \omega_3}{n_1 n_3 c^2}|\mathcal{E}_2|^2 \tag{B.56}$$

and the depletion of the mid-infrared light during the process is given by

$$\frac{d\mathcal{E}_1^2}{dz^2} = -\xi^2 \mathcal{E}_2 \tag{B.57}$$

The general solution to this equation is different than that which describes difference-frequency generation due to the minus sign. In this case, we have

$$\mathcal{E}_1(z) = A\cos(\xi z) + B\sin(\xi z) \tag{B.58}$$

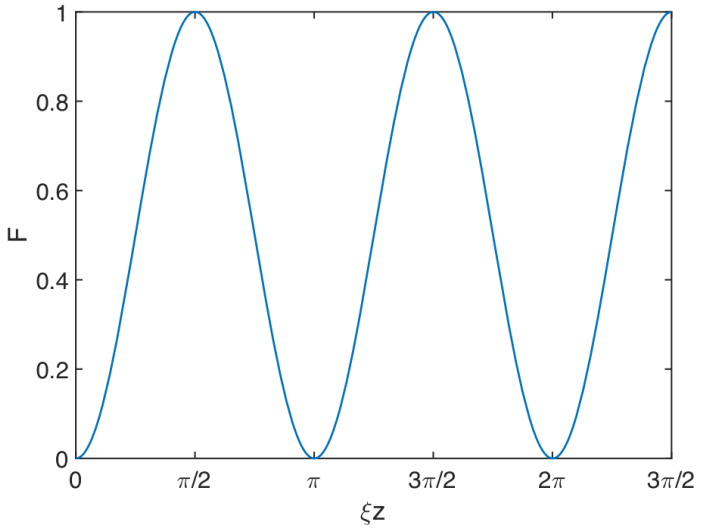

Figure B.3: Photon efficiency of upconversion given by equation B.62

and by substitution into our earlier expression for $d\mathcal{E}_1/dz$,

$$\mathcal{E}_3(z) = \frac{A\xi}{\xi_1}\sin(\xi z) + \frac{B\xi}{\xi_1}\cos(\xi z) \tag{B.59}$$

For the upconversion of mid-infrared to near-infrared light via sum-frequency generation, the boundary conditions are $\mathcal{E}_3(0) = 0$ and $\mathcal{E}_1(0)$ a specified constant. The boundary conditions lead to $A = \mathcal{E}_1(0)$ and $B = 0$ so that

$$\mathcal{E}_1(z) = \mathcal{E}_1(0)\cos(\xi z) \tag{B.60}$$

$$\mathcal{E}_3(z) = i\mathcal{E}_1(0)\frac{\mathcal{E}_2}{|\mathcal{E}_2|}\sqrt{\frac{n_1\omega_3}{n_3\omega_1}}\sin(\xi z) \tag{B.61}$$

and we have used the conversion $|\mathcal{E}_2|/\mathcal{E}_2^* = \mathcal{E}_2/|\mathcal{E}_2|$. Note the qualitative difference in behavior of these solutions compared to the case of parametric amplification. In the former process the two generated waves grow exponentially with ξz while in the present case, the total field amplitude oscillates between the ω_1 and ω_3 waves.

The conversion efficiency of photons at ω_1 to photons at ω_3 is of primary experimental impor-

tance when using sum-frequency generation as a detection scheme. This is known as upconversion. We can obtain the efficiency from the intensity defined as $I = 2n\epsilon_0 c|\mathcal{E}|^2 = \frac{N\hbar\omega}{A\Delta t}$ where N is the number of photons, A is the beam area and Δt is some unit interval of time. Since each high-frequency photon must correspond to a low-frequency photon, the upconversion efficiency F is

$$F \equiv \frac{N_3}{N_1 + N_3} = \frac{\sin^2(\xi z)}{\sin^2(\xi z) + \cos^2(\xi z)} \tag{B.62}$$

F takes the form of a periodic function oscillating between 0 and 1, and the maxima occur when ξz is an odd multiple of $\frac{\pi}{2}$ as shown above.

B.7 Crystal Optics

In most practical implementations of nonlinear optical frequency conversion, the nonlinear medium is a birefringent crystal with a bandgap much greater than the photon energies for the interacting waves. The large bandgap ensures that linear and nonlinear absorption is minimal, and it also ensures that Kleinman symmetry and Miller's criterion are approximately satisfied. The birefringence is critical for satisfaction of the phasematching condition. To understand why this is the case, consider again the generic case of three waves of frequencies ω_1, ω_2 and ω_3 interacting in a medium. Since all frequencies are below the material resonance, $\frac{dn}{d\omega} > 0$ and $\Delta k = 0$ is impossible unless there are multiple possible refractive indices for a given light frequency. This is the defining property of birefringent materials, characterized by an ordinary index n_o and extraordinary index $n_e(\theta)$ for the orthogonal polarization. The latter depends on the angle θ between the beam and the crystal optic axis, which by convention is the z axis in a right-handed system. To see how the birefringence accomplishes phasematching, consider parametric amplification in β-BaB_2O_4 (BBO) with the wave of wavelength λ_3 propagating in the xz plane. One possible phasematching condition is $k_3^e = k_1^o + k_2^o$ for $n_e = n_x$ and $n_o = n_y$. This is the so-called "type-I" interaction because the low-frequency waves have the same polarization. The "type-II" interaction involves

orthogonally-polarized low-frequency waves. For the above type-I interaction, we must find the value of θ which solves the equation

$$\frac{2\pi n^e(\lambda_3, \theta)}{\lambda_3} = \frac{2\pi n^o(\lambda_1)}{\lambda_1} + \frac{2\pi n^o(\lambda_2)}{\lambda_2} \tag{B.63}$$

for a given set of wavelengths that obey the energy conservation condition $\frac{1}{\lambda_3} = \frac{1}{\lambda_1} + \frac{1}{\lambda_2}$. The angular dependence of the extraordinary index is given by

$$n_e(\theta) = n_o \sqrt{\frac{1 + \tan^2(\theta)}{1 + (n_o/n_e)^2 \tan^2(\theta)}} \tag{B.64}$$

and $n_o(\lambda)$ and $n_e(\lambda)$ are obtained from the crystal's Sellmeier equations. In parametric amplification, λ_3 is the fixed wavelength of the pumping laser and the other wavelengths are generated/amplified. Rotating the crystal changes the wavelengths that phasematch with λ_3, creating a tunable light source. Analogous phasematching principles apply to sum-frequency generation/upconversion.

REFERENCES

[1] R. W. Boyd, *Nonlinear Optics*. Academic Press, 3 ed., 2008.

[2] Y.-R. Shen, *The Principles of Nonlinear Optics*. John Wiley Sons, 1984.

[3] A. Yariv, *Quantum Electronics*. John Wiley Sons, 3 ed., 1989.

[4] C. Homann and E. Riedle, "Direct measurement of the effective input noise power of an optical parametric amplifier," *Laser Photon. Rev.*, vol. 7, no. 4, pp. 580–588, 2013.

[5] D. A. Kleinman, "Theory of Optical Parametric Noise," *Phys. Rev.*, vol. 174, no. 1967, pp. 1027–1041, 1968.

[6] W. H. Louisell, A. Yariv, and A. E. Siegman, "Quantum Fluctuations and Noise in Parametric Processes. I.," *Phys. Rev.*, vol. 124, no. 6, pp. 1646 – 1654, 1961.

[7] V. Dmitriev, G. Gurzadyan, and D. Nikogosyan, *Handbook of Nonlinear Optical Crystals*. Berlin: Springer-Verlag, 3e ed., 1999.

[8] R. D. Guenther, *Modern Optics*. John Wiley Sons, 1990.

[9] J. Peatross and M. Ware, *Physics of Light and Optics*. https://optics.byu.edu/textbook, 2015.

APPENDIX C

OPTICAL APPARATUSES

C.1 Overview

This appendix describes design and performance characteristics of the home-built optical apparatuses used in this thesis: a Nd:YLF regeneratively-amplified laser, a BBO-KTA optical parametric amplifier (OPA) operating from 1.2 - 4.5 μm wavelength, a LBO-LGS OPA operating in the 3 - 7 μm region, and a photoluminescence upconversion apparatus operating from 2 - 5 μm. Beyond those given in the Appendix B, useful references are the excellent laser texts by Siegman [1] and Eberly [2].

C.2 Nd:YLF Laser System

C.2.1 Overview

Lasers emitting around 1 μm are convenient pump sources for mid-infrared parametric amplification because most nonlinear optical crystals for such applications do not have strong linear or nonlinear absorption for at these wavelengths. The present system produces in parallel a pair of 8 ps, 1053 nm, 0.95 mJ pulses at 1 kHz. This specification is motivated by a compromise between temporal resolution, spectral resolution, and robustness. The 8 ps pulse duration is sufficiently short to study most dynamical phenomena in semiconductor quantum dots, such as Auger recombination and cooling, laser pumping, and excitonic energy transfer processes. 0.95 mJ pulse energies are suitable for seeded OPA schemes, and the narrow pulse spectral bandwidth in principle enables good spectral resolution with relatively simple frequency-scanning apparatuses.

Nd:YLF at 1.4 % doping presents a number of advantages over Nd:YAG for the production of high average power, kHz repetition rate picosecond laser pulses in regenerative amplification. The 12 cm^{-1} bandwidth of the Nd $^4F_{3/2}$ - $^4I_{11/2}$ 9497 cm^{-1} (1053 nm) line in a YLF host [3]

in principle allows the direct generation of shorter pulses compared to Nd in YAG while utilizing standard YAG optics. The 500 μs fluorescence lifetime of Nd in YLF is almost double that of Nd in YAG and, alongside a comparable absorption cross section, leads to good population inversion under gentler pumping conditions [3, 4, 5, 6]. Combined with the larger thermal conductivity and weaker thermal lensing, this facilitates straightforward design and efficient operation of regenerative amplifiers that work over a range of thermal loading. The present design builds upon earlier reports utilizing slightly different seed and extraction schemes [5, 4, 6].

A block diagram of laser system is shown below. The oscillator is a mode-locked fiber laser producing 8 ps pulses at 80 MHz centered at 1053 nm. The oscillator output is coupled into the resonator and the optical switch created by the Pockels cell, quarter-wave plate and polarizer traps a single pulse in the cavity to seed regenerative amplification. After a suitable number of passes, the pulse is extracted from the cavity and leaves the regenerative amplifier with a final energy of 0.8 mJ. Both pulses are the amplified further in two passes through a pair of laser heads. The final result is a pair of 0.95 mJ, 8 ps, 1053 nm pulses produced at 1 kHz in beams exhibiting good TEM_{00} mode quality.

C.2.2 Optical layout

The telescope formed by the fiber pigtail termination (L1) and a $f = 10$ cm lens (L2) approximately matches the seed beam size and divergence to the resonator mode. The resonator is a so-called "long" hemispherical design with one flat mirror (M2, radius of curvature $R_2 = \infty$) and one focusing mirror (M1, radius of curvature $R_1 = 3$ m) spaced by a distance $L = 2.22$ m. The $1/e^2$ intensity radii w at the waist, M1 and M2 are

$$\begin{aligned} w_2^2 &= \frac{L\lambda}{\pi}\sqrt{\frac{g}{1-g}} = w_0^2 \\ w_1^2 &= \frac{L\lambda}{\pi}\sqrt{\frac{1}{g-g^2}} \end{aligned} \tag{C.1}$$

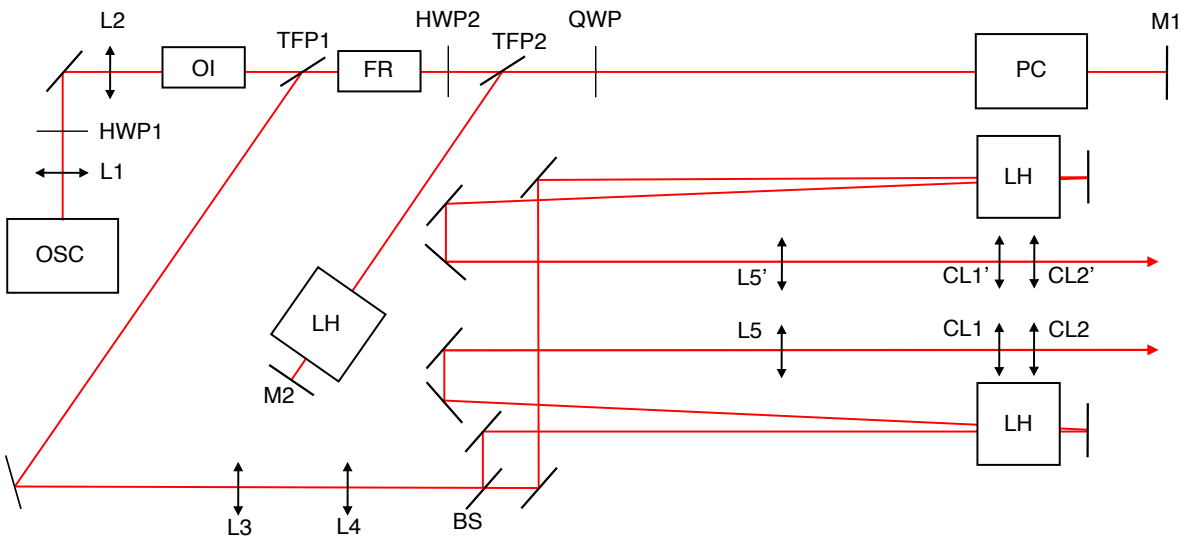

Figure C.1: Block diagram of the Nd:YLF laser system. OSC: fiber oscillator; LH: diode-pumped Nd:YLF laser head; PC: Pockels cell; FR: Faraday rotator; OI: optical isolator, BS: 50-50 beam-splitter; TFP: thin-film Brewster polarizer; QWP: quarter-wave plate; HWP: half-wave plate; CL: cylindrical lens, L: spherical lens. All optics are antireflection coated at 1053 nm.

where $g = 1 - L/R_1$. The expected beam waist is 0.65 mm and occurs at M2, while the beam is largest at M1 with a calculated 1.3 mm radius. This mode profile minimizes the energy density at the KD*P Pockels cell, which has a relatively low damage threshold and high nonlinear refractive index, while remaining compact enough at the 1.5 mm radius laser rod to produce negligible aperture diffraction. The electrooptic switch consists of a quarter-wave plate, thin-film polarizer TFP2, and the Pockels cell with associated driving electronics. The thin-film polarizers are oriented at Brewster's angle for p-transmission and s-reflection. The switch is therefore configured to extract a single p-polarized pulse from the cavity, which then undergoes rotation with a half-wave plate and Faraday rotator to exit the amplifier s-polarized.

The size and divergence of the exiting beam are that of the resonator mode, and this is insufficient for subsequent amplification without aperture diffraction from the laser rods. A a pair of f = 10 cm lenses (L3 and L4) form an effective long-f positive lens and produce 0.9 mm beam radii at the external laser heads. Thermal birefringence in the pumped rods imparts substantial astigmatism to the exiting beams. Spherical-cylindrical Keplerian telescopes formed by L5 (f = 30 cm),

CL1 (f_h = 10 cm) and CL2 (f_v = 13 cm) correct most of the astigmatism and produce round beams of 1.1 mm radius and M^2 = 1.1.

C.2.3 Operation and performance

The regenerative amplifier operation my be broken into four steps. The seed beam is first coupled into the resonator. The electrooptic switch then simultaneously traps a single seed pulse in the resonator and spoils the cavity for all subsequent oscillator pulses with an 8 ns risetime. The single trapped pulse then seeds lasing action in the pumped Nd:YLF rod and experiences gain over many round trips in the resonator. Finally, upon saturation of the available gain, the pulse is cavity-dumped and extracted.

The major parameters which determine the output characteristics of the regenerative amplifier are the circulation time of the pulse in the cavity, and the pumping strength and duration on the Nd:YLF laser rod. Stronger and longer rod pumping increases the population inversion, and therefore the output power and single-pass gain, but this also leads to greater amplified spontaneous emission (ASE) and "free running" of the laser. Similar effects occur when the cavity is closed for too long. Longer pulse circulation in the cavity does, however, promotes a better-defined spatial mode. The present configuration utilizes a 78 amp, 167 μs square pulse to the pumping diodes. The cavity is closed for a 730 ns window near the end of the diode pulse where the gain is largest. With these parameters the laser operates as a proper regenerative amplifier, with saturated and stable output under a wide range of seed energies, and minimal output in the absence of a seed. Although a small ASE background is visible in Figure C.2a as the low-level signal that builds up in between pulses passes, it is not efficiently outcoupled from the cavity and the external pulse contrast ratio is $\sim 10^3$.

The maximum pulse energy which can be obtained without distorting the pulse shape or spectrum is determined by gain saturation and nonlinear refraction effects. For a pulse that is much

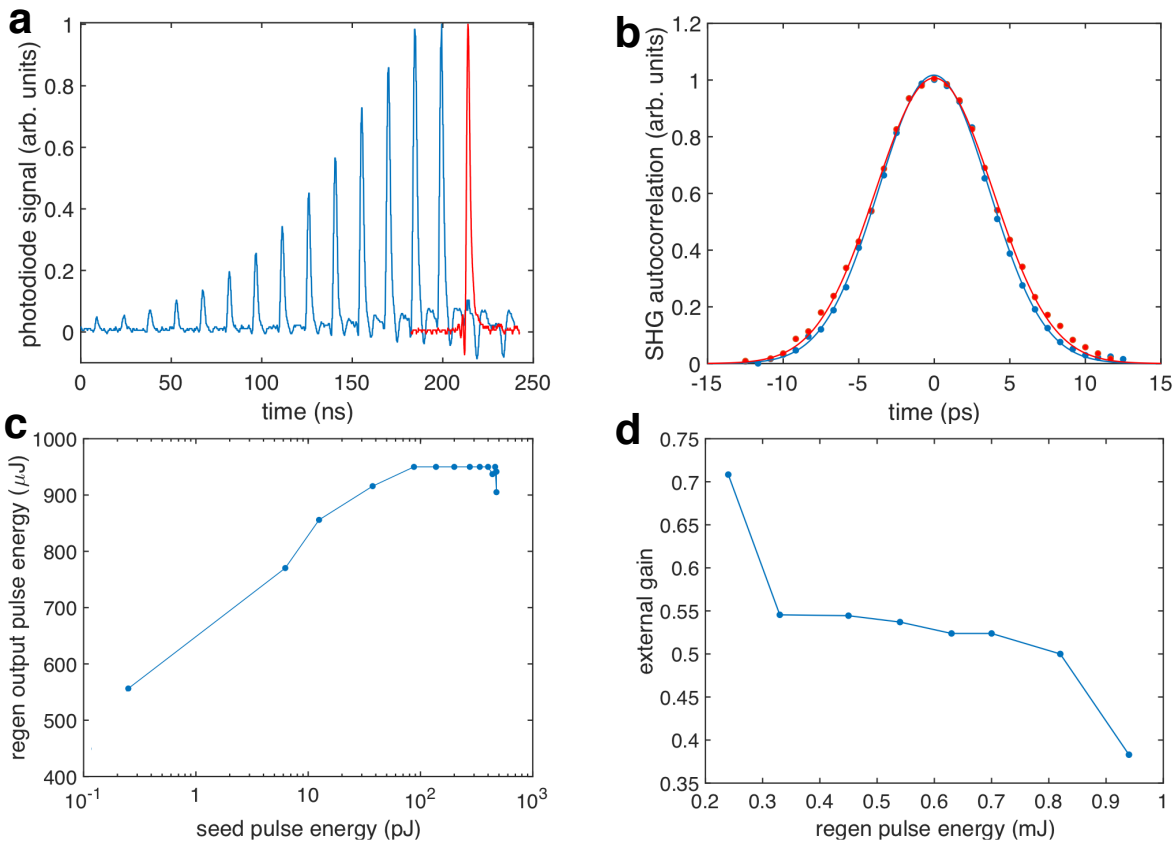

Figure C.2: Summary of Nd:YLF laser performance. (a) Pulse buildup characteristics in the regenerative amplifier cavity (blue) and cavity-dumped pulse (red); (b) Second-harmonic autocorrelation traces of the pulse after regenerative amplification (blue) and external amplification (red) with respective 8.1 and 8.9 ps fwhm Gaussian fits; (c) Dependence of the regenerative amplifier output on seed pulse energy; (d) Single-pass gain of the external laser heads.

shorter than the lifetime of the lower lasing transition, the saturation fluence is

$$U_s = \frac{\hbar\omega}{2\sigma} \tag{C.2}$$

where σ is the cross section [1]. In Nd:YLF, $\sigma \approx 2\times10^{-19}$ cm^2 [3, 7] and $U_s = 500$ mJ/cm^2. The optical fluence at the laser rod is about 65 mJ/cm^2 and saturation effects should be negligible.

The spectral effects of nonlinear refraction can be estimated by examining the imparted chirp [1]. The electric field for a Gaussian pulse expressed in terms of the pulse propagation parameters a and b is $E(t) = \exp\left(at^2\right)\exp\left(i(\omega_0 t + bt^2)\right)$. ω_0 is the carrier frequency, a characterizes the pulse

width, and b describes the linear chirp. The intensity is $I(t) = I_0 \exp\left(at^2\right)$, the phase is $\phi = \omega_0 t + bt^2$, and the instantaneous frequency is $\omega = d\phi/dt = \omega_0 + 2bt$. From the Fourier transform, the pulse fwhm bandwidth is $\Delta\omega = 2\sqrt{2\ln(2)}\sqrt{a\left(1 + b^2/a^2\right)}$. For a given pulse width, the presence of a frequency chirp broadens the spectral bandwidth by $\sqrt{2}$ when $a = b$. The phase acquired across a length L due to a nonlinear index n_2 is $\phi(t) = 2\pi(n_0 + n_2 I(t))L/\lambda$. Equating the phase shift $d\phi/dt$ due to n_2 and the definition in terms of a and b, we find that the approximate intensity at which $\Delta\omega$ increases by $\sqrt{2}$ is

$$I_0 = \frac{\lambda}{2\pi n_2 L} \tag{C.3}$$

This intensity is 1×10^{10} W/cm^2 for the 63 mm laser rod with $n_2 = 1.7 \times 10^{-16}$ cm^2/W. The peak intensities in the laser rods are also about 1×10^{10} W/cm^2. The calculated value considers just a single pass, and the accumulated broadening over several passes for the strong pulses just before outcoupling may be appreciable. This type of broadening will accumulate until the bandwidth approaches the 12 cm^{-1} gain bandwidth of Nd:YLF [3], after which spectral windowing and nonlinear chirp can produce more complicated effects such as satellite pulses [5]. Future increases of the regenerative amplifier output power should be possible with chirped-pulse amplification or a larger diameter beam and laser rod. At higher energies, however, additional effects such as Pockels cell thermal blooming may become important [6].

After extraction from the regenerative amplifier, the 0.8 mJ pulse is split into two 0.4 mJ pulses for additional amplification. The external laser rods are 3×63 mm just as in the laser cavity, but the pumping diodes are configured for stronger excitation. The absence of a cavity relaxes restrictions on the strength and duration of diode pumping, and they are pumped in series with 80 amps for 120 μs by a single diode driver. The single-pass gain under these conditions is shown in Figure C.2d. Stronger or longer pumping does not appreciably increase the gain, indicating that these conditions produce the maximum population inversion.

After a single pass through the external laser heads, the clean Gaussian beam from the regenerative amplifier acquires a noticeable astigmatism when the external diode current is greater

than about 40 amps. Rapid cessation of diode pumping causes the astigmatism to disappear on a timescale visible to the eye, about 1 second, and the astigmatism is therefore assigned to a birefringent thermal lens. Although Nd:YLF indeed presents a weaker lower thermal lens than Nd:YAG [8], it remains substantial under the present pumping conditions, in contrast to early studies [8]. This may be due to the kHz repetition rate and absence of mode-selecting cavity. The thermal lens was measured as previously done for Nd:YLF [9] by overfilling the laser rod with a cw probe beam and measuring the intensity transmitted by a narrow slit placed a distance d from the rod exit face. The transmitted probe is focused into a silicon detector with a cylindrical lens oriented perpendicular to the slit, and the slit orientation gives the horizontal or vertical effective focal length f. They are determined from the measurement as

$$f = \frac{d}{1 - I/I_0} \tag{C.4}$$

where I_0 is the probe intensity transmitted by the slit in the absence of diode pumping and I is the transmitted intensity with diode pumping. At 530 nm we find $f_h = 1830$ cm and $f_v = -530$ cm for a single pass with s-polarized light. With p-polarized light the measurement gives $f_h = 1000$ cm and $f_v = 4200$ cm. The focal lengths for s polarization are consistent with measurements of the amplified 1053 nm beam. After both passes through the external amplifier, the input 1053 nm beam with $w_h = 0.91 \pm 0.05$ and $w_v = 1.0 \pm 0.07$ exhibits $w_h = 1.17 \pm 0.3$ mm and $w_v = 0.78 \pm 0.1$ mm at a distance of 130 cm.

Due to this thermal lens, more than two passes of external amplification would necessitate multiple telescopes and a more complicated optical setup. It is also likely that the thermal lens constitutes a notable loss mechanism in the regenerative amplifier. Although intracavity cylindrical lenses could in principle compensate for these losses and produce a more efficient laser operation, this would come at the cost of a substantially more difficult cavity alignment.

C.3 BBO-KTA Optical Parametric Amplifier

The BBO-KTA OPA is a two-stage apparatus which produces tunable near- and mid-infrared light of moderate intensity appropriate for probe and weak pump pulses. The major advantage of KTA over the more common phosphorus isomorph, KTP, is the greater infrared transparency window reaching beyond 4 μm, and it has seen considerable usage in nanosecond optical parametric oscillators [10, 11, 12, 13, 14]. In the present scheme, the idler wave produced by parametric generation in BBO seeds the signal wave for parametric amplification in KTA, and idler wave generated in KTA is used for mid-infrared experiments. This scheme is utilized and optimized later in the LBO-LGS apparatus described in the following section. Figure C.3 shows a block diagram of the KTA apparatus and phasematching curves for BBO and KTA using the appropriate Sellmeier equations [15, 16] are shown in Figure C.4.

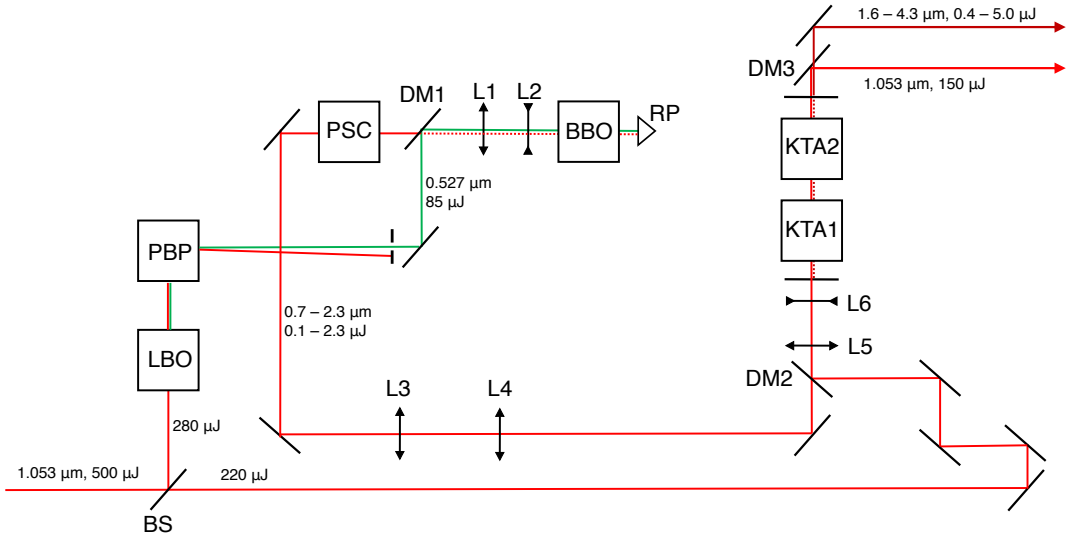

Figure C.3: Block diagram of the BBO-KTA OPA. LBO: LiB_3O_5 crystal; BBO: β-BaB_2O_4 crystal; KTA: $KTiOAsO_4$ crystal; BS: beamsplitter; PBP: Pellin-Broca prism; DM: dichroic mirror; RP: right-angle retroreflecting prism; PSC: polarization-rotating periscope.

1053 nm, s-polarized 500 μJ pulses in a 1.8 mm ($1/e^2$ intensity diameter) beam from the Nd:YLF regenerative amplifier are split in two by an approximate 50-50 beamsplitter to pump the seed and amplifier stages. In the seed stage, the 1053 nm light is first frequency-doubled in a 7

mm long LBO crystal cut for type-I phasematching (cut angles $\theta_c = 90°$, $\phi_c = 12°$) to produce 85 μJ pulses of p-polarized 527 nm light in a single pass. The second harmonic is separated from the fundamental by a Pellin-Broca prism and aperture. In the absence of this spectral filtering, residual 1053 nm light acts as a seed for degenerate parametric generation and strongly reduces the desired angle-tuned output. The angle-tuned BBO is 8 mm long, cut at $\theta_c = 23°$, $\phi_c = 0°$ for $k_3^e = k_1^o + k_2^o$ phasematching and pump propagation in the $x-z$ plane. A Galilean telescope reduces the 527 nm pump beam to 0.6 mm diameter at the crystal with a divergence of about 0.5 mrad. This pumping configuration is chosen to maximize the pump intensity while also attempting to mitigate unavoidable spatial walkoff effects. In negative crystals such as BBO, the internal walkoff angle ρ between the pump experiencing n_e and generated beams experiencing n_o is [17]

$$\rho = \arctan\left(\left(\frac{n_o}{n_e(\theta)}\right)^2 \tan(\theta)\right) - \theta \tag{C.5}$$

This gives $\rho \approx 3°$ and corresponds to a total displacement of 0.4 mm over the 8 mm crystal length, reducing the wave interaction length and single-pass parametric gain. Indeed, we only observe single-pass output exceeding 10 nJ close to degeneracy under these pumping conditions. To reverse the walkoff and increase the interaction length, the pump and parametric fluorescence are retroreflected for a second amplification pass by a 4 mm-hypotenuse fused silica right angle prism placed immediately behind the crystal. We then obtain s-polarized parametric generation across the 700 - 2300 nm range.

The seed beam exits the device via a standard green YAG mirror (DM1) with about 60% efficiency to produce usable output of a few nJ. A periscope rotates the polarization to p for appropriate phasematching in the KTA amplification stage. A telescope consisting of two positive achromats (L3 and L4) in the 1.2 - 2.1 μm range corrects the beam divergence and approximately matches the beam size to that of the KTA pump. A stronger angle-independent red output around 650 nm is also generated which we tentatively attribute to stimulated Raman scattering from the BBO crystal. We empirically find this output to be much stronger when the pump beam overlaps with a damage

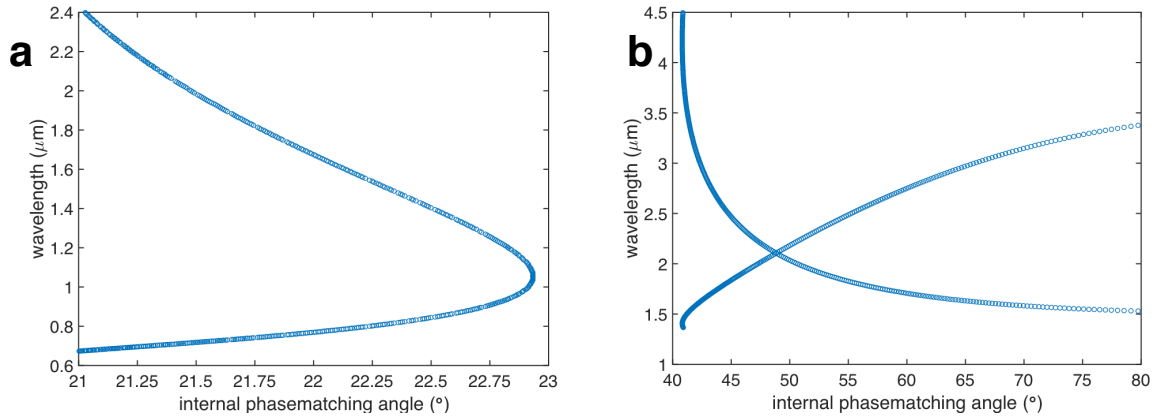

Figure C.4: Calculated phasematching curves for parametric amplification. (a) Phasematching curve for BBO pumped at 527 nm; (b) Phasematching curve for KTA pumped at 1053 nm.

spot on the crystal surface. Even in the absence of visible damage, however, this signal is $\sim$ 100 nJ and constitutes a substantial parasitic effect.

After suitable delay of the 1053 nm pump pulse, the parametric generation and 1053 nm laser light are made collinear by a standard 1053 nm high reflector (DM2), reduced in size by a telescope (L5 and L6), and propagated through a pair of 10 mm long KTA crystals cut at $\theta_c = 41°$, $\phi_c = 0°$ for $k_3^o = k_1^o + k_2^e$ phasematching and pump propagation in the $x - z$ plane. For angle-tuned phasematching and an s-polarized pump, the crystal is oriented with the y-axis normal to the optical table. Rotation allows access to the entire parametric amplification spectrum in about 9° of internal angle, as shown in the above phasematching curve. A gold mirror sends the pump and parametric beams back for a second amplification pass at a small elevation, and a second gold mirror sends the light out horizontally above the crystals. The pump beam diameter at the input face of KTA1 is 0.4 mm. This spot size and focusing was chosen to maximize the average intensity across both crystals and passes while retaining reasonable spatial pump/signal/idler overlap and avoiding optical damage. Under these pumping conditions, the first pass sees self-focusing reduce the beam size by about 20% across KTA1 and a further 30% across KTA2. This consistent with the reported nonlinear index $n_2 = 2 \times 10^{-15}$ cm^2/W [18, 19] and a self-focusing angle $\sqrt{2n_2 I/n}$ for peak intensity I and linear index $n = 1.8$ [20]. To minimize further self-focusing leading to intensities

above the crystal damage threshold, the gold mirror is placed at such a distance to allow for some diffractive spreading of the small beam.

The final result is strong infrared pulses tunable from 5 μJ near the 2.1 μm degeneracy point to 0.4 μJ at 4.3 μm. The signal and idler beams are respectively p- and s-polarized at these angles. The infrared conversion drops sharply at longer wavelengths due to linear absorption in the KTA crystal. For near-infrared pump mid-infrared probe studies, a CaF_2 dichroic mirror reflects approximately 70% of the unconverted 1053 nm light to serve as a pump beam and a Ge plate oriented at Brewster's angle with respect to the idler filters out the signal and residual pump light.

C.4 LBO-LGS Optical Parametric Amplifier

The BBO-KTA OPA just described is sufficient to produce stable probe beams out to about 4 μm, but it cannot extend to longer wavelengths due to infrared absorption of the KTA crystal and it also does not produce pulse energies suitable for strong optical pumping. Both of these shortcomings are solved with the LBO-LGS OPA described below. The LBO here is operated in a noncritical phasematching configuration to produce a stronger and more stable seed. Parametric generation and amplification in noncritically phasematched LBO has been reported previously [21, 22, 23, 24, 25, 26], but it has not to our knowledge been used to seed OPAs. The LGS crystal is a relatively new material that has recently been used in place of the more common AGS for parametric amplification beyond 4 μm [27, 28, 29, 30]. Its nonlinearity is smaller than that of AGS, but its larger damage threshold and wider gap enables direct strong pumping at 1053 nm and simpler optical designs.

C.4.1 Optical layout

A block diagram of the parametric amplifier is shown below. The amplified laser pulse is split into two portions by a polarizing beamsplitter and a half-wave plate. The weaker portion is frequency-doubled by a 7 mm LBO crystal ($\theta_c = 90^\circ$, $\phi_c = 12^\circ$) and filtered by a Pellin-Broca prism and

aperture. It is critical that the aperture be placed far enough from the prism to completely remove the 1053 nm light because it otherwise seeds degenerate parametric generation and spoils the seed generation efficiency. The 527 nm beam is focused by an $f = 75$ cm lens L1 into a 15 mm long LBO crystal cut for type-I noncritical phasematching ($\theta_c = 90°$, $\phi_c = 0°$), and the crystal is contained in a home-built brass oven held in a mirror mount. The spot size $2w_0$ is 0.1 mm in air. The parametric generation and pump beams are separated by a dichroic mirror DM1' with transparency > 90% between 560 and 2400 nm and > 98% reflectivity at 527 nm. Both beams are collimated by lenses L2 and L3. The former is an $f = 40$ cm lens placed 40 cm from the crystal and the focus of L1. The latter is an $f = 50$ cm lens placed about 40 cm from the L1 focus. This offset corrects for spatial modifications of the beam as it is focused through the LBO. Both beams are reflected back to focus and overlap in the crystal for additional amplification. The beams are collimated again by L1 and the parametric generation is extracted by DM1, which is identical to DM1'. It is then reduced in size by a 2:1 telescope to approximately mode-match the 1053 nm pump beam and sent collinear with a dichroic mirror which is highly reflective from 1150 - 1600 nm and transparent at 1053 nm. The beams travel unfocused through a 7 mm LGS crystal cut for type-I phasematching ($\theta_c = 49°, \phi_c = 0°$) for two passes with a small vertical angle. Most of the 1053 nm pump beam is removed by reflection from a ZnSe window at Brewster's angle, and the signal wave and residual 1053 nm are by a 2.4 μm dielectric longpass filter. ZnSe is chosen over the more common Ge or Si because even at Brewster's angle, the 1053 nm creates enough free-carrier absorption to reduce the transmitted idler energy by roughly $5 - 10\times$. The ZnSe/dielectric filtering scheme produces pure idler output from the OPA with a much higher throughput.

C.4.2 Operation and performance

The noncritically phasematched LBO is an ideal medium for seed generation because the walkoff angle is zero under these conditions. This enables the use of long crystals and focusing to maximize the pump intensity and interaction length. With the present optics, the pump confocal length

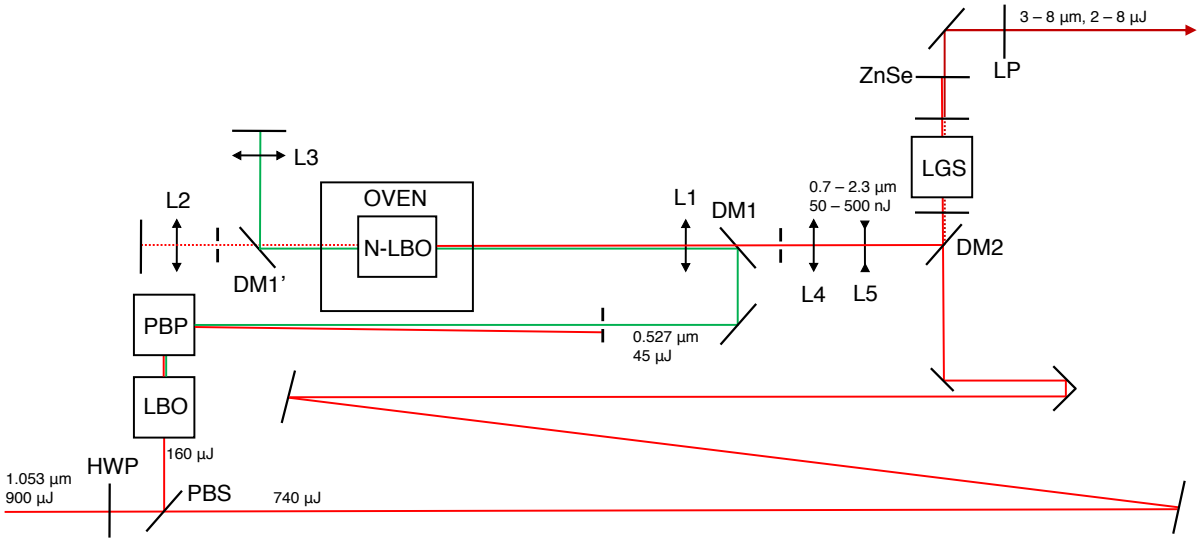

Figure C.5: Block diagram of the LBO-LGS OPA. LBO: LiB_3O_5 crystal; N-LBO: LiB_3O_5 crystal cut for noncritical phasematching; OVEN: home-built crystal oven; DM: dichroic beamsplitter;

$2\pi w_0^2 n/\lambda$ is about 80 mm in air, and the beam size is essentially constant across the entire crystal length. This promotes a narrower bandwidth of parametric generation because the angular acceptance is quite large under noncritical phasematching conditions. Under these pump conditions, a noticeable red signal is also generated. It may arise from stimulated Raman, as noted before in BBO, but it is also consistent with reports of the noncritical LBO parametric fluorescence spectrum that show a peak around 700 nm across the entire temperataure range [26], consistent with calculated phasematching [26, 24]. In either case, it is desirable to minimize this signal because it takes energy away from the idler which ultimately seeds the OPA. Much of the parametric generation occurs collinear with the pump beam while the red output occurs in a broader cone, and a pinhole placed between DM1' and L2 prevents further amplification of the red signal on the second pass. The optimal pinhole diameter is empirically found to be about 2 mm, allowing enough of the desired signal to be amplified while removing most of the parasitic red signal. Although these focusing conditions allow pump pulse energies up to about 140 μJ before approaching the LBO damage threshold the overall parametric amplification efficiency at the LGS stage plateaus around at 45 μJ of 527 nm and then falls beyond 60 μJ, likely because the stronger seed is offset by the

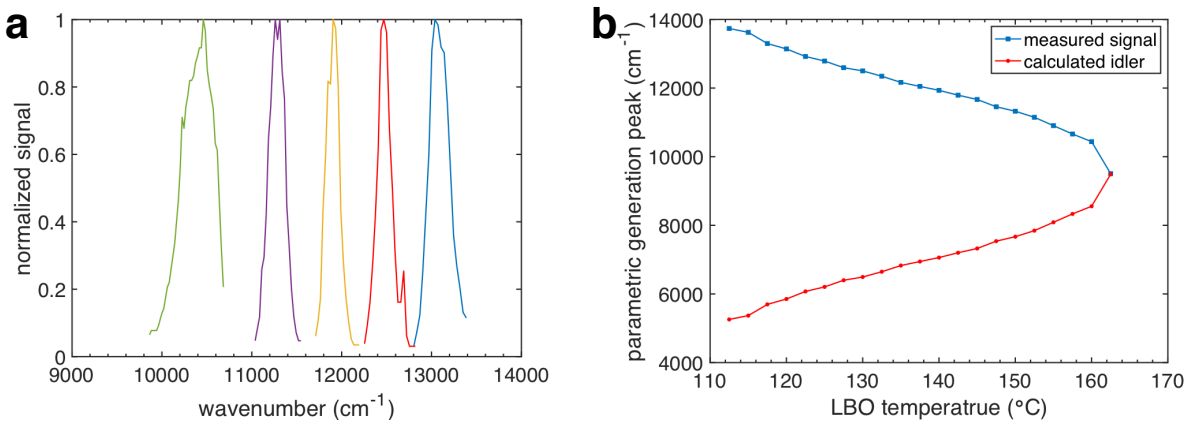

Figure C.6: (a) Representative signal spectra from 527 nm-pumped LBO under noncritical phasematching; (b) Experimental phasematching curve under the same pumping conditions.

lower 1053 nm pump energy. Spectra and an experimental phasematching curve are shown below.

The first pass through the LBO produces strong parametric generation that saturates standard biased InGaAs and Si photodiodes, but the generated light exhibits large shot-to-shot intensity fluctuations and total energies remain below 10 nJ except at the degeneracy point. After the second pass and outcoupling through DM1, the output is more stable and pulse energies are a few hundred nJ. The bandwidths are generally narrower than other reports of noncritically phasematched parametric fluorescence in LBO, and this may be due to the pump beam profile and pinhole. Both the bandwidth and pulse energy grow larger close to the 9497 cm^{-1} degeneracy point where the phasematching curve becomes vertical. Measured average pulse energies and fwhm bandwidths are shown in Figure C.7.

The parametric generation beam after outcoupling from DM1 is about 3× larger than the 1053 nm beam and recollimated 527 nm beam. This may be due to the large angular acceptance of noncritical phasematching and the additional gain from the second pass. A 2:1 telescope is used to reduce the seed beam size to approximately match the spatial profile of the 1053 nm beam. Measurable parametric amplification occurs in a single pass through the LGS crystal, and powers increase roughly threefold with the second pass. The resulting idler spectra, bandwidths and pulse

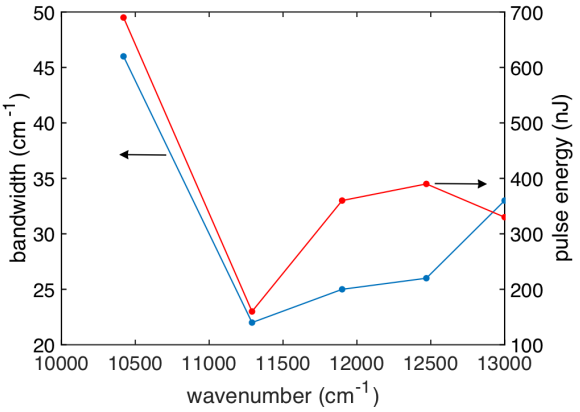

Figure C.7: Bandwidths and pulse energies corresponding to the spectra shown above for 527 nm-pumped LBO under noncritical phasematching.

energies are shwon in Figure C.8. The parametric amplification should be exponential with the effective crystal length as shown in Appendix B, and this implies much greater than threefold gain upon an effective doubling of the crystal length. Walkoff effects are unlikely due to the relatively large diameters of both beams, and imperfect mode matching or alignment is a more likely culprit. The absolute energies are also less than expected based on the seed pulse energies. Nevertheless, the overall quantum efficiency of conversion from 1053 nm to the mid-infrared is better than 5% without further optimization. These quantum efficiencies exceed typical values of 0.1 - 1% for parametric amplification, possibly due to the use of collimated beams and efficient seed generation. Unusually, the idler bandwidths exceed the seed bandwidths by almost a factor of two. The origin of this larger bandwidth is not yet clear but it may be related to the temporal behavior described below.

Sum- and difference-frequency crosscorrelations were measured to characterize the parametric amplification pulse widths and they are shown in Figure C.9. Both are asymmetric and markedly shorter than the harmonic autocorrelation of the 1053 nm laser pulse. The sum-frequency crosscorrelation was performed between the 1053 nm pump and 1300 nm seed by replacing the LGS with a KDP crystal, and varying the optical path length for the pump. It displays a fwhm of 4 ps. The OPA crosscorrelation was performed with the LGS crystal and again varying the pump path length,

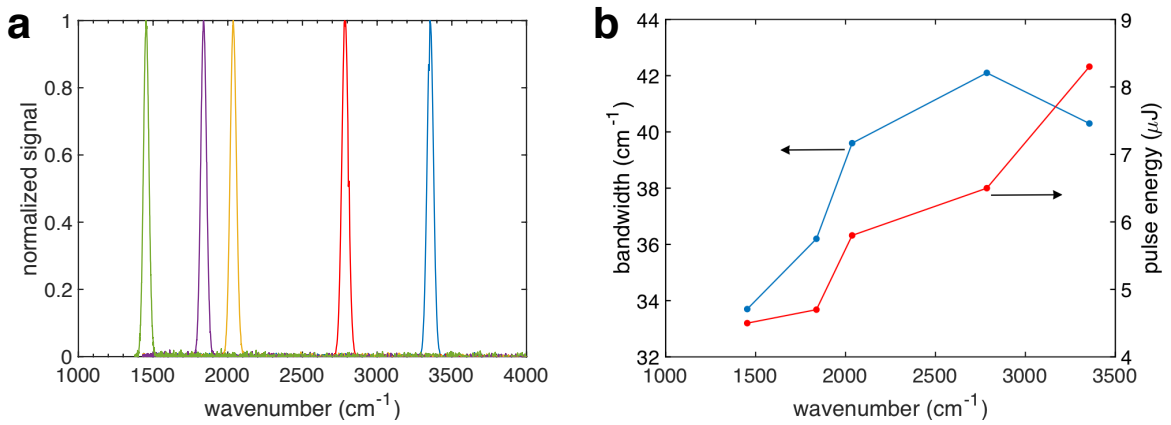

Figure C.8: Summary of LGS idler characteristics. (a) Representative idler spectra from seeded LGS pumped at 1053 nm; (b) Corresponding pulse energies and spectral bandwidths.

giving a 2.5 ps fwhm. The pump pulse is clearly modified in both media, and more drastically so in the LGS. This is qualitatively consistent with a nonlinear process due to the greater nonlinearity of LGS compared to KDP. Although the data exhibit some qualitative features of self-steepening, a more complete determination will require dedicated studies. These pulse distortions may benefit time-domain spectroscopy by shortening the effective pulse width, but if they are related to the bandwidth broadening noted previously, they could require correction in applications such as hole burning that require narrow bandwidths.

The pulse widths and energies should be sufficient to perform echo and saturation spectroscopies on mid-infrared electronic transitions. An echo experiment generates the strongest signal when π pulses are available. The π pulse corresponds to $\sigma N = 1$ where N is the optical fluence and σ is the transition cross section. For a typical value $\sigma = 2\times10^{-16}$ cm^2 and 5 μJ at 2000 cm^{-1}, corresponding to 10^{14} photons, π pulses are achieved with focusing to an area of 0.02 cm^2.

In a saturation spectroscopy such as dynamic hole burning, weaker pulses would be used to avoid power broadening. The laser bandwidth, however, should be considerably smaller than the homogeneous linewidth of the probed transition. This will likely require bandwidths around 10 to 15 cm^{-1}. Provided that the seed bandwidth controls the overall parametric amplification bandwidth, spectral narrowing of the seed should directly enable narrower mid-infrared output. This

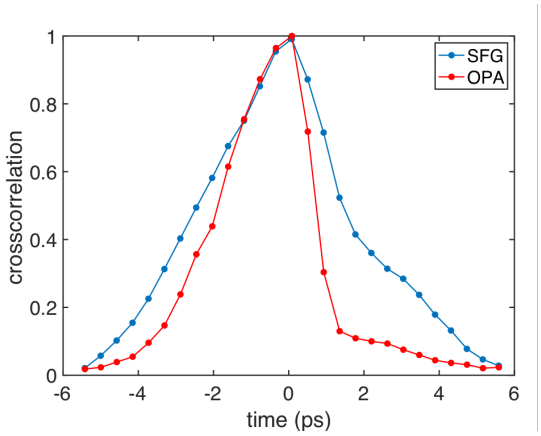

Figure C.9: Seed-pump sum-frequency crosscorrelation (blue) and seed-pump difference-frequency (OPA) crosscorrelation (red) for a 1300 nm seed.

can be done by replacing the mirror adjacent to L2 with a grating in the Littrow configuration [21, 24, 31]. Prior works have demonstrated sub-10 cm^{-1} bandwidths using such schemes with only moderate reductions in efficiency [21, 31]. An etalon could also be used, possibly with a higher efficiency at the cost of reduced tunability.

C.5 Photoluminescence Upconversion Apparatus

The photoluminescence upconversion apparatus adapts the early work of Hartmann and Laubereau [32] to the detection of transient photoluminescence signals in the 2 - 5 μm region with $\sim$ 10 ps time resolution. Upconversion commonly used in the visible region to obtain photoluminescence on timescales faster than accessible with avalanche photodiodes or streak cameras. In the infrared, however, avalanche photodiodes are extremely expensive and limited to about 100 ps, and streak cameras do not exist. Upconversion is therefore the most direct route to picosecond infrared photoluminescence data.

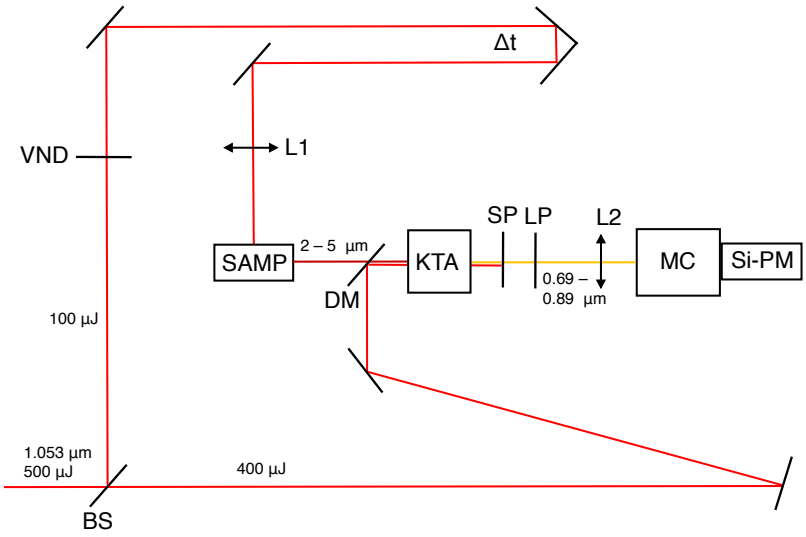

Figure C.10: Block diagram of the photoluminescence upconversion apparatus. BS: 80-20 beam-splitter; VND: variable neutral density filter; KTA: $KTiOAsO_4$ crystal; SAMP: sample; DM: dichroic 1053 nm 70% reflector on CaF_2; SP: dielectric 950 nm short-pass filter; LP: dielectric 690 nm long-pass filter; MC: 0.17 m monochromator with 0.5 mm slits; Si-PM: near-infrared sensitized silicon photomultiplier; L: lenses.

C.5.1 Optical layout

A block diagram of the upconversion apparatus is shown in Figure C.10. Pulses from the regenerative amplifier are split into two paths by a 20% dielectric reflector. The weak path photoexcites a sample after attenuation and variable mechanical optical delay. An optional cylindrical or spherical lens (L1) may be used to focus the excitation depending on the particular situation. The photoluminescence is nominally emitted into 4π solid angle and a fraction is collinear with the strong laser pulse after the latter's reflection from a dichroic mirror (DM). The dichroic reflects about 70% of the 1053 nm and has a transmission around 70 and for p-polarized light in the near- and mid-infrared. The photoluminescence and laser pulse mix in a KTA crystal ($\theta_c = 41°$, $\phi_c = 0°$) with $k_3^o = k_1^o + k_2^e$ phasematching to generate a p-polarized pulse at the sum-frequency. For angle-tuning with an s-polarized pump, the crystal is oriented with the y-axis parallel to the optical table. Dielectric filters (SP and LP) filter out the laser light and weak second-harmonic which is also generated, and a 15 cm lens (L2) focuses the sum-frequency light into a 0.17 m monochromator

with 0.5 mm slits. Detection is accomplished with a near-infrared sensitized silicon photomultiplier and a gated integrator discriminates the sum-frequency signal from background photons. The experimental background signal is dominated by scattered 1053 nm light and great care is taken to minimize it with light baffles and seals.

C.5.2 Performance characteristics

The main figures of merit in an upconversion apparatus are the spectral resolution, detection efficiency and time resolution. The time resolution is dominated by the laser pulse properties and our subsequent discussions therefore emphasize the resolution and efficiency. The spectral resolution is the convolution of the monochromator bandwidth and the phasematching bandwidth of the sum-frequency generation process. The latter may be determined from the equation

$$\Delta k = \frac{\partial(\Delta k)}{\partial \nu} \Delta \nu_P \tag{C.6}$$

for a wavenumber ν and $\Delta k = k_3 - k_1 - k_2$. The λ_1 (photoluminescence) wave has a wide bandwidth and λ_2 has a narrow spectrum in an upconversion experiment. In this situation, calculating the point at $\Delta k = 0.886\pi/L$ which corresponds to the FWHM output power, we obtain

$$\Delta \nu_P = \frac{0.886}{L} \left| n_{o1} - n_{o3} - \lambda_1 \frac{\partial n_{o1}}{\partial \lambda_1} + \lambda_3 \frac{\partial n_{o3}}{\partial \lambda_3} \right|^{-1} \tag{C.7}$$

where L is the crystal length [17]. Shown below is the calculation for $L = 1$ cm using the Sellmeier equations of Fenimore [16]. The phasematching bandwidth is below 25 cm^{-1} throughout the near-infrared, while it is much larger in the mid-infrared due to a divergence at 2300 cm^{-1}. This divergence corresponds to the vertical idler region shown earlier in the phasematching curve for the BBO-KTA OPA.

The resolution of a monochromator with $f-$matched imaging, neglecting the grating resolving

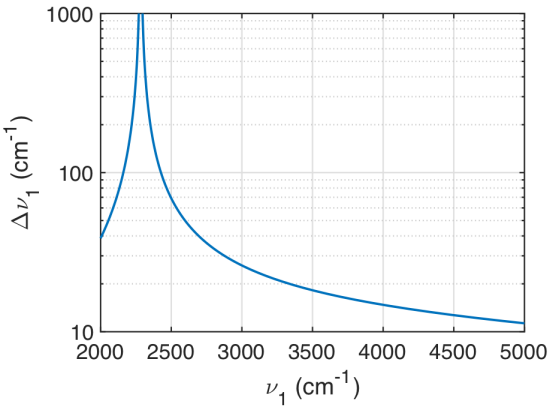

Figure C.11: Calculated phasematching bandwidth for $k_3^o = k_1^o + k_2^e$ sum-frequency generation in KTA with $\lambda_2 = 1053$ nm.

power, is

$$\Delta\lambda_M = \frac{D}{f}\left(\frac{d\lambda}{d\theta}\right) \tag{C.8}$$

where D is the slit width, f is the focal length of the focusing lens, and $\frac{d\lambda}{d\theta} = 1/a\cos\theta$ for grating groove spacing a and diffraction angle $\theta = \arcsin(\lambda/a)$. It is plotted below for the experimental parameters $a = 833$ nm, $f = 150$ mm and $D = 0.5$ mm for both the raw monochromator wavelengths and corresponding upconversion wavenumbers. The vanishing bandwidth calculated at longer wavelengths is unphysical and corresponds to $\lambda > a$, where solutions to the standard grating equation are complex.

The contribution from the grating resolving power is

$$\Delta\lambda_R = \frac{\lambda}{N} \tag{C.9}$$

where N is the number of illuminated grating grooves. Assuming the sum-frequency beam diameter decreases as the square-root [20] and taking a pump beam diameter of 3 mm, we have $\Delta\lambda_R = 0.4$ nm at 800 nm wavelength. This contribution will be small over most of the spectral range. The instrument bandwidths are generally comparable to the phasematching bandwidths in the near-infrared, while the overall bandwidth will be clearly dominated by the instrumentation in

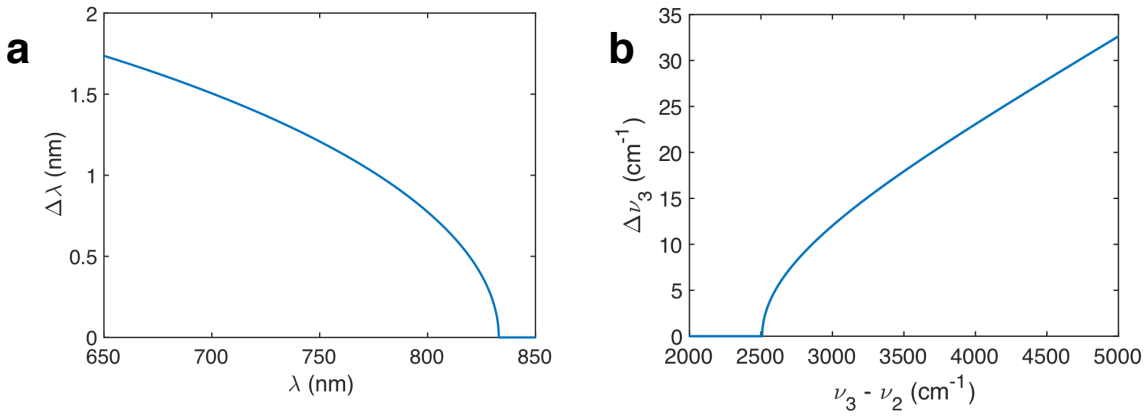

Figure C.12: Calculated monochromator resolutions in upconversion. (a) Monochromator wavelength resolution versus sum-frequency wavelength; (b) Monochromator wavenumber resolution versus low-frequency wavenumber.

the mid-infrared.

The total bandwidth $\Delta\nu$ is obtained by convoluting the contributing spectral functions. In the approximation of Gaussian lineshapes, the reciprocal convoluted bandwidth is the sum of reciprocal contributing bandwidths and we therefore have

$$\Delta\nu = \frac{1}{1/\Delta\nu_P + 1/\Delta\nu_M + 1/\Delta\nu_R} \tag{C.10}$$

The final result is a calculated resolution better than 50 cm^{-1} FWHM across the 2000 - 5000 cm^{-1} region. This could be verified with a narrowband mid-infrared light source.

The overall per-pulse detection efficiency η for infrared photons in the visible is given by the product of contributions from the pulse width, radiative rate, bandwidth, upconversion angular acceptance and efficiency, detector sensitivity, and grating efficiency:

$$\eta \sim \frac{\tau_P}{\tau_R} \times \frac{\Delta\nu}{\Delta\nu_E} \times \frac{\Omega}{4\pi} \times \frac{I}{I_c} \times \eta_G \times \eta_D \tag{C.11}$$

Here τ_P and τ_R are respectively the laser pulse width and sample radiative lifetime, $\Delta\nu_E$ is the sample emission bandwidth, Ω is the phasematched solid angle, I/I_c is the ratio of the pump

intensity to the critical intensity for complete upconversion, η_G is the grating diffraction efficiency, and η_D is the detector efficiency. This equation is illustrates the tradeoffs between sensitivity, time resolution and spectral resolution which are inherent to upconversion.

Ω is determined by the angular phasematching bandwidth $\Delta\theta$ under conditions of perfect phasematching. The bandwidth is obtained in a manner analogous to the spectral bandwidth, giving

$$\Delta\theta = \frac{0.886\lambda_2\Big(1 + (n_{o2}/n_{e2})^2 \tan^2\theta\Big)}{L\tan\theta\Big(1 - (n_{o2}/n_{e2})^2\Big)n_2^e(\theta)} \tag{C.12}$$

$\Delta\theta$ is about 1.5 mrad for the sum-frequency interactions considered here [17] and corresponds to an external angle $\Delta\theta_x = 2.7$ mrad for $n = 1.8$. With a pump beam of diameter $2w$ at the crystal face, we may estimate the light "collected" by the crystal by treating it as a lens of diameter $2w$, with image distance $z = 2w/\Delta\theta_x$ and solid angle $\Omega = \pi w^2/z$. This gives $\Omega = 6 \times 10^{-3}$ sr with the experimental value $w = 1.5$ mm.

The pump intensity needed for complete upconversion, following the development in the previous appendix and setting $\xi z = \pi/2$, is

$$I_c = \frac{\pi^2 c^3 n_1 n_2 n_3 \epsilon_0}{8L^2 d_{eff}^2 \omega_1 \omega_3} \tag{C.13}$$

where L is the crystal length and $d_{eff} \equiv 2\chi^{(2)}$ in the appropriate crystal direction. We find $I_c = 4 \times 10^8$ W/cm^2 using $n_1 \approx n_2 \approx n_3 = 1.8$, $d_{eff} = d_{32}\sin\theta \approx 2$ pm/V and $L = 1$ cm. In practice, increasing upconversion signal with increasing pump intensity is still observed at intensities around 8×10^8 W/cm^2, indicating that the above calculation underestimates I_c by at least 2×. This may come from spatial and temporal pulse profile contributions which have not been considered. The present estimate is likely to be correct within an order of magnitude, however, and we approximate $I/I_c \sim 1$ in the following. For the other parameters we have 10 ps pulses, a 500 ns radiative lifetime for mid-infrared transitions, 500 cm^{-1} emission bandwidth, 20% grating efficiency and 20% detector efficiency. This gives a total upconversion efficiency $\eta \sim 10^{-10}$.

The low value of η means that an average detection of one sum-frequency photon per laser pulse requires 10^{10} emitters in the photoexcited sample volume. This is readily achieved in close-packed quantum dot films or concentrated solutions, and signals at 1 kHz are detectable at lower densities with gated integration or lock-in detection. A few tens of photons per pulse are detected in practice for mid-infrared experiments, leading to good signal levels at the 1 kHz laser repetition rate with with gated integration.

Although signal enhancements at the level of orders of magnitude are not possible, there are some optimizations which may benefit experimental signal levels. One possibility is to optimize the monochromator grating, currently a specimen with 833 nm groove spacing and 400 nm blaze wavelength. Commercial gratings with 750 nm blaze wavelength and 1667 nm groove spacings are readily available and offer > 60% efficiency in the 700 - 850 nm region. In principle, a second direction is optimizing the photoluminescence upconversion fraction, but this will have small effects with the present configuration. Since $I/I_c < 1$ in practice, this ratio may be increased for a fixed crystal and laser pulse energy by reducing the beam size w or increasing the crystal length L, with an overall scaling $I/I_c \propto L^2/w^2$. However, these same changes affect the light collection as $\Omega \propto w/L$ and $\Delta\nu/\Delta\nu_E \propto 1/L$ so that $\eta \propto 1/w$ in the absence of walkoff and optical damage. This corresponds to $\eta \propto \sqrt{I}$. Materially increasing the upconversion efficiency is therefore likely to require new mixing crystals with larger d_{eff} or larger pump pulse energies. A common nonlinear material with a much larger d_{eff} is $AgGaS_2$ (AGS). Although preliminary experiments with AGS have been hampered by a broad autofluorescence background, this could be mitigated by optimizing the intensity or placing the mixing crystal far from the monochromator and detector.

REFERENCES

[1] A. E. Siegman, *Lasers*. Sausalito: University Science Books, 1986.

[2] P. W. Milonni and J. H. Eberly, *Laser Physics*. Hoboken: John Wiley Sons, 2010.

[3] A. L. Harmer, A. Linz, and D. R. Gabbe, "Fluorescence of Nd3+ in lithium yttrium fluoride," *J. Phys. Chem. Solids*, vol. 30, no. 6, pp. 1483–1491, 1969.

[4] P. Bado, M. Bouvier, and J. S. Coe, "Nd:YLF mode-locked oscillator and regenerative amplifier," *Opt. Lett.*, vol. 12, no. 5, pp. 319–321, 1987.

[5] J. S. Coe, P. Maine, and P. Bado, "Regenerative amplification of picosecond pulses in Nd:YLF: gain narrowing and gain saturation," *J. Opt. Soc. Am. B*, vol. 5, no. 12, pp. 2560–2563, 1988.

[6] M. Saeed, D. Kim, and L. DiMauro, "Optimization and characterization of a high repetition rate, high intensity Nd:YLF regenerative amplifier.," *Appl. Opt.*, vol. 30, no. 18, pp. 2527–2532, 1991.

[7] J. R. Ryan and R. Beach, "Optical absorption and stimulated emission of neodymium in yttrium lithium fluoride," *J. Opt. Soc. Am. B*, vol. 9, no. 10, pp. 1883–1887, 1992.

[8] J. E. Murray, "Pulsed Gain and Thermal Lensing of Nd:YLF," *Quantum Electron. Lett.*, vol. 19, no. 4, pp. 488–491, 1983.

[9] H. Vanherzeele, "Thermal lensing measurement and compensation in a continuous-wave mode-locked Nd:YLF laser," *Opt. Lett.*, vol. 13, no. 5, pp. 369–371, 1988.

[10] H. R. Chuang, T., Kasinski, J., Verdun, "A KTA Optical Parametric Oscillator Pumped by a Q-Switched, Injection-seeded Nd:YAG Laser," in *OSA TOPS Adv. Solid-State Lasers*, vol. 27, pp. 579–586, 1996.

[11] M. S. Webb, P. F. Moulton, J. J. Kasinski, R. L. Burnham, G. Loiacono, and R. Stolzenberger, "High-average-power KTiOAsO˙4 optical parametric oscillator," *Opt. Lett.*, vol. 23, no. 15, p. 1161, 1998.

[12] S. Das, S. Gangopadhyay, C. Ghosh, and G. C. Bhar, "Singly-resonant optical parametric oscillator based on KTA crystal," *Pramana - J. Phys.*, vol. 64, no. 1, pp. 67–74, 2005.

[13] X. L. Dong, B. T. Zhang, J. L. He, H. T. Huang, K. J. Yang, J. L. Xu, C. H. Zuo, S. Zhao, G. Qiu, and Z. K. Liu, "High-power 1.5 and 3.4 um intracavity KTA OPO driven by a diode-pumped Q-switched Nd:YAG laser," *Opt. Commun.*, vol. 282, no. 8, pp. 1668–1670, 2009.

[14] Q. Liu, J. Liu, Z. Zhang, and M. Gong, "A high energy 3.75 μm KTA optical parametric oscillator at a critical angle," *Laser Phys. Lett.*, vol. 10, no. 7, p. 075407, 2013.

[15] K. Kato, "Second-Harmonic Generation to 2048 Å in β-BaB2O4," *IEEE J. Quantum Electron.*, vol. 22, no. 7, pp. 1013–1014, 1986.

[16] D. L. Fenimore, K. L. Schepler, U. B. Ramabadran, and S. R. McPherson, "Infrared corrected Sellmeier coefficients for potassium titanyl arsenate," *J. Opt. Soc. Am. B*, vol. 12, no. 5, p. 794, 1995.

[17] V. Dmitriev, G. Gurzadyan, and D. Nikogosyan, *Handbook of Nonlinear Optical Crystals*. Berlin: Springer-Verlag, 3e ed., 1999.

[18] H. P. Li, C. H. Kam, Y. L. Lam, F. Zhou, and W. Ji, "Nonlinear refraction of undoped and Fe -doped KTiOAsO4 crystals in the femtosecond regime," *Appl. Phys. B Lasers Opt.*, vol. 70, pp. 385–388, 2000.

[19] H. Li, C. Kam, Y. Lam, and W. Ji, "Femtosecond Z-scan measurements of nonlinear refraction in nonlinear optical crystals," *Opt. Mater. (Amst).*, vol. 15, no. 2, pp. 237–242, 2001.

[20] R. W. Boyd, *Nonlinear Optics*. Academic Press, 3 ed., 2008.

[21] G. Banfi, R. Danielius, P. D. Trapani, A. Piskarskas, R. Righini, C. Solcia, and R. Torre, "Travelling-wave parametric generation in LBO with microjoules pump pulses," in *Conf. Lasers Electro-Optics Eur.*, pp. 186–CWA6, 1994.

[22] T. Traub, F. Ruebel, and J. A. L'Huillier, "Efficient injection-seeded kHz picosecond LBO optical parametric generator," *Appl. Phys. B Lasers Opt.*, vol. 102, no. 1, pp. 25–29, 2011.

[23] D. R. Walker, C. J. Flood, and H. M. van Driel, "Kilohertz all-solid-state picosecond lithium triborate optical parametric generator," *Opt. Lett.*, vol. 20, no. 2, p. 145, 1995.

[24] J. Y. Zhang, J. Y. Huang, Y. R. Shen, and C. Chen, "Optical parametric generation and amplification in barium borate and lithium triborate crystals," *J. Opt. Soc. Am. B*, vol. 10, no. 9, pp. 1758–1764, 1993.

[25] J. Y. Huang, Y. R. Shen, C. Chen, and B. Wu, "Noncritically phasematched second-harmonic generation and optical parametric amplification in a lithium triborate crystal," *Appl. Phys. Lett.*, vol. 58, no. 15, pp. 1579–1581, 1991.

[26] S. Lin, J. Y. Huang, J. Ling, C. Chen, and Y. R. Shen, "Optical parametric amplification in a lithium triborate crystal tunable from 0.65 to 2.5 um," *Appl. Phys. Lett.*, vol. 59, no. 22, p. 2805, 1991.

[27] S. B. Penwell, L. Whaley-Mayda, and A. Tokmakoff, "Single-stage MHz mid-IR OPA using LiGaS ¡sub¿2¡/sub¿ and a fiber laser pump source," *Opt. Lett.*, vol. 43, no. 6, p. 1363, 2018.

[28] M. Seidel, X. Xiao, S. A. Hussain, G. Arisholm, A. Hartung, K. T. Zawilski, P. G. Schunemann, F. Habel, M. Trubetskov, V. Pervak, O. Pronin, and F. Krausz, "Multi-watt, multi-octave, mid-infrared femtosecond source," *Sci. Adv.*, vol. 4, no. 4, 2018.

[29] I. Pupeza, D. Sanchez, J. Zhang, N. Lilienfein, M. Seidel, N. Karpowicz, T. Paasch-Colberg, I. Znakovskaya, M. Pescher, W. Schweinberger, V. Pervak, E. Fill, O. Pronin, Z. Wei,

F. Krausz, A. Apolonski, and J. Biegert, "High-power sub-two-cycle mid-infrared pulses at 100 MHz repetition rate," *Nat. Photonics*, vol. 9, no. 11, pp. 721–724, 2015.

[30] K. Kaneshima, N. Ishii, K. Takeuchi, and J. Itatani, "Generation of carrier-envelope phase-stable mid-infrared pulses via dual-wavelength optical parametric amplification," *Opt. Express*, vol. 24, no. 8, pp. 8660–8665, 2016.

[31] W. R. Bosenberg, W. S. Pelouch, and C. L. Tang, "High-efficiency and narrow-linewidth operation of a two-crystal β-BaB2O4 optical parametric oscillator," *Appl. Phys. Lett.*, vol. 55, no. 19, pp. 1952–1954, 1989.

[32] H.-J. Hartmann and A. Laubereau, "Sensitive detection of IR photons with picosecond time resolution," *Appl. Opt.*, vol. 20, no. 24, pp. 4259–4262, 1981.